Continuum Mechanical Models for Design and Characterization of Soft Robots

by

Audrey Sedal

A dissertation submitted in partial fulfillment
of the requirements for the degree of
Doctor of Philosophy
(Mechanical Engineering)
in The University of Michigan
2020

Doctoral Committee:

Professor Sridhar Kota Co-Chair
Professor Alan Wineman, Co-Chair
Professor Vikram Gavini
Professor R. Brent Gillespie
Professor C. David Remy, Institute for Nonlinear Mechanics, University of Stuttgart

Audrey Sedal

asedal@umich.edu

Orcid ID:0000-0002-5890-5326

ACKNOWLEDGEMENTS

I would like to thank my committee. Sridhar Kota saw the big picture in my research and helped me describe its broader impacts. Alan Wineman's guidance in mechanics and physical modeling was invaluable. David Remy's rigorous technical discussion about modeling in robotics resulted in two excellent papers. Brent Gillespie helped me become a stronger technical communicator. Vikram Gavini provided a fresh perspective on my work. My committee were advocates for me in my career. Alan Wineman was always ready to share opportunities, David Remy to connect me with others in my field, and Brent Gillespie to review application materials. Thank you to the Toyota Research Institute for funding, and to liaison Alejandro Castro. Thank you to Facebook Reality Labs for a wonderful internship, especially Amir Memar, Tianshu Liu, Yiğit Mengüç, and Nick Corson for their support and insight. I would like to thank Talia Moore and the members of EMBiR Lab, and Ram Vasudevan and the members of ROAHM Lab for their help broadening my research perspective and presenting my work well. Keith Buffinton provided helpful comments and discussion, and Andy Poli provided experimental insight. Thank you to Margaret Kohler, Yixuan Wang, Yuxin Chen, Max Howarth, Sravan Balaji, Maria Mathew, Daniel Haley, and Michael Fisher. Thank you to ME IT (Michele Goci, Jonathan Klozik, Nick Cantu and Matthew New) for fixing various computer problems, and ME Facilities (Murray LaPointe, Charlie Weger and Matt Jastrzembowski) for making sure that lab runs properly. Thank you to my friends and family. My parents, Janice and Andrew Sedal provided support and encouragement. Steven Parkison was always ready to help me debug my code. Marie Rice introduced me to key mechanical tools and theories, and Aritra Sasmal helped me with mathematics.

PREFACE

Chapters 2-7 have been written as separate manuscripts. For this reason, there is some repetition of information, particularly in the motivating material, as well as small discrepancies in mathematical notations.

TABLE OF CONTENTS

CHAPTER

LIST OF FIGURES

Figure

LIST OF TABLES

<u>**Table**</u>

ABSTRACT

The emergence of “soft” robots, whose bodies are made from stretchable materials, has fundamentally changed the way we design and construct robotic systems. Demonstrations and research show that soft robotic systems can be useful in rehabilitation, medical devices, agriculture, manufacturing and home assistance. Increasing need for collaborative, safe robotic devices have combined with technological advances to create a compelling development landscape for soft robots.

However, soft robots are not yet present in medical and rehabilitative devices, agriculture, our homes, and many other human-collaborative and human-interactive applications. This gap between promise and practical implementation exists because foundational theories and techniques that exist in rigid robotics have not yet been developed for soft robots. Theories in traditional robotics rely on rigid body displacements via discrete joints and discrete actuators, while in soft robots, kinematic and actuation functions are blended, leading to nonlinear, continuous deformations rather than rigid body motion.

This dissertation addresses the need for foundational techniques using continuum mechanics. Three core questions regarding the use of continuum mechanical models in soft robotics are explored: (1) whether or not continuum mechanical models can describe existing soft actuators, (2) which physical phenomena need to be incorporated into continuum mechanical models for their use in a soft robotics context, and (3) how understanding on continuum mechanical phenomena may form bases for novel soft robot architectures. Theoretical modeling, experimentation, and design prototyping tools are used to explore Fiber-Reinforced Elastomeric Enclosures (FREEs), an often-used soft actuator, and to develop novel soft robot architectures based on auxetic behavior.

This dissertation develops a continuum mechanical model for end loading on

FREEs. This model connects a FREE's actuation pressure and kinematic configuration to its end loads by considering stiffness of its elastomer and fiber reinforcement. The model is validated against a large experimental data set and compared to other FREE models used by roboticists. It is shown that the model can describe the FREE's loading in a generalizable manner, but that it is bounded in its peak performance. Such a model can provide the novel function of evaluating the performance of FREE designs under high loading without the costs of building and testing prototypes. This dissertation further explores the influence viscoelasticity, an inherent property of soft polymers, on end loading of FREEs. The viscoelastic model developed can inform soft roboticists wishing to exploit or avoid hysteresis and force reversal. The final section of the dissertations explores two contrasting styles of auxetic metamaterials for their uses in soft robotic actuation. The first metamaterial architecture is composed of beams with distributed compliance, which are placed antagonistic configurations on a variety of surfaces, giving ride to shape morphing behavior. The second metamaterial architecture studied is a "kirigami" sheet with an orthogonal cut pattern, utilizing lumped compliance and strain hardening to permanently deploy from a compact shape to a functional one. This dissertation lays the foundation for design of soft robots by robust physical models, reducing the need for physical prototypes and trial-and-error approaches. The work presented provides tools for systematic exploration of FREEs under loading in a wide range of configurations. The work further develops new concepts for soft actuators based on continuum mechanical modeling of auxetic metamaterials. The work presented expands the available tools for design and development of soft robotic systems, and the available architectures for soft robot actuation.

CHAPTER 1

Introduction

1.1 Motivation

Living organisms including plants, invertebrates, and humans benefit from compliance in their bodies every day, whether bending in the wind, crawling through tight spaces, or absorbing the shock of a footfall. Advances in polymer chemistry, economic interests, and evolving social needs have introduced a capability and will to mass produce mechanisms that emulate these natural ones.

Mass-produced compliant mechanisms range from the mundane to the high-tech. Shampoo lids and other kinds of packaging often have a thin piece of plastic acting as a hinge. The compliance of a zip-tie allows it to wrap around objects of different sizes. Roboticists can create safer, easier to use, more precise, and more collaborative robots by incorporating compliant hardware into their mechanical designs [18]. These compliant parts may be lumped into specific locations in the robot (e.g. [33, 134]), or distributed across the entire robot's body [67, 84, 147]. The latter are early examples of "soft" robots: robotic mechanisms characterized by bodies made almost entirely from soft, stretchy materials.

Soft robotics research has been by economic needs in manufacturing, agriculture, and medical care. Devices have been researched in many of these areas, including rehabilitation [38, 120, 176], medical devices [23, 44], agriculture devices [89], and in-home assistive devices [1].

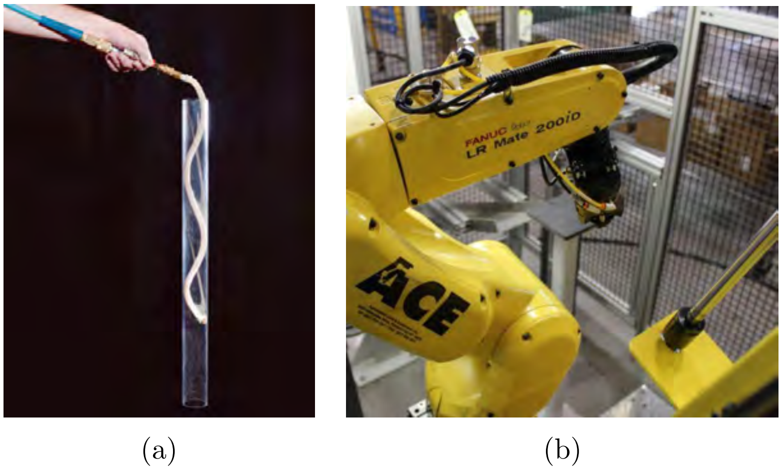
(a) (b)

Figure 1.1: A soft robot (left) and a rigid robot (right, Fanuc).

The promise shown by soft robots for human-collaborative uses is not yet realized outside of academia because of an inherent contradiction: the key aspects of soft robots that give them this great potential are also the ones that make them difficult to understand and challenging to deploy. These key aspects are listed below.

1. Soft mechanisms do not resemble traditional robots in a kinematic sense. The traditional format of a robot, with a separate power source (e.g. a battery), actuation (e.g. servo motors) and structure (e.g. metal linkages), is the basis for much of current theory in robotics [2]. However, in many proposed soft robot designs, these parts are not necessarily distinguishable from one another. For example, in the chemically powered soft robots of Shepherd et al. [151] and Mirvakili et al. [101], dissipated chemical energy changes the structure and attributes of the soft robot: its internal volume expands and its interior is pressurized. Or, in articulated soft robots like [71], soft actuators form the robot's main structure.

2. Compared to rigid robots, soft robots undergo large local deformations during typical use [135], enabling them to deform around delicate objects or maneuver in small spaces. This idea does not fit comfortably into existing robotic theory:

a soft, stretchy body can be said to have infinite degrees of freedom (DoF) [166] because it can be deformed or undergo tension and compression in any local region. With infinite DoF to choose from, it is a challenging task to isolate which of those is important and how the context may inform that importance. Further, the local deformations undergone by these materials often have a nonlinear stress response, making it difficult to create linear systems of differential equations that describe the robot's motion. It follows that traditional control algorithms and design methods have limited success for soft robots.

3. Finally, soft robots are often impedance- or compliance-matched to their environments [50, 74, 92]. For a robot to handle delicate items like biological tissues, to deform around obstacles, or to avoid injuring a human collaborator while still effectively completing a task, a its kinetics may be coupled to those of relevant environmental actors. These coupled dynamics may be nonlinear, especially if the robot changes shape.

These characteristics – blended function across the robot's structure, deformability across a robot's surface, and nonlinear impedance matching – give soft robots their core advantages of "mechanical intelligence" [135] and "inherent" potential for safety [7]. However, it is also because of these characteristics that problems in soft robot design and control have not been solved. Without a well-developed theory of soft robotics, we lack the fundamentals to create effective devices.

1.1.1 Overview

Roboticists have developed theories for a variety of traditional robot architectures by building simplified expressions of a robot's physics that still capture the core phenomena most important to the use of the robot in its intended context. Soft roboticists have generally operated earlier in this modeling life cycle, depicted in Figure 1.2. Most existing soft robotic architectures have been created in the last decade, and a large part of the soft robotics community continues to focus on novel soft robot architectures and simple models that enable proof-of-concept devices to be created (e.g. [8, 36, 53, 57, 69, 151]).

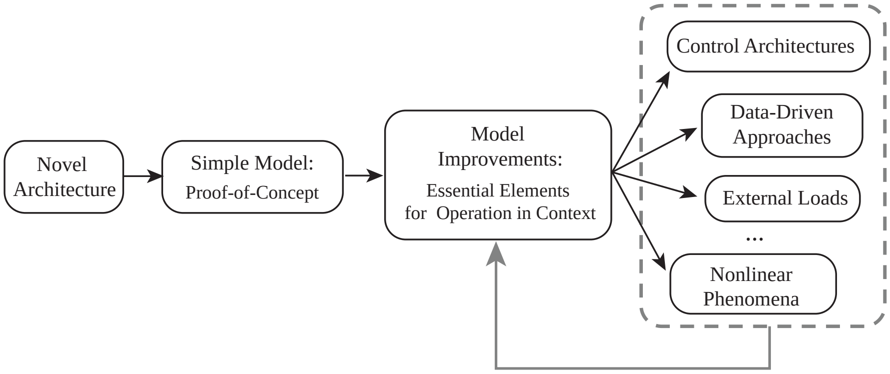

Figure 1.2: Life cycle of design and modeling of soft robots.

Work to improve models for soft robot use in context is increasing; older architectures like McKibben actuators have been more thoroughly investigated [73, 74, 166, 182] and newer ones are beginning to have more sophisticated models associated with them. However, even these improved soft robot models are not exhaustive: they might neglect external loads in certain directions ([26]) or from certain environmental actors (e.g. gravity), or approximate the robot's deformation with a thin beam approximation, [95, 175], or approximate behavioral properties like elasticity with lumped, linear components [33]. While these modeling techniques are mostly viable in the cases in which they are evaluated, they can potentially fall short in a larger use context: for example, a soft robot that is impedance-matched to its environment will almost certainly encounter significant end loads. And, a nonlinearly elastic component approximated with a simpler one could have unexpected shape changed or unaccounted-for instabilities.

Another way soft roboticists face these challenges is by using data-driven models whose parameters do not reflect physical quantities. Soft roboticists often use measurements taken on an already-built or already-proven system to determine task-appropriate model structure and parameters. These data-driven approaches can include machine learning or fitting virtual physical parameters (e.g. fitting values in a compliance matrix without reasoning about physical components).

Several researchers have shown that behavioral simplifications and data-driven approaches can work. However, since soft robotics is a new field, we still lack the tools to assess a priori what simplifications are admissible, or what data-driven approaches are viable. **This work aims to study key phenomena underlying soft robot behavior, while building tools and reasoning based on these phenomena that can be used to design and control soft robots.**

Understanding key phenomena (or, even, knowing which phenomena are 'key') is especially difficult in soft robotics. When thinking about physical phenomena in engineering systems, we might choose to reason either about gross behaviour of bodies, or about the ways that individual constituent particles interact. Most of the time, a method of reasoning is clearly dictated by the task. A roboticist making a simple model of a rigid manipulator would not reason about the molecular arrangement inside its metal links, and would instead be concerned with gross parameters like their strength. A chemist or materials scientist trying to model a stereolithography process, on the other hand, would reason about particles and connect this reasoning to curing behavior a polymer.

In soft robotics, the scale on which we should reason is not clear. Researchers have had success when reasoning about gross body behaviour [95], but have also successfully reasoned about material microstructure to create novel soft robotic functionality [83]. Both of these scales can work, but each can also be intractable. A soft robot's physics might be oversimplified to the point of providing to useful information, and particle-level reasoning including many potential physical phenomena can be computationally heavy. This kind of physics could require too much computation, may be subject to randomness that isn't important to gross object behaviour, or may depend on too many unknown parameters or conditions to yield a meaningful prediction.

This dissertation will investigate a view between these two extremes. Continuum mechanics offers a wealth of physical theories for material behavior with various properties under various conditions. Unlike rigid robotics, continuum mechanical theory describes material behavior. But unlike chemistry or statistical mechanics, continuum mechanical theory does not consider the activity of individual material particles. Instead, we use continuum mechanics to reason about the behavior of *homogenized* blocks of material. Since material behaviour, but not necessarily material chemistry, plays an important role in soft robot behaviour, it makes sense to investigate whether, and how, we can reason at this scale in soft robotics.

My dissertation will investigate how techniques and frameworks from continuum mechanics might be useful in soft robot design, modeling and control. I propose to show how insight about material behaviour how reasoning about homogenized blocks of material can improve our understanding of soft robots. I will highlight three behaviors which either have already formed, or might in the future form the basis for significant advances in soft robotics. They are:

1. Nonlinear Elasticity,
2. Viscoelasticity,
3. Auxetic, or Negative Poisson's Ratio (NPR) behaviour.

Soft robots often have highly elastic bodies. Common design frameworks for soft robots like PneuNets [67] and Fiber Reinforced Elastomeric Enclosures (FREEs) [8] involve patterning highly elastic polymers (e.g. PDMS, rubbers) with stiffer restraining elements (e.g. beams, fiber networks) to design soft robots with desirable shape changes on actuation. In continuum mechanics, *hyperelastic* material models are often used to describe highly stretchy polymers. These models focus on creating nonlinear representations of a material's *strain energy density*, i.e. the Helmholtz free energy stored inside the material as it locally expands or contracts [107]. In contrast to linear elastic models, these strain energy models can predict stress in materials at large deformations [156]. Ideally, models like these would allow design of better-suited soft systems to specific tasks, increased resilience, and better monitoring of the robot's activity during operation. Though researchers have shown that nonlinear elastic models can reflect soft robotic behaviour in specific cases, it is unclear how viable these techniques are in larger parameter spaces: we do not know what applications (if any) can best benefit from use of nonlinear elasticity, and we do not understand how nonlinear elastic models generalize across the diverse styles and constructions of today's soft robots. For these reasons, I will first investigate how nonlinear elasticity models can be used to predict loading on FREEs.

A second inherent property of polymeric soft robots is viscoelasticity, i.e. energy dissipation over time in a stressed material, which can cause stress relaxation, creep, and hysteresis. While soft roboticists are beginning to incorporate nonlinear elasticity into their models, viscoelasticity is a largely untouched phenomenon. Some researchers say it is “difficult” [69] to model: this may be due to experimental barriers in characterizing physical parameters, potential for heavy computation requirements, or challenges in identifying appropriate viscoelastic models for observed phenomena. Frequently, viscoelasticity is characterized on existing systems with data-driven techniques as a way of correcting errors in calculated plant dynamics [54, 72]. Frequently, this hysteretic behaviour is seen as an undesireable phenomenon that should be mitigated; the common choice of low-hysteresis polymers like silicone in the construction of soft robots is evidence if this view. However, viscoelastic energy dissipation can also be advantageous if we seek to add damping to soft robotic systems or match impedance with the environment.

Auxetic, or negative Poisson’s ratio (NPR) behavior might also be desirable in soft robotic systems. Including negative Poisson’s ratio materials in soft systems further expands the space of possible kinematics that the soft robot may have, possibly enabling better customization of that system to specifc tasks or environments. Auxetic materials have several other potential advantages in soft robotics that are not obvious: they can offer large net shape changes without large local strains, in contrast to the hyperelastic systems described above [19], can be designed to absorb shock and sound, and may have superior toughness and tear resistance than positive Poisson’s ratio materials [179].

1.1.2 State of the Art

This project exists at the intersection of mechanical modeling and robotics. For this reason I will first give a brief overview of existing mechanical techniques for modeling soft, stretchy bodies, and then describe their current usage in soft robotics research.

Physicists, mathematicians, and engineers have created models that describe soft,

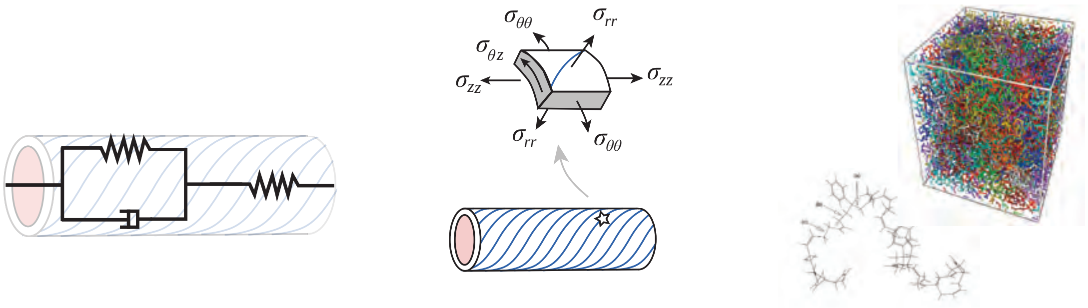

(a) (b) (c)

Figure 1.3: Schemata representing three ways to model soft devices. (a) Approximating the device with a lumped-parameter model. (b) A continuum mechanical model on a homogenized system with stresses $\boldsymbol{\sigma}$. (c) Molecular models. On the left, a molecule of SBR Rubber [20]. On the right, a representative volume element of a generalized rubber [6].

stretchy bodies at several different scales, and used them in several different contexts. We can differentiate them both by scale and by the phenomena considered at each scale. Lumped-parameter models, like those in Figure 1.3a, tend to operate at the scale of the body, separated into discrete elements (Figure 1.3a shows two springs and a damper) with separate, well-defined static or dynamic behaviors. Analysis of lumped systems becomes more computationally expensive as lumped elements, or networks of lumped elements are added. At the opposite end in terms of physical scale are molecular and atomistic models. Visual examples of such models are shown in Figure 1.3c; the left image is the lowest-energy configuration of a molecule of Styrene Butadyene Rubber (SBR) found in [20]; the right image is a representative volume element of a generalized elastomer used in a statistical rubber model in [6]. Because an elastomeric body is composed of many molecules that can have several physical interactions, molecular mechanical models are often computationally expensive. Continuum models fall somewhere in between these two extremes. By assuming that behaviors are homogenized across a body or a portion of a body, we can describe nonlinear behaviour of infinitesimally small volumes using a reduced amount of computation compared to large, complicated discrete models.

Continuum mechanical models can describe soft, stretchy objects with nonlinear loading-deformation characteristics, without the scaling computational load of an atomistic model. This balance makes them a strong candidate for use in soft robotics. Below, I summarize relevant continuum mechanical models in the three key areas described above, and describe how soft roboticists are currently implementing continuum mechanical reasoning.

1.1.3 Nonlinear Elasticity

A nonlinear elastic material is one whose stress and strain have a nonlinear relationship and where dissipation within the material is not significant. Both natural (e.g. biological tissues) and man-made (e.g. filled rubber in tires) stretchy materials are often studied using nonlinear elasticity theory. Many engineering applications for soft, highly elastic materials are concerned with defining boundaries on performance. We might ask, for example, what kind of load profile is required to break a rubber film. And, indeed, nonlinear continuum models have been studied for these purposes for decades [156]. Study of failure mechanisms like fracture of soft materials is an active research topic [27]. Nonlinear elastic models are also useful to characterize biological systems like arteries [62].

Nonlinear, elastic, incompressible materials have a specific constitutive relationship, derived from physical principles [131]. Rubber is often modeled under this description. This constitutive relationship connects the Cauchy stress tensor $\boldsymbol{\sigma}$ to the deformation gradient $\mathbf{F}$, a tensor describing the finite deformation of the body. The expression uses the Helmholtz free energy per volume ($\Psi(\mathbf{F}, \bar{b})$) dependent on the deformation gradient and any other relevant parameters ($\bar{b}$) and a Lagrange multiplier (q) that ensures expansions in the material's principal directions defined by the identity tensor ($\mathbf{I}$) follow volume conservation. The constitutive equation is shown below in Equation 1.1:

$$\boldsymbol{\sigma} = \frac{\partial \Psi(\mathbf{F}, \bar{b})}{\partial \mathbf{F}} \mathbf{F}^T - q\mathbf{I}. \tag{1.1}$$

Possible expressions for $\Psi(\mathbf{F})$ are varied. Depending on the phenomena that a researcher wishes to capture, they may build an expression for Ψ that includes terms relating to specific phenomena or principles. One example is the neo-Hookean model [130], which captures Helmholtz free energy stored due to stresses in principal directions of the material. Another example is the Mooney-Rivlin model[102, 130], which accounts for the neo-Hookean energy with improvements at higher stretches ($> 50\%$).

The soft robotics community is increasingly using this constitutive law for both design and control purposes. Klute et al. [73] use a Mooney-Rivlin strain energy density function to characterize the elastic stresses present in the elastomeric bladder of a McKibben actuator, concluding that the stresses stored by this bladder play an important role in the overall behaviour of the actuator. This work was recently extended in [154], where researchers use a constrained maximization formulation to solve the resulting problem when the fibers are allowed to be wound in asymmetic helices and the tube has pinched ends. Soft robotics authors also build on models developed for biomechanical systems: the authors of [26] use a theory of fiber-reinforced elastic material first presented to characterize the mechanical behaviour of the arterial walls [62]. Continuum mechanical theory predicts a reversal in direction of motion and/or axial force of a fiber-reinforced nonlinear-elastic tube [34, 51] that has been observed in soft robot prototypes [8].

However, these investigations are limited by assumptions that do not necessarily apply to the system's context of operation. In [73] and [154], the fibers are treated as completely inextensible, and in [26] external loads from the environment are not considered (e.g. leading due to contact in a haptic system, a wearable system, or manipulation of an object). Further, the importance of elastic nonlinearities across the wide variety of system architectures, tasks, and environments seen in soft robotics is not yet well characterized.

1.1.4 Viscoelasticity

Viscoelasticity is an umbrella term to describe material behaviour that is simultaneously influenced by both viscous phenomena, i.e. dissipative forces inside of the material structure, and elastic phenomena, i.e. energy storage inside the material structure under strain. Polymers like rubber [167] and silicone [129] are inherently viscoelastic in many of their use cases.

Similarly, biomechanical systems like arterial walls [61] and ligaments [113] have been found to be exhibit viscoelastic behaviour.

Viscoleasticity is a subject of extensive study in theoretical continuum mechanics [119, 133, 177], and is increasing in importance in robotics. Because viscoelasticity is an inherent property of polymers, and because soft robots are made from a wide variety of polymers, viscoelastic phenomena like creep, stress relaxation, and hysteresis are present on some level in every soft robotic system.

Soft roboticists often rely on extensive mechanical characterization of already-realized systems to understand their time-dependent properties. For example, the authors of [72] use a neural network and a full mechanical characterization to model hysteresis in a soft tactile sensor. In [169] and [103], cyclic experiments are done to characterize hysteresis of Pneumatic Artificial Muscles (PAMs) and PneuNets. Though appropriate mechanical characterization can successfully inform models of a particular system, it cannot necessarily inform the creation of new systems, predict how viscoelastic materials act together (e.g. a soft robot manipulating biotissue, or a soft robot made of a polymeric composite), or appropriately inform the control of such a system outside of known situations.

For these reasons, soft roboticists are beginning to use continuum viscoelastic theory in hardware design and controller development. The simplest viscous polymer models consider the polymer's elemental volumes as combinations of linear springs and dampers. At their simplest, they can be arranged in series, i.e. the Maxwell element in Figure 1.4a, or in parallel, i.e. the Kelvin-Voigt model in Figure 1.4b.

These simple models enable the creation of differential equations that connect stresses and strains in the material, and may be solved under known initial conditions.

(a) Maxwell material element comprised of a spring and damper in series.

(b) Kelvin-Voigt material element comprised of a spring and damper in parallel.

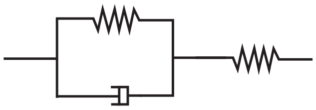

(c) Standard Linear Solid material element.

Figure 1.4: Kelvin-Voigt, Maxwell, and Standard Linear Solid model diagrams.

For example, [105], authors use a hyperelastic Yeoh rubber in parallel with a damper as in the Kelvin-Voigt model to create a dynamic model of a soft actuator. The dynamic model created there is shown to allow position control of a parallel module of FREEs.

However, these simple models have key limitations in a robotics context. The series damper of the Maxwell model describes liquid-like behaviour under imposed forces or deformations in the limit where time goes to infinity, limiting its potential accuracy for longer-term use situations of a soft robot. The parallel damper of the Kelvin-Voigt model does not allow for any instantaneous energy storage, meaning that this model may overestimate the necessary energy input to move a soft robot quickly. Indeed, the model presented by [105] increases in error as the input pressure rate to their system increases.

The Standard Linear Solid (SLS), modeled by the combination of springs and damper shown in Figure 1.4c, offers elastic-like behaviour in both the instantaneous and infinite-time cases. The authors of [153] use a Standard Linear Solid model to describe the impedance of a soft robotic fingertip, demonstrating that such a model could be used to match impedance to softer environments.

However, even the SLS model is limited in its ability to capture the viscoelastic behaviour of polymers. A material whose elemental volumes are described as combinations of linear springs and dampers will necessarily exhibit a proportional scaling between stresses and strains, but mechanicians as well as soft roboticists [26, 120], have repeatedly observed that this stress-strain linearity does not exist in their systems under normal operation circumstances.

As novel, functional materials are developed for use in soft robotic systems, an understanding of inherent viscoelastic behaviour will become increasingly important. Further, designs for soft robots are becoming more sophisticated - incorporating patterns of constraining elements and stretching elements, or incorporation of light-, magnetic-, temperature-, or electric field-influenced polymers. These developments require the development of a viscoelastic theory that can describe a wide variety of nonlinear viscoelastic behaviour for individual materials as well as patterns of materials that may differ in viscoelastic properties.

1.1.5 Auxetic Materials

Auxetic materials expand in all directions under tension, often due to specific geometry of their microstructure [80, 82, 89]. Auxetic behaviour is a *designed* or “mechanically programmable” property of a soft material. Unlike hyperelasticity and viscoelasticity, auxetic behaviour is not inherent to the polymers we see in soft robotics. This behavior may be incorporated by deliberately building structure or microstructure with specified geometry that influences the Poisson’s ratio.

Soft system prototypes and design methodologies using auxetic repeating cells have been developed. Of particular interest, mechanical “meta” materials have been created by modifying the macrostructure of existing materials such as polymers and foams. Some of these are based on projections of planar lumped compliant mechanisms [76, 77, 97]. Others are focussed on the relationship between the auxetic property and loading performance: [88] gives an overview of how networks of asymmetrically wound helical fibers or beams, exhibit auxetic behaviour and loading asymmetry. In [85], researchers show that a mechanical instability in certain foams can cause them to behave like auxetic materials.

Further, auxetic materials and metamaterials are popular in sports applications like shoe soles because of their potential shock-absorption properties [29, 137]. However, many of these design methodologies become more complex as the amount and dimension of repeating units increases, or require additional physical understanding to predict loading capabilities, failure, and other three-dimensional effects.

1.2 Organization of the Document

This dissertation discusses whether continuum mechanical models are capable of describing soft actuators, evaluates viscoelasiticity for its potential effects on soft actuator behaviour, and leverages auxetic behaviour of metamaterials to develop new designs concepts for soft robots . Chapter 2 offers a solution to a nonlinear elastic problem reflecting a deformed soft robotic actuator, and clarifies its potential use through two design case studies. Chapter 3 presents a validation of the model of Chapter 2 across the actuator design space and a comparison with other models of the same actuator for use in a robotics context. Chapter 4 presents a viscoelastic model for fiber-reinforced actuator and a simulation-based study of the effect of viscoelastic phenomena like stress relaxation and hysteresis on soft actuators. Chapters 5, 6 and 7 present various studies of auxetic metamaterials in soft robotics. Chapter 5 presents a design building block for synthesis of auxetic reinforcements for soft robots with a kinematic evaluation. Chapter 6 presents an expansion of the basic kinematic ideas of Chapter 5 to include patterning of auxetic mechanisms on a wider variety of surfaces. It further investigates the effects of auxetic reinforcements on fluid flow within a soft pneumatic robot. Chapter 7 presents kirigami patterns as a separate design building block for auxetic soft robot reinforcement, and shows how strain hardening of a deformed kirigami metamaterial may be leveraged in soft robotics. Chapter 8 offers conclusions of the dissertation and a pathway for future work.

CHAPTER 2

Nonlinear FREE Model and Design Case Studies

This chapter has been previously published and is used with permission from the American Society of Mechanical Engineers (ASME). It may referenced as:

> Sedal, Audrey, Bruder, Daniel, Bishop-Moser, Joshua, Vasudevan, Ram, and Kota, Sridhar. A Continuum Model for Fiber-Reinforced Soft Robot Actuators. *Journal of Mechanisms and Robotics* 10(2): 024501.

2.1 Introduction

The Fiber-Reinforced Elastomeric Enclosure (FREE) is a pneumatic actuator which consists of an elastomeric tube with fibers wound around it in specified helical configurations. Pneumatic actuators can be particularly useful in soft robotic applications due to their flexibility under loading, physical adaptability, and the ready availability of air, the working fluid [135]. Pneumatically actuated soft robots have demonstrated capabilities in biomimetic locomotion [96, 150, 160], assistive wearable devices [111, 139], and manipulators [98, 99]. Fiber reinforcement enables soft robots to create sophisticated motions and loading, including axial extension, rotation, and torsion [8–10, 78], but poses additional complexity in modeling.

Soft roboticists have developed a variety of methods to determine the behavior of FREEs under internal pressure. Many of these models rely on kinematic or kinetic assumptions that constrain the design space, like fiber symmetry [148, 164] and negligible external loading [26]. Others are built on assumptions that simplify the model formulation but demand lengthy experimental parameter determination like fitting shear moduli with an equibiaxial tension experiment [154], or separate design characterization for every prototype [13]. Finite element methods (FEM) can predict FREE movement [79]; however, the time-consuming nature of FEM and its inability to predict trends make it intractable for design optimization or control. It is therefore important to develop a model that captures the nonlinear relationship between a FREE's material, loading, and deformation and the coupling behavior it exhibits between axial stretch and torsion.

This chapter relates a FREE's torsional stiffness to its deformation and internal fluid pressure by extending a known hyperelastic composite modeling framework [62]. A major advantage of this formulation is its ability to predict physical phenomena, like torsion and radial expansion, in a computationally tractable way with a minimum of experimental parameter determination. In Section 2.2, a continuum model is described for a FREE with one fiber family, which is the simplest system exhibiting a combination of elongation and twist when pressurized. In Section 2.3, the model's computation and its experimental validation are explained. Section 2.4 compares the model's predictions with the measured behavior, and quantifies error. Section 2.5 illustrates possible design cases where the model is useful. Section 2.6 discusses potential avenues for error reduction and Section 2.7 describes possible future work.

2.2 Model

The properties of the FREE determine its behavior and impact decisions about how to model it. Our prototypes are made of latex rubber tubes with embedded woven threads. Therefore, we consider the FREE wall as a composite material with a hyperelastic matrix and embedded fibers.

The mode is built on four key assumptions:

1. A continuum approximation that ignores voids in the material and irregularity

Figure 2.1: FREE behavior when relaxed.

Figure 2.2: FREE behavior when relaxed (left) and pressurized (right) [13].

in the fiber deposition.

2. Neglecting interaction effects like sliding friction between the fiber and elastomer, and local buckling. This enables us to superpose the stress contributions of the fiber and elastomer. Models considering these assumptions have captured the behavior of composites in a number of engineering contexts [58, 62]; a detailed study of the effects of interaction effects in FREEs is left to future work.

3. The composite material of the FREE wall is assumed to be incompressible. This assumption is justified for FREEs since they are mainly composed of natural rubber, which commonly assumed to be incompressible [43].

4. Finally, the deformed FREE is assumed to be roughly cylindrical. This assumption is justified by the photos taken of inflated FREEs, as shown in Figures 2.1 and 2.2.

Together, these assumptions constitute a simple and efficient continuum framework that captures the key behaviors of FREEs, including nonlinear behavior of the fiber and elastomer, and axial stretch-torsion coupling.

2.2.1 Continuum Mechanical Framework

Below, the continuum framework are given and the key equations of the FREE actuator model are presented. Further foundational reading may be found in [34, 43, 62, 107].

$$\left\{ \begin{array}{c} \text{End-to-End Rotation } \Phi \\ \text{Axial Stretch } \lambda_z \\ \text{External Radius } r_o \end{array} \right\} \Leftrightarrow \left\{ \begin{array}{c} \text{Internal Pressure } P \\ \text{Twisting Moment } M \\ \text{(Axial Force F)} \end{array} \right\} \tag{2.1}$$

The FREE has three kinematic quantities and three loading quantities which fully define its shape and loading. When any three of the quantities in Equation 2.1

are fixed, the rest of the quantities are fully defined. So, we fix three quantities and use the continuum framework to create a system of equations that will allow us to solve for the others.

Since we are interested in the unique torsion-generating capabilities of FREEs, we solve for the twisting moment. To do this, we fix rotation Φ, axial extension λ_z and internal pressure while measuring the twisting moment. Under the continuum and cylindrical assumptions noted above, we create a geometric definition of the FREE's change of shape, and relate it to the stresses stored in the FREE wall. Integrating these stresses across the surfaces on which they act gives the loading.

2.2.2 Defining FREE Movement

Before finding the loading, a mathematical description of the FREE's shape-changing activity must be derived. This section presents the deformation gradient for a FREE, defining the continuous deformation of its surface.

Consider a FREE with a single fiber family that is wound at an angle Γ from the central axis, and consider a point on the FREE skin with coordinates R, Θ, Z as shown in in Figure 2.3. When inflated, the FREE undergoes a length change $L \to l$, a radius change $R_o, R_i \to r_o, r_i$, and the rotation of one endcap relative to another in radians defined by Φ. Assuming that the FREE is not buckled, the transformation of any point in the FREE wall can be written as a change of cylindrical coordinates from $R, \Theta, Z \to r, \theta, z$ as shown in Figure 2.3. The sign conventions used here are shown in Figure 2.4.

$$r = \sqrt{\frac{R^2 - R_i^2}{\frac{l}{L}} + r_i^2}, \tag{2.2a}$$

$$\theta = \Theta + Z\frac{\Phi}{L}, \tag{2.2b}$$

$$z = \frac{l}{L}Z = \lambda_z Z \tag{2.2c}$$

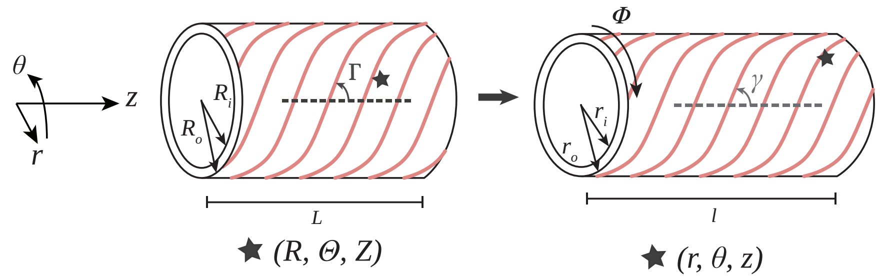

Figure 2.3: Motion of a point on the FREE wall. As the FREE inflates, the reference point changes coordinates (in the cylindrical coordinate system shown) from (R, Θ, Z) to (r, θ, z).

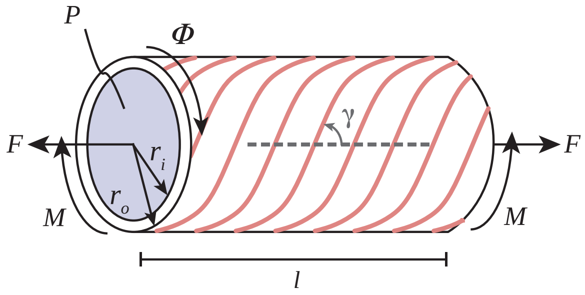

Figure 2.4: Torsional moment, rotation, and fiber angle sign conventions.

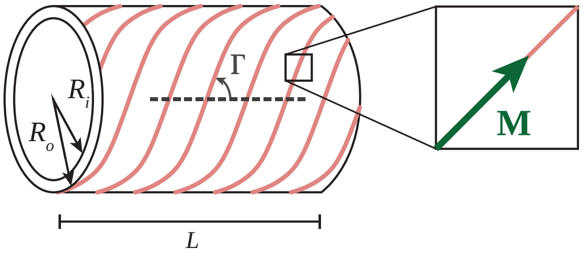

Figure 2.5: Fiber direction on a continuum element of the FREE wall.

Assuming incompressibility of the FREE skin, no end effects, and uniform stretching, the relationships of Equations 2.2a, 2.2b, 2.2c define this shape change.

The deformation gradient **F**, shown below, is the gradient of the coordinate transformation in Equations 2.2a, 2.2b, 2.2c.

$$\mathbf{F} = \begin{bmatrix} \frac{\partial r}{\partial R} & \frac{\partial r}{R\partial \Theta} & \frac{\partial r}{\partial Z} \\ \frac{r\partial \theta}{\partial R} & \frac{r\partial \theta}{R\partial \Theta} & \frac{r\partial \theta}{\partial Z} \\ \frac{\partial z}{\partial R} & \frac{\partial z}{R\partial \Theta} & \frac{\partial z}{\partial Z} \end{bmatrix} = \begin{bmatrix} \frac{R}{r\lambda_z} & 0 & 0 \\ 0 & \frac{r}{R} & r\frac{\Phi}{L} \\ 0 & 0 & \lambda_z \end{bmatrix} \tag{2.3}$$

As the FREE deforms, the helix created by the fiber changes. We define a unit vector **M** tangent to the fiber in the FREE's initial configuration as shown in Figure 2.5, and we can see below that pre-multiplying it by **F** gives the deformed, stretched fiber direction:

$$\mathbf{M} = \begin{bmatrix} 0 \\ \sin(\Gamma) \\ \cos(\Gamma) \end{bmatrix} \tag{2.4}$$

$$\mathbf{m} = \mathbf{FM} = \begin{bmatrix} 0 \\ \frac{r}{R}\sin(\Gamma) + \frac{r\Phi}{L}\cos(\Gamma) \\ \lambda_z \cos(\Gamma) \end{bmatrix} \tag{2.5}$$

This fiber transformation applies only to a taut fiber; configurations where the fiber buckles inside the substrate are left to future work. These mathematical descriptions are used in the following section to find expressions for the stresses.

2.2.3 Relating Stress and Strain through Strain Energy

Previous successful models for hyperelastic fiber-reinforced tubes use invariant-based strain energy functions to approximate the Helmholtz free energy [62]. In contrast with statistical or stretch-based models, invariant-based models are built from quantities which are *invariant* to changes in the FREE's configuration that reflect the directional properties of the material. For example, a tensile force in any direction in space on an isotropic material will create the same stresses. Or, if our anisotropic FREE has rotated in space but not undergone any stretching, it will not store any strain energy. A detailed discussion of invariants can be found in [107], and a derivation of all of the invariants of a pressurized fiber-reinforced tube can be found in [62].

In order to demonstrate the usefulness of a continuum framework in this soft actuator design context, we use the simplest available strain energy models - that is, the ones that depend on the fewest possible invariants. Out of the several possible invariants for a single fiber-family tube, the neo-Hookean model (Eq. 2.7) has one invariant for the matrix and the standard fiber model (Eq. 2.8) has one invariant for the fiber. For designers seeking greater accuracy, or using elastomer and fibers with different (e.g. shear) behavior, models including additional invariants may be used in the same framework presented here. Many of these models are discussed in [43, 107], and [62].

Stress is connected to strain though a strain energy function $\Psi = f(\mathbf{F}, C_i)$, where $\mathbf{F}$ is the deformation gradient and C_i are material properties. Ψ models the Helmholtz free energy (in units of energy per reference volume) of the deformed body. We find the total strain energy Ψ through superposition of elastomer and fiber energy:

$$\Psi = \Psi_{elastomer} + \Psi_{fiber} \tag{2.6}$$

A modeling framework like this one enables a choice of any physically viable strain energy model. To demonstrate the viability of our continuum framework for modeling FREEs, we choose the simplest available strain energy models. The neo-Hookean model [107] used for the elastomer and the standard fiber model for the fiber [34] enable the choice of any material moduli C_1 for the elastomer and C_2 for the fiber. These energy models are shown below:

$$\Psi_{elastomer} = \frac{C_1}{2}(I_1 - 3) \tag{2.7}$$

$$\Psi_{fiber} = \frac{C_2}{2}(I_4 - 1)^2 \tag{2.8}$$

$$I_1 = tr(\mathbf{F}^T\mathbf{F}) = \lambda_z^2 + \frac{r^2}{R^2} + \frac{R^2}{\lambda_z^2 r^2} + \frac{r^2\Phi^2}{L^2} \tag{2.9}$$

$$\begin{aligned} I_4 &= (\mathbf{FM}) \cdot (\mathbf{FM}) \\ &= \mathbf{M} \cdot (\mathbf{F}^T\mathbf{FM}) \\ &= \lambda_z^2 cos^2(\Gamma) + \frac{r^2\Phi^2 cos^2(\Gamma)}{L^2} + \\ 2&\frac{r^2\Phi cos(\Gamma) sin(\Gamma)}{LR} + \frac{r^2 sin^2(\Gamma)}{R^2} \end{aligned} \tag{2.10}$$

In Equation 2.10, "·" symbolizes a vector dot product. I_1 and I_4 are invariants related to the motion undergone by the FREE skin and the fibers (Eqns. 2.9, 2.10).

The Cauchy or "true" stress tensor gives the magnitudes of differential stresses in the FREE in cylindrical coordinates. The relationship between Cauchy stress $\boldsymbol{\sigma}$, strain energy, and deformation is shown below:

$$\boldsymbol{\sigma} = \begin{bmatrix} \sigma_{rr} & \sigma_{r\theta} & \sigma_{rz} \\ \sigma_{\theta r} & \sigma_{\theta\theta} & \sigma_{\theta z} \\ \sigma_{zr} & \sigma_{z\theta} & \sigma_{zz} \end{bmatrix} = \frac{\partial \Psi}{\partial \mathbf{F}}\mathbf{F}^T - p\mathbf{I} \tag{2.11}$$

Here, the hydrostatic pressure variable p is a Lagrange multiplier arising from the incompressibility of the FREE wall.

When the strain energy is known, we can relate it to stress with the Cauchy stress expression shown in Equation 2.11. A detailed explanation of the Helmholtz free energy, its relation to energy density in the material, and a derivation of the Cauchy Stress can be found in [40].

Using deformation gradient (Eq. 2.3) and the strain energy models (Eqns. 2.7, 2.8), we can find the Cauchy stress tensor with the constitutive relation in Eqn. 2.11.

$$\begin{aligned} \mathbf{C} &= \mathbf{F}^T\mathbf{F}, \\ \mathbf{b} &= \mathbf{F}\mathbf{F}^T \end{aligned} \tag{2.12}$$

Equation 2.12 introduces the right ($\mathbf{C}$) and left ($\mathbf{b}$) Cauchy-Green deformation tensors, which are useful quantities for computing the stress. Below, we use the superposition of the fiber and matrix with the chain rule and Equations 2.7, 2.8, 2.9 and 2.10 to evaluate Equation 2.11:

$$\begin{aligned} \boldsymbol{\sigma} &= \frac{\partial \Psi_{elast} + \Psi_{fiber}}{\partial \mathbf{F}}\mathbf{F}^T - p\mathbf{I} \\ &= \frac{\partial \Psi_{elast}}{\partial I_1}\frac{\partial I_1}{\partial \mathbf{F}}\mathbf{F}^T + \frac{\partial \Psi_{fiber}}{\partial I_4}\frac{\partial I_4}{\partial \mathbf{F}}\mathbf{F}^T - p\mathbf{I} \\ &= \frac{C_1}{2}\frac{\partial I_1}{\partial \mathbf{F}}\mathbf{F}^T + C_2(I_4 - 1)\frac{\partial I_4}{\partial \mathbf{F}}\mathbf{F}^T - p\mathbf{I} \\ &= \frac{C_1}{2}\frac{\partial tr(\mathbf{F}^T\mathbf{F})}{\partial \mathbf{F}}\mathbf{F}^T + C_2(I_4 - 1)\frac{\partial(\mathbf{FM}) \cdot (\mathbf{FM})}{\partial \mathbf{F}}\mathbf{F}^T - p\mathbf{I} \\ &= \frac{C_1}{2}2\mathbf{F}\mathbf{F}^T + C_2(I_4 - 1)2\mathbf{FM}(\mathbf{FM})^T - p\mathbf{I}. \end{aligned} \tag{2.13}$$

An alternate expression of Equation 2.13 using Equation 2.12 and the definition of the tensor product $\otimes$ [107] is shown below.

$$\boldsymbol{\sigma} = -p\mathbf{I} + C_1\mathbf{b} + 2C_2(I_4 - 1)\mathbf{FM} \otimes \mathbf{FM}. \tag{2.14}$$

2.2.4 Contribution of Internal Pressure

The Cauchy stress depends on r, which is not a fixed quantity here. We find the new radii through the FREE's hydrostatic equilibrium equations, along with the incompressibility assumption of Equation 2.2a and fiber extensibility. The relationship between pressure P and the deformed FREE radii is shown below:

$$-P = \int_{r_i}^{r_o} \frac{1}{r}(\sigma_{rr} - \sigma_{\theta\theta})dr \tag{2.15}$$

A detailed derivation of Equation 2.15 is below.

In FREE applications, length and rotation are often controlled, but radius change is left free. Under the fixed pressure, stretch and twist, the new radii r_i and r_o need to be determined.

Radius can be determined by assuming the deformed FREE stresses satisfy hydrostatic equilibrium; that is, that on an arbitrarily chosen subsection of the FREE wall, there is no net stress. The FREE wall needs to be incompressible for this equilibrium to hold [34, 107]. This assumption is justified for FREEs since elastomers are often assumed to be incompressible, and the fibers have less volume overall than the elastomeric matrix.

$$\nabla \cdot \boldsymbol{\sigma} = 0 \tag{2.16}$$

In cylindrical coordinates, Equation 2.16 becomes the system of partial differential equations shown below.

$$\begin{aligned}
\frac{\partial \sigma_{rr}}{\partial r} + \frac{1}{r}\frac{\partial \sigma_{r\theta}}{\partial \theta} + \frac{\partial \sigma_{rz}}{\partial z} + \frac{1}{r}(\sigma_{rr} - \sigma_{\theta\theta}) = 0 \\
\frac{\partial \sigma_{r\theta}}{\partial r} + \frac{1}{r}\frac{\partial \sigma_{\theta\theta}}{\partial \theta} + \frac{\partial \sigma_{\theta z}}{\partial z} + \frac{2}{r}\sigma_{r\theta} = 0 \\
\frac{\partial \sigma_{rz}}{\partial r} + \frac{1}{r}\frac{\partial \sigma_{\theta z}}{\partial \theta} + \frac{\partial \sigma_{zz}}{\partial z} + \frac{1}{r}\sigma_{rz} = 0
\end{aligned} \tag{2.17}$$

Equation 2.16 shows hydrostatic equilibrium, which is expanded in cylindrical coordinates in Equation 2.17. With our previous assumptions of uniformity in z and around the FREE wall, we can conclude that none of the stresses vary in the θ- or z directions along the FREE wall. Additionally, we can see by the form of $\mathbf{F}$ that $\sigma_{r\theta} = \sigma_{rz} = 0$ and Equation 2.17 reduces to:

$$\begin{aligned} \frac{\partial \sigma_{rr}}{\partial r} + \frac{1}{r}(\sigma_{rr} - \sigma_{\theta\theta}) &= 0 \\ \frac{1}{r}\frac{\partial \sigma_{\theta\theta}}{\partial \theta} &= 0 \\ \frac{\partial \sigma_{zz}}{\partial z} &= 0 \end{aligned} \tag{2.18}$$

Eqns. 2.17 then simplify to Eq. 2.18. Because of axial symmetry and uniform stretch, we are primarily interested in the first hydrostatic equilibrium equation. Re-arranging it, we have:

$$-\frac{\partial \sigma_{rr}}{\partial r} = \frac{1}{r}(\sigma_{rr} - \sigma_{\theta\theta}) \tag{2.19}$$

We use the boundary conditions $\sigma_{rr}(r_i) = P$ and $\sigma_{rr}(r_o) = P_{atm} = 0$. Integrating Equation 2.19 in r, and then applying a change of variables from r to R (using Eq.'s 2.2a and 2.2b) gives:

$$\begin{aligned} \sigma_{rr}(r_i) &= \int_{r_i}^{r_o} \frac{1}{r}(\sigma_{rr} - \sigma_{\theta\theta})dr \\ &= \int_{R_i}^{R_o} \frac{R}{r}\frac{1}{R}(\sigma_{rr} - \sigma_{\theta\theta})\frac{dr}{dR}dR \\ &= \int_{R_i}^{R_o} \frac{R}{r}\frac{1}{R}(\sigma_{rr} - \sigma_{\theta\theta})\frac{R}{\lambda_z r}dR \\ &= \int_{R_i}^{R_o} \frac{R}{R^2 - R_i^2 + r_i^2\lambda_z}(\sigma_{rr} - \sigma_{\theta\theta})dR \end{aligned} \tag{2.20}$$

Here, using Equations 2.14 and 2.2a, and substituting 2.3 with the FREE dimensions:

$$\sigma_{rr} - \sigma_{\theta\theta} = C_1 \frac{R^2}{r^2\lambda_z^2} - 2C_2(I_4 - 1)\left(\frac{r\Phi cos(\Gamma)}{L} + \frac{rsin(\Gamma)}{R}\right)^2 \tag{2.21}$$

Applying the boundary condition gives:

$$\begin{aligned} -P = -p(r_i) &= \sigma_{rr}(r_i) \\ &= \int_{R_i}^{R_o} \frac{R}{R^2 - R_i^2 + r_i^2\lambda_z}(\sigma_{rr} - \sigma_{\theta\theta})dR \end{aligned} \tag{2.22}$$

Under incompressibility of the FREE wall,

$$r_o = \sqrt{r_i^2 + \frac{R_o^2 - R_i^2}{\lambda_z}} \text{ and } r = \sqrt{r_i^2 + \frac{R^2 - R_i^2}{\lambda_z}} \tag{2.23}$$

due to volume conservation.

Equations 2.22 and 2.23 enable us to find the new interior and exterior radii r_i and r_o. Once Equation 2.22 is solved, we know all of the kinematic quantities in the FREE's deformed configuration and can solve for the loads. Please note that this procedure yields a different results when the fibers are inextensible.

We can find the expression for p by adding $\frac{dp}{dr}$ to both sides of Equation 2.19:

$$\frac{dp}{dr} = \frac{d}{dr}(\sigma_{rr} + p) + \frac{\sigma_{rr} - \sigma_{\theta\theta}}{r} \tag{2.24}$$

We can note that using equation 2.11 that $\sigma_{rr} + p$ in Equation 2.24 is only a function of the deformation. Then, we can replace $\sigma_{rr} + p$ with Q_{rr} and perform a change of coordinates from r to R:

$$\frac{dp}{dR} = \frac{dQ_{rr}(R)}{dR} + \frac{\sigma_{rr} - \sigma_{\theta\theta}}{R\frac{r}{R}}\frac{dr}{dR} \tag{2.25}$$

Integrating Equation 2.25 under the same boundary condition (Eq. 2.22) gives the hydrostatic pressure expression necessary to find the radial, axial, and circumferential

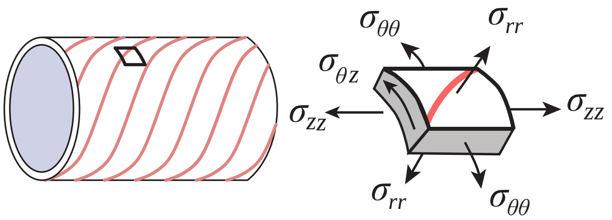

Figure 2.6: Differential element of the FREE wall and associated stresses

forces:

$$p(R) = Q_{rr}(R) - P + \int_{R_i}^{R} \frac{R}{R^2 - R_i^2 + r_i^2\lambda_z}(\sigma_{rr} - \sigma_{\theta\theta})dR. \tag{2.26}$$

2.2.4.1 Torsional Load

Given the deformed radius (Eq. 2.15) and the constitutive relationship between stress and deformation (Eq. 2.11), we can now solve for each component of the FREE wall stress, visualized in Figure 2.6.

Of specific interest here is the torsional load produced by the FREE, which we find by integrating the contribution to the moment caused by the shear stress $\sigma_{\theta z}$ direction across the deformed cross-section of the FREE wall. Since $\sigma_{\theta z}$ is an off-diagonal entry of $\boldsymbol{\sigma}$, p does not appear in the expression for the moment.

$$M = \iint_A \sigma_{\theta z} r dA \tag{2.27}$$

where

$$\sigma_{\theta z} = C_1\lambda_z\frac{r\Phi}{L} + 2rC_2\lambda_z\cos(\Gamma)(I_4 - 1)\left(\frac{\Phi\cos(\Gamma)}{L} + \frac{\sin(\Gamma)}{R}\right). \tag{2.28}$$

The expression in Equation 2.27 gives the torsional moment as a function of the FREE's initial state, deformation and material parameters.

Equation 2.28 affords a heuristic way to understand several facets of FREE behavior in torsion without fabricating a FREE or doing extensive experimental parameter determination. We can understand:

1. Sensitivity of a given design to the deformation, including the FREE's length change λ_z,
2. Coupling effects between moment M and axial force F,
3. Relative tension storage in the fiber due Ψ_{fiber} and elastomer due to $\Psi_{elastomer}$, respectively,
4. The effect of proposed material properties C_1 and C_2 on the design's torque generation ability.

2.2.4.2 Model Discussion

One key advantage of this model is its ability to be used as a heuristic framework to help designers understand FREE behavior in situations where various behaviors are fixed and others are unknown. Here, we outline some of the insights that this model captures.

The problem setup described above has fixed P, Φ, and λ_z. We then need Equations 2.15, 2.27 and 2.28 to find the torsional moment. However, as noted in Section 2.1, the FREE is fully determined when only three of the kinematic and force quantities are fixed. Below, we examine potential variations of the problem where input P remains fixed but the axial stretch λ_z and/or the twist angle Φ may be unconstrained, or the radius r is constrained. Validating each variation of the problem experimentally is left to future work, as is a detailed study of the force generation capabilities of FREEs.

First, we can contrast the problem setup described previously with one in which the length change of the FREE is not fixed (e.g. if the end of the FREE were on a roller). Then, the net axial force would be zero by default. Since the axial stretch of the FREE λ_z is still a part of the shear stress expression in Equation 2.28, we need to solve an additional equation to find the moment.

Axial force is found by integrating the axial stress and sum it with the force due to pressure on the ends of the FREE to fund the force:

$$F = \iint\limits_{A} \sigma_{zz} dA + 2\pi r_i^2 P \tag{2.29}$$

where

$$\begin{aligned} \sigma_{zz} = & -p + C_1\lambda_z^2 + \\ & 2C_2\lambda_z^2 \cos^2(\Gamma)\Bigg(\lambda_z^2 \cos^2(\Gamma) + \frac{r^2\Phi^2\cos^2(\Gamma)}{L^2} \\ & + \frac{2r^2\Phi\cos(\Gamma)\sin(\Gamma)}{LR} + \frac{r^2\sin^2(\Gamma)}{R^2}\Bigg) \end{aligned} \tag{2.30}$$

Since the FREE's length is unconstrained, we can expect that it produces no axial force. Solving Equation 2.29 with $F = 0$ in conjunction with the hydrostatic pressure as described below gives the FREE's axial stretch λ_z. Plugging λ_z back in to Equations 2.15,3.21 and 2.28 gives the moment. A similar procedure can be used for other fixed, nonzero values of axial force by setting F to a different value in Equation 2.29.

When the twist angle Φ is unconstrained, there will be no resultant torsion on the FREE. So, we can then find Φ by setting $M = 0$ in Equation 3.21 with the pressure-radius relationship defined in Equation 2.15. Similarly, setting $M = M_{known}$ in Equation 3.21 gives the twist at that fixed moment.

If length *and* twist are unconstrained, then the FREE is moving without any constraints and both F and M are fixed to zero.

If either the inner or outer radius of the FREE were to be fixed (e.g. through a pipe or bladder) it becomes straightforward to solve for P, F, and M under fixed Φ and λ_z since the kinematic quantities already appear in Equations 2.15, 2.28, and 2.30. If either or both of Φ or λ_z are unconstrained instead, we can again use the procedures outlined above to find them.

2.2.5 Significance of Fiber Extensibility

Fiber extensiblity expands the design space for FREEs past what is afforded by the inextensibility assumption: we can now design FREEs with new kinds of helical constraining elements such as polymers. The expanded design space includes fibers which may be more readily available, stronger, or have desired properties for the required working environment of the FREE without aligning closely with an inextensibility assumption.

We can further contrast this model with a version in which the fiber is assumed to be inextensible. An inextensible fiber will have $I_4 \to 1$ and will store stress without lengthening or shortening, i.e. $C_2 \to \infty$. However, a fully inextensible fiber will primarily store tension when the interior volume of the FREE has a non-cylindrical shape. (Consider a FREE with fibers parallel to the central axis that turns into an ellipsoid when inflated.) This behavior changes the kinematics and the pressure-radius relationships from what is presented here. Then, we may either 1) solve for the deformed shape with a series of partial differential equations with known boundary conditions at the FREE endcaps, which is not computationally expedient, or 2) assume a different deformed shape of the FREE, though our photos of inflated FREEs indicate that a cylinder most closely approximates the deformed FREE. A detailed mathematical description of the hydrostatic pressure balance for inextensible fibers can be found in [118].

2.2.6 Model Implementation and Testing

The model results were compared with experimental measurements of torsion of FREEs at various deformations and pressures.

2.2.7 Model Computation

The model was implemented on Wolfram Mathematica for a sample set of single fiber-family FREEs with reference lengths of 9.7-10.1cm, initial external radii varying from 6.3 to 7.4mm, at fiber angles of $\Gamma = 60°$, $\Gamma = 40°$ and $\Gamma = 30°$. Fabrication error causes variation in the radius of each sample: the FREEs are made by hand-layering elastomer and fiber over a commercially extruded elastomeric tube, so there is variation from sample to sample and some variation along the wall of each FREE sample.

Each of the elastomer and fiber properties, C_1 and C_2, can be observed in a simple tension test. The elastomeric matrix was tested between 0 and 300% strain. Fitting to the Neo-Hookean model gave $C_1 = 0.5$ MPa, which agrees with values from the literature [43]. The fiber was found to have $C_2 = 1$ MPa. The total computation time for this data set was about 14 seconds.

2.3 Preliminary Experimental Validation

The FREE's axial stretch, rotation, and interior pressure were fixed while the torsional loading was measured. The position-controlled test bed that performed the experiment is shown in Figure 2.7. The FREE was clamped at each end while a linear actuator at the left end extended the FREE axially, a servo rotated one end, and the air inlet enabled pressurization. The load cells shown measured axial force and moment at a rate of 1Hz. (The force measurements were used only for error analysis, which is explained further below.) The camera photographed the FREE in its deformed and pressurized state, allowing buckled configurations to be observed. The scheme of imposing deformation and measuring loading is frequently used in mechanics experimentation.

2.3.1 Measurement Techniques

After deformation and internal pressure were fixed, the FREE was held in place for 20 seconds to allow it to approach static equilibrium. Pressure was fixed using a pressure regulator (Wilkerson ER1). Force and torque measurements were sampled at 1Hz over the 20 second period in several such conditions with strain-gauge sensors (LoadStar RAS1-25lb and LoadStar RST1-6Nm respectively), and pressure feedback was taken at 1Hz. Each data point in Figures 2.8a thru 2.8c represents a sample over

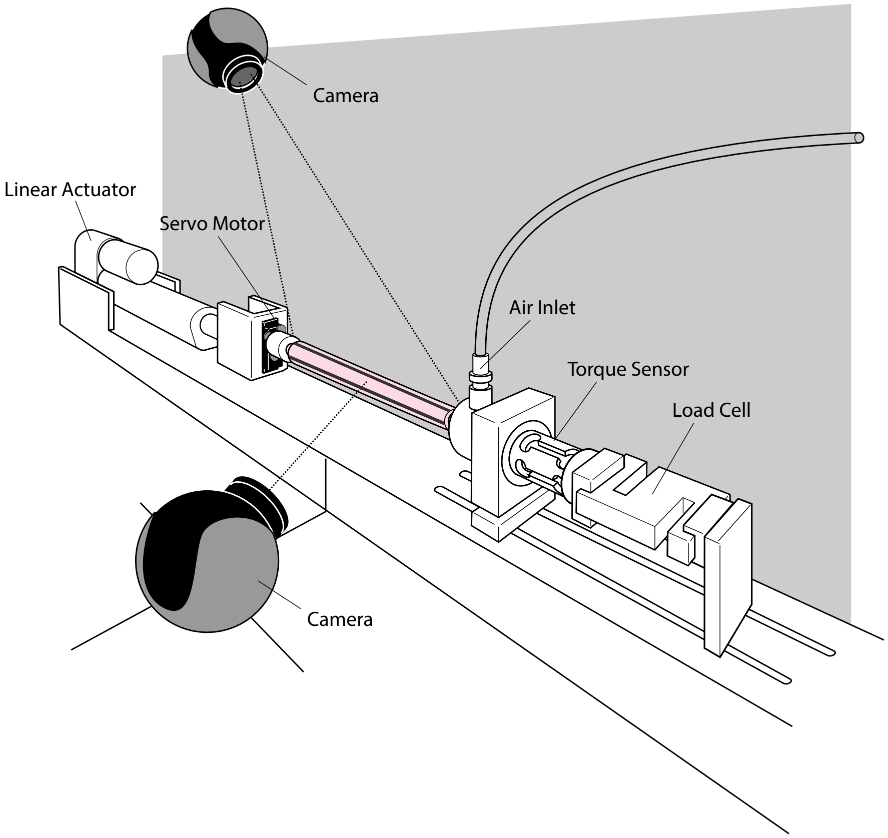

Figure 2.7: The position-fixed test bed, which measures torsion at various deformation and pressure states.

one second. Measurements were taken at various rotations for each FREE sample at extensions between 1mm and 2mm. These small pre-extensions were applied to limit the possibility of reaching critical buckling conditions. Since the cylindrical assumption is violated if the FREE wall is buckled, analysis of buckled configurations is left to future work. The resulting axial stretches $1.009 < \lambda_z < 1.021$ were used in the inputs to Equation 2.28 when the model predictions were calculated, and each sample had the same λ_z throughout the tests. Test inclusion criteria were measurements in which the pressure was increased relative to the previous measurement and the FREE did not buckle. A detailed analysis of the associated axial force is left to future work. Moment produced by the mounting of the FREE to the grips was subtracted from the measured torque.

2.3.2 Measurement Error

Sensor noise, sensor cross-talk, parasitic friction, FREE wall irregularity, and stress relaxation are the known potential sources of error.

The torque and force sensors employed here have a quoted accuracy of 0.02% for the force sensor and 0.2% for the torque sensor. However, since they are mounted in series we need to account for cross-talk - that is, the possibility that an axial force imposed on a torsional load cell may change its resistance reading. To characterize cross-talk error, we imposed axial forces between 0 and 12N without torsion on the RST1. We measured 0.6Nmm/N of cross-talk error due to axial force on the torque sensor. While testing the FREEs we took force measurements (none of which exceeded 11N) throughout, enabling us to calculate the cross-talk error of each FREE in each specific configuration. Parasitic friction was an additional concern. To avoid bending moments on the force and torque sensors, a Delrin bushing was placed at the interface between the torque sensor and air inlet as shown in Figure 2.7. Friction from the torque sensor sliding against the bushing may introduce error to the force measurements. To estimate this error, we used a spring scale to cycle between tensile loads of 6N and 0N at a rate of roughly 0.05Hz (comparable to the 20s time that the FREEs were held fixed). Comparing the force sensor readings at 0N after 6 cycles

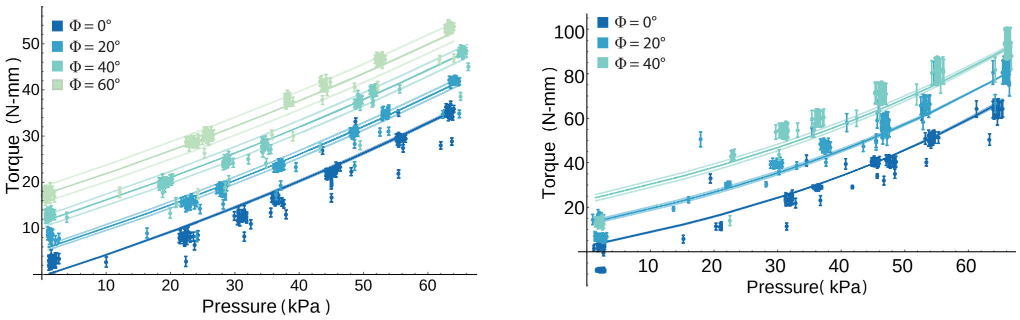

(a) Predicted (-) and measured moment generation by pressure 60°design angle FREE.

(b) Predicted (-) and measured moment generation by pressure 40°design angle FREE.

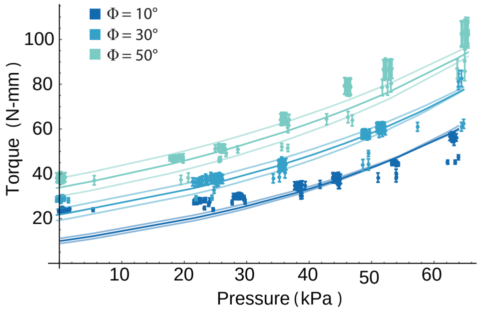

(c) Predicted (-) and measured moment generation by pressure 30°design angle FREE.

Figure 2.8: Predicted (-) and measured moment generation by pressure for FREEs with $\Gamma = 30°, 40°, 50°$ at extensions of +1mm.

gave a range of 0.08N. Carrying this force sensor error forward into the cross-talk error, we found 0.6Nmm/N $\times$ 0.08 N = 0.0048 Nmm of additional error. The sensor error, cross-talk error and parasitic friction error are included in the error bars of the measurements plotted in Figures 2.8a thru 2.8c.

During fabrication, irregularities occur in the wall thickness between FREEs and along wall of each FREE. The radius inputs to the model are the mean of three measurements on the same sample. The shaded lines in Figures 2.8a, 2.8b, and 2.8c represent the model predictions at $\pm$ 1 standard deviation of radius. The standard deviations were: 0.14mm for the $\Gamma = 60°$ FREE, 0.1mm for the $\Gamma = 40°$ FREE, and 0.13mm for the $\Gamma = 30°$ FREE.

Since FREEs are made partly from rubber, we expected that experimental error would arise from relaxation of the FREEs over time. However, upon observation of our torsion measurement over 20s, we did not see changes in torsion measurements that exceeded sensor noise and cross-talk as characterized above. Therefore, time-dependent behavior of FREEs is left for future study.

2.4 Results

The model quantifies the relationship between torsional loading on the FREE and FREE deformation in the R, Θ and Z directions. Figures 2.8a thru 2.8c show the experimental data plotted against the moment predictions for each FREE sample at various internal pressure and deformation states.

The Root Mean Square Error (RMSE) between the measured data and the model predictions is shown in Tables 2.1, 2.2, and 2.3. Some predictions do not fall within the experimental and fabrication error as described above. We expect that higher accuracy could be achieved by using more refined strain energy models which take shears, interaction between the fiber and elastomer, and the woven nature of the fibers into account. Without these refinements, the model captures the general concave-up relationship between pressure, torque and deformation.

Torques shown in Figures 2.8c-2.8a are not necessarily 0 when $P = 0$. This is due to the axial stretch of up to +1mm imposed on these FREEs; the model captures a

Table 2.1: TORQUE ERROR for 60 °DESIGN ANGLE.

Φ [°]	0°	20°	40°	60°
M Error [Nmm]	2.6	2.1	2.0	1.9

Table 2.2: TORQUE ERROR for 40 °DESIGN ANGLE.

Φ [°]	0°	20°	40°
M Error [Nmm]	5.5	5.4	8.1

Table 2.3: TORQUE ERROR for 30 °DESIGN ANGLE.

Φ [°]	10°	30°	50°
M Error [Nmm]	6.9	4.4	6.8

coupling effect between axial stretch and torsion.

2.5 Design Case Studies

The continuum model is useful for finding not only the particular operating conditions leading to a desired FREE torque, but also for exploring the space of available designs and operating conditions to satisfy a variety of constraints. Two case studies are presented. The first shows the model as an analysis tool for determining operational parameters, and second uses the model for design synthesis. In the first case study, the pressure is found for a given FREE to produce the desired torque at a given torsion. The second case study shows the the fiber design angle Γ of a FREE to produce the desired torque for a given operating pressure and torsion.

2.5.1 Selection of Operating Parameters

Once a FREE is manufactured at a given fiber angle Γ, it is important to control the behavior. In many instances this means controlling the pressure to derive a

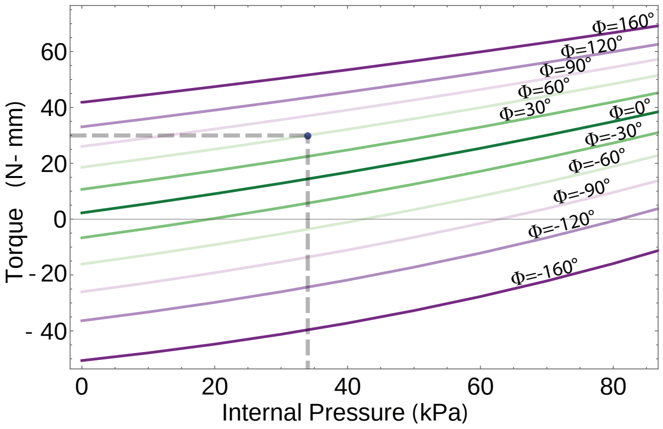

Figure 2.9: Torque by pressure curve for a FREE with design angle $\Gamma = 40°$ at various deformations.

desired moment and twist. The problem is formulated in Equation 2.31.

$$\begin{aligned} &\text{Choose } P \\ &\text{s.t. } M = M_{spec} \\ &\quad\;\; \Phi = \Phi_{spec} \\ &\quad\;\; \lambda_z = \lambda_{z,spec} \end{aligned} \tag{2.31}$$

Equation 2.27 is used to relate the pressure to torque for a given torsion. Geometry was assumed to be $\Gamma = 40$ °, and relaxed length, interior radius and wall thickness 79mm, 4mm, and 1mm respectively. Axial stretch λ_z was assumed to be 1.013 (that is, a length change of +1mm). Material properties were $C_1 = 0.64$MPa and $C_2 = 4$MPa. To obtain $M_{spec} = 30$N-mm and $\Phi_{spec} = 60$, we find the required pressure to be 34.1 kPa. This analysis is shown in Figure 2.9, along with the operational space of pressure, torque, and twist.

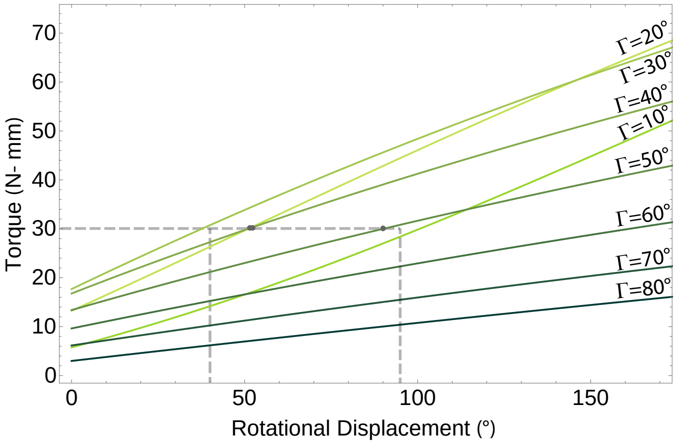

Figure 2.10: Torque-displacement profiles of a design set of FREEs at 40kPa with feasible designs emphasized.

2.5.2 Design Synthesis of Fiber Angle

If operating parameters are known, we can determine which design angle Γ of FREE will satisfy the task requirements. In this case study, we apply the model to find the design angle Γ that produces a desired range of twist angles Φ and a desired torque at a given pressure. This problem is stated in Equation 2.32.

$$\begin{aligned} &\text{Find all } \Gamma \\ &\quad \text{s.t. } M = M_{spec} \\ &\qquad\quad P = P_{spec} \\ &\qquad\quad \lambda_z = \lambda_{z,spec} \\ &\qquad\quad \Phi \in \{\Phi_{min}, \Phi_{max}\} \end{aligned} \tag{2.32}$$

We use identical initial dimensions and material properties as the previous case study. Equation 2.27 is again used to define the relationship between torque, rotations (Φ), and design angle (Γ) for a fixed pressure and 10°steps of design angle. $M_{spec} = 30Nmm$. $P_{spec} = 40$ kPa, $\Phi_{min} = 40°$, and $\Phi_{max} = 95°$are used for this case study.

Figure 2.10 shows the torque-rotation angle Φ relationships for each design angle Γ. The areas where the grey surface and green lines intersect demonstrate the feasible design angles Γ that meet the required rotation angle Φ and torque constraints. The feasible design examples are then see that the feasible designs are $\Gamma = 20°$, $\Gamma = 40°$, and $\Gamma = 50°$ with deformations of 51.08°, 51.06°and 90.1°respectively.

The model can be used to compute a feasible design set or optimize parameters in both the continuous and discrete domains for a variety of operating conditions.

2.6 Discussion

The general concave-upward trends of the measurements are captured by the model, demonstrating the viability of the model as a heuristic tool for FREE design synthesis and further justifying the model assumptions. Furthermore, the material properties characterized for the elastomer and fiber indicate that fiber extensibility does contribute to the FREE behavior.

The RMSE exceeds the estimated measurement error. More features may be added to the model to improve its accuracy such as higher-fidelity elastomer models [43], fiber-matrix interaction models [58], a fiber model specifically for woven materials [114] and corrections for irregularities in the geometry. The fabrication process may produce minor perturbations in the fiber angle which may cause the model to disagree with the experiments. Or, local bulging may occur between the fibers, breaking the framework's assumption of evenly distributed fibers throughout the FREE wall.

2.7 Conclusion

The model presented in this paper has the potential to be the basis for a heuristic, top-down design methodology for pneumatic soft robots, in which material properties, fiber angles, and tube dimensions can be chosen for any given application, deformation, or loads. We use a continuum mechanical framework to relate the displacement, torsional loading, and internal pressure of fiber-reinforced soft pneumatic mechanisms. The model captures the fundamental trends of experimental data at each of the configurations tested as well as the nonlinearity of a FREE's behavior due to coupling between loading and deformation. The assumptions of this continuum framework can be used to calculate FREE torsion and design FREEs with minimal experimental parameter determination, in an expanded design space that includes extensible fibers. The moment-pressure relationship of a proposed FREE and its moment-rotation relationship are presented as specific examples of the use of the model in a design context.

We illustrated the possibility of such a model both to find operating conditions for an existing FREE design which allow it to meet a given torque requirement, and to find the feasible design space for a FREE under known conditions.

Future directions of this work include experimental verification on the complete single-fiber FREE design space, an exploration of axial loading on FREEs, and a study of how material defects and manufacturing variation affect FREE torsion.

2.8 Summary

Fiber-reinforced elastomeric enclosures (FREEs) generate sophisticated motions when pressurized, including axial rotation, extension, and compression, and serve as fundamental building blocks for soft robots in a variety of applications. However, most modeling techniques employed by researchers do not capture the key characteristics of FREEs to enable development of robust design and control schemes. Accurate and computationally efficient models that capture the non-linearity of fibers and elastomeric components are needed. This paper presents a continuum model that captures the nonlinearities of the fiber and elastomer components as well as non-linear relationship between applied pressure, deformation and output forces and torque. One of the key attributes of this model is that it captures the behavior of FREEs in a computationally tractable manner with a minimum burden on experimental parameter determination. Without losing generality of the model, we validate it for a FREE with one fiber family, which is the simplest system exhibiting a combination of elongation and twist when pressurized. Experimental data in multiple kinematic configurations shows agreement between our model prediction and the moments that the actuators generate. The model can be used to not only determine operational parameters but also to solve inverse problems, i.e., in design synthesis.

CHAPTER 3

Experimental Validation of Nonlinear Elastic Continuum Model and Model Comparison

This chapter has been previously published and is used with permission from SAGE. It may referenced as:

Sedal, Audrey, Wineman, Alan, Gillespie, Brent R., and Remy, C. David. Comparison and Experimental Validation of Predictive Models for Soft, Fiber-Reinforced Actuators. *International Journal of Robotics Research.*

3.1 Introduction

Soft robots make use of elastic behavior in their constituent materials and therefore often encounter physical phenomena that are neglected in rigid robotic theory. Since soft robots are made from deformable materials and deform themselves, such behaviors include unexpected relationships between expanding and constraining structural elements, as well as deformation- and direction-dependent nonlinear stiffnesses. Accurate soft robot models need new fundamental frameworks that capture multi-dimensional elastic behavior. Further exacerbating the modeling need is the great variety of available soft system designs and control techniques that may require models. Authors publishing under the soft robotics umbrella make use of a broad set of structural schemes at both the actuator level (e.g. cable robots vs.

fluid-driven robots) and the system-wide level (e.g. rigid connection between actuators vs. monolithic soft systems), as well as broad choices of materials, models, and functionalities [135]. A number of candidate modeling approaches can be considered to address the need for competent soft robot models.

Successful soft robot modeling approaches appearing in recent literature can be broadly placed into two groups: data-driven strategies and first principle-based strategies. Data-driven strategies have been used on physically realized systems to characterize dynamic behavior, and, in some cases, to develop control policies. Diverse schemes have been proven on a variety of soft systems, including neural networks [46–48, 163], genetic algorithms [49], and other regression techniques [15, 37, 170]. Within first principles-based models, two subcategories emerge. [32] and others [13, 15, 33, 141, 164] show that lumped-parameter models can be used in design and control tasks. Continuum mechanical formulations have recently been demonstrated to be useful in soft system design and control [25, 26, 31, 52, 104, 122, 168]. First principles-based models can also be used to study specific behaviors of soft actuators such as interactions between components [164, 174].

Many of the models cited above were developed as part of a larger effort to demonstrate capabilities of specific soft systems. Others perform the complementary task of exploring a design space comprised of many possible systems, and determining the optimal design for a given task. Yet, a broad comparison of model structure and features is missing: why, when, and how data-driven models, lumped-parameter models, and continuum mechanical formulations succeed and fail in soft robotics is not well understood.

The aim is to build this understanding by showing how these three model types compare in capturing the gross behavioral trends and specific features of a popular class of soft actuators. First, we developed three distinct soft actuator models —a lumped-parameter model, a continuum mechanical model, and a neural network— that relate the multi-dimensional loading and deformation of this actuator. These models differ in mathematical structure, reaching from simple linear equations to integral expressions to sums of weighted functions. The models also differ in how many parameters they require to be identified from experiment, and in the physical meaning (if any) of the parameters. Next, we generated benchmark data by testing eight soft pneumatically driven actuator samples with varied design parameters, across 22,880 kinematic configurations and pressures. Finally, we compared the models on the gross behavioral features that they were able to capture, and on their performance at predicting kinetics across the design space.

In particular, soft, fiber-reinforced, pneumatic actuator known as the Fiber-Reinforced Elastomeric Enclosure (FREE) [8], or Fiber-Reinforced Soft Actuator (FRSA) [26], were investigated. The FREE consists of a cylindrical, elastomeric tube whose wall is embedded with 1, 2, or 3 families of fibers wound in helices. The helical pitch of these fibers guides the motion that the tube undergoes when internally pressurized. FREEs are used in several existing systems including exoskeletons [75, 111, 121, 155], soft manipulators [99, 124], grippers and hands [31], vibration isolators [142], bio-inspired slithering systems [12], and parallel groupings that augment force generation [132].

FREEs are a strong candidate for comparative study because they have core mechanical features that are shared in other soft robot architectures. The pressurizeable, nonlinear and hyperelastic wall of the FREE is shared by the PneuNet [150] and other soft inflatable robot architectures, while the constraint provided by the fiber is structurally similar to fiber constraints in soft cable-driven robots like the octopus-inspired robot created by [84]. We use single fiber-family FREEs because their asymmetric fiber arrangement causes coupling between length change and twisting when the FREE is pressurized [26, 143]. Together, these key behaviors contrast with the behavior of traditional rigid or series elastic actuators: the FREE design exhibits unexpected relationships between expanding and constraining elements, as well as a nonlinear direction-dependent deformation-loading relationship. FREE models hence demand different governing assumptions than a traditional actuator and may not change their behaviour in a predictable manner when the design angle of the fiber family is changed. In a related contribution on a FREE-based manipulator and one McKibben actuator, [136] have compared several models in a control task, noting which ones seemed best-suited for control of that system. Complementing this work, we focus on evaluating model features quantitatively across a

Figure 3.1: Face, side, and isometric views of a FREE in an unloaded, un-pressurized reference configuration (top) and a loaded, pressurized configuration (bottom).

broad space of available designs. The FREE serves as a useful investigative platform that captures core problems in soft robotics.

In this work, we investigate the performance of three distinct models on a set of 8 single fiber-family FREEs that span the space of possible designs in terms of fiber angle. Spanning the full variety of available designs allows us to undertake a more meaningful study of model behaviour than could have been undertaken had we trained and evaluated on the same system. By evaluating performance under various combinations of fitting and test data, we can quantitatively understand the unique dependencies present in each model between its peak performance, generalizability, and required quantity of training data. In Section 3.2, we present each of the three models and the performance metric on which they are compared. In Section 3.3, we describe the actuator samples and experiments. In Section 3.4, we present the experimental results and error analysis of the models. In Section 3.5, we compare the gross trends and specific features of each model to those of the data, and compare the performance of the models.

3.2 Modeling

Each model was formulated to relate the FREE's deformation, design parameters, and loading quantities. The unloaded reference configuration of the FREE is a thick-walled, cylindrical tube with length L, inner radius R_i, and outer radius R_o that is wound with a helical fiber family. The angle Γ between a line tangent to the helix and the axis of the tube defines the geometry of the fiber family (see Figure 3.1). The set of design parameters $\bar{p} = \begin{bmatrix}\Gamma & L & R_i & R_o\end{bmatrix}$ describes the FREE's unloaded geometry.

For simplicity, we limited the degrees of freedom (DoFs) under consideration to the FREE's axial elongation and to its end-to-end rotation about the longitudinal axis. This is the intended region of motion of this actuator. The radius is left free to expand or contract. We assumed all other DoFs to be physically constrained. Thus, the current, loaded kinematic state of the FREE is defined by its new length l and its end-to-end twist angle φ. The vector of generalized coordinates is hence given by $\vec{q} = \begin{bmatrix} l & \varphi \end{bmatrix}^T$. The forces corresponding to the coordinates in $\vec{q}$ are the axial load F and the axial moment M, given by the vector of generalized forces $\vec{\tau} = \begin{bmatrix} F & M \end{bmatrix}^T$. An important consequence of this assumption is that the modeled FREE retains its cylindrical shape under any deformation in our choice of kinematic state $\vec{q}$. This assumption is valid for cylindrical FREEs which have not undergone a buckling instability. It is also a good approximation for a lightly bent actuator whose bending radius greatly exceeds its cross-sectional radius. Then, for a FREE with a given set of design parameters $\bar{p}$, the goal of our modeling effort is to characterize the relationship between the kinematic state $\vec{q}$ and the generalized force output $\vec{\tau}$, and to express this relationship as a function of the applied fluid pressure P.

Without loss of generality, we chose to formulate this relationship in terms of a force prediction problem and sought to develop and compare different types of models that establish the following functional relationship:

$$\vec{\tau} = \boldsymbol{f}(\vec{q}, P, \bar{p}). \tag{3.1}$$

The inverse problem of finding an actuator's kinematic state $\vec{q}$ given its generalized forces $\vec{\tau}$ and design parameters $\bar{p}$ may be solved numerically, in the case of first principles models, or by re-training, in the case of data-driven models. The three models presented in the following sections differ significantly in their mathematical structure and in the number of free parameters that must be identified through experimental data. The physical meaning (if any) of these parameters is also discussed.

3.2.1 Linear Lumped-Parameter Model

The primary assumption of our first model is that fibers of the FREE are inextensible and create a perfect kinematic constraint forming a helix that encloses the elastomeric tube. Considering only the unbuckled case in which the FREE retains its cylindrical shape, we use this assumption to derive an analytic expression for the outer radius r_o of the deformed FREE (Fig. 3.1) as a function of the state $\vec{q}$ and the design parameters $\bar{p}$ [15]:

$$r_o\left(\vec{q}, \bar{p}\right) = \frac{\sqrt{B^2 - l^2}}{\left|\Phi + \varphi\right|}. \tag{3.2}$$

Here, the fiber length B is given by $B = L\frac{1}{\cos\Gamma}$ and the initial wrapping angle Φ by $\Phi = \frac{L}{R_o}\tan\Gamma$.

Neglecting the wall thickness of the FREE (i.e., assuming that the inner radius $r_i \approx r_o$), we can employ this expression to compute the volume V of the fluid inside the FREE:

$$V\left(\vec{q}\right) = \pi l r_i^2 = \pi\frac{lB^2 - l^3}{(\Phi + \varphi)^2}. \tag{3.3}$$

Taking the partial derivative of this expression with respect to the kinematic state $\vec{q}$ yields the fluid Jacobian $\mathbf{J}_V$:

$$\mathbf{J}_V = \frac{\partial V}{\partial \vec{q}} = \begin{bmatrix} \pi\frac{B^2-3l^2}{(\Phi+\varphi)^2} & -2\pi\frac{lB^2-l^3}{(\Phi+\varphi)^3} \end{bmatrix}. \tag{3.4}$$

The transpose of this Jacobian allows us to compute the generalized forces $\vec{\tau}_{fluid}$ that are created by the fluid pressure P [15]:

$$\vec{\tau}_{fluid} = \mathbf{J}_V^T P. \tag{3.5}$$

These fluid forces are summed with the elastic forces that result from the deformation of the FREE wall in axial compression, axial twist, and radial compression:

$$\vec{\tau} = \vec{\tau}_{fluid} + \vec{\tau}_{wall}. \tag{3.6}$$

The second major assumption of this model is that the FREE wall provides a linear elastic response to deformations in $\vec{q}$. Using $\Delta\vec{q} = \begin{bmatrix} l - L & \varphi \end{bmatrix}^T$ for the deformation along the generalized coordinates, we can compute these elastic forces as:

$$\vec{\tau}_{wall} = -\mathbf{K}\Delta\vec{q} = -\begin{bmatrix} k_a & k_c \\ k_c & k_b \end{bmatrix}\Delta\vec{q}. \tag{3.7}$$

The stiffness matrix $\mathbf{K}$ is a positive-definite, symmetric matrix that is found by fitting model parameters k_a, k_b, and k_c to experimental data. The diagonal elements in this matrix, k_a and k_b, approximately correspond to the lumped stiffness of the wall in axial compression and twist, respectively. Because of the fibers in a FREE, it is necessary to also include off-diagonal elements k_c in $\mathbf{K}$. As expressed in Eq. (3.2), motion in l and φ induces a change in the radius of the FREE and hence a radial compression of the wall. The elastic response to this compression is transferred by the fibers back into the generalized torques $\vec{\tau}$. This effect causes an elastic coupling between the twist and axial directions, resulting in the off-diagonal terms in $\mathbf{K}$.

We can express the complete lumped parameter model for a FREE by combining these expressions:

$$\vec{\tau} = \mathbf{J}_V^T P - \mathbf{K}\Delta\vec{q}, \tag{3.8}$$

which is the special form of Eq. 3.1 for the linear lumped-parameter model.

For this particular model, it is worth noting that the radius r_o, the volume V, and the fluid Jacobian may have singular terms when $\varphi = -\Phi = -\frac{L}{R_o}\tan\Gamma$. This deformation corresponds to a configuration in which the actuator has been rotated such that the fibers are parallel to the tube's central axis. In this case, the radius and internal volume become ill-defined and the fibers can store any amount of tension or compression in axial directions. In this formulation, the model parameters that must be fit experimentally are the three parameters of lumped stiffness k_a, k_b, and k_c.

3.2.2 Nonlinear Continuum Model

In our second model, we predict the generalized forces $\vec{\tau}$ in Equation (3.1) with a continuum-based, non-linear relationship. Though we continue to assume that the FREE is a cylindrical tube, its wall thickness is no longer neglected and the fiber is considered to be extensible. Extensible fibers cannot kinematically define the tube's geometry; the radius and internal volume of the FREE in this model depend not only on the generalized coordinates $\vec{q}$, but also on the internal pressure P. Finally, we replace the assumption of a linear elastic response and replace it with a nonlinear response arising from consideration of the wall's deformation and occupied volume.

To establish a well-defined problem, we assume that:

1. The actuator deforms from a thick-walled tube to a thick-walled tube of different dimensions,
2. the volume occupied by the material of the FREE wall stays constant (i.e. the FREE wall is incompressible, as evidenced for rubbers according to [43]), and
3. the fiber is perfectly embedded into the elastomer and evenly distributed through it, such that the interaction phenomena are homogenized throughout the FREE wall and the fiber remains locally tangent to the elastomeric tube.

These assumptions enable a modified implementation of a continuum mechanical framework proposed by [62]. This specific model implementation has been presented before [143] and is summarized here for completeness.

Under the assumptions listed above, the FREE transforms from a tube with initial dimensions $\{L, R_i, R_o\}$ for length, interior radius, and exterior radius, and no end-to-end twist ($\varphi = 0$) to a tube with new dimensions $\{l, r_i, r_o\}$ and end-to-end twist φ (Figure 3.1). To define this deformation, we track an arbitrarily chosen elemental volume in the FREE wall. The elemental volume has location coordinates $\vec{X} = [R\ \Theta\ Z]^T$ in the FREE's load-free configuration, and coordinates $\vec{x} = [r\ \theta\ z]^T$ in the current, loaded configuration such that $\vec{x} = \mathbf{g}(\vec{X})$. The following functions define the new coordinates $\vec{x} = \mathbf{g}(\vec{X})$ of any point $\vec{X}$ in the unloaded configuration:

$$r = \sqrt{\frac{R^2 - R_i^2}{\lambda_z} + r_i^2}, \tag{3.9}$$

$$\theta = \Theta + Z\frac{\varphi}{L}, \tag{3.10}$$

$$z = \lambda_z Z, \tag{3.11}$$

$$\text{where } \lambda_z := \frac{l}{L}. \tag{3.12}$$

The deformation gradient **F**, which describes the deformation of the particles in the FREE, is defined as:

$$\mathbf{F} = \begin{bmatrix} \frac{\partial r}{\partial R} & \frac{\partial r}{R\partial\Theta} & \frac{\partial r}{\partial Z} \\ \frac{r\partial\theta}{\partial R} & \frac{r\partial\theta}{R\partial\Theta} & \frac{r\partial\theta}{\partial Z} \\ \frac{\partial z}{\partial R} & \frac{\partial z}{R\partial\Theta} & \frac{\partial z}{\partial Z} \end{bmatrix} = \begin{bmatrix} \frac{R}{r\lambda_z} & 0 & 0 \\ 0 & \frac{r}{R} & r\frac{\Phi}{L} \\ 0 & 0 & \lambda_z \end{bmatrix}. \tag{3.13}$$

In Holzapfel's framework [62], composite materials are modeled by considering the "strain energy," i.e. Helmholtz free energy, stored in the deformed material.

The previously listed assumptions allow us to write the strain energy Ψ_{total} of the FREE wall as a superposition of the free energy from the elastomer and the free energy from the fiber:

$$\Psi_{total} = \Psi_{isotropic} + \Psi_{anisotropic}. \tag{3.14}$$

Here, each free energy depends on the deformation gradient **F** so as to describe the following features in the FREE wall material behaviour: the fiber is a "standard" fiber that is anisotropic in space [43, 62] and the elastomer is an isotropic neo-Hookean solid [107]. The neo-Hookean solid model introduces a material parameter C_1 and the invariant quantity $I_1 = I_1(\mathbf{F}^T\mathbf{F})$ associated with the elastomer's isotropy [157], such that:

$$\Psi_{isotropic} = \frac{C_1}{2}(I_1 - 3), \tag{3.15}$$

The standard fiber model gives the energy associated with the fiber anisotropy by introducing a material parameter C_2 and the invariant quantity $I_4 = I_4(\mathbf{F}^T\mathbf{F}, \Gamma)$

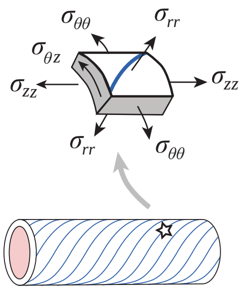

Figure 3.2: Arbitrary elemental volume of the FREE wall (marked by a star) with relevant stresses shown.

associated with the fiber stretch [157]:

$$\Psi_{anisotropic} = \frac{C_2}{2}(I_4 - 1)^2. \tag{3.16}$$

The stresses (i.e. Internal forces per area) inside the FREE wall are found by taking the derivative of the total Helmholtz free energy Ψ_{total} with respect to the deformation gradient $\mathbf{F}$ and including a Lagrange multiplier b that accounts for the FREE wall incompressibility. The expression for three-dimensional stress stored in the deformed FREE wall is then:

$$\boldsymbol{\sigma} = \begin{bmatrix} \sigma_{rr} & \sigma_{r\theta} & \sigma_{rz} \\ \sigma_{\theta r} & \sigma_{\theta\theta} & \sigma_{\theta z} \\ \sigma_{zr} & \sigma_{z\theta} & \sigma_{zz} \end{bmatrix} = \frac{\partial \Psi_{total}}{\partial \mathbf{F}} \mathbf{F}^T - b\mathbf{I}. \tag{3.17}$$

Using the continuum approach enables a system of partial differential equations for the stresses which express the equilibrium of the material under $\vec{\tau}$. In cylindrical coordinates and under the symmetry of the FREE, it is possible to manipulate these equations to develop an expression for b. See the Appendix of [143] for a detailed derivation. Since the FREE's radii r_i and r_o are unconstrained, we use the same equations of equilibrium in [143], subject to the boundary condition of the FREE's internal pressure P, to solve for r_i:

$$-P = \int_{r_i}^{r_o} \frac{1}{r}(\sigma_{rr} - \sigma_{\theta\theta})dr \tag{3.18}$$

where r_o is found using the material's incompressibility:

$$r_o = \sqrt{r_i^2 + \frac{R_o^2 - R_i^2}{\lambda_z}}. \tag{3.19}$$

Having established r_i and r_o, we compute the axial force and moment on the FREE by integrating the stresses over the radius of the FREE:

$$F = -2\pi \int_{r_i}^{r_o} \sigma_{zz} r dr + \pi r_i^2 P \tag{3.20}$$

$$M = -2\pi \int_{r_i}^{r_o} \sigma_{\theta z} r^2 dr. \tag{3.21}$$

Here, the stresses are expressed in terms of $\bar{p}, \vec{q}$, and P through the use of Eqs. (3.17), (3.14), and (3.13). This establishes a nonlinear expression:

$$\vec{\tau} = \boldsymbol{f}_c(\vec{q}, P, \bar{p}). \tag{3.22}$$

In this formulation, the model parameters that must be fit experimentally are the two material parameters C_1 and C_2 which represent the stiffness of the elastomer and fiber.

3.2.3 Neural Network Model

In our third model, we predict the generalized forces in Eq. (3.1) with a data-driven approach using a neural network. Our network implementation is based on the previous success of neural networks in modeling the kinetics [47] and statics [48] of a system structurally similar to the FREE. In particular, we implemented the neural network presented by [48] using the inputs and outputs of the FREE statics

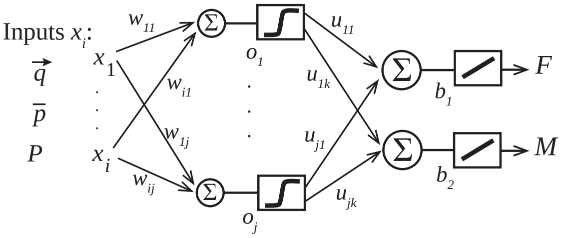

Figure 3.3: Schematic of the neural network, with inputs $\vec{q}$, $\bar{p}$ and P (x_i for $i \in \{1, ..., 7\}$), hidden layer neurons o_j with $j \in \{1, ..., 6\}$ and outputs F and M.

problem as defined in Eq. (3.1). We refer to the reader to this publication for a more detailed description of the neural network, but summarize our implementation below for completeness.

The set of inputs to our neural network consisted of the kinematic state $\vec{q}$, the internal pressure P, and the design parameters $\bar{p}$ of each sample. The outputs of the neural network were the components F and M of the generalized forces $\vec{\tau}$. This neural network was implemented as a shallow network with a single fully connected hidden layer containing 6 neurons using a hyperbolic tangent activation function. A schematic of the neural net with inputs x_i, weights and biases w, u, o and b, and outputs F, M is shown in Fig. 3.3.

The weights $w_{i,j}$ and $u_{j,k}$, and biases o_j and $b_{1,2}$ were fit experimentally through training with a back propagation algorithm. With our chosen network topology, 7 inputs, 2 outputs, and 6 neurons on a fully-connected hidden layer, the network had a total of 42 weights $w_{i,j}$, 12 weights $u_{j,k}$, 6 biases o_j and 2 biases $b_{1,2}$. This gives a total of 62 parameters that must be computed using training data. However, unlike in the other models, these parameters have no physical interpretation.

3.3 Hardware Experiments

To determine the predictive ability of each model, we performed a suite of experiments on a set of eight FREE samples spanning the design space under various loading conditions and imposed kinematic states.

Sample	1	2	3	4	5	6	7	8
Γ (°)	15	25	36	40	50	62	73	76
L (mm)	90.48	120.52	98.42	90.48	120.40	99.00	128.9	103.22
R_i (mm)	4.77	4.77	4.77	4.77	4.77	4.77	4.77	4.77
R_o (mm)	6.13	6.62	6.74	6.13	6.41	6.36	6.40	6.18

Table 3.1: Design parameters $\bar{p}$: fiber orientation Γ (°) and initial dimensions of length L, inner radius (R_i) and outer radius (R_o) for each sample.

3.3.1 Samples

All sample FREEs were made from cotton thread ("Aunt Lydia's", Size 10) adhered to rubber tubing. Natural rubber tubing with specified 9.5 ± 0.25 mm inner diameter, 1.6 ± 0.02 mm thickness (Kent Elastomer) was coated with a thin layer of rubber cement (Elmer's), resulting in sample wall thickness between 1.3 and 2 mm. During winding, the fiber angle was prescribed by a 3D-printed template inserted into the rubber tube. Fiber spacing was 1.67 ± 0.25 mm. After winding, a thin layer of liquid latex (TAP) was applied by hand to further secure the fibers on the tube. Samples were cut between 8 and 12 cm in length.

We created eight samples with fiber orientations Γ spanning the design space $\Gamma \in (0°, 90°)$ in increments of roughly 10°. Fiber orientation of the finished samples was measured through a photograph in three locations and averaged. Standard deviation of the measured fiber orientation did not exceed 1°. Though Γ is the main design variable, our samples also differed somewhat in length and wall thickness. The dimensions of length and thickness were measured with a micrometer three times on each FREE sample and averaged. Standard deviation of sample length and thickness measurements did not exceed 0.10 mm and 0.13 mm respectively. Table 3.1 shows the fiber orientation and initial dimensions of each sample.

After fabrication, the samples were fit using parallel zip ties to the barbed side of 9.5 mm (3/8 in) single barb to "1/8 in NPT" style pneumatic fittings.

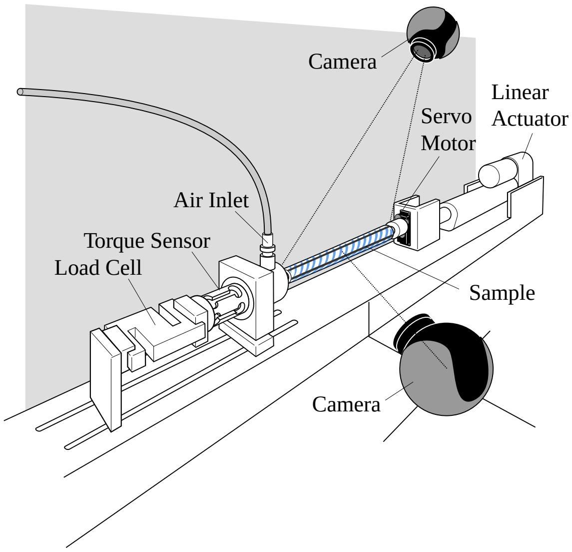

Figure 3.4: FREE test bed. The sample FREE, shown with blue fibers, is mounted in the center. On the right (wr.t the reader), the linear actuator and servo motor fix the length and twist. On the left, the torque sensor and load cell measure the loads while the FREE is inflated via the air inlet through a flexible, lightweight tube. Between the air inlet and the sensors is a cylindrical Teflon^{tm} bushing. Top and side camera take low resolution video and high resolution photos.

3.3.2 Testing Platform

Each sample was fitted into a custom-built testing platform (Figure 3.4) designed to elongate, twist and pressurize the samples under computer control (NI LabVIEW) while measuring loading at the tip and photographing the sample's outer wall.

3.3.3 Testing Protocol

Prior to testing, test bed error was characterized. The linear actuator and rotational servo were tested to ensure position control capabilities within 0.146 mm and 0.35° respectively. Cross-talk between the load cells was measured using known forces and torques between 0 and 10 N and 0 and 100 Nmm. Error due to cross-talk on the force sensor was 3.43E-3 N/Nmm, and the same error on the torque sensor was 6E-1 Nmm/N. Parasitic friction on the platform was measured by cycling known tensile loads between 0 and 7 N, and was found not to exceed sensor resolution.

Each FREE sample was mounted into the test bed using custom NPT thread attachments and teflon tape. Aligned markings were placed on the FREE sample and mounting points to observe potential slippage. Then, each sample was tested for all possible combinations of the following kinematic states $\vec{q}$ and internal pressures P:

$$\Delta l(\text{mm}) = \{-5, -4, ..., -1, 0, 1, ..., 4, 5\} \tag{3.23}$$

$$\Delta\varphi(^\circ) = \{-120, -110, ..., -20, -10, -1, 1, 10, 20, ..., 110, 120\} \tag{3.24}$$

$$P_{in}(\text{Volts} \times 10^{-1}) = \{0, 1, 2, 3, 4, 5, 6, 7\} \tag{3.25}$$

Iterating through these configurations, we first commanded the rotational servo and linear actuator to create a desired end-to-end rotation and axial stretch/compression. As shown by Eqns. (3.23)-(3.25), each sample was tested in 286 distinct kinematic states $\vec{q}$. Then, gauge pressure was set by a voltage signal that corresponded to pressures between 0 and 72.5 kPa. Each sample was inflated to a control signal for 72.5 kPa in eight steps, and deflated back to atmospheric pressure in two additional steps during which measurements were also taken. Overall, this resulted in 2,860 configurations tested per sample. After the command pressure was reached, each of these configurations was held for 20 seconds while data (force, torque, and pressure) were collected at 1 Hz. This data set was synchronized and averaged to yield a single measurement triplet of $\vec{\tau}$, $\vec{q}$, and P. Throughout each test, the top camera took time-stamped video at 15 fps to capture any unforeseen events. After the 20 seconds, the side camera photographed the FREE sample wall and then the command for the next configuration was sent. Each photo was later manually classified as to whether the FREE sample had buckled in the given configuration or not. All buckled samples were excluded from further analysis. Over all eight samples, loading data and images were collected for 22,880 configurations. After testing was completed, samples were inspected and it was verified that none had been damaged throughout the test.

3.3.4 Model Comparison Procedure

Parameter fitting and model evaluation were performed on the separated data sets. We randomly partitioned the data obtained from the un-buckled configurations of each sample into a training set (80% of the data) and test set (20% of the data). Thus, there were eight distinct, randomly chosen and randomly ordered training sets, and eight distinct and randomly chosen test sets. We then created two additional training-test pairs by aggregating the training and test data for the even-numbered samples (Samples 2, 4, 6, and 8) and by aggregating the training and test data from all the samples.

As an aggregated error metric across a set of n data, we expressed the model error E as the root mean square error (RMSE) of force and moment errors normalized by their maximal measured values across all samples F_{meas}^{max} and M_{meas}^{max}, respectively. This error metric was both used to fit model parameters to training data and to determine model performance against test data:

$$E = \sqrt{\frac{1}{n}\sum_{i=1}^{n}\left(\frac{F^{i}_{meas} - F^{i}_{model}}{F^{max}_{meas}}\right)^2 + \left(\frac{M^{i}_{meas} - M^{i}_{model}}{M^{max}_{meas}}\right)^2} \tag{3.26}$$

Model parameters were fit to training data by minimizing the error metric E (Eq. (3.26)). The fitting operation was undertaken for each of the three models individually on all ten training data sets. Each individually trained model, with its corresponding parameter values, was then used to predict the relationship between loading, pressure, and kinematic state for each of the eight test data sets and the two aggregate test sets. Predicted values were then compared with the measured values to determine model performance using E. For the continuum model, we additionally calculated E on all test sets using model parameters gathered from tests on isolated materials.

The three model parameters k_a, k_b, and k_c of the linear lumped model were fit through a constrained minimization of E over a given training data set. The required positive-definiteness of the stiffness matrix $\mathbf{K}$ was implemented as a positivity constraint on the eigenvalues of $\mathbf{K}$. The constrained optimization problem was solved with a gradient based interior-point algorithm (*fmincon*) in Matlab. The algorithm was initialized at order of magnitude estimates of $k_a = k_b = k_c = 1$.

In a similar fashion, we found the two parameters of the nonlinear continuum model, using the positivity constraint $C_{1,2} > 0$. The initial estimates for C_1 and C_2 were 2×10^5 and 10^6 Pa respectively. These are order of magnitude estimates based on previous physical measurements of rubber and cotton fibers [43, 143]. The constrained optimization problem was again solved using *fmincon*. In addition to fitting $C_{1,2}$ from composite sample measurements as described above, we also evaluated the continuum model's performance using individual constituent values of $C_{1,2}$ of the elastomer and fiber respectively from [143].

The 62 parameters of the neural network were fit with back propagation on normalized input values. We performed training using an unconstrained gradient based method (Levenberg-Marquardt algorithm), implemented with Matlab's *train* func-

(a) An un-buckled FREE sample.

(b) Axially buckled sample.

(c) Torsionally buckled sample.

(d) Axial and torsional buckling.

Figure 3.5: Images from experiment of sample configurations: (a) un-buckled, (b) axially buckled, (c) torsionally bucked, and (d) both axially and torsionally buckled.

tion. Unlike the other models, the neural network requires the data to be partitioned into 3 sets. Thus, we used 64% for training, 16% for validation, and 20% for testing. Up to 1000 epochs were permitted. The training of the neural network was based on E^2 as objective function, which has the same global minimum as E.

Parameter optimization was performed in MATLAB on a laptop computer (MSI WE63). Computation took roughly 10 minutes for the linear model, 45 minutes for the continuum model, and 5 minutes for the neural network.

3.4 Results

3.4.1 Buckling

Out of the 22,880 tested configurations, 12,611 conditions (55.1%) were unbuckled, while 10,269 (44.9%) showed signs of either axial buckling, torsional buckling, or both (Figure 3.5). Since the geometric assumptions of Section 3.2 are broken in buckled FREEs, they were not included in subsequent analysis. The remaining un-buckled configurations are indicated in Figure 3.6h. It is not too surprising that the FREEs buckled under several tested conditions: the broad, standardized set of kinematic states and pressures imposed on all samples irrespective of their designed operating range included many configurations outside of the typical range of use of a given FREE.

We were not able to identify a clear pattern for when buckling occurred. While

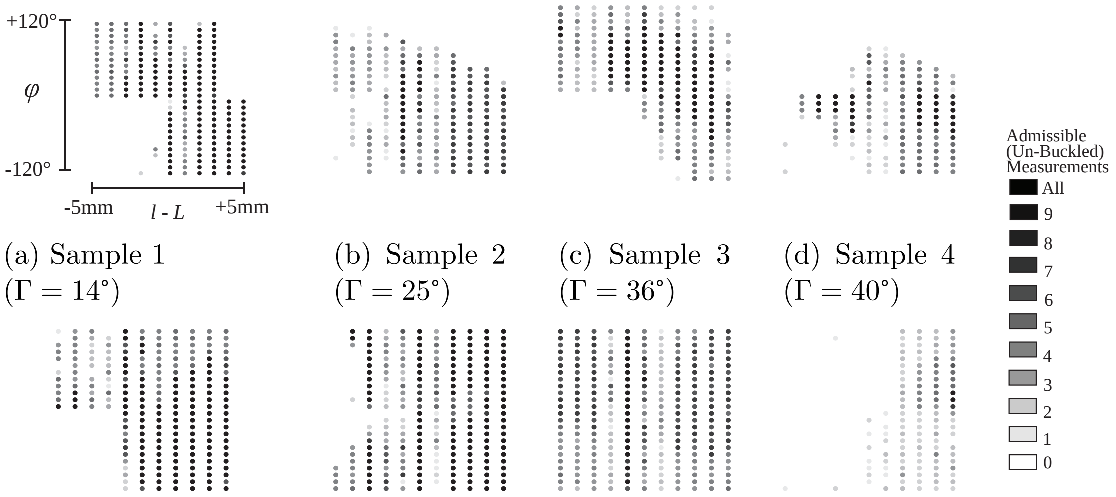

(a) Sample 1 ($\Gamma = 14°$)

(b) Sample 2 ($\Gamma = 25°$)

(c) Sample 3 ($\Gamma = 36°$)

(d) Sample 4 ($\Gamma = 40°$)

(e) Sample 5 ($\Gamma = 50°$)

(f) Sample 6 ($\Gamma = 62°$)

(g) Sample 7 ($\Gamma = 73°$)

(h) Sample 8 ($\Gamma = 76°$)

Figure 3.6: Diagrams showing admissible data (from un-buckled trials) to be used for analysis. Data are organized by kinematic state $\vec{q}$ for all 8 samples. The horizontal axis is the length change $l - L$ in mm, while the vertical axis gives the twist φ in degrees. At each of these kinematic states, the FREE did not necessarily stay buckled or un-buckled across the pressure range imposed. The relative proportion of admissible (i.e. un-buckled) measurements at each kinematic state $\vec{q}$ is reflected by the color of the circle.

there appears to be some tendency for buckling under axial compression and negative end-to-end rotations, this did not hold for all samples: buckling was also observed in axial stretch and positive end-to-end rotation. Furthermore, some samples buckled primarily at high input pressures, while others buckled at low pressures. This lack of a pattern is likely attributed to the presence of multiple different modes of buckling that depend on a sample's initial geometry, loading, kinematic state and fiber angle [56, 90], as well as defects and imperfections in the samples. A deeper investigation and classification of the observed buckling modes was not the focus of this project.

3.4.2 Actuator behavior & Model Features

To highlight the general behavior of the models, we first present a selection of data: two data sets recorded at specified kinematic states with corresponding comparisons of the modeled (all three models) and measured axial force F and moment M as functions of input pressure P (Figures 3.7 and 3.8).

As a further precursor to the comparison of performance by all three models, we present all the recorded behavior of a particular FREE sample (Figure 3.9). Figure 3.7 shows the data for Sample 6 at $\vec{q} = [4mm\ 80°]^T$ (i.e. under axial extension and positive twist) at 10 pressure values between 1.54 kPa and 63.9 kPa. The models shown here were all trained on the data from Sample 6. Figure 3.7a shows the axial force F arranged as a function of internal pressure P, and Figure 3.7b shows the moment M as a function of P. Figure 3.7c shows the same measurements arranged to show the F-M relationship parameterized by P. Similarly, Figure 3.8 shows the data for Sample 3 at $\vec{q} = [-5mm\ 10°]^T$ (i.e. axial compression and positive twist) and five pressure values between 37.3kPa and 64.4kPa, with all model parameters trained on Sample 3. In the data set of Figure 3.8, five configurations, all at pressures lower than 37.3kPa, have been excluded from the analysis because the sample was buckled.

In Figure 3.9, F-M relationship parameterized by P is shown for Sample 3 for the full set of un-buckled measurements across all imposed axial stretch and twist configurations listed in Eqns. 3.23 and 3.24. Here, the F-M relationship is shown as a vector (i.e. the vector of generalized forces $\vec{\tau}$). The correspondence of the data sets is shown by the pink insert, also present in Figure 3.8d. From the full behavior of the sample in Figure 3.9, we can observe general system trends including the relative influence of kinematic state and internal pressure on the magnitude and direction of F and M. The forces and torques produced at un-buckled configurations are characterized by behaviors due to the wall's elasticity, and behaviors due to the pressure input. Force and moment offsets reflect elastic behavior of a FREE at an imposed kinematic state $\vec{q}$, at $P \approx P_{atm}$. Loading trends reflect how the loads $\vec{\tau}$ change as a function of pressure input P. Both of these depend on the initial design parameters $\bar{p}$.

In general, the generalized forces $\vec{\tau}$ produced by an actuator are highly dependent on its kinematic state $\vec{q}$. Throughout the experimental data set, larger magnitudes of $\vec{\tau}$ tend to occur at higher pressures P and larger deformations $\vec{q}$. This is reflected for Sample 3, where the magnitudes of $\vec{\tau}$ in the upper right and left quadrants of Sample 3's kinematic space (Figure 3.9) are larger than those in the center. Further, the largest magnitudes of $\vec{\tau}$ of Sample 3 occur in the upper right quadrant, where the kinematic states impose tension on the fibers. In the lower left quadrant, low forces occur near kinematic states where the FREE was buckled for all the pressures P tested (Figure 3.6c). These low forces may indicate the onset of the buckling instability, where the fibers are no longer in tension but the wall has not yet buckled. At each kinematic configuration, the direction of $\vec{\tau}_{meas}$ can vary with pressure. Comprehensive measurements for all samples at all un-buckled configurations are found in the data packet available as a supplement to this paper.

Model comparisons to these data are also shown in Figures 3.7 and 3.8. The shapes of the pressure-force, pressure-moment, and force-moment relations for the linear model (shown in blue) are all straight lines. The $x-$ and $y-$ intercepts of each of these straight lines are set by the experimentally determined parameters of the FREE wall stiffness matrix $\mathbf{K}$, while the fluid Jacobian J_V determine their slopes as a function of pressure P. The lines of the linear model (straight by design) and continuum model (slightly curved, because of model nonlinearities in terms of geometry and strain energy) continue in the same direction outside the range of available data. In contrast, the line of the neural network model changes its direction outside the range of available data: it did not necessarily extrapolate in a comparable way to the linear and continuum models.

Model performance varied widely across samples, kinematic states, and input pressures. The curves of Figures 3.7 and 3.8 are representative of how each model's mathematical structure affects its behavior, and give a visual aid to conceptualize the error metric used in this study. However, they should not be used to draw conclusions about which model is most accurate across the data set, or about the physical behaviour of FREEs with other fiber angles or kinematic configurations. A gross performance comparison of the models organized by experimental parameter training set is given in Section 3.4.3.

3.4.3 Model Comparison

After partitioning the data into training and test sets, we evaluated model performance for every possible training-test pair. The result is 100 error calculations per model, which are depicted on the heat maps of Figure 3.10. Since the parameters of the continuum model may also be fit through separate experiments on the FREE's individual component materials, 10 additional error figures are shown in Figure 3.11.

The heat map of the linear model (Figure 3.10, left) is characterized by two low-error rectangular zones: a larger one at the top right and a smaller one at the bottom left. The low-error rectangular zones show regions where the linear model generalizes. When the stiffness parameters in $\mathbf{K}$ are fit to any of Samples 2 through 4, the model extrapolates relatively well in the corresponding test sets, shown by the relatively paler regions in the subplot. Similarly, models trained on Samples 5 through 8 extrapolate well across those test sets. Indeed, the lowest error achieved by the linear model is 2.15% for the training and test sets of Sample 8. This is also the lowest error achieved by any of the models for any training-test pair. Along the bottom, top, and left edges of the heat map, bands of higher error appear; these occur near the singularity described in Section 3.2.1. The value of twist that gives a singular configuration of Sample 1 occurs at $\varphi = -\frac{L}{R_o}\tan(\Gamma) = 122.4°$; some kinematic states of Sample 1 in this experiment nearly overlap with the singularity. Because of this proximity to the singularity, the linear model parameter fit and loading predictions for Sample 1 are poor compared to other samples. The "All" test set, which includes Sample 1, also has higher error. Here, the fitted parameters of the stiffness matrix $\mathbf{K}$ differed by a maximum factor of 63.8 across all samples (k_a trained from Sample 8 vs. k_a trained from Sample 1), but by a maximum factor of 2.9 within the range of Samples 5 through 8 (k_a of Sample 8 vs. k_a of Sample 5) , and a maximum factor of 3.8 between Samples 3 and 4 (k_a of Sample 4 vs. k_a of Sample 3).

The heat map of the continuum model (Figure 3.10, center) is characterized by

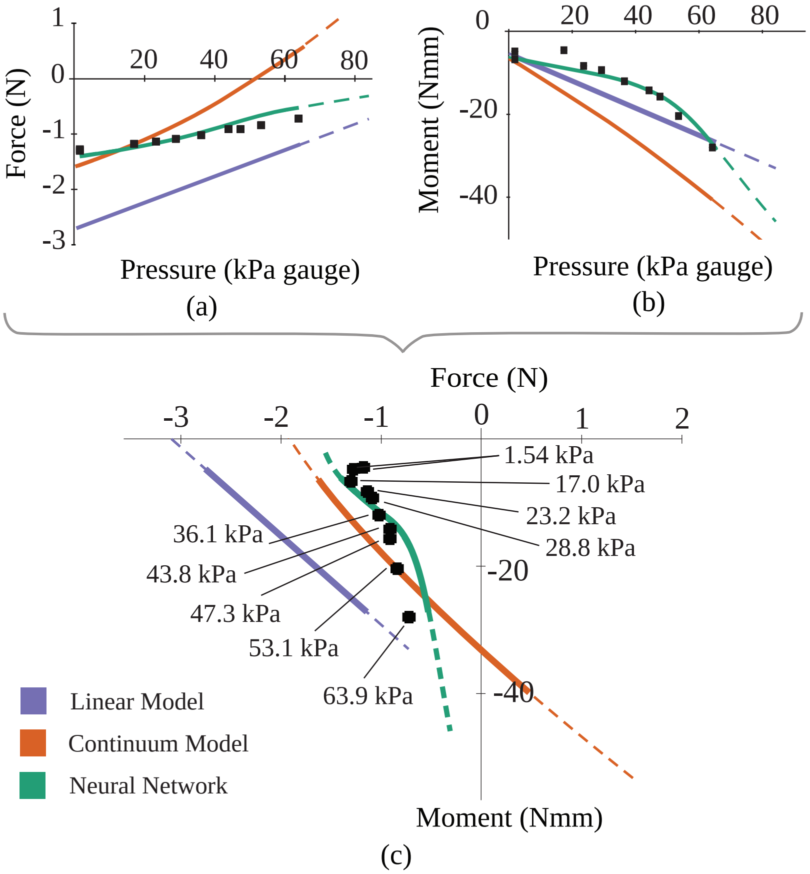

Figure 3.7: Force and moment models (curves) compared to measurement (black squares) for Sample 6 at $\vec{q} = [4mm\ 80°]$. From top left: (a) force F by pressure, (b) moment M by pressure, and (c) curves of $\vec{\tau} = [FM]^T$ parameterized by pressure P. In subfigures (a)-(c), solid lines show the predictions of $\vec{\tau}$ corresponding to the pressures $P \in \{1.54,\ 63.9\}$ in which loading measurements were taken. Dashed lines show a larger modeled range for this sample from $P = 0$ kPa (upper left end) to $P = 70.0$ kPa (lower right end).

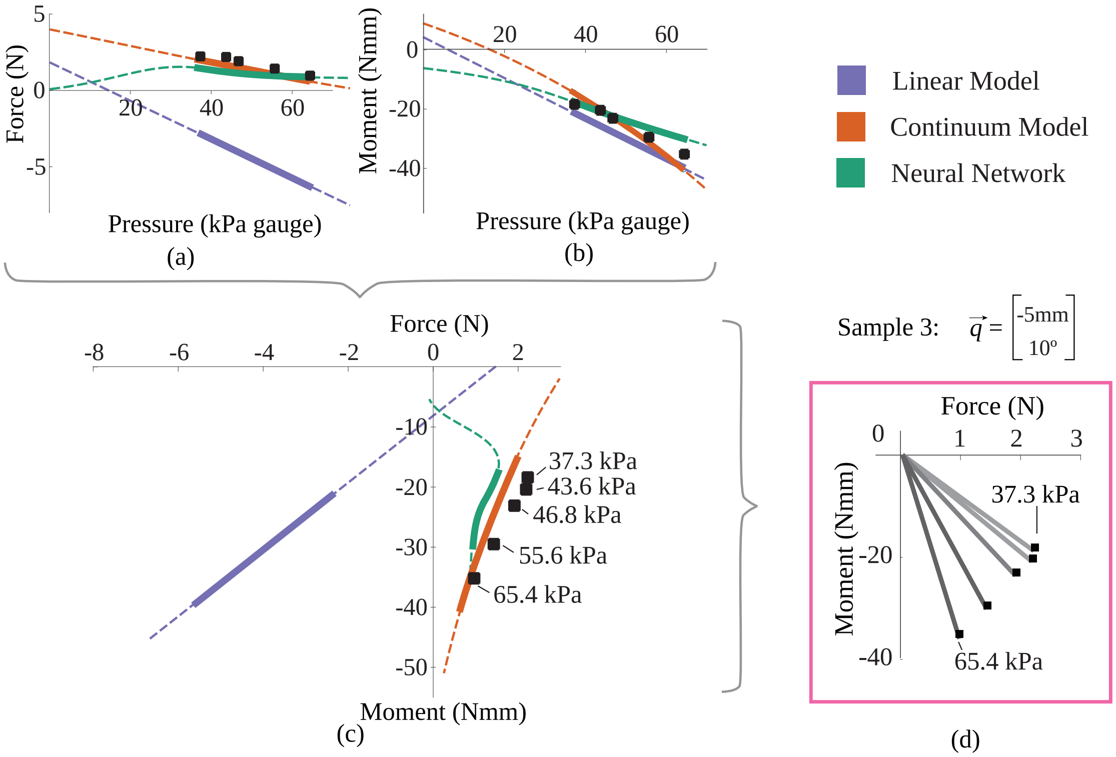

Figure 3.8: Force and moment models (curves) compared to measurement (black squares) for Sample 3 at $\vec{q} = [-5mm\ 10°]$. From top left: (a) force F by pressure, (b) moment M by pressure, and (c) curves of $\vec{\tau} = [FM]^T$ parameterized by pressure P. In subfigures (a)-(c), solid lines show the predictions of $\vec{\tau}$ corresponding to the pressures $P \in \{37.3,\ 64.4\}$ in which loading measurements were taken. Dashed lines show a larger modeled range for this sample from $P = 0$ kPa (upper right end of part c) to $P = 69.4$ kPa (lower left ends of part c). In subfigure (d), loading measurements are represented as vectors.

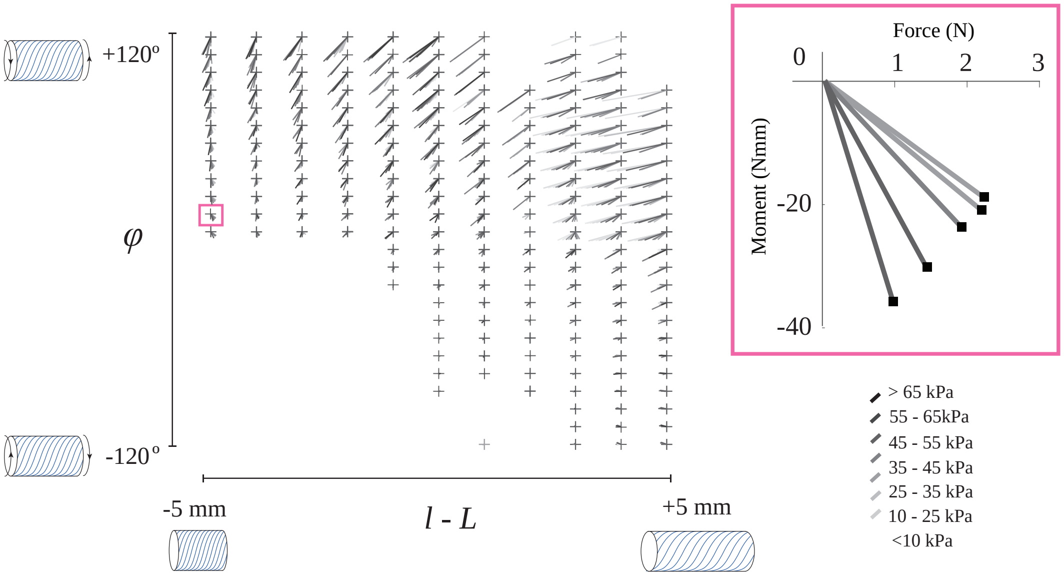

Figure 3.9: Raw loading data of Sample 3, shown as vectors $\vec{\tau}$ for all pressures across the space of deformation states $\vec{q}$. The pink square shows one example of how $\vec{\tau}$ changes with internal pressure at $\vec{q} = [-5mm,\ 10°]^T$.

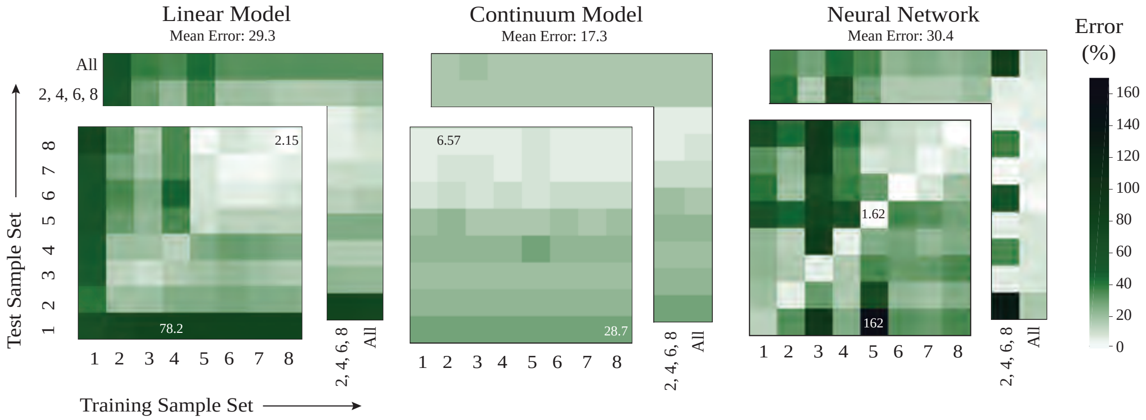

Figure 3.10: Normalized error, as described in Eq. 3.26, shown as heat maps, for all possible training-test pairs. Within each heat map, each square's color designates the error value according to the scale shown on the far right in the figure, with darker squares indicating higher error. The horizontal axis indicates which training data were used to fit parameters, while the vertical axis indicates the test set used to evaluate performance. Training and test sets were created individually for Samples 1 through 8, and for two composite sets of Samples 2, 4, 6 and 8 and all the samples, respectively. Maximum and minimum normalized errors for each model are shown in percent in the corresponding cells of the heat maps. Mean normalized error of each model is noted above its heat map.

its low variation in error: no regions of the map are particularly bright or dark. Instead, regions of relatively high and low error of the continuum model form horizontal "bands" corresponding with the test set used. For example, the error of Samples 7 and 8 is lower than the minimum error of Sample 2, no matter to which measurements the parameters $C_{1,2}$ were fit. A particularly dark band occurs when the test set used is Sample 4, but the maximum error of this model (28.7% for the model parameters fit from the Sample 2 training set and tested on the Sample 4 test set) is still substantially lower than the maximum error of the other models. This lower range of error is further reflected in the lower range of parameters fit across the design space. Here, the parameters fit within the continuum model differed across all samples by a maximum factor of 2.5, ($C_1 \in \{1.23 \times 10^5,\ 3.12 \times 10^5\}$ for Sample 8 and $C_2 \in \{0.88 \times 10^6,\ 1.07 \times 10^6\}$ for Sample 5).

The continuum model was also evaluated with the physical parameters $C_{1,2}$ of individual constituent materials (i.e. elastomer and fiber) in [143]. These are shown in Figure 3.11. The minimum error here (6.52%) is close to the minimum error achieved in the earlier heat map (6.57%), within the tolerance used , while the maximum error is slightly higher (28.7% vs 34.1%). Material constants used here ($C_1 = 5 \times 10^5$ Pa and $C_2 = 1 \times 10^6$ Pa) and the material constants identified in our experiment were within an order of magnitude.

The heat map of the neural network (Figure 3.10, right) is characterized by its bright, low-error diagonal. Performance of the neural network is especially strong when training and test data from the same sample are used, shown by the lower errors on the diagonal of the heat map. Indeed, the neural network produces the lowest error of any model for the test sets of Samples 1 through 7, though the linear model has the lowest error for Sample 8. Further, the relatively lower errors of Samples 6, 7, and 8 persist in the neural network model, shown by the brighter region of the heat map in the upper right hand quadrant. Elsewhere, the neural network has much higher off-diagonal errors.

The neural network heat map in Figure 3.10 provides evidence of over-fitting when aggregate training sets are used. Neural networks trained on one of the eight single-sample data sets are ill-equipped to extrapolate or interpolate to other designs: since the design parameters $\bar{p}$ remain constant throughout the entire training set, weights and biases tend toward relatively low values which are often orders of magnitude less than the weights for kinematic state variables or input pressures. In contrast, the aggregate sets offer variation in the design parameters $\bar{p}$ (according to Table 3.1). This variation gives more information which allows fitting of higher-magnitude weights on the design parameters, and the possible expectation that the neural network become capable of interpolating and extrapolating (i.e., generalizing) to new FREE designs. Yet, the ability of the neural network to generalize diminishes further when this design variation is introduced. When trained on Samples 2, 4, 6, and 8, the neural network performed relatively poorly at predicting the behavior of Samples 1, 5 and 7, with 134%, 56.4%, and 39.6% error respectively. The influence of this effective addition of parameters is also seen by comparing neural network error on Sample 5: trained on Samples 2,4,6, and 8, the neural network gives 56.4% load prediction error on Sample 5. This is higher than its error on Sample 5 when trained only on Sample 2 (45.4%) , only on Sample 6 (36.2%) , only on Sample 7 (32.4%) , or only on Sample 8 (27.7%) . Indeed, error here was lower when we effectively ignored the differences in design parameters than when we tried to fit to them.

3.5 Discussion

Though specific modeling techniques have been validated against realized soft robotic systems in the past, a model comparison across classes of models on a broader design parameter space has not been made. To address this gap, we developed and compared distinct models that relate the loading and deformation of Fiber-Reinforced Elastomeric Enclosures (FREEs). Three static models were developed and evaluated: a linear lumped-parameter model, a nonlinear continuum mechanical model, and a neural network. We compared predictions of the three models to 12,611 loading measurements that form the broadest (to the authors' knowledge) data set of FREE loading. The data set spans eight varied designs under over hundreds of distinct kinematic deformations and input pressures. Together, these evaluations

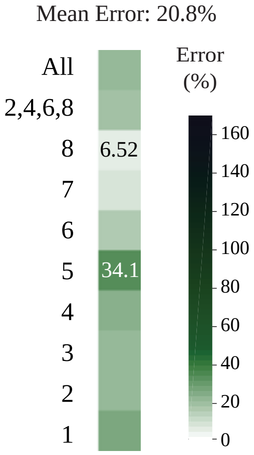

Figure 3.11: Normalized error of the continuum model using material properties $C_{1,2}$ determined on the individual constituent materials in [143]. Maximum and minimum normalized error are shown on the test set for which they occurred, and mean error is noted above the figure.

of model performance enable a comparison of the models for peak performance, generalizability, and system identification effort.

We begin this discussion by regarding the peak performance of each model. Intuition may suggest that each model would perform best when its system identification and evaluation use measurements from the same sample — i.e., the diagonal of the heat maps of error in Figure 3.10. The neural network heat map displays this pattern in a pronounced way, with a brighter diagonal than the linear or continuum models. The average neural network error along the diagonal for the eight samples is 5.51% , while the same average error is 17.4% for the linear model and 17.0% for the continuum model. Along the diagonal, the neural network achieves the lowest error $(13.65\%, 6.42\%, 6.95\%, 5.47\%, 1.62\% 1.76\%,$ 3.0% and 5.84% for Samples 1-8 respectively). Bounded high performance could be especially useful for building models that support control schemes for already-realized soft systems in clearly defined environments. [48] use the neural network for this task, learning inverse statics of their soft tentacle system from measurements taken across all of its possible kinematic configurations.

We have shown an example where peak performance of a model is high for a specific set of design parameters. We now consider how well the models generalize across the eight samples. A model that generalizes well maintains its performance even as its training and test set vary, resulting in a uniform color across its heat map. To generalize well, a model might need to extrapolate to new design parameters, outside of the range in training, or interpolate between parameters used in the training set. The continuum model follows this pattern, having the smallest error range of all models across the training-test pairs (22.13%) , and the lowest average error of 17.3% . In contrast, the linear model has an error range of 76.1% and a mean error of 29.3% , and the neural network has an error range of 160.38% and a mean error of 30.4% . Instead of contrasting diagonals and off-diagonals, the continuum model heat map has horizontal "bands" of similar color, with Samples 6-8 performing best. These results suggest that the continuum model's nonlinear mathematical structure is crucial to its performance: neither its parameters $C_{1,2}$ (as noted in Section 3.4.3) nor its range of error differ as much as those of the other models across training sets.

The linear model also generalizes, but does so in rectangular regions, described in greater depth in Section 3.4.3. This type of linear model has successfully predicted loads for specified parallel combinations of FREEs [15], but faces limitations due its singularity and the delineation of the training-test pairs for which it performs best.

When training and test samples differ, the neural network fails to generalize. This behavior is indicated by the bright diagonal and contrasting darker off-diagonals on the neural network heat map. The neural network's higher amount of experimentally determined parameters (62) and its lack of pre-defined physical structure are the likely cause of this behavior. The neural network over-fits when evaluated over the relatively sparse (compared to the kinematic configurations and input pressures) design set, and potentially captures artifacts like fiber irregularity. While physical models with parameter tuning also have this risk, in this analysis they are more likely to extrapolate and interpolate in ways that are physically consistent. In a neural network, on the other hand, weights are assigned to specific input-output pairs, making this structure much more flexible to learning about new parameter relationships. These new physical phenomena, however, may not occur again or in the same ways on a different sample.

In general, the performance of all models presented here is best for Samples 6-8 for any training set used. The key distinction of these samples from Samples 1-5 is in the winding angle Γ of the helical fiber (Table 3.1), though the initial dimensions also differ slightly. Improved performance may, then, be due to the relatively more important role of a high-angle fiber in constraining the radial expansion of the FREE, making it act more like a cylindrical piston and better constraining the radial expansion of the FREE. Or, higher fiber angles may be easier to manufacture consistently. This phenomenon should be the subject of future study.

Though our results show that the continuum model's structure is crucial in its performance, it is not clear which aspect of its nonlinear structure is most important. In contrast to the nonlinear strain energy models presented here, [25] show that finite element material models with nonlinear actuator deformations but linear stress-strain relationships have sufficient accuracy to enable control of a PneuNet-like soft robot, a soft cable robot, and a compliant mechanism. To our knowledge, a continuum model structure with linear material and nonlinear deformation assumptions has not been evaluated systematically for fiber-reinforced actuators; studying how structural aspects of continuum models of FREEs affect their behavior should be the subject of future work.

We can also compare the system identification effort necessary in each of the models. A model with more experimental parameters is likely to require more dense experimental data to perform well, hence leading to a longer and more exacting data collection scheme. In contrast, a model with an appropriate mathematical structure may perform well with fewer experimentally determined parameters and less data collection. The linear model and the continuum model have 3 and 2 experimentally determined parameters respectively, contrasting with the neural network which has 62 experimentally determined parameters. Even when the linear and continuum model fail, they do not reach error figures as high as the maximum errors of the neural network. As indicated by Figures 3.7 and 3.8, the physical assumptions on which these models are built give them mathematical structure which enables extrapolation across kinematic states and input pressures. Figures 3.10 and 3.11 show that they can also extrapolate across designs. The continuum model has the most flexibility in system identification. This is because the parameters $C_{1,2}$ have physical meaning that relates to the stiffnesses of a FREE's constituent materials, rather than its design. As shown by the comparable errors of the continuum model in Figures 3.10 and 3.11, a roboticist could fit $C_{1,2}$ using data from any existing FREE or from un-assembled constituent materials, and obtain comparable model performance as they might on the exact system that they plan to use. For the linear model, generalization occurs in bounded regimes (shown by the brighter rectangles of the linear model heat map in Figure 3.10): roboticists, then, are able to perform system identification for this model from a limited choice of other assembled FREE designs.

The key manner in which to improve the performance of the linear and continuum models is to incorporate additional or refined physical phenomena. These new phenomena could be specific to an experiment or context, including interactions between our sample and test bed or the effect of defects in the FREE wall. It is possible that for some phenomena to be incorporated into a model, new experimentally determined parameters will need to be added. And, as parameters are added, roboticists will presumably have to trade between model performance and expedient system identification. However, the results here suggest that an appropriate mathematical structure can reduce the need for experimental parameters and fitting procedures.

The neural network is likely to require the strongest system identification effort. This paper has shown that the same neural network architecture, with the same number of neurons, can at once outperform first principles-based models in some cases and under-perform in others. Specifically, we see instances when the neural network over-fits even when trained on a larger quantity of measurements compared to other cases: in the composite training set of Samples 2, 4, 6, and 8, the neural net is trained on thousands of data points but fails to generalize to similar FREE designs. For example, the neural net can predict the behaviour of Sample 2 ($\Gamma = 25°$) and Sample 4 ($\Gamma = 40°$) when trained on those samples, but does not as accurately learn the behaviour of Sample 3 ($\Gamma = 36°$.) As noted in Section 3.4.3, the neural network has a strong performance when trained on data for a single sample with a dense array of kinematic states and input pressures, but over-fits when trained on multiple FREE samples, which more sparsely occupy the available design space. This distinction between sparse and dense data requirements is especially important in design tasks. A roboticist wishing to evaluate the performance of a new, not-yet-constructed design would likely prefer to extrapolate from few data points, as each one could have a lengthy fabrication process. To further investigate the issue of potential over- or under-fitting in the training of the neural net, we performed a detailed parameter study in which we varied the hidden layer size of the neural network architecture between 3 and 68 neurons. The mean error (average of the heatmap in figure 3.10) across 5 training trials for each layer size is shown in Figure 3.12. The data seem to confirm that the chosen network size of 6 neurons is adequate and that adding further model parameters does not improve the average neural network performance when unknown samples are included in the testing data.

In addition to the performance-, generalization-, and system identification-based metrics above, we might evaluate the models on the ease of performing the parameter fitting computation. To keep uniformity in the parameter fitting techniques used, we used Matlab's Levenberg-Marquardt implementation for all parameter fitting in this work. All fits were performed using Matlab's Levenberg-Marquadt implementation, and for the physical models all fits were performed from the same starting points of $[1, 1, 1]$ for the linear model and $[2, 10] \times 10^5$ for the continuum model. With this uniform fitting procedure, convergence was reached in all cases within the 1000 epochs allowed for the neural network, and from the initial starting points stated above for the physical models. This uniformity of training procedure shows that all three of these models can be trained with a standard method in a reasonable amount of time, and converge. Even using these potentially slow methods, one could train all of these models in a few hours of work. Optimizing the training time, and selecting specific techniques for model training are useful avenues for future work. However, this contrasts with the varying experimental effort required by each model. Gathering data for just one of the samples took roughly 15 hours, and we see from Figure 3.10 and the subsequent discussion that each model requires a different amount of training measurements.

Limitations of our study are discussed below. We chose three models —a linear lumped-parameter model, a continuum model, and a neural network— to span a wide space of first principles-based (for the linear and continuum models) and data-driven (for the neural network) techniques. The linear and continuum models are the simplest of their respective classes, and any improved versions of these will inherit their core structure from the models presented here. Conclusions we draw about these classes of models are likely to hold for refined model versions even as performance may improve. In contrast, the neural network is not equally representative of the broad class of data-driven models. It is a popular choice in recent soft robotics modeling work, but its core features and fit parameters are not necessarily inherited by other data-driven techniques. Other data-driven methods relying on fundamentally different mathematical structures may be better at capturing the FREE's underlying physics. [159] note that deep learning techniques have "been shown to learn predictive physics-based models." [14] show the potential of the Koopman operator in modeling parallel structures of FREEs and [140] uses deep reinforcement learning to model a manipulator made from FREEs. Further, ensemble-based methods, like those proposed in [115], might be helpful in addressing network over-fitting.

We chose to study FREEs specifically because they share core structural features with both PneuNet-type soft robots and soft cable robots. Despite these similarities, the modeling styles presented here may have different behaviors when applied to other actuator styles. One result of the choice to analyse FREEs as compared to other soft robots is an implicit limitation to the stretches undergone. In our experiment and anticipated use cases, engineering strains on FREEs do not exceed values of about 25%. A strain of 25% is large, and firmly in the nonlinear behavioural regime according to classical continuum mechanics. Yet, other soft robot examples (e.g. [67]) likely do undergo larger strains than that, reaching the order of 100% - and our work does not capture soft systems at these levels of strain. A similar model comparison on non-FREE actuators is an avenue for future work.

The test settings defined in Eqns. 3.23, 3.24, 3.25 were applied uniformly to all samples, knowing already that many of these settings were not within the typical operating range of the individual samples. These settings thus resulted in buckled actuators that were excluded from the data set after the experiments were finished.

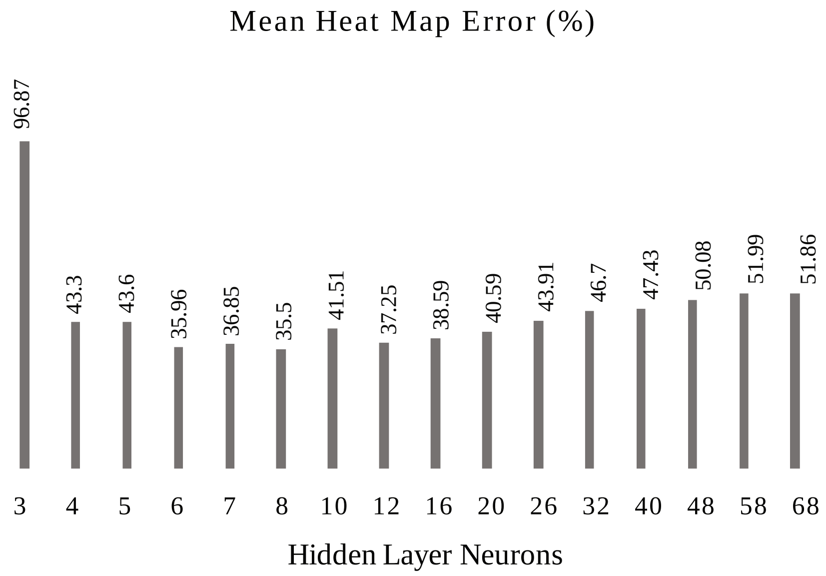

Figure 3.12: Mean heat map prediction error (%) over 5 randomized neural network trials, organized by the quantity of neurons on the hidden layer.

The advantage of this strategy was that it allowed us to generate the largest possible data set without overly restricting the possible testing conditions for each sample. Even after the removal of the buckled states, each sample had still at least 412, up to 2600, and an average of 1576 individual data points). The disadvantage of this approach was that such an a-posteriori selection can potentially introduce bias in the data. It is thus important to note that our results are only valid for un-buckled FREEs.

The static nature of the experimental validation is another limitation of this work. We also did not model or analyze hysteresis in this work. Measuring hysteresis could require a FREE experiment spanning several timescales (in contrast to this experiment, where the timescale is kept uniform), and offers the potential to evaluate novel mechanical models. It is an important avenue for future work. Further, the addition of significant inertial forces to an experiment would clearly change the loading outcomes. A new experiment would be required for a study of the dynamic behavior of FREEs, but all of the models presented here could be adapted to include dynamics.

The linear and continuum models here may be extended to include dynamics [142], and the neural network could be fit on experimental data that includes dynamic phenomena. Having demonstrated the strengths and weakness of these models on predicting the static behavior of FREEs, a dynamic investigation should be the next step.

The work presented here provides a broad experimental benchmark enabling comparison of distinct modeling styles found across the soft robotics literature. While the modeling approaches presented here have been previously proven on a variety of individual, fully functional soft robotic systems, a comparison on a common data set spanning a design and configuration space had not yet been realized. Naturally, selecting how to model a complex system is an endeavor that is best undertaken with multiple factors in mind, including whether any mechanisms underlying system behavior are known, whether data for parameter-fitting, model training, and model validation are available, and for what purposes and to what performance requirements the model will be deployed. This work first built a large and comprehensive data set that allowed us to rigorously assess the performance of three distinct models. Oftentimes a comprehensive data set it not available and experiments are expensive. Such is usually the case, for example, in the enterprise of design, when data may only exist from rough prototypes or not at all. It then becomes necessary to build or train a model on a small, narrow, or sparse data set and then to depend on the model's ability to extrapolate or interpolate (by *generalize*, we signify a capacity to both extrapolate and interpolate). Off-diagonal cells pertaining to FREE samples 1-8 in the heat maps of Fig. 10 can be considered tests of extrapolation from narrow data sets, in that fiber angle and length parameters did not vary in the fitting/training sets. Cells pertaining to aggregate data set formed using the even-numbered FREE samples and tested on individual FREEs 3, 5, and 7 are tests of interpolation. Evidently, even though a broad variation in fiber angle was present in this aggregate data set, that variation was still too sparsely sampled for the training needs of the neural net as indicated by the checkered pattern in column 9 of Fig. 3.10c.

The results shown here confirmed some behaviors already suggested by intuition (e.g. that models with a higher number of experimentally determined parameters may also have the highest peak performance). Yet, this analysis also uncovered trends of model performance and physical system behavior across the fiber-reinforced soft actuator design space that are not observable in isolated cases. A study like the one presented here would, of course, be impossible to perform on all permutations of articulated FREE-based systems. This is where our work complements existing papers like those of [136], [140], [163], [99] and others. The broad, actuator-level understanding presented here can help roboticists in various phases of soft system development and validation: our demonstration of the strengths, weaknesses, and failure points of each of these models can guide model choice for articulated systems of FREEs or soft actuators similar to FREEs, guide design as roboticists find which schemes best suit their modeling capabilities, and inform the development of a next generation of improved soft actuator models.

3.6 Summary

Successful soft robot modeling approaches appearing in recent literature have been based on a variety of distinct theories, including traditional robotic theory, continuum mechanics, and machine learning. Though specific modeling techniques have been developed for and validated against already realized systems, their strengths and weaknesses have not been explicitly compared against each other. In this work, we show how three distinct model structures —a lumped-parameter model, a continuum mechanical model, and a neural network— compare in capturing the gross trends and specific features of the force generation of soft robotic actuators. In particular, we study models for Fiber Reinforced Elastomeric Enclosures (FREEs), which are a popular choice of soft actuator and that are used in several soft articulated systems, including soft manipulators, exoskeletons, grippers, and locomoting soft robots. We generated benchmark data by testing eight FREE samples that spanned broad design and kinematic spaces and compared the models on their ability to predict the loading-deformation relationships of these samples. This comparison shows the predictive capabilities of each model on individual actuators and each model's generalizability across the design space. The continuum mechanical model generalized best across the design space similarly-sized FREEs with differing fiber orientations, but did not achieve as high a peak performance as the neural network even when fit and evaluated fon the same FREE sample. Its nonlinear structure and explicit description of fiber stretchability allowed it to model FREEs in kinematic configurations where the fiber was nearly parallel to the FREE's central axis. The results highlight the essential roles of mathematical structure and experimental parameter determination in building high-performing, generalizable soft actuator models with varying effort invested in system identification.

CHAPTER 4

Nonlinear Viscoelastic Model

This chapter (except Section 4.1) has been submitted for publication as a journal article and upon publication may be referenced as:

> Sedal, Audrey and Wineman, Alan. Force Reversal and Energy Dissipation in Composite Tubes through Non-Linear Viscoelasticity of Component Materials.

4.1 Motivation: “Magic Angle” and Stress Relaxation in FREEs

The previous chapters focused on quasi-static, time-independent responses of FREEs to internal pressure and imposed end displacement. The experiments in the previous chapters were carefully designed so that a quasi-static response rather than a dynamic response or a damped one could be measured. While the previous modeling work provides understanding of fundamental behaviors of FREEs, understanding of damping is used to create effective robotic systems such as walking robots [117] when stretchable polymers form the robot’s main structure.

Yet, the effect of viscoelasticity on behavior of fiber-reinforced polymers is not as well established in solid mechanics or in soft robotics. Phenomena such as the “magic angle” phenomenon [34, 51], in which changes of fiber orientation determine whether a fiber-reinforced material will undergo tension or compression at a given stretch, can significantly change the behavior of a soft robot. It is not yet known how these phenomena can interact to change FREE behavior.

Figure 4.1 shows an example of the magic angle phenomenon occurring in the data set of Chapter 3. At low pressures ($P < 10$kPa), the FREE is under a tensile force, but as its internal pressure increases, the constraint by the fiber causes it to move into the tensile regime.

Viscoelastic behavior was observed in FREEs in the data set of Chapter 3. In the sign convention of this data set, a compressive force is positive and a tensile force is negative. Figure 4.2 shows stress relaxation of a FREE having a single fiber family with fiber angle $\Gamma 80^\circ$ with respect to the tube's central axis, under and imposed axial extension of +4mm and no imposed twist. Despite internal pressure staying relatively similar throughout this time frame, the FREE force relaxes from a tensile force of 2.44N to one of 2.38N. The curve showing force over time follows a path resembling exponential decay, which is common in viscoelastic polymers.

For evaluation of a quasi-static model as in Chapter 3, this quantity of stress relaxation (which is similar to stress relaxation occurring elsewhere in the dataset) is not problematic. However, a full exploration has not been done of what circumstances may cause viscoelastic effects to be more influential. Further, novel polymers that are developed to be "active" in response to heat, magnetic or electric fields, or polymers that are developed to improve the resilience and extend the lifetime of FREEs may have the byproduct of undergoing additional stress relaxation as a consequence of their chemical composition. Interaction with the magic angle effect, use of novel "active" polymers, and controllers that aim to increase the precision and energy efficiency of soft robot motion could all benefit from a deeper exploration of viscoelasticity.

An exhaustive experimental study on the wide variety of component materials and configurations of soft actuators is prohibitively large. Instead, a new theory is proposed that is base don physical principles and describes viscoelastic effects in both the fiber and the matrix of a FREE. A simulated study is performed with the goal of finding combinations material properties, configurations, interaction with known physical effects (such as the magic angle phenomenon) that could produce

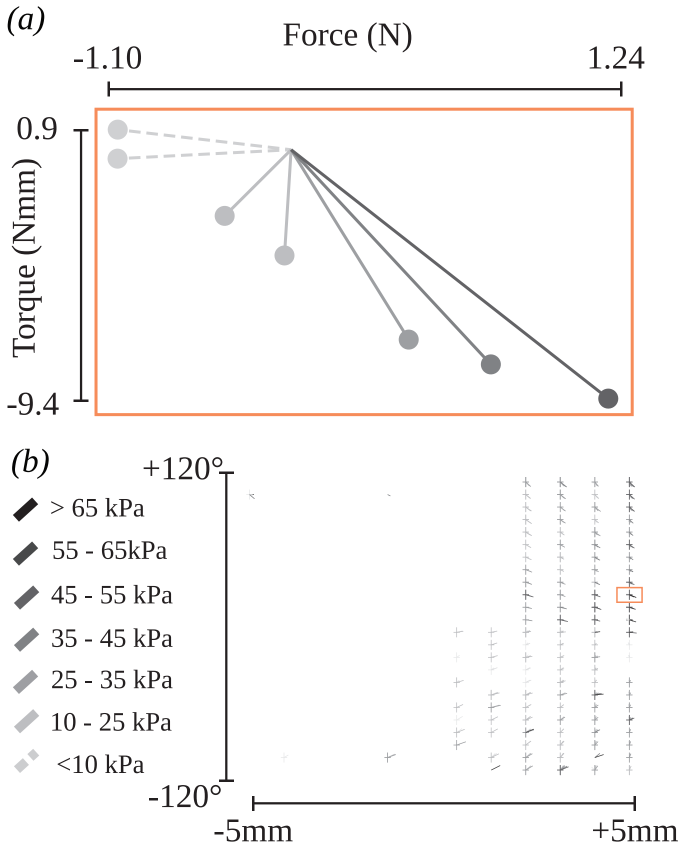

Figure 4.1: Transition of force from tensile ($P < 10$kPa) axial force to compressive ($P \geq 10$kPa) axial force on a FREE with a single fiber family having fiber angle $\Gamma = 80°$ w.r.t. the tube's central axis, at an imposed axial extension of +5mm and an imposed twist of 10°. In the sign convention of this data set, a compressive force is positive and a tensile force is negative.

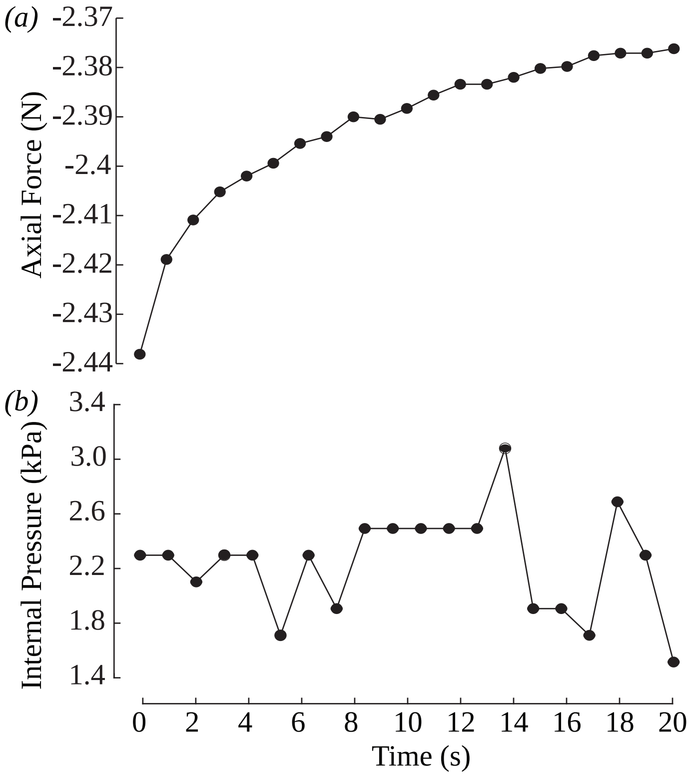

Figure 4.2: Stress relaxation of a FREE having a single fiber family with fiber angle $\Gamma = 80°$ w.r.t the tube's central axis, under and imposed axial extension of +4mm and no imposed twist. *(a)* Axial force over 20 seconds. *(b)* Internal pressure over time. In the sign convention of this data set, a compressive force is positive and a tensile force is negative.

unexpected behaviour in FREEs.

In the remaining parts of this chapter, the sign convention of Chapter 3 is not used. Instead, a tensile force is positive and a compressive force is negative.

4.2 Introduction

Soft, anisotropic materials consisting of a matrix embedded with patterned filaments are commonly found in nature. Skin, blood vessels, ligaments, plants and muscle all share this basic structure. In "soft" robotics, a subfield of robotics concerned with building systems that leverage soft materials to create safer and more mechanically intelligent systems, researchers have used such structures extensively to create actuators [86], manipulators [16, 106] and shape-morphing robots [60]. Unlike traditional robots, soft robots are compliant in all directions except for the actuated direction, meaning that they can bend around obstacles or conform to the shape of delicate objects without breaking them. This compliance gives soft robots special potential in human-interactive applications like assistive technology, in-home robotics, and surgical devices.

Reinforced soft structures offer key functional advantages over un-reinforced soft structures. These structures transmit stress anisotropically, meaning that they can be especially stretchy or stiff in selected directions. For example, muscles are strong in axial tension, and that muscle-like anisotropy has been mimicked robotically by soft "Pneumatic Artificial Muscles" (PAMs) [21]. In mechanics, nonlinearly elastic fiber-reinforced materials have been studied extensively [55, 64, 100, 125]. The anisotropy and resulting robotic behaviour of FREEs have been extensively studied [22, 26, 145].

In contrast, viscoelastic phenomena in soft robots are less studied. Polymers used in soft robots, such as rubber [167] and silicone [129], are inherently viscoelastic. They act as elastic solids, but internal friction between long-chain molecules influences behaviour. Damping, hysteresis, energy dissipation and creep are key facets of soft robotic behaviour that result from viscoelasticity of a soft robot's component materials. Because viscoelasticity is an inherent property of polymers, and because soft robots are made from a wide variety of polymers, viscoelastic phenomena are present on some level in every soft robotic system.

Understanding viscoelasticity can enable development of devices that match stiffness characteristics with human tissues and absorb impact. For example, Parnell and De Pascalis [112] propose a novel soft, viscoelastic metamaterial with tunable impact absoprtion and applicability in soft robotics. Further, bio-mechanical systems like the walls of arteries [61], muscle [70], skin and ligaments [113] have been found to be both anisotropic and viscoelastic; soft robot designs that accurately match behaviour with human tissues would then need to have viscoelasticity. With nonlinear, anisotropic models of viscoelasticity, soft robots can achieve their potential for safer, more seamless human interaction.

Viscoelastic behaviours of soft robots are most often characterized on a finished system after its construction, rather than chosen beforehand with specific functionality in mind. In soft robotics, it is common practice to rely on extensive mechanical characterization of already-constructed systems to understand their time-dependent properties. For example, Kim et al. [72] use a neural network and a full mechanical characterization to model hysteresis in a soft tactile sensor. Van Damme et al. [169] and Hošovskỳ et al. [65] use cyclic experiments to characterize hysteresis and damping of Fiber-Reinforced Elastomeric Enclosures (FREEs). Bai et al. [3] characterize the viscoelastic behaviour of dielectric elastomer actuators with cyclic experimentation. Mosadegh et al. [103] perform experiments to characterize hysteresis of silicone elastomer moulded “PneuNets.” Della Santina et al. [32] use a rigid-body approximation of a soft PneuNet-like robot to experimentally characterize its damping properties. In control of soft robots, linear viscoelastic models have been used. Shimoga and Goldenberg [153] use the Standard Linear Solid model to describe and characterize impedance control for a soft finger tip. Mustaza et al. [105] add some nonlinearity: they use a nonlinear spring to describe a hyperelastic rubber in parallel with a linear damper to develop a dynamic model of a soft actuator similar to the Kelvin-Voigt model. In each of these cases, viscoelastic behaviour is characterized on a robotic system that has already been designed and built.

With an appropriate modeling tool, soft roboticists could leverage knowledge of viscoelastic polymeric behaviours to design and control higher-performing soft systems. Damping and hysteretic behaviour could be analyzed before a system's construction and carefully matched to the impedance requirements of the robotic task at hand. Common models of viscoelastic are linear and fall into three categories [178]: the Maxwell model (Fig. 4.3c), the Kelvin-Voigt model (Fig. 4.3d), and the Standard Linear Solid (SLS) (Fig. 4.3e). However, viscoelasticity in soft robotics is difficult to analyse in a generalizeable way with linear models of viscoelasticity. A material whose elemental volumes are described as combinations of linear springs and linear dampers will necessarily experience a linear scaling between stresses and strains, but mechanicians as well as soft roboticists [26, 120], have repeatedly observed stress-strain nonlinearity in soft, fiber-reinforced systems under normal operation circumstances. Indeed, Mustaza et al.[105] add elastic nonlinearity to the viscoelastic model that they develop for control. Below, we present a model that tracks the evolution of a material's stresses and anisotropy over time as the various patterned materials each relax according to their own chemistry. This work will show new physical phenomena resulting from stress relaxation properties of a pressurized tube's fibers and matrix, highlighting how these properties combine with design parameters like fiber orientation to produce differing end behaviours.

In this paper, we develop and examine a non-linear viscoelastic model of soft, fiber-reinforced actuators. With this model, roboticists can simulate, inspect and optimize actuator designs for broad applications under a variety of environmental conditions. We study a thick-walled, fiber-reinforced tube in which two fiber families are wound symmetrically around a pressurizeable soft circular tube. This architecture shows the basic features of anisotropy and how this anisotropic behaviour changes as the fiber and matrix each relax at their own pace. In Section 4.3, we present the constitutive equation. In Section 4.4, the problem of a pressurized, thick-walled, fiber-reinforced tube is formulated. Section 4.5 gives the governing equations of the problem. Sections 4.6 and 4.7 concern the numeric solutions: Section 4.6 outlines the numerical methods used, while Section 4.7 discusses pertinent examples. Section 4.8 offers concluding comments.

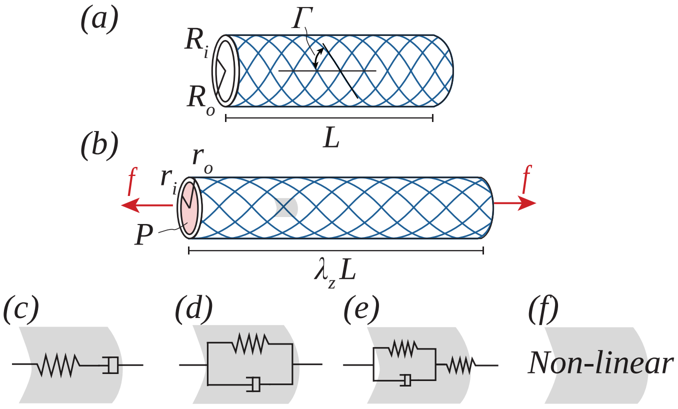

Figure 4.3: *(a)* Tube actuator in reference configuration with initial fiber angle Γ, initial length L, internal radius R_i, external radius R_o and atmospheric pressure in the interior. *(b)* Actuator in the current configuration with internal pressure P, length $\lambda_z L$, radii $r_{i,o}$ and force f on the endcaps. The representative volume element shown in grey may be modelled in a variety of ways: *(c)* the Maxwell mechanical analog, *(d)* the Kelvin-Voigt mechanical analog, *(e)* the Standard Linear Solid, or *(f)* a non-linear formulation.

4.3 Constitutive Equation

In soft robotics, fiber-reinforced tubular actuators are most often made with a braided structure of discrete polymeric fibers. This braid can be adhered to an elastomeric tube, or moulded with elastomer around the fibers. These actuators have been given a variety of names: McKibben actuators and Pneumatic Artificial Muscles (PAMs) [21, 22], fiber-reinforced Elastomeric Enclosures (FREEs) [8], or Fluidic Flexible Matrix Composites (F2MCs) [116, 149]. Throughout the work we will refer to this actuator as a FREE, even though the internal pressurization may come through any working fluid and not necessarily a gas.

We anaylse such actuators under a homogenization assumption - i.e., assuming that the fibers are continuously distributed rather than forming discrete parts of the structure [34, 51]. We further assume that there are no interaction effects such as friction between the elastomer and the fiber components. These assumptions enable a simple analysis for this exploration of time-dependent effects in such actuators.

Further, the homogenization assumption chosen here enables the use of an analytical framework where additional phenomena, e.g. fiber-matrix interaction, or temperature effects, can be added later as necessary.

A distinguishing feature of nonlinear viscoelastic materials is that the stress at some instant during the response depends on the preceding history of deformation. This means that it is necessary to distinguish between the current time t and a typical earlier time s, with $s \in (-\infty, t]$. We assume that at all times $t < 0$, the body is at rest in a stress-free configuration: this is taken as the reference configuration. The position of a particle in the body in its reference configuration is given by $\mathbf{X}$ and at later time t by $\mathbf{x}(t)$. The quantities needed to describe that deformation are presented next.

The tube's deformation over time is described by a relationship of the form:

$$\mathbf{x}(t) = \boldsymbol{\chi}(\mathbf{X}, t), \quad t \geq 0. \tag{4.1}$$

For clarity, there will be no further explicit indication of the independent variable $\mathbf{X}$ in the remaining equations. The deformation gradient is

$$\mathbf{F}(t) = \partial \mathbf{x}(t) / \partial \mathbf{X}. \tag{4.2}$$

The nonlinear fiber-reinforced material of the tube is assumed to be incompressible. Then, $\det \mathbf{F}(t) = 1$ for all particles and all times. The right Cauchy-Green strain tensor $\mathbf{C}$ at a time t is given by:

$$\mathbf{C}(t) = \mathbf{F}(t)^T \mathbf{F}(t). \tag{4.3}$$

The invariants of $\mathbf{C}(t)$ are:

$$I_1[\mathbf{C}(t)] = tr[\mathbf{C}(t)], \tag{4.4}$$

and

$$I_2[\mathbf{C}(t)] = \left[I_1[\mathbf{C}(t)]^2 - tr[\mathbf{C}(t)^2] \right] / 2 \tag{4.5}$$

We further assume that the material can be described by the Pipkin-Rogers single-integral constitutive equation for nonlinear viscoelastic response [119],[177]. For an incompressible nonlinear viscoelastic solid, the Pipkin-Rogers constitutive equation can be written as:

$$\boldsymbol{\sigma} = -q(t)\mathbf{I} + \mathbf{F}(t)\mathbf{\Pi}(t)\mathbf{F}(t)^T, \tag{4.6}$$

$$\mathbf{\Pi}(t) = \mathbf{R}[\mathbf{C}(t), 0] + \int_0^t \frac{\partial}{\partial(t-s)}\mathbf{R}[\mathbf{C}(s), t-s]ds. \tag{4.7}$$

Here, $\boldsymbol{\sigma}$ gives the Cauchy stress. The function $q(t)$ is a Lagrange multiplier included due to the incompressibility of the tube wall. A tensor-valued, deformation-dependent relaxation property is denoted by $\mathbf{R}[\mathbf{C}, t]$. In a step deformation history when the right Cauchy-Green strain tensor $\mathbf{C}$ is fixed, $\mathbf{R}[\mathbf{C}, t]$ decreases monotonically from the initial values $\mathbf{R}[\mathbf{C}, 0]$ to a non-zero limit denoted by $\mathbf{R}[\mathbf{C}, \infty]$.

For a material with two fiber families whose directions in the reference configuration are denoted by unit vectors $\mathbf{L}$ and $\mathbf{M}$ [157],

$$\begin{aligned}
\mathbf{R}[\mathbf{C}, t] = \alpha_0[I[\mathbf{C}], t]\mathbf{I} + \alpha_1[I[\mathbf{C}], t]\mathbf{C} + \alpha_2[I[\mathbf{C}], t]\mathbf{C}^2 \\
+\alpha_3[I[\mathbf{C}], t]\mathbf{L}\otimes\mathbf{L} + \alpha_4[I[\mathbf{C}], t](\mathbf{L}\otimes\mathbf{CL} + \mathbf{CL}\otimes\mathbf{L}) \\
+\alpha_5[I[\mathbf{C}], t]\mathbf{M}\otimes\mathbf{M} + \alpha_6[I[\mathbf{C}], t](\mathbf{M}\otimes\mathbf{CM} + \mathbf{CM}\otimes\mathbf{M}) \\
+\alpha_7[I[\mathbf{C}], t](\mathbf{L}\otimes\mathbf{M} + \mathbf{M}\otimes\mathbf{L}).
\end{aligned} \tag{4.8}$$

The symbol $I[\mathbf{C}]$ denotes the set of invariants including I_1 and I_2 (Eqns. 4.4 and 4.5) and the invariants listed below:

$$\begin{aligned}
I_3 &= 1, \\
I_4 &= \mathbf{L}^T\mathbf{C}\mathbf{L}, \qquad I_5 = \mathbf{L}^T\mathbf{C}^2\mathbf{L}, \\
I_6 &= \mathbf{M}^T\mathbf{C}\mathbf{M}, \qquad I_7 = \mathbf{M}^T\mathbf{C}^2\mathbf{M}.
\end{aligned} \tag{4.9}$$

Invariants I_{1-3} are associated with the matrix, and I_{4-7} are associated with the fibers.

4.3.1 Relation to Nonlinear Elastic Fiber Reinforced Materials

There are two important cases when the Pipkin-Rogers constitutive equation for an incompressible non-linear viscoelastic fiber reinforced material becomes independent of the preceding deformation and depends only on the current deformation.

1. A step change in deformation at $t = 0$.

   In a step change, $\mathbf{F}(0-) = \mathbf{I}$ and $\mathbf{F}(0^+) \neq \mathbf{I}$. Then $\mathbf{C}(0^+) = \mathbf{F}(0^+)^T\mathbf{F}(0^+) \neq \mathbf{I}$. The stress is given by (4.10) with $\mathbf{F} = \mathbf{F}(0^+)$, $\mathbf{C} = \mathbf{C}(0^+)$ and scalar coefficients $\tilde{\alpha}_i = \alpha_i[I[\mathbf{C}(0^+)], 0^+]$.

2. A fixed deformation as $t \to \infty$.

   Let the body approach a fixed deformed state, i.e. $\mathbf{F}(t) \to \mathbf{F}(\infty)$. Then, as in linear viscoelasticity ([178]), because of stress relaxation, it can be expected that the stress in the fixed deformed state is given by (4.10), with $\mathbf{F} = \mathbf{F}(\infty)$, $\mathbf{C} = \mathbf{C}(\infty) = \mathbf{F}(\infty)^T\mathbf{F}(\infty)$ and scalar coefficients $\tilde{\alpha}_i = \alpha_i[I[\mathbf{C}(\infty)], \infty]$.

The stress then responds only on the current deformation and is given by:

$$
\begin{aligned}
\boldsymbol{\sigma} = \ & -q\mathbf{I} + \mathbf{F}\Big[\tilde{\alpha}_0[I[\mathbf{C}]]\mathbf{I} + \tilde{\alpha}_1[I[\mathbf{C}]]\mathbf{C} + \tilde{\alpha}_2[I[\mathbf{C}]]\mathbf{C}^2 + \tilde{\alpha}_3[I[\mathbf{C}]]\mathbf{L}\otimes\mathbf{L} \\
& +\tilde{\alpha}_4[I[\mathbf{C}]](\mathbf{L}\otimes\mathbf{CL} + \mathbf{CL}\otimes\mathbf{L}) \\
& +\tilde{\alpha}_5[I[\mathbf{C}]]\mathbf{M}\otimes\mathbf{M} + \tilde{\alpha}_6[I[\mathbf{C}]](\mathbf{M}\otimes\mathbf{CM} + \mathbf{CM}\otimes\mathbf{M}) \\
& +\tilde{\alpha}_7[I[\mathbf{C}]](\mathbf{L}\otimes\mathbf{M} + \mathbf{M}\otimes\mathbf{L})\Big]\mathbf{F}^T, \qquad (4.10)
\end{aligned}
$$

which is the constitutive equation for an incompressible fiber reinforced elastic solid.

4.3.2 Specific Assumptions on Material Properties

Several assumptions can now be made about the scalar coefficients $\alpha_i[I[\mathbf{C}], t]$. It is first assumed that the fiber families have identical properties so that in Eqn. 4.8 ,

$\alpha_3 = \alpha_5$ and $\alpha_4 = \alpha_6$. Second, as is done in previous work using this model [34, 51], that $\alpha_4 = \alpha_6 = \alpha_7 = 0$.

The scalar coefficients of $\alpha_i[I[\mathbf{C}], t]$ are given as

$$\alpha_0[I[\mathbf{C}], t] = 2G_1(t)[1 - I_2\Phi] + 2G_2(t)[I_1 - 2I_2\Phi] \tag{4.11}$$

$$\alpha_1[I[\mathbf{C}], t] = 2G_1(t)I_1\Phi + 2G_2(t)[2I_1\Phi - 1] \tag{4.12}$$

$$\alpha_2[I[\mathbf{C}], t] = -2\Phi[G_1(t) + 2G_2(t)] \tag{4.13}$$

$$\alpha_3 = 2G_3(t)[I_4 - 1]. \tag{4.14}$$

Here,

$$\Phi = exp[-(I_1 - 3)]. \tag{4.15}$$

The functions $G_i(t), i \in \{1, 2, 3\}$ are relaxation functions, chosen as exponential functions in terms of instantaneous value $G_i(0)$, asymptotic value $G_i|_{t\to\infty}$, and time constant τ_i. The functions $G_{1,2}(t)$ are associated with the Mooney-Rivlin terms of the matrix, while the function $G_3(t)$ is associated with the fiber. We assume that $G_2(t) = 0$, i.e. a neo-Hookean matrix. Then we rename $G_1(t) = G_m(t)$ for the relaxation function associated with the matrix and $G_3(t) = G_f(t)$ for the relaxation function associated with the fiber.

This choice for the scalar coefficients $\alpha_i[I[\mathbf{C}, t]$ in terms of $G_i(t)$ is made so that the limits at $t = 0$ and as $t \to \infty$, the constitutive equation 4.10 has the same form as the standard reinforcing model used in previous studies [34, 51]. The function Φ (Eqn. 4.15) is chosen so that the constitutive equation approaches the linearized theory in the limit of small strains.

$$G_m(t) = G_m|_{t\to\infty} + (G_m(0) - G_m|_{t\to\infty})e^{-\frac{t}{\tau_m}} \tag{4.16}$$

$$G_f(t) = G_f|_{t\to\infty} + (G_f(0) - G_f|_{t\to\infty})e^{-\frac{t}{\tau_f}}. \tag{4.17}$$

To simplify the notation throughout the rest of this paper, we use $G_m(\infty)$ to denote $G_m|_{t\to\infty}$ and $G_f(\infty)$ for $G_f|_{t\to\infty}$. Normalizing all stresses in the pressure

$P(t)$ by $G_m(0) = 1$ and all time units by τ_m gives normalized functions $\bar{G}_{m,f}(t)$ as

$$\bar{G}_m(t) = \frac{G_m|_{t\to\infty}}{G_m(0)} + \left(1 - \frac{G_m|_{t\to\infty}}{G_m(0)}\right)e^{-t} \tag{4.18}$$

$$\bar{G}_f(t) = \frac{G_f|_{t\to\infty}}{G_m(0)} + \left(\frac{G_f(0)}{G_m(0)} - \frac{G_f|_{t\to\infty}}{G_m(0)}\right)e^{-t\frac{\tau_m}{\tau_f}}. \tag{4.19}$$

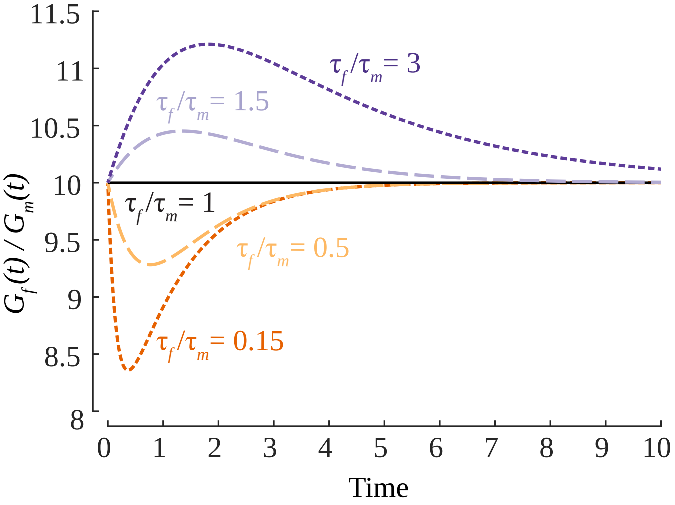

Figure 4.4: Relative stiffness $G_f(t)/G_m(t)$ for a fiber-reinforced material with $G_m(\infty)/G_m(0) = 0.75$, $G_f(0)/G_m(0) = 10$, $G_f(\infty)/G_m(0) = 7.5$. At $t = 0$, $G_f/G_m = 10$, and as time approaches infinity, G_f/G_m reaches an asymptote of 10 as well. In between, the various values τ_f/τ_m affect the relative stiffness of the fiber to the elastomer, which influences the role of the fiber in determining stresses.

Since both the matrix and the fiber are viscoelastic in this model, their relative stiffness, and therefore their relative contributions to net loading, can change over time. Figure 4.4 shows some of the potential diversity in the shape of the relative stiffness curves $G_f(t)/G_m(t)$. The initial and final values of stiffness are the same of all of the examples shown. Yet, if the fiber relaxes more quickly or more slowly than the matrix, the stiffness behaviour of the system changes. For example, in Figure 4.4, $G_f(t)/G_m(t)$ initially decreases when $\tau_f/\tau_m < 1$ and initially increases when $\tau_f/\tau_m > 1$. In some cases, the fiber becomes less stiff relative to the matrix before reaching its stiffness asymptote, while in others, the fiber initially becomes even stiffer than the matrix. For example, the case with $\tau_f/\tau_m = 0.15$ has a local minimum of relative fiber stiffness around 8.4, but the case with $\tau_f/\tau_m = 3$ has a local maximum of fiber stiffness around 11.3.

4.4 Formulation for Fiber-Reinforced Tubes

Here, we formulate the problem for nonlinearly viscoelastic, thick-walled cylindrical tubes reinforced by two families of nonlinear viscoelastic fibers symmetric about the tube's central axis (Fig. 4.3*a*). Consider a tube in its reference configuration with length L, inner radius R_i, outer radius R_o. For the first family, the fiber angle relative to the tube's axis is defined by Γ. The angle of the second fiber family is then $-\Gamma$. Circular caps enclose the tube at each end.

A uniform pressure $P(t)$ is distributed over the inner surface of the tube, and an axial force f is applied to each end of the tube, parallel to its axis. The outer surface of the tube, other than the caps, is traction-free. In the current configuration, the tube has length $l(t)$, inner radius $r_i(t)$ and outer radius $r_o(t)$, as shown in Fig. 4.3 *b*.

The coordinates of a particle are (R, Θ, Z) in the reference configuration and (r, θ, z) in the current configuration. Particles in the incompressible tube wall will undergo the time-dependent motion defined by:

$$\begin{aligned} r(t) &= \sqrt{\frac{R^2 - R_i^2}{\frac{l(t)}{L}} + r_i^2(t)}, \\ \theta &= \Theta, \\ z(t) &= \frac{l(t)}{L} Z. \end{aligned} \tag{4.20}$$

The current outer radius $r_o(t)$ is related to the current inner radius $r_i(\theta)$ by

$$r_o(t) = \sqrt{\frac{L(R_o^2 - R_i^2)}{l(t)} + r_i^2} \tag{4.21}$$

Let

$$\lambda_z(t) = \frac{l(t)}{L}. \tag{4.22}$$

The deformation gradient is

$$\mathbf{F}(t) = \begin{bmatrix} \frac{R}{r(t)\lambda_z(t)} & 0 & 0 \\ 0 & \frac{r(t)}{R} & 0 \\ 0 & 0 & \lambda_z(t) \end{bmatrix}. \tag{4.23}$$

Let

$$\lambda_r(t) = \frac{R}{r(t)\lambda_z(t)} \tag{4.24}$$

and

$$\lambda_\theta(t) = \frac{r(t)}{R}. \tag{4.25}$$

By the incompressibility constraint,

$$\lambda_z(t) = \frac{1}{\lambda_r(t)\lambda_\theta(t)}. \tag{4.26}$$

The right Cauchy-Green tensor is

$$\mathbf{C}(t) = \begin{bmatrix} \lambda_r(t)^2 & 0 & 0 \\ 0 & \lambda_\theta(t)^2 & 0 \\ 0 & 0 & \lambda_z(t)^2 \end{bmatrix}. \tag{4.27}$$

The invariants of $\mathbf{C}(t)$ in Eqns. 4.4 and 4.5 are

$$I_1[\mathbf{C}(t)] = \lambda_r(t)^2 + \lambda_\theta(t)^2 + \frac{1}{(\lambda_r(t)\lambda_\theta(t))^2}, \tag{4.28}$$

$$I_2[\mathbf{C}(t)] = \frac{1}{\lambda_r(t)^2} + \frac{1}{\lambda_\theta(t)^2} + (\lambda_r(t)\lambda_\theta(t))^2. \tag{4.29}$$

For symmetric helical fiber families, we can describe the fiber directions $\mathbf{L}$ and

M by

$$\mathbf{L} = \begin{bmatrix} 0 \\ \sin(\Gamma) \\ \cos(\Gamma) \end{bmatrix}, \mathbf{M} = \begin{bmatrix} 0 \\ -\sin(\Gamma) \\ \cos(\Gamma) \end{bmatrix}. \tag{4.30}$$

The invariant I_4 (Eqn. 4.9 in terms of the stretches is then

$$I_4 = \lambda_\theta^2 \sin^2(\Gamma) + \lambda_z^2 \cos^2(\Gamma). \tag{4.31}$$

In Eqns. 4.6 and 4.7, let $\boldsymbol{\sigma} = -q(t)I + \boldsymbol{\mathcal{F}}(t)$ where $\boldsymbol{\mathcal{F}}(t) = \mathbf{F}(t)\mathbf{\Pi}(t)\mathbf{F}(t)^T$. Then, using Eqn. 4.23 and Eqns. 4.27-4.31,

$$\begin{aligned} \mathcal{F}_{11} = \mathcal{F}_{rr} &= \left(\frac{R}{r(t)\lambda_z(t)}\right)^2 [\mathrm{R}_{11}[\mathbf{C}(t), 0] + \int_0^t \frac{\partial}{\partial(t-s)} \mathrm{R}_{11}[\mathbf{C}(t), t-s] ds] \\ \mathcal{F}_{22} = \mathcal{F}_{\theta\theta} &= \left(\frac{r(t)}{R}\right)^2 [\mathrm{R}_{22}[\mathbf{C}(t), 0] + \int_0^t \frac{\partial}{\partial(t-s)} \mathrm{R}_{22}[\mathbf{C}(t), t-s] ds] \\ \mathcal{F}_{33} = \mathcal{F}_{zz} &= \lambda_z(t)^2 [\mathrm{R}_{33}[\mathbf{C}(t), 0] + \int_0^t \frac{\partial}{\partial(t-s)} \mathrm{R}_{33}[\mathbf{C}(t), t-s] ds]. \end{aligned} \tag{4.32}$$

With Eqns. 4.3 and 4.7 and the assumption that $\alpha_3 = \alpha_5$ and $\alpha_4 = \alpha_6$ the matrix expression for $\mathbf{R}[\mathbf{C}, t]$ is given by

$$
\begin{aligned}
\mathbf{R}[\mathbf{C}(t),s] &= \alpha_0(t,s)\begin{bmatrix}1&0&0\\0&1&0\\0&0&1\end{bmatrix} + \alpha_1(t,s)\begin{bmatrix}\lambda_r^2(t)&0&0\\0&\lambda_\theta^2(t)&0\\0&0&\lambda_z^2(t)\end{bmatrix}\\
&+\alpha_2(t,s)\begin{bmatrix}\lambda_r^4(t)&0&0\\0&\lambda_\theta^4(t)&0\\0&0&\lambda_z^4(t)\end{bmatrix} + 2\alpha_3(t,s)\begin{bmatrix}0&0&0\\0&\sin^2(\Gamma)&0\\0&0&\cos^2(\Gamma)\end{bmatrix}\\
&+4\alpha_4(t,s)\begin{bmatrix}0&0&0\\0&\lambda_\theta\sin^2(\Gamma)&0\\0&0&\lambda_z\cos^2(\Gamma)\end{bmatrix} + \alpha_7\begin{bmatrix}0&0&0\\0&-2\sin^2(\Gamma)&0\\0&0&2\cos^2(\Gamma)\end{bmatrix}. \qquad (4.33)
\end{aligned}
$$

With the assumption that $\alpha_4 = \alpha_7 = 0$ given in Section 4.34.3.2, **R** is diagonal with components

$$\mathrm{R}_{11} = \alpha_0(s) + \alpha_1(s)\lambda_r^2 + \alpha_2(s)\lambda_r^4 \qquad (4.34)$$

$$\mathrm{R}_{22} = \alpha_0(s) + \alpha_1(s)\lambda_\theta^2 + \alpha_2(s)\lambda_\theta^4 + 2\alpha_3(s)\sin^2(\Gamma) \qquad (4.35)$$

$$\mathrm{R}_{33} = \alpha_0(s) + \alpha_1(s)\lambda_z^2 + \alpha_2(s)\lambda_z^4 + 2\alpha_3(s)\cos^2(\Gamma) \qquad (4.36)$$

Since **F** in Eqn. 4.23 and each matrix in the expression for **R** (Eqns. 4.34, 4.35, 4.36) is diagonal, the Cauchy stress $\boldsymbol{\sigma}$ is diagonal as well.

Explicit expressions for the stress components are obtained by combining the expressions for α_i in Eqns. 4.11-4.14, 4.34-4.36, and 4.33.

4.5 Governing Equations

Eqns. 4.21 and 4.22 show that the deformation of the FREE depends parameterically on R (or, equivalently $r_i(t)$) and $\lambda_z(t)$. By Eqn. 4.33, $\boldsymbol{\mathcal{F}}_{ii}$ then also depend on R.

It is assumed that the motion of the PAM is slow enough that inertial effects can be neglected. It is also assumed that body forces can be neglected. The stresses on the PAM must then satisfy these partial differential equations of equilibrium at each time t at every point in the current configuration. Letting $\boldsymbol{\mathcal{F}}_{ii}(r) = \boldsymbol{\mathcal{F}}_{ii}$,

$$\begin{aligned}
\frac{\partial \boldsymbol{\sigma}_{rr}}{\partial r} + \frac{1}{r}\frac{\partial \boldsymbol{\sigma}_{r\theta}}{\partial \theta} + \frac{\partial \boldsymbol{\sigma}_{rz}}{\partial z} + \frac{\boldsymbol{\sigma}_{rr} - \boldsymbol{\sigma}_{\theta\theta}}{r} &= 0, && (4.37)\\
\frac{\partial \boldsymbol{\sigma}_{r\theta}}{\partial r} + \frac{1}{r}\frac{\partial \boldsymbol{\sigma}_{\theta\theta}}{\partial \theta} + \frac{\partial \boldsymbol{\sigma}_{\theta z}}{\partial z} + 2\frac{\boldsymbol{\sigma}_{r\theta}}{r} &= 0, && (4.38)\\
\frac{\partial \boldsymbol{\sigma}_{rz}}{\partial r} + \frac{1}{r}\frac{\partial \boldsymbol{\sigma}_{\theta z}}{\partial \theta} + \frac{\partial \boldsymbol{\sigma}_{zz}}{\partial z} + \frac{\boldsymbol{\sigma}_{rz}}{r} &= 0. && (4.39)
\end{aligned}$$

As shown earlier, $\boldsymbol{\mathcal{F}}$ is a function of r and t, or equivalently, $\mathbf{R}$ and t. In general, the Lagrange multiplier $q = q(r, \theta, z, t)$ is an unknown function that is to be determined by analysis. When the stresses are substituted into the equilibrium equations, Eqn. 4.38 implies $\partial q/\partial \theta = 0$ and Eqn. 4.39 implies $\partial q/\partial z = 0$. Thus, here $q = q(r, t)$. Since $\boldsymbol{\sigma}$ is diagonal, $\boldsymbol{\sigma}_{r\theta} = \boldsymbol{\sigma}_{rz} = 0$ and Eqn. 4.37 reduces to

$$\frac{\partial \boldsymbol{\sigma}_{rr}}{\partial r} + \frac{\boldsymbol{\sigma}_{rr} - \boldsymbol{\sigma}_{\theta\theta}}{r} = 0. \tag{4.40}$$

Integrating Eqn. 4.40, noting that the PAM's interior pressure is equal to the radial stress at the interior boundary (i.e., $-P = \boldsymbol{\sigma}_{rr}(r_i)$), and recalling that $\boldsymbol{\sigma} = -q\mathbf{I} + \boldsymbol{\mathcal{F}}$, we obtain the result

$$q(r) = P + \mathcal{F}_{rr} + \int_{r_i}^{r} \frac{\mathcal{F}_{rr} - \mathcal{F}_{\theta\theta}}{r'} dr' \tag{4.41}$$

Performing the change of variables $r' \to R'$ to the integral in Eqn. 4.41 gives

$$q(r) = P + \mathcal{F}_{rr} + \int_{R_i}^{R} \frac{\mathcal{F}_{rr} - \mathcal{F}_{\theta\theta}}{R'\lambda_\theta(t)^2\lambda_z(t)} dR' \tag{4.42}$$

which gives an explicit expression for $q(r, t)$. Further, given that the PAM is operating in an environment at atmospheric pressure, the boundary condition at the exterior surface is given by $\boldsymbol{\sigma}_{rr}(r_o) = 0$. Then, from 4.10:

$$-P = \int_{r_i}^{r_o} \frac{\mathcal{F}_{rr} - \mathcal{F}_{\theta\theta}}{r} dr. \tag{4.43}$$

Performing the change of variables $r \rightarrow R$ to the integral in Eqn. 4.43 gives

$$-P = \int_{R_i}^{R_o} \frac{\mathcal{F}_{rr} - \mathcal{F}_{\theta\theta}}{R\lambda_\theta(t)^2\lambda_z(t)} dR. \tag{4.44}$$

The equation for the internal pressure is then

$$-P(t) = \int_{r_i(t)}^{r_o(t)} \frac{\boldsymbol{\mathcal{F}}_{rr} - \boldsymbol{\mathcal{F}}_{\theta\theta}}{r} dr. \tag{4.45}$$

With $q(r)$ from Eqn. 4.42,

$$\boldsymbol{\sigma}_{zz} = -P + \mathcal{F}_{zz} - \mathcal{F}_{rr} + \int_{R_i}^{R} \frac{\mathcal{F}_{\theta\theta} - \mathcal{F}_{rr}}{R'\lambda_\theta(t)^2\lambda_z(t)} dR'. \tag{4.46}$$

The net axial force on the cross-section of the tube N is found by integrating the axial stress across the tube wall, giving

$$N = 2\pi \int_{R_i}^{R_o} \boldsymbol{\sigma}_{zz} R\lambda_\theta(t)\lambda_r(t) dR. \tag{4.47}$$

Th relation between the axial force f on the end cap of the tube, the force on the cross-section on the tube, and the force from the interior pressure P on the end of the tube is

$$f = N - P\pi r_i^2(t). \tag{4.48}$$

The equation for the axial force is then

$$f(t) = -Pr_i^2\pi + 2\pi\left[\frac{Pr_i^2}{2} + \int_{r_i}^{r_o} (\boldsymbol{\mathcal{F}}_{zz} - \boldsymbol{\mathcal{F}}_{rr}) + \frac{1}{2}(\boldsymbol{\mathcal{F}}_{rr} - \boldsymbol{\mathcal{F}}_{\theta\theta}) r dr\right]. \tag{4.49}$$

The axial force $f(t)$ is presented above in terms of the internal pressure $P(t)$ as well as $\lambda_z(t)$ and $r_i(t)$. If any two quantities of $\{f(t), P(t), \lambda_z(t), r_i(t)\}$ are specified, there then exists a system of equations that may be solved to find the remaining two quantities. Together, Equations 4.45 and 4.49 form the governing Equations of the system.

4.6 Numerical Methods of Solution

To investigate the effect of material properties on force-displacement behaviour, we considered the resultant force of a FREE with geometric design parameters $\bar{p} = \{L, \Gamma, R_i, R_o\}$ and material properties $G_f(t)$, $G_m(t)$, and τ_f/τ_m. The geometric parameters in $\bar{p}$ refer to the actuator length, fiber angle (with fiber orientations for each family defined in Eqn. 4.30), and internal and external radii in the reference configuration. Each of these parameters is given in 4.1. The actuator length is normalized such that $L = 1$, and radii are normalized such that $R_i = 1$. To make a study possible, limitations are applied to the design parameter space: all cases studied here have $R_o = 1.2$. The fiber orientation was varied in this study with $\Gamma \in \{20, 40, 60, 80\}^\circ$.

The material stiffnesses and the internal pressure are are normalized by $G_m(0) = 1$, and the time constants are normalized so that $\tau_m = 1$. To make a study possible, limitations are applied to the material stiffnesses: $G_m(\infty)/G_m(0) = 0.75$, $G_f(0)/G_m(0) = 10$, $G_f(\infty)/G_m(0) \in \{7.5, 8\}$. The time constant ratio τ_f/τ_m was varied in this study.

Limitations on the operating conditions are given in Table 4.2. The axial stretch $\lambda_z(t)$ was varied, but always had the form $kh(t)$, where $h(t)$ is a step function and k is a constant. Various cases of pressure input $P(t)$ are studied.

Specific choices were also made in the numerical solution methods. Both time and space integrals were solved numerically with the trapezoidal rule.

Error due to numeric approximation is estimated by halving the size of the radius and time increments (when applicable) and measuring the difference between two results for the same configuration. Error did not exceed 1.3%, and error bars on the

Parameter Type	**Symbol**
Material Stiffnesses	$G_m(0) = 1$
	$G_m(\infty)/G_m(0)$
	$G_f(0)/G_m(0)$
	$G_f(\infty)/G_m(0)$
Material Relaxation Time Constants	$\tau_m = 1$
	τ_f/τ_m
Design Parameters	L
	Γ
	R_i
	R_o

Table 4.1: Parameter table of FREE material properties and design parameters. Due to both the to normalized variables used and the large available parameter space, some parameters are fixed. Fixed and variable parameters in our study are noted in the table.

Parameter Type	**Symbol**
Axial Stretch	$\lambda_z(t) = l(t)/L$
Input Pressure	$P(t)$

Table 4.2: Operating parameters tested for FREEs in this study. Owing to the large possible space of time-valued functions, step stretches are studied here along with step, pulse or cyclical applied internal pressure.

graphs do not exceed the thickness of the lines shown.

Space integrals were solved with the trapezoidal rule in increments of size 5.71×10^{-3} or 2.86×10^{-3}. Time integrals were also solved with the trapezoidal rule with time steps of either 1.60×10^{-2} or 8.0×10^{-3}. Details of each simulation are given alongside the result plots in the following section.

4.7 Numerical Examples

We studied the model behaviour for a variety of FREE designs with differing fiber orientations Γ under various input pressures and operating conditions. As noted in Section 4.5, if any two of the quantities l, r_i, f, P are known, a system of equations exists such that the remaining quantities can be found.

One key assumption of this work is that pressure control into the tube is achievable; in practice, pressure regulators with proportional, integral and/or derivative control may be used to set a specific pressure inside a FREE. Dynamics associated with fluid flow into the FREE and compressible fluid volume are left to future work. Therefore, we have chosen to set the interior pressure $P(t)$ as a step function or sinusoid, and impose a length change $\lambda_z(t)$ as a step function. We found that under these conditions, axial force reversal and energy dissipation of the FREE were apparent.

4.7.1 Transition of End Force Under Step Pressure

Figure 4.5 shows the axial force f on the end of a FREE with $\Gamma = 40°$ at various step stretches $\lambda_z \in [0.85, 1.15]$ and a step pressure input of $P = 0.15$. The instantaneous response is shown in dark purple, while the response as $t \to \infty$ is shown in light purple. Both the instantaneous and long-term responses to step pressure have a concave-up relationship with length. For $\lambda_z = 1.005 \pm 0.001$, the curve for the instantaneous force response crosses over the curve for the long-term response; this crossover point is marked by $\text{C}_{40°}$. At the point when these curves cross, the instantaneous axial force and force when $t \to \infty$ are the same.

Each of the transitions A → A' and B → B' shows an exponential transition

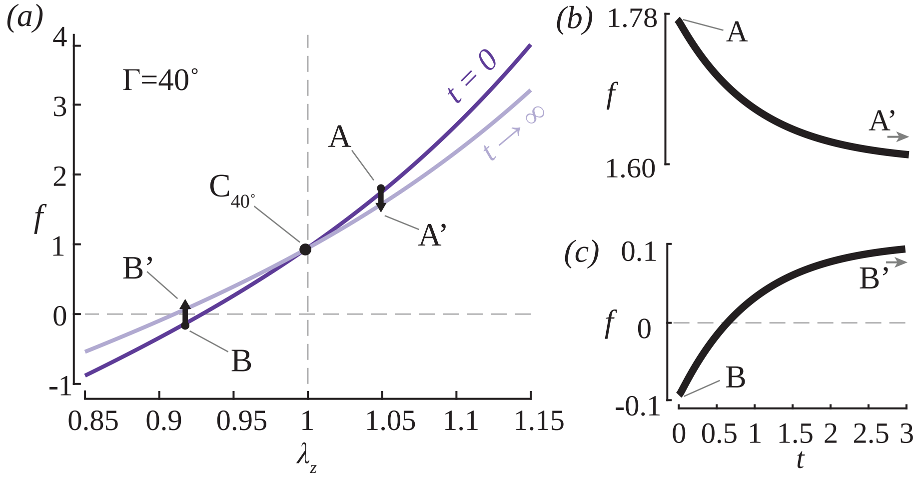

Figure 4.5: End force response of a FREE with $\Gamma = 40°$, $\tau_f/\tau_m = 1$, $G_m(\infty) = 0.75$, $G_f(0) = 10$, and $G_f(\infty) = 7.5$ under step pressure $P = 0.15$. *(a)* Axial force on the FREE under step stretch conditions $\lambda_z \in [0.85, 1.15]$ at $t = 0$ (dark purple line) and as $t \to \infty$ according to Eqn. 4.25(light purple line). The point where the two force curves cross is marked with a circle. Radius increments of size 1.25×10^{-3} were used. *(b)* Decrease in FREE end force over time at step $\lambda_z = 1.05$ and step $P = 0.15$. The points A and A', showing the instantaneous force response and horizontal asymptote respectively, correspond to A and A' in part *a*, and the curve corresponds to the black arrow connection between A and A' in part *a*. *(c)* Increase in FREE end force from compression to tension at step $\lambda_z = 0.92$ and step $P = 0.15$. The points B and B', showing the instantaneous force response and horizontal asymptote respectively, correspond to B and B' in part *a*, and the curve corresponds to the black arrow connecting B and B' in part *a*. For parts *b* and *c*, radius increments of size 2.5×10^{-3} were used and time increments of size 0.015 were used.

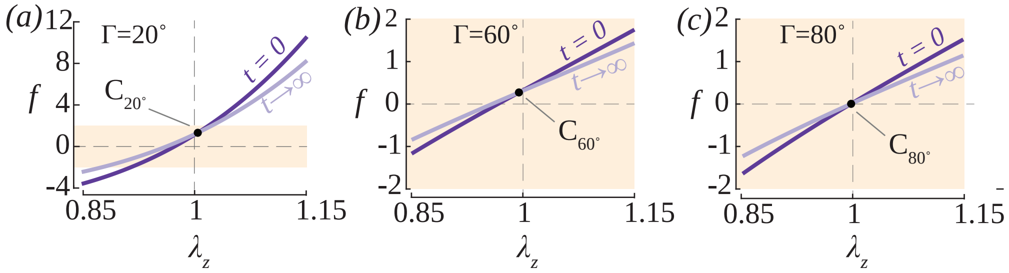

Figure 4.6: End force response of a FREE with $\tau_f/\tau_m = 1$, $G_m(\infty) = 0.75$, $G_f(0) = 10$, and $G_f(\infty) = 7.5$ under step pressure $P = 0.15$ and step stretch conditions $\lambda_z \in [0.85, 1.15]$. Instantaneous response at $t = 0$ is shown by a dark purple line and long-term response as $t \to \infty$ is shown by a light purple line. *(a)* Force on a FREE with $\Gamma = 20°$. *(b)* Force on a FREE with $\Gamma = 60°$. *(c)* Force on a FREE with $\Gamma = 80°$. The pale orange boxes correspond to the same range of f and λ_z in all graphs. Each point where the instantaneous and long-term force curves cross is marked with a black circle. Radius increments of 1.25×10^{-3} were used for all cases shown here.

toward a horizontal asymptote. For λ_z exceeding the crossover point C, the axial force on the FREE decreases over time. Points A and A' in Figure 4.5*(a)*, where $\lambda_z = 1.05$, show one example of the decrease. The transition from A to A' is shown in further detail in Figure 4.5*(b)*. Here, the instantaneous force is 1.772 but decreases to 1.611 when $t = 3$. For λ_z less than the "no-change" value, the force on the FREE increases over time. The transition from B to B' is shown in part *(c)* of Figure 4.5. Between points B and B', when $\lambda_z = 0.92$, the FREE transitions from an instantaneous compressive end force to a long-term tensile end force. At $t = 0$, $f = -0.093$, but at $t = 3$ the force has risen to 0.096.

Similar force transitions exist in other FREE designs. Figure 4.6 shows the relationship between stretch λ_z and the instantaenous and long-term axial forces on the forces on FREEs $\Gamma = 20°$, $\Gamma = 60°$ and $\Gamma = 80°$.

All of the examples in Figure 4.6 exhibit the same crossover phenomenon as the example in Figure 4.5. For stretches λ_z to the left of the crossover point, the instantaneous force response less than the long-term force response, and the FREE has a net increase in force. For λ_z to the right of the crossover, the FREE undergoes a net decrease in force. Further, the FREEs with $\Gamma = 20°$ (Fig. 4.6a) and $\Gamma = 60°$ (Fig. 4.6a) exhibit a net transition from axial compressive forces to tensile forces over time.

However, a FREE's intial fiber orientation Γ does affect the location of the crossover point and the force behaviour around it. The value of Γ greatly affects the range of forces f output by the FREE. For example, the FREE with $\Gamma = 20°$ (Fig. 4.6a) has axial forces $f \in (-4, 12)$ while the FREEs with $\Gamma = 60°$ and $\Gamma = 80°$ have axial forces $f \in (-2, 2)$.The location of the crossover point $\mathrm{C}_{20°}$ in Figure 4.6a is located at $\lambda_z \in [1.004, 1.005]$ and $f \in [1.282, 1.382]$. The FREE with $\Gamma = 20°$ then has its "no-change" condition of axial force at a slightly elongated configuration and a relatively axial force. The FREE with $\Gamma = 60°$ (Fig. 4.6b) has $\mathrm{C}_{60°}$ at $\lambda_z \in [9.940 \times 10^{-1}, 9.952 \times 10^{-1}]$ and $f \in [2 \times 10^{-3}, 3 \times 10^{-3}]$; a slightly compressive axial stretch and a lower force. The FREE with $\Gamma = 80°$ has its crossover $\mathrm{C}_{80°}$ at $\lambda_z \in [9.964 \times 10^{-1}, 9.976 \times 10^{-1}]$ and $f \in [-1 \times 10^{-3}, 2 \times 10^{-2}]$; again a slightly compressive axial stretch and a low force. The behaviour around the crossover point also differs with Γ. For the FREEs with $\Gamma = 20°$ (Fig. 4.6a) and $\Gamma = 40°$ (Fig. 4.5), the instantaneous and long-term force-stretch curves are concave-up. For $\Gamma = 80°$ (Fig. 4.6c), the force-stretch curves are concave-down. The curves for the FREE with $\Gamma = 60°$ (Fig. 4.6b) have a relatively straight appearance and are only slightly concave-down.

4.7.2 Effect of Relaxation Time on Axial Force

Even when the instantaneous and long-term properties of two FREEs are the same, the ratio of relaxation times $\tau_{/}\tau_m$ influences output behaviour in finite time. One example of such an influence is shown in Figure 4.7. In part a, the axial forces on FREEs with the same step inputs ($\lambda_z = 0.95$ and $P = 0.2$), fiber orientation $\Gamma = 40°$ and relaxation properties $(G_m(\infty)/G_m(0) = 0.75, G_f(0)/G_m(0) = 10, G_f(\infty)/G_m(0) = 7.5)$ are shown. Yet, the relaxation time ratio τ_f/τ_m varies in each case. We can see from Figure 4.7b that though the instantaneous force at $t = 0$ is the same, the axial force behaviour for $t \in (0, 0.4]$ differs with τ. The FREE with

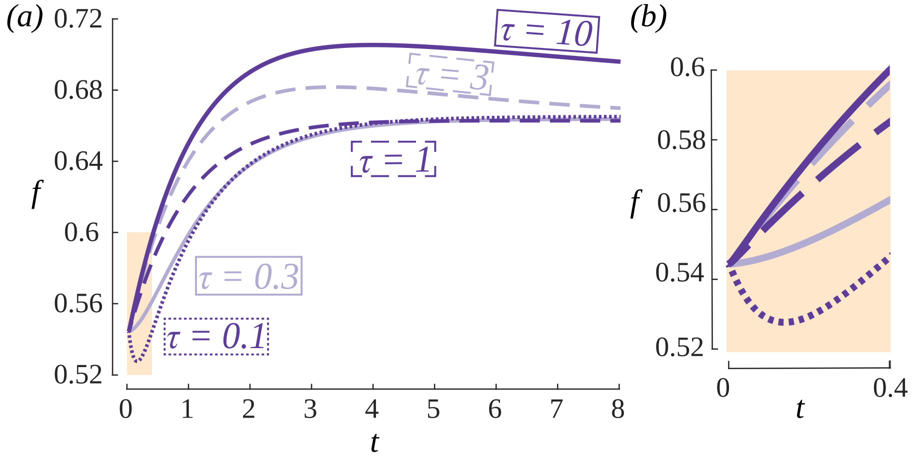

Figure 4.7: *(a)* Time-valued axial force f on FREEs with $\Gamma = 40°$ under step stretch $\lambda_z = 0.95$ and step pressure $P = 0.2$. For these FREEs, $G_m(\infty)/G_m(0) = 0.75$, $G_f(0)/G_m(0) = 10$, $G_f(\infty)/G_m(0) = 7.5$, and fiber relaxation time τ_f varies between 0.1 and 10. *(b)* Enlarged shaded (orange) part of the graph in part a, showing FREE forces for $t \in [0, 0.4]$. For all cases shown here, radius increments of 2.5×10^{-3} were used. For $\tau = \{0.3, 1, 3, 10\}$, time increments of size 6.25×10^{-3} were used. For $\tau = 0.1$, time increments of size 3.125×10^{-3} were used.

$\tau_f = 0.1$ decreases in axial force, hitting a minimum of $f = 0.528$ at $t = 0.1406$. The other FREEs all increase in axial force as time increases. The FREEs with $\tau_f > 1$ increase initially. They reach local maxima in between $t = 2$ and $t = 5$, and then decrease toward the force asymptote at 0.665 ± 0.002. Although we show results for $t \in [0, 8]$, we expect that all curves will eventually reach a common asymptote as $t \to \infty$.

The shape of the axial force curves over time somewhat resembles the shape of the curves for $G_f(t)/G_m(t)$ shown in Figure 4.4, which shows the evolution of the relative stiffness of the fiber to the matrix under the same conditions for $G_m(0), G_f(0)$, and $G_f(\infty)$. As shown in Figure 4.4, cases when $\tau_f/\tau_m > 1$ have curves G_f/G_m that initially increase, reach a local maximum, and decrease toward the asymptote (here, $G_f(\infty)/G_m(\infty) = 10$). The initial increase and local maximum mirror the axial force output of the FREE when $\tau_f/\tau_m = 3$ and $\tau_f/\tau_m = 10$ in Figure 4.7. Cases when $\tau_f/\tau_m < 1$ initially decrease in relative stiffness $G_f(t)/G_m(t)$, reaching local minima, and then increase toward the same asymptote. This behaviour is mirrored by the case when $\tau_f/\tau_m = 0.1$ in Figure 4.7. The case when $\tau_f/\tau_m = 0.3$ does not have a local force minimum, but Figure 4.7*b* shows that its initial force curve is concave-up. The qualitative similarity of behaviour in axial force and $G_f(t)/G_m(t)$ shows how the changing relative fiber and matrix stiffnesses affect FREE outputs.

4.7.3 Hysteresis under Cyclic Pressure Inputs

Visco-elastic analysis shows how FREEs dissipate energy during pressure cycles. Figure 4.8 shows energy dissipation of one FREE. Figure 4.8*a* shows the force response of the FREE to the cyclic pressure shown part *b* of the same figure. Figure 4.8*c* shows how the pressure input varies with the FREE's resultant internal radius r_i. The area enclosed in each subsequent loop indicates energy dissipation through the pressure cycling process.

Further, the energy dissipation of the FREE changes over time. Initially, the FREE is at $P = 0$ and $r_i = 1$, but it does not return to these initial conditions even when the pressure is subsequently reduced to zero. The FREE appears to eventually

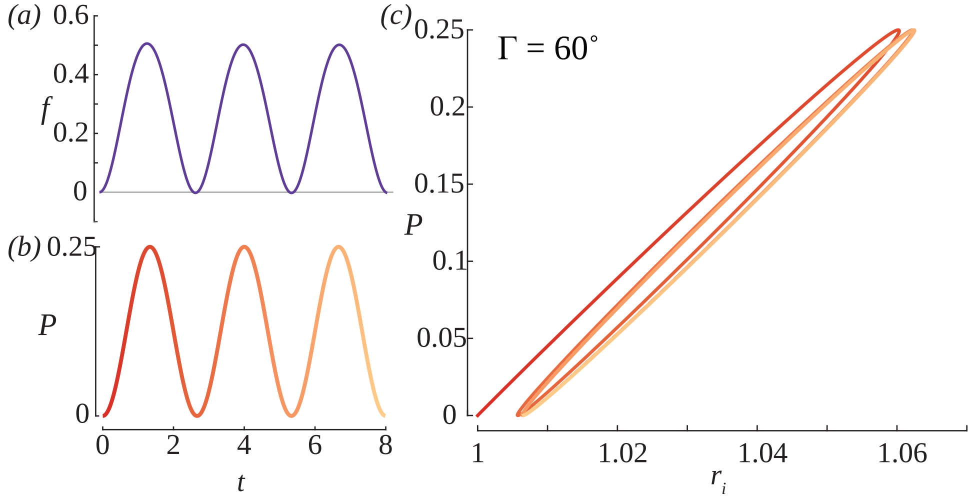

Figure 4.8: *(a)* Axial force of FREE with $\Gamma = 60°$, $\tau_f/\tau_m = 1$, $G_m(\infty) = 0.75$, $G_f(0) = 10$, and $G_f(\infty) = 8$, an imposed axial stretch of $\lambda_z = 1$ and *(b)* an input pressure consisting of three periods of a sinusoid of frequency 0.75. *(c)* Input pressure P by calculated internal radius r_i for the FREE. Radius increments of size 2.5×10^{-3} and time increments of size 1.25×10^{-2} were used.

reach a limit cycle with larger minimum and maximum r_i. Despite these changes in radius and energy storage, the output force of this FREE f changes relatively little. The low change in force here contrasts with the behaviours shown in the previous studies, where the f changes significantly.

The design parameter Γ affects both axial force output and energy storage in FREEs. Figure 4.9 shows the force and radius response of various FREEs to the a "pulse" pressure input consisting of one period of a sinusoid followed by zero pressure. Figure 4.9a shows the axial force on FREEs with $\Gamma \in \{20, 40, 60, 80\}°$, part *(b)* shows the pressure input used, and part *(c)* shows the pressure input P versus interior radius r_i. The FREE with $\Gamma = 20°$ has the highest output force as well as the largest hysteresis loop. In addition to having the highest tensile force, the FREE with $\Gamma = 20°$ has a force reversal into the compressive regime at the end of the pulse, as shown in Figure 4.9a. Its hysteresis loop has a higher peak radius, and a shape that deviates most, compared to the other examples shown here, from

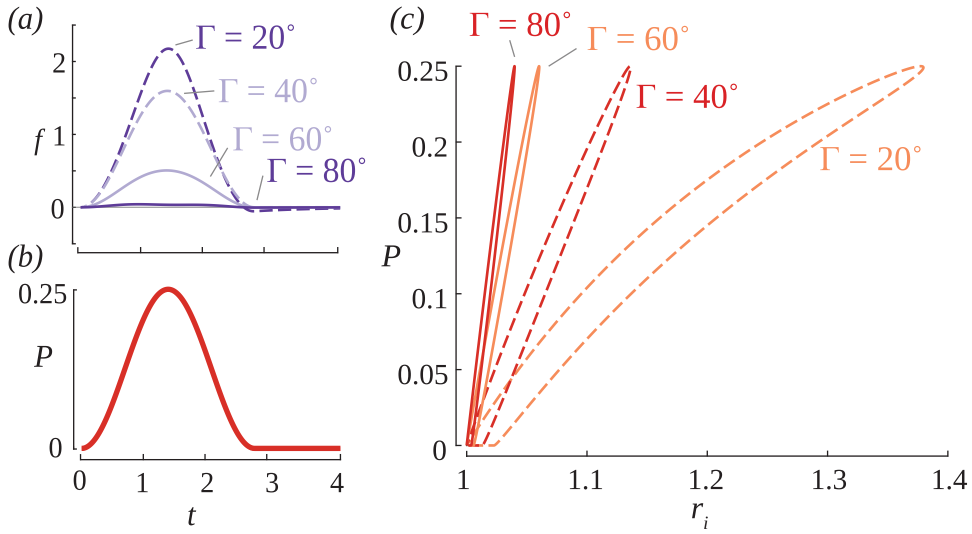

Figure 4.9: *(a)* Axial force of FREEs with $\Gamma \in \{20, 40, 60, 80\}^\circ$, $\tau_f/\tau_m = 1$, $G_m(\infty) = 0.75$, $G_f(0) = 10$, and $G_f(\infty) = 8$, an imposed axial stretch of $\lambda_z = 1$ and *(b)* an input pressure "pulse" consisting of one period of a sinusoid of frequency 0.75 followed by zero pressure input. *(c)* Input pressure P by calculated internal radius r_i for each of the FREEs of varying Γ. Radius increments of size 2.5^{-3} and time increments of size 1.25×10^{-2} were used.

an ellipse. This loop indicates nonlinearity in the FREE and higher levels of energy dissipation. Finally, the hysteresis loop for the FREE with $\Gamma = 20°$ has a horizontal segment at $P = 0$. This flat segment indicates that the radius r_i decreases with time even after the pressure has returned to zero.

For the FREEs shown here, the hysteresis loop size decreases as Γ increases. Following the FREE with $\Gamma = 20°$, each subsequent loop between $\Gamma = 40°$ and $\Gamma = 80°$ shown has less variation in radius and less internal area. fiber orientations that are more closely aligned with the tube's center line (i.e. $\Gamma = 20°$ and $\Gamma = 40°$) tend to have higher tensile axial forces and larger hysteresis loops.

4.8 Conclusion

The approach presented here addresses the mechanical response of a pressurized tubular actuator, composed of nonlinear time-dependent materials, when it is likely to deform into the component materials' nonlinear response regimes. We have shown that the material and layout properties can introduce unusual phenomena in the response of the structure. In particular, relative stress relaxation between the fiber and matrix, as well as fiber layout properties, are found to be key parameters that produce force reversal and hysteresis in the actuator. The tools developed here can be leveraged to design soft actuators that accommodate time-dependent changes in required tasks or in the environment.

Soft robot design and control would benefit from understanding nonlinearity and viscoelastic effects in fiber-reinforced, inflatable devices. The Pipkin-Rogers constitutive theory used here accounts for the essential features of the nonlinear viscoelasticity of both the fiber and the matrix, and is convenient for analysis. The model used here is suitable for materials with strongly nonlinear and time-dependent stress-strain relationships undergoing large deformations.

This study establishes the effect of fiber orientation and relative fiber and matrix relaxation times on the soft, pressurized composite tubes making up PAMs. We perform a detailed study of parameters Γ, τ_f/τ_m, and input axial stretch λ_z and pressure $P(t)$ in selected subspaces to illustrate their influence on each PAM's relaxation behaviour in terms of change in radius and axial force on the closed ends of the PAM. We found that when both the fibers and matrix relax under stress, axial force on PAMs can increase or decrease over time (Fig. 4.5). These changes in force can include a transition from axial compression on the PAM to axial tension. The exact stretch λ_z at which this transition occurs depends on fiber orientation Γ, even if the internal pressure P and fiber and matrix relaxation properties are kept equal (Fig. 4.6). Further, we found that changes in the relative relaxation time of the fiber and matrix τ_f/τ_m influences the time-dependent behaviour of otherwise-similar PAMs under step pressure $P(t)$. As shown in Figure 4.7, a short time τ_f/τ_m can result in an initial decrease in axial force, while a large time constant ratio can result in an increase to a local maximum. Finally, we showed how time and fiber orientation influence hysteresis in PAMs whose fibers and matrix are viscoleastic (Figs. 4.8 and 4.9).

The fiber orientations and normalized stiffness values studied here are in the same range as experimental results from previous studies of PAMs [143, 145], where the fiber was found to be 5-10 times stiffer than the matrix. The stretch ratios encountered in the study here are consistent with stretch ratios in PAMs, not exceeding 40% (i.e., $\lambda_\theta \leq 1.4$ for the PAM with $\Gamma = 20°$ in Fig. 4.9). Stretch ratios in other soft actuators that lack fiber reinforcement like PneuNets [67] are higher, on the order of hundreds of percent.

Future work in this area would involve expanding this analysis beyond the assumption of perfect pressure- and length control. While this context is useful for a number of applications of PAMs, such as the parallel configurations of the OctARM device [99] and the soft manipulator of Bruder at al. [16], other contexts can be imagined in which the length of a PAM is not constrained or where the weight on the PAM plays a more important role. Or, pressure-based control may not be available and volume-based fluidic control may be preferred. For example, the quasi-linear viscoelasticity theory developed by De Pascalis et al. [30] describes the time-dependent inflation of a viscoelastic bladder. It may be that a different constitutive theory is found to better describe the behaviour of a particular choice of materials used in a specified soft robotic actuator. The results presented here show the features of the response that could be expected to occur when both the fiber and the matrix are allowed to relax.

Here, each simulation was run with radius and time increments specified in Section 4.6. In general, cases with lower τ_f/τ_m required more time steps to reach the precision criteria discussed. We believe this is because systems with low τ_f/τ_m exhibit rapidly changing stiffness due to anisotropy. Such a change is shown in Figure 4.4, where the ratio G_f/G_m for $\tau_f/\tau_m = 0.15$ has the largest-magnitude slope compared to cases with larger τ_f/τ_m, occurring between $t = 0$ and $t = 0.5$. If material properties evolve relatively quickly, it is likely that smaller time steps are needed to capture this evolution accurately. Sensitivity of novel and existing numeric techniques to these parameters should be studied.

Our focus on fiber layout, relative fiber and matrix relaxation, axial force, and hysteresis addresses key issues encountered in the use of soft actuation. The approach presented here bridges the gap between continuum mechanical theory and the study of soft robotics in cases where time-dependent polymeric architectures are used.

4.9 Summary

Fiber-reinforced, fluid-filled structures are commonly found in nature and emulated in devices. Researchers in soft robotics have used such structures to build lightweight, impact-resistant and safe robots. The polymers and biological materials in many soft actuators have these advantageous characteristics because of viscoelastic energy dissipation. Yet, the gross effect of underlying viscoelastic properties have not been studied. Nonlinear viscoelasticity is explored in soft, pressurized fiber-reinforced tubes, which are a popular type of soft actuation and a common biological architecture. Relative properties of the reinforcement and matrix materials lead to a rich parameter space connecting actuator inputs, loading response, and energy dissipation. We solve a mechanical problem in which both the fiber and the matrix are nonlinearly viscoelastic, and the tube deforms into component materials' nonlinear response regimes. It is shown that stress relaxation of an actuator can cause the relationship between the working fluid input and the output force to reverse over time compared to the equivalent, non-dissipative case. It is further shown that differences in design parameter and viscoelastic material properties can affect energy dissipation throughout the use cycle. This approach bridges the gap between viscoelastic behavior of fiber-reinforced materials and time-dependent soft robot actuation.

CHAPTER 5

Auxetic Beam Reinforcement for Soft Robots

This chapter has been previously published and is used with permission from the Institute of Electrical and Electronics Engineers (IEEE). It may be referenced as:

> Sedal, Audrey, Fisher, Michael, Bishop-Moser, Joshua, Wineman, Alan, and Kota, Sridhar. Auxetic Sleeves for Soft Actuators with Kinematically Varied Surfaces. *2018 IEEE/RSJ International Conference on Intelligent Robots and Systems (IROS)*, 464-471.

5.1 Introduction

Soft fluidic robots have the inherent ability to interact safely across several loci within their environments [78, 135]. These interactions have been applied in exosuits [42], in-home assistance [7], surgery [24], pipe inspection [45, 147], and motion through continuum media such as water or dirt [71, 94, 108, 165]. Desired motions and shapes are often generated by a reinforcing layer of fibers adhered to the actuator [8, 45], shape memory alloys [147], or braided sleeves [22, 164] placed on the actuator's outside surface. While these methods have created an array of useful kinematics, there are numerous tasks and applications that would be enabled or greatly improved through a novel reinforcement system with enhanced functionality. Examples include robots in continuum environments, where control over both diameter and length of the entirety of the actuator are critical for functionality, or anchoring and grasping applications, where actuator shape may change over its length or circumference as the robot interacts with the environment.

A reinforcement method for soft fluidic actuators comprised of repeating negative Poisson's ratio (NPR) structures enables the generation of a rich set of kinematics. This includes novel length-radius relationships and easy implementation of complex motions. Selectively varying the parameters of the NPR structure throughout the actuator opens the possibility for the creation of a near infinite set of motions and shapes.

While the value of auxetic elements has been demonstrated at the material microstructure level [81, 152], applications in soft macro-scale structures have been more limited. Soft actuators made from foams with auxetic voids have been realized [85], but tolerance and repeatability are limited by fabrication methods that are still highly experimental [28]. Outside of soft actuators, larger-scale shearing auxetic structures have been demonstrated using networks of helical beams [88]. Lumped-compliant mechanisms such as re-entrant honeycombs [17, 81] or petal structures [173] have also been employed to generate auxetic behavior. However, these design approaches may suffer from sliding friction, leading to power loss and imprecision [164], inability to change kinematic behavior circumferentially across the actuator surface, or stress concentrations, leading to limited operating ranges and pre-mature failure.

This chapter presents a novel framework for reinforcement of a soft actuator using a generalized NPR element, henceforth called a Representative Auxetic Element (RAE). Key contributions include:

1. A novel design analysis method that enables the generalization of the RAE, and ways to pattern it circumferentially or axially to achieve a variety of motions.
2. Experimental validation of the newly enabled kinematic behavior.
3. A comparison of the actuator behavior to traditional re-entrant honeycomb and McKibben actuator structures.

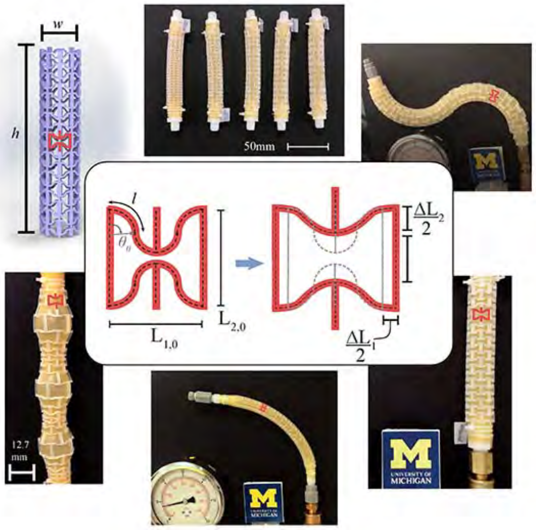

Figure 5.1: The Representative Auxetic Element (RAE) demonstrated on (clockwise from top left): a model sleeve, extending actuators, s-curve actuator, extending actuator, simple bending actuator, and varying diameter actuator. The Michigan logo is 50mm wide.

Section 5.2 introduces the RAE, defining its key design parameters and contrasting it with existing actuator reinforcements. Sections 5.3 and 5.4 describe the Poisson's function method for creating soft actuator sleeves with patterned RAEs. Sections 5.5 and 5.6 contain an experimental validation of the auxetic sleeve performance, including an evaluation of the Poisson's function models and an empirical comparison with McKibben actuator braids. Section 5.7 discusses the experimental results. Section 5.8 explores avenues for future work.

5.2 The Representative Auxetic Element

We define a Representative Auxetic Element (RAE) whose geometry is shown in Figures 5.1, 5.2, 5.3 and 5.5. The RAE is a planar distributed compliant mechanism containing four leaf springs, each comprised of two symmetric circular arcs. Each leaf spring meets the supporting beam at a right angle in order to provide the minimum

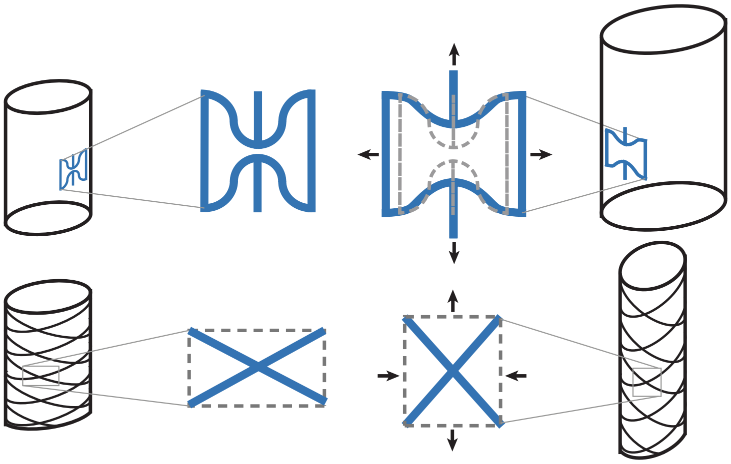

Figure 5.2: Motion of representative kinematic elements for the proposed reinforcement design and the commonly used McKibben actuator. As shown, the proposed design will expand or contract in all directions (NPR behavior) while the McKibben actuator will contract in directions orthogonal to its expansion (positive PR behavior).

stress concentration. The shape of the RAE is defined by two design parameters l (the leaf spring length) and θ_0 (the initial arc angle), both defined in Figure 5.1. The parameter θ defines the motion of the RAE: large θ results in an RAE compressed in $\underline{e}_1$ and $\underline{e}_2$, while small θ results in an expanded RAE, shown in Figure 5.3. Each of these parameters is defined according to the skeletal backbone of the RAE, which is denoted by a dashed line in Figures 5.1 and 5.5b.

5.2.1 Representative Auxetic Element Design Assumptions

The RAE design and analysis follow four key assumptions:

1. The beams of the RAE do not change length. By design, the beam thickness is small relative to the curved beam lengths so that the centerlines do not deform [4].

2. The circular arcs of length l remain circular throughout the RAE's motion, justified by experimental observations.

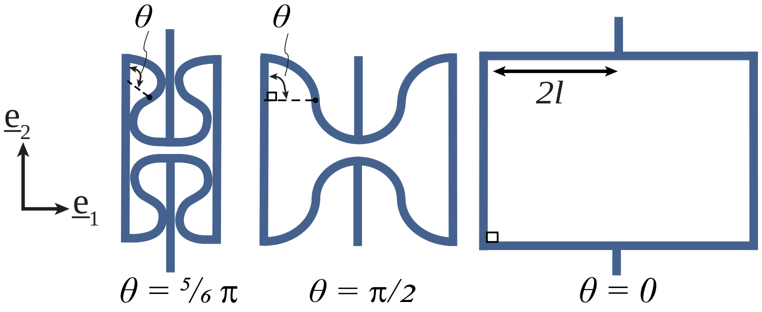

Figure 5.3: Family of deformations with respect to θ for a fixed arc length geometry.

3. The beam of length $L_{2,0}$ forms a right angle with the circular arc. This is a design constraint imposed to reduce stress concentrations.

4. There are no restrictions on the magnitude of the Poisson's ratio of the RAE. One can distinguish the *local* Poisson's ratio of the beam material ν_{mat}, which may be thermodynamically constrained [5], and the *structural* Poisson's ratio of the RAE ν_{RAE}.

RAEs may be patterned onto an elastomeric chamber to produce novel shape changes when the chamber is pressurized. Some possible combinations are shown in Figure 5.1. Below, we outline functional advantages of an RAE-patterned actuator when compared to other soft actuation schemes.

As shown in Figure 5.4, the distributed-compliant designs overall store have less volume of yielded material. In the case of sample 5 in particular, the amount of yielded material is so small relative to the RAE design that it is only truly visible in the isometric view.

5.2.2 Comparison with existing soft actuators

Figure 5.4 shows a Finite Element Analysis (FEA) comparison of three RAE designs across the design space with equivalent re-entrant honeycombs, a common auxetic structure [81]. This FEA was performed using the yield and tensile specifications of Formlabs's Durable V2 material. The highest width change seen in the

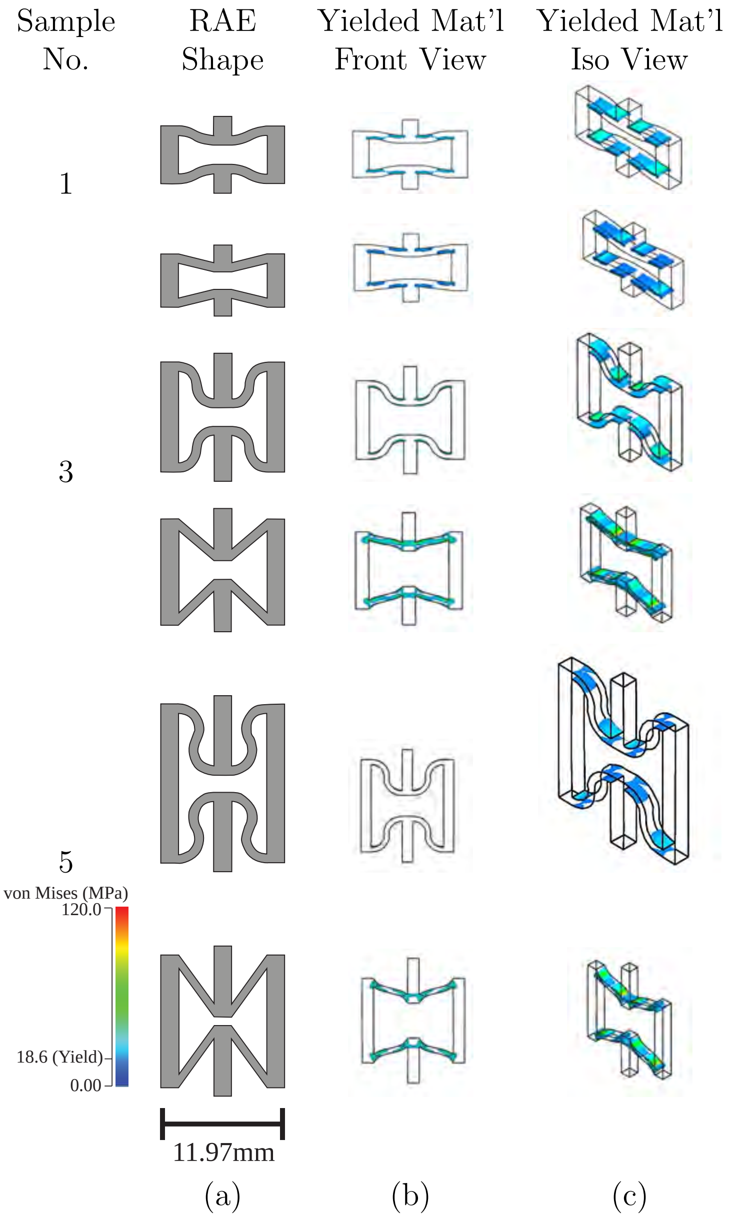

Figure 5.4: Finite element analysis of Samples 1, 3, and 5 at their highest measured deformation, presented alongside analysis of comparable traditional re-entrant honeycombs. Column (a) shows the design shape of each element. Columns (b) and (c) show two views of the FEA results, highlighting the parts of the RAE that have exceeded the material yield stress.

experiment (Section 5.6 below) was imposed here to each of the elements; this corresponds to +5% for Sample 1, +20% for Sample 3 and +35% for Sample 5, as depicted in Figure 5.4. Columns (b) and (c) show the results of this FEA, highlighting those portions of the element that exceeded the material's yield stress. In all but Sample 1, where the curved and traditional designs resemble each other closely, the curved beam design has a visible reduction in the amount of yielded material, implying higher repeatability and precision of motion for the RAE compared to the re-entrant honeycomb design.

McKibben Actuators McKibben actuators are soft, pneumatic devices that leverage the angle between overlapping, symmetrically wound fiber helices to produce axial expansion or compression of a cylindrical chamber. Since the fibers are stiffer than the chamber, they constrain the tube to become either shorter and wider or longer and thinner [7, 22] when pressurized, as shown in Figure 5.2. The fiber pattern on the tube causes it to elongate and decrease in width under pressurization (Fig. 5.2). In contrast, the RAE is designed to become either larger or smaller in *all* directions. Further, the RAE design can vary circumferentially on one actuator while the fiber helices must remain symmetric about the central axis. The relative motion between fibers in the McKibben braids at their crossing creates friction, causing energy dissipation and imprecise motion [164]. Unlike the McKibben braid element shown in Figure 5.2, the RAE can be made as a monolithic structure without overlapping parts, eliminating this possibility for friction.

Having outlined the potential advantages of an RAE-patterned actuator, we introduce a detailed design methodology for a soft RAE actuator in the following sections.

5.3 Poisson's Functions of Representative Elements

In this section we derive expressions for the Poisson's ratios of representative elements including the RAE and a representative element of a McKibben actuator braid. It is shown that the Poisson's functions of each of these elements are different.

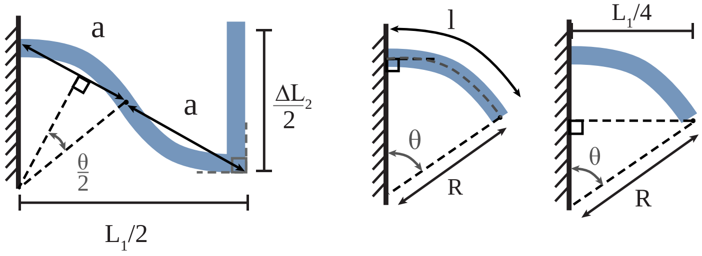

(a) (b) (c)

Figure 5.5: Parameterization of the RAE using a pair of circular arcs. The key parameters are the arc length l, and arc angle θ.

5.3.1 Defining the Poisson's Ratio of the RAE

The Poisson's ratio of the RAE is derived using the design and motion parameters l and θ under the assumptions described in the previous section. Below, it is shown that Poisson's ratio is a function of the motion parameter θ.

5.3.1.1 Relating the RAE Dimensions

The 2D RAE shown in Figure 5.1 has two size dimensions: L_1, the deformed width of the RAE, and L_2, its deformed height. In order to define the Poisson's ratio, we need to find the relationship between the change in L_1 (ΔL_1) and the change in L_2 (ΔL_2) in terms of our design and motion parameters l and θ. L_1 and L_2 can be related using the Pythagorean theorem on the triangle with hypotenuse $2a$ shown in Figure 5.5a:

$$\begin{aligned}\left(\frac{L_1}{2}\right)^2 + \left(\frac{\Delta L_2}{2}\right)^2 &= 4a^2 \\ &= 16R^2 sin^2\left(\frac{\theta}{2}\right)\end{aligned} \tag{5.1}$$

However, the width is further constrained. The law of sines on the triangle shown in Figure 5.5c is used to find the width:

$$\frac{L_1}{4} = R\sin(\theta) \tag{5.2}$$

Furthermore, since the leaf spring is made of circular arcs, we know that:

$$R = \frac{l}{\theta} \tag{5.3}$$

Finally, using Equation 5.3 to relate R to the design parameter l and the motion parameter θ, one can find expressions for the height L_2 and width L_1:

$$L_1(\theta, l) = 4\frac{l}{\theta}\sin\theta \tag{5.4a}$$

$$L_2(\theta, l) = L_{2,0} - 2\frac{l}{\theta}\sqrt{4\sin^2\left(\frac{\theta}{2}\right) - \sin^2\theta} \tag{5.4b}$$

Now, L_1 and L_2 are fully parameterized in terms of l and θ.

5.3.1.2 Poisson's Functions of the RAE

Then, the RAE has two Poisson's ratios, called ν_1 and ν_2, in the directions $\underline{e}_1$ and $\underline{e}_2$, respectively (Fig. 5.3). Each of these is defined in terms of the engineering strains ϵ_1 and ϵ_2 or stretches λ_1 and λ_2 undergone by the RAE [5, 87, 123]:

$$\nu_1 = -\frac{\epsilon_1}{\epsilon_2} = -\frac{\lambda_1 - 1}{\lambda_2 - 1} \tag{5.5a}$$

$$\nu_2 = -\frac{\epsilon_2}{\epsilon_1} = -\frac{\lambda_2 - 1}{\lambda_1 - 1} \tag{5.5b}$$

where $\lambda_1 = \frac{L_1+\Delta L_1}{L_1}$ and $\lambda_2 = \frac{L_2+\Delta L_2}{L_2}$.

However, ΔL_1 and ΔL_2 are nonlinear in θ as shown in Equations 5.4a and 5.4b. Therefore, the Poisson's ratio of the RAE is only valid for small perturbations $\delta\theta$ about a chosen θ.

One can find the instantaneous Poisson's ratios in each direction using Equations

5.5a and 5.5b:

$$\nu_1(\theta) = -\lim_{\delta\theta \to 0} \frac{\frac{L_1(\theta+\delta\theta,l)}{L_1(\theta,l)} - 1}{\frac{L_2(\theta+\delta\theta,l)}{L_2(\theta,l)} - 1} \tag{5.6a}$$

$$\nu_2(\theta) = -\lim_{\delta\theta \to 0} \frac{\frac{\Delta L_2(\theta+\delta\theta,l)}{\Delta L_2(\theta,l)} - 1}{\frac{\Delta L_1(\theta+\delta\theta,l)}{\Delta L_1(\theta,l)} - 1} \tag{5.6b}$$

Evaluating these limits gives:

$$\nu_1(\theta) = \frac{\theta \cot\theta - 1}{\theta \cot\left(\frac{\theta}{2}\right) - 1} \tag{5.7a}$$

$$\nu_2(\theta) = \frac{\theta + \theta\cos\theta - \sin\theta}{\theta\cos\theta - \sin\theta} \tag{5.7b}$$

Equations 5.7a and 5.7b show that the Poisson's ratios of the RAE are functions of the motion parameter θ. A detailed comparison of the predictions of these equations with experimental results is found in Section 5.6

5.3.2 Poisson's Functions of a McKibben Actuator

The motion parameter of a McKibben actuator is the fiber angle α. The design parameters are the initial fiber angle α_0 and fiber spacing q. Figure 5.6 shows the deformation of a McKibben actuator fiber at various α.

Using methods comparable to those used for the RAE, one can find the dimensions of the McKibben representative element:

$$L_1(\alpha, q) = 2q\sin\alpha \tag{5.8a}$$

$$L_2(\alpha, q) = 2q\cos\alpha \tag{5.8b}$$

Using the Poisson's function definitions from Equations 5.5a and 5.5b, one can find the Poisson's functions of a McKibben actuator in terms of its motion parameter.

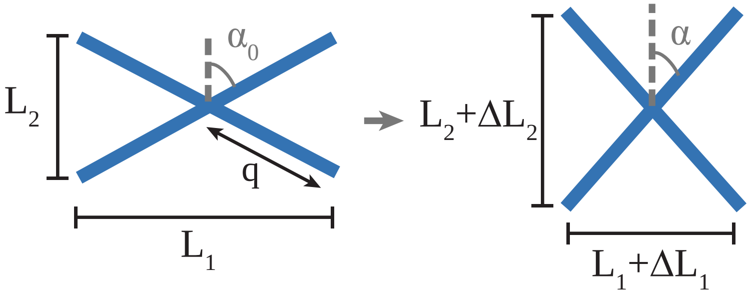

Figure 5.6: Deformation profile of a McKibben actuator's repeating element, parameterized by α, the fiber angle, and q, the braid spacing.

$$\nu_1(\alpha) = -\lim_{\delta\alpha \to 0} \frac{\frac{L_1(\alpha+\delta\alpha, q)}{L_1(\alpha, q)} - 1}{\frac{L_2(\alpha+\delta\alpha, q)}{L_2(\alpha, q)} - 1} = \cot^2 \alpha \tag{5.9a}$$

$$\nu_2(\alpha) = -\lim_{\delta\alpha \to 0} \frac{\frac{L_2(\alpha+\delta\alpha, q)}{L_2(\alpha, q)} - 1}{\frac{L_1(\alpha+\delta\alpha, q)}{L_1(\alpha, q)} - 1} = \tan^2 \alpha \tag{5.9b}$$

The Poisson's functions of individual units for both the curved RAE and the traditional McKibben braid are now established. The following section will detail how these elements produce gross behavior when patterned onto soft cylindrical shells.

5.4 Design Synthesis of the Soft Sleeve

The RAE can be designed and patterned onto any fluidic enclosure to provide the chosen kinematic behavior when pressurized. In this section, we map the RAE parameters onto the global motion of a fluidic actuator patterned with RAEs.

5.4.1 Global Deformation

Here, we restrict the kinematics to cylindrical sleeves due to their ability to be combined in parallel [8] and their popularity as soft graspers [128] and crawlers [45].

Other geometries are left to future work.

5.4.1.1 Global Width and Length

Designers wishing to create a soft actuator to specific kinematic specifications may benefit from finding the explicit width-to-height relationship of a given actuator design parameterized by θ and l of the RAE. Assuming the sleeve has n RAE's along its diameter and m RAE's longitudinally, one can use the expressions for L_1 and L_2 in Equations 5.4a and 5.4b respectively to design an RAE with the desired axial to radial expansion relationship. The length h and the diameter w of the sleeve are defined as follows:

$$\begin{aligned} w(\theta, l) &= \frac{nL_1(\theta)}{\pi} \\ &= \frac{n}{\pi}\frac{4l}{\theta}\sin\theta \end{aligned} \tag{5.10a}$$

$$\begin{aligned} h(\theta, l) &= mL_2(\theta) \\ &= m(L_{2,0} + \Delta L_2) \\ &= m\left(L_{2,0} - 2\frac{l}{\theta}\sqrt{4\sin^2\left(\frac{\theta}{2}\right) - \sin^2\theta}\right) \end{aligned} \tag{5.10b}$$

5.4.1.2 Global Poisson's Ratio

We have previously found the Poisson's function of the RAE (Eqns. 5.7a, 5.7b). Here, we will show that, for a structure patterned throughout with the same RAE, the Poisson's functions of the RAE and the Poisson's functions $N_1(\theta)$ and $N_2(\theta)$ of the structure are equivalent.

Once again using the definition in Equations 5.5a and 5.5b, one can find the Poisson's ratio of the entire structure by computing the limits of the global stretch ratios for small $\Delta\theta$:

$$N_1(\theta) = -\lim_{\delta\theta \to 0} \frac{\frac{w(\theta+\delta\theta)}{w(\theta)} - 1}{\frac{h(\theta+\delta\theta)}{h(\theta)} - 1} \tag{5.11a}$$

$$N_2(\theta) = -\lim_{\delta\theta \to 0} \frac{\frac{h(\theta+\delta\theta)}{h(\theta)} - 1}{\frac{w(\theta+\delta\theta)}{w(\theta)} - 1} \tag{5.11b}$$

One can parameterize Equations 5.11a and 5.11b in terms of θ using Equations 5.10a and 5.10b. Since the multipliers m and $n/2\pi$ cancel, taking the limit and evaluating then gives:

$$N_1(\theta) = \nu_1(\theta) \tag{5.12a}$$

$$N_2(\theta) = \nu_2(\theta) \tag{5.12b}$$

Thus, $N_1(\theta)$ and $N_2(\theta)$ are equivalent to the local Poisson's functions $\nu_1(\theta)$ and $\nu_2(\theta)$ for a tube patterned with a single RAE. The same analysis can be done for the McKibben actuator or any other cylindrical actuator with a repeating element.

Figure 5.7 shows how Equations 5.10a and 5.10b may be used to map the dimensional design space by l. Each curve shown gives the width-to-height relationship of a design with $L_{2,0} = 17.96$mm, $m = 11$ and n =5 where l varies from 2mm to 16mm. The shaded area shows the infeasible space, which is bounded by the asymptotes in $\nu_1(\theta)$ at $\theta = \frac{3\pi}{4}$ as shown in Equation 5.7a and in $\nu_2(\theta)$ at $\theta = 0$ as shown in Equation 5.7b. The instability of ν_1 at $\theta = 3\pi/4$ is the frontier at which the circular arcs begin to overlap with the beam, and the sign of the Poisson's ratio flips. This is reflected by the fact that h is at its global minimum.

A comparison of the sample's performance with the predictions in Equations 5.10a and 5.10b is found in Section 5.6.

5.4.2 Varying Poisson's Ratio Along a Sleeve

One can achieve useful kinematics for the auxetic sleeve by printing it with different RAE designs instead of repeating the same one. Be varying the local Poisson's

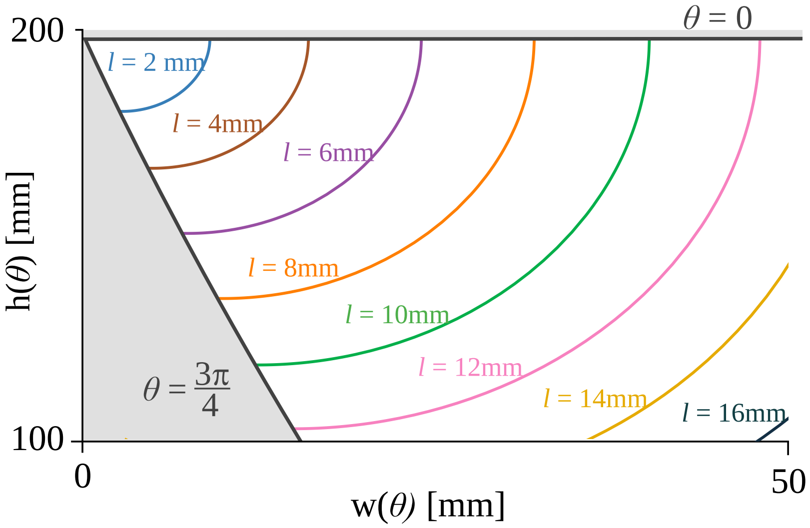

Figure 5.7: Curves representing the relationship between height h and width w of an RAE actuator with $m = 12$ and $n = 5$ parameterized by kinematic parameter θ at fixed beam length l values.

ratio across a chosen region of the sleeve, one can create useful behaviours. Two such examples are considered below.

5.4.2.1 Bending

Printing RAE's on one side of the sleeve, with an inextensible soft beam on the other allows bending with tunable curvature (Fig. 5.1, top right and bottom).

5.4.2.2 Diameter

By varying the RAE design parameters along the z axis of the sleeve, one can tune the radius of the soft actuator (Fig. 5.1, bottom left). This may be especially useful for peristalsis, pipe inspection, or other locomotion.

5.5 Experimental Evaluation

We evaluated the capabilities of the RAE to provide programmable auxetic behaviour by 3D printing and actuating a series of five sleeves with various RAE design parameters.These are then compared to McKibben actuators.

5.5.1 Fabrication

The samples consist of a latex tube (Kent Elastomer, ID 12.7mm, wall thickness 3.2mm) and a 3D printed sleeve with repeating auxetic elements along its circumference and length. The actuator is fabricated by sliding the auxetic sleeve over the elastomeric tube and closing the end caps. This is done with 1/2in NPT barbed pneumatic connectors and zip-ties (Figs. 5.8 and 5.9). Supports were added to the print files to bridge the ends of the RAE in order to make the geometry printable without overhangs. The sleeves were printed on a Form 2 printer using Durable V2, washed with isopropyl alcohol for 10 minutes without post-curing. Supports were removed with flush cutters. The 3D printed sleeves were placed over lengths of latex tubing. 3/4in barb to 1/4in NPT fittings were attached to both ends of the latex tubing using zip ties.

5.5.2 Experiment Description & Uncertainties

Five RAE actuator samples were fabricated with varying l and θ_0. Design parameters are shown in Table 5.1. For comparison, we used the same method to fabricate three McKibben actuator samples with varied motion parameter α_0 with commercial McKibben sleeves from McMaster-Carr (Part #s 9284K3, 9284K6). The commercial braid's fiber spacing q was roughly 1.25mm. Design parameters of the McKibben actuator samples are shown in Table 5.2.

We pressurized each of the samples between 0 and 140 kPa and back in increments of roughly 5 kPa ± 0.9 with small perturbations to the pressure above and below each target pressure. If a specimen failed, a new one was fabricated and the sample was pressurized to roughly 5kPa below the failure pressure. At each configuration, we

Sample	$L_{2,0}$ [mm]	l [mm]	θ_0	m	n
1	6.0	6.1	0.48	29	5
2	9.0	6.7	1.11	21	5
3	12.0	7.6	1.56	16	5
4	15.0	8.8	1.9	13	5
5	18.0	10.0	2.1	11	5

Table 5.1: Design parameters of each RAE actuator sample.

Sample	h_0 [mm]	w_0 [mm]	α_0	m	n
1	227	15.35	29.4	55	36
2	200	18.7	39.5	54	36
3	135	46.2	75.1	93	38

Table 5.2: Design parameters of each McKibben actuator sample.

Figure 5.8: Experimental platform to measure actuator deformation including sample, analog pressure gauge, digital pressure transducer, and camera for image measurements. Image scale is 50mm.

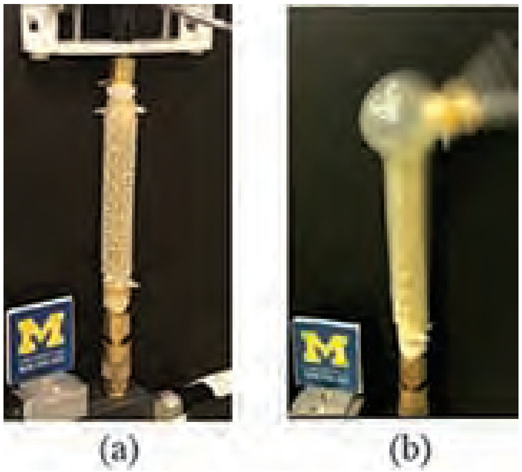
(a) (b)

Figure 5.9: Actuator failure occurs due to aneurysms in the elastomeric tubing at high pressures.

used a scaled image to measure the specimen's height h and diameter w. Both h and w were means of three measurements. The uncertainty of each was calculated based on the standard deviation and image resolution error of ±0.13mm. These are propagated to find the uncertainties on θ and α and the experimental Poisson's functions, which are derived in the following paragraph.

5.5.3 Computing Key Parameters

The motion parameter θ and the Poisson's functions ν_1 and ν_2 were computed from experimental data. Though an attempt was made to measure θ_i at each test condition i directly from the images, finding the point at which the circular arcs meet was imprecise. Instead, the following method was used.

Using $h(\theta)$ and $w(\theta)$ from Equations 5.10a and 5.10b, one can relate the motion parameter θ to the measured width and height of the specimen:

$$\frac{\pi w_i}{n4l} = \frac{\sin\theta}{\theta} \tag{5.13a}$$

$$L_{2,0} - \frac{h_i}{m} = \frac{l}{\theta}\sqrt{4\sin^2\left(\frac{\theta}{2}\right) - \sin^2\theta} \tag{5.13b}$$

Since height h_i and width w_i at each test condition i per specimen are both measured, θ_i can be determined from either of the Equations 5.13a and 5.13b. When predicting $\nu_1(\theta)$, $\nu_2(\theta)$, and $h(\theta)$ θ was estimated with Equation 5.13a. When computing $w(\theta)$, we used Equation 5.13b.

The values of the Poisson's functions $\nu_1(i)$ and $\nu_2(i)$ at any test point i are given by a numerical approximation of Equations 5.11b and 5.11b:

$$\nu_1(i) = -\frac{\frac{w_i+\delta w(i)}{w_i} - 1}{\frac{h_i+\delta h(i)}{h_i} - 1} \tag{5.14a}$$

$$\nu_2(i) = -\frac{\frac{h_i+\delta h(i)}{h_i} - 1}{\frac{w_i+\delta w(i)}{w_i} - 1} \tag{5.14b}$$

The values of $h(i)$ and $w(i)$ can be found in the following way:

$$\begin{aligned} \delta h(i) &= \frac{h(i+1) - h(i-1)}{2} \\ \delta w(i) &= \frac{w(i+1) - w(i-1)}{2} \\ i &= 2 + 3k,\ \ k = 1, 2, ... \end{aligned} \tag{5.15}$$

where $i+1$ and $i-1$ are both small perturbations about the input pressure at i. The following section outlines the results obtained with this procedure.

5.6 Results

Using the procedures outlined above, we measured the values of ν_1 and ν_2 for each sample at each actuation pressure. These measurements are shown alongside the Poisson's function curves in Figure 5.10 for the McKibben actuator samples and the RAE actuator samples. In addition to these dimensionless Poisson's functions, we evaluated the width-height relationship of each RAE actuator. Figure 5.11 shows the height-width data for each specimen alongside prediction curves that are generated using Equations 5.10b and 5.10a. Tables 5.3 and 5.4 show the Root Mean

Sample	$\varepsilon\ \nu_1$	$\varepsilon\ \nu_2$	ε h(w) [mm]	ε w(h) [mm]
1	0.3	7.6	35.9	3.4
2	0.5	1.2	2.1	0.4
3	0.4	0.2	1.2	0.3
4	1.7	0.3	0.9	0.4
5	6.5	0.3	1.6	1.6

Table 5.3: RMSE for each RAE actuator sample.

Sample	$\varepsilon\ \nu_1$	$\varepsilon\ \nu_2$
1	1.4	0.2
2	0.3	0.4
3	2.2	3.73

Table 5.4: RMSE for each McKibben actuator sample.

Square Error (RMSE) of the predictions and measurements.

5.7 Discussion

RAE actuators achieve large magnitude negative Poisson's ratios while McKibben actuators have positive Poisson's ratios. The trends of Poisson's ratio and dimensions determined from the measured data agree with predictions of $\nu_1(\theta)$ and $\nu_2(\theta)$ with an average error of 1.92 and maximum error of 7.6 for the RAE actuators and and average error of 1.37 and a maximum error of 3.73 for the McKibben actuators. The NPR behavior of the RAE actuators is further elucidated in Figure 5.11, where the positive trend of the height-width relationship of these actuators varies with RAE design. The height-width relationship of the RAE samples agrees with an average error of 4.8 mm and a maximum error of 35.9mm. Error was particularly high for all measurements of RAE actuator Sample 1. Finite element analysis shows that this sample has larger portions of material in the plastic regime (Fig. 5.4) compared to the RAE designs where the curved beams are longer, indicating that model assumptions 1 and 2 may have been broken in this design. A new iteration with the same θ_0 and l but lower thickness t is likely to perform more accurately.

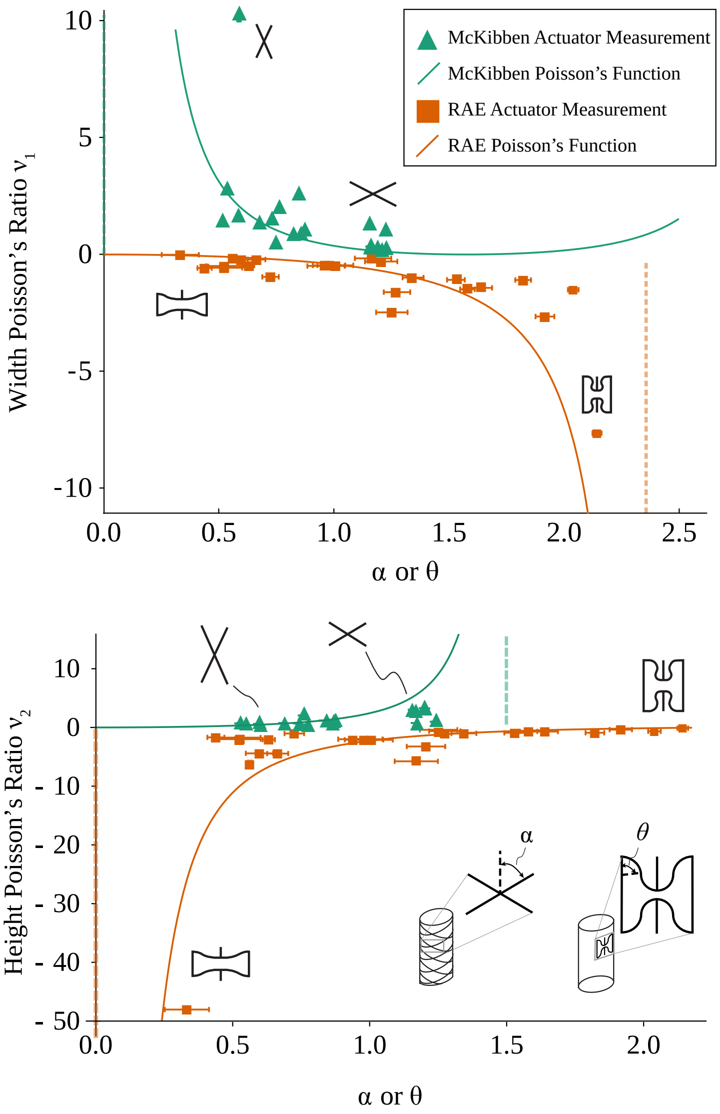

Figure 5.10: Experimental data of measured ν_1 (top) and ν_2 (bottom) for all samples with respect to the motion parameter α or θ as defined in Eqns. 5.14a and 5.14b. Parameter α refers to the McKibben actuator motion and θ refers to the RAE actuator. Lines represent the Poisson's functions $\nu_{1,2}(\alpha)$ (Eqns. 5.9a, 5.9b) or $\nu_{1,2}(\theta)$ (Eqns. 5.7a, 5.7b) for the McKibben and RAE actuators respectively.

Hysteresis We did not observe significant hysteresis of the sleeve designs in this experiment. As shown in Figure 5.11, attempts to trace hysteresis loops would largely fall within the height and width measurement error. This is evidence that the design of the RAE succeeds in keeping the stresses on the material mostly within the elastic regime.

Friction Previous studies on McKibben actuators have identified friction between the overlapping fibers as the major source of error [22, 164]. RAE sleeves are made of a single monolithic element with no overlapping parts and therefore they do not have this drawback. However, these modeling methods have assumed that the interior elastomeric chamber is "rigidly connected", i.e. there is no slip, to the reinforcing elements because of the outward-facing air pressure inside the chamber. Therefore, the friction due to slip between the elastomer and the reinforcements is not considered [22, 164]. Our design and modeling of RAE actuators have also been predicated on this assumption, and therefore the interactions between the elastomeric chamber and the reinforcing sleeves are considered as a minor source of error. This source of error is likely captured in the error bars on the data in Figures 5.10 and 5.11.

Aneurysm We observed failure by aneurysm of some samples at pressures between 76 and 146 kPa gauge. Aneurysm is an inherent failure mode for soft fluidic actuators: even in a material without local weaknesses, there will be a pressure at which the elastomer ruptures. A detailed study of aneurysm specifically would require a new experimental setup including cameras with a high frame rate to avoid blurring (Fig. 5.9b).

5.8 Conclusion

This work investigates the novel Representative Auxetic Element (RAE) as a design building block to create a soft sleeve with specified auxetic behavior. Soft actuators with RAE sleeves achieved negative Poisson's ratios with both small and large magnitudes for various designs (Fig. 5.10). These kinematic possibilities can enable new soft robotic motion when RAE actuators are combined in series and/or parallel. . The kinematics of an RAE are mapped to the global deformation of the actuator by using two design parameters l and θ_0 to create a Poisson's function that relates Poisson's ratio to RAE parameters. This method allows designers to mechanically program a soft actuator with a chosen Poisson's ratio profile. Experimental data taken across the design space for RAE and McKibben actuators agrees with the Poisson's function models with comparable error, showing that RAE patterns form a novel design space for soft actuators with predictable behaviour.

Future work should lead to analytical connections between the local material properties, loading, and deformation of the sleeves. It should also investigate series and parallel actuation of the sleeves to achieve complex robotic motion and evaluate the suitability of RAE actuators to specific tasks. Characterizing the relationship between pressure and the motion of the RAE actuator will allow creation of a design scheme for specified stiffness or compliance as well as Poisson's ratio. Expanding the global sleeve kinematics to non-cylindrical sleeve geometries will enable further new and useful motions.

5.9 Summary

Soft actuators with auxetic, or negative Poisson's ratio (NPR), behavior offer a way to create soft robots with novel kinematic behavior. This chapter presents an original framework for reinforcement of a soft actuator using a generalized NPR element, called a Representative Auxetic Element (RAE), and an experimental validation of the kinematic behavior that it enables. A generalized kinematic model is built that enables the design of RAE-patterned actuators and reveal the distinct auxetic behavior of RAE actuators with comparable model accuracy to the legacy McKibben actuators. A simple, reproducible way of designing and fabricating RAE actuators is described and varied prototypes are shown. This design scheme can create actuators with specified kinematics like bending, extension, and radial expansion that vary across the actuator's surface both circumferentially and axially.

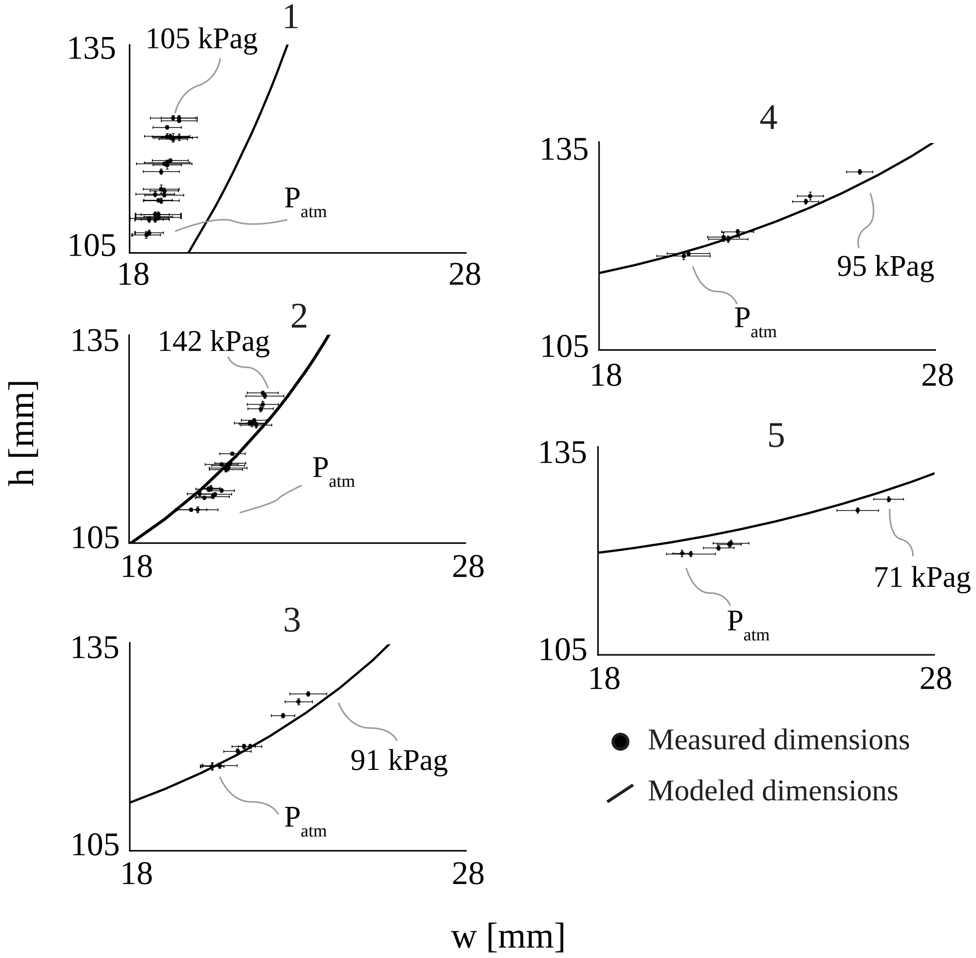

Figure 5.11: Height-width relationship for each RAE actuator sample throughout pressurization. Points represent RAE actuator measurements while lines represent height-width predictions found with Eqns. 5.10b and 5.10a. The integer at the top center of each figure refers to the sample number from Table 5.1.

CHAPTER 6

Design Synthesis of Soft Robots with Auxetic, Conic Surfaces

6.1 Introduction

There is a need to develop soft robots with the capability to perform complex sequential tasks without human or electronic intervention or signals. Soft robots show inherent potential in exploratory and human-interactive tasks due to their mechanical intelligence [135]. By leveraging their high, multi-directional compliance, soft robots can navigate unstructured environments and interact with delicate objects. In pneumatic soft robots, mechanical designers focus on ways to change a system's input-output behaviour. For instance, Fiber-Reinforced Elastomeric Enclosures (FREEs) [8] and PneuNets [67] use arrangements of inextensible fibers with highly extensible elastomers to design specific directions in which these soft systems will move instantaneously. These basic design building blocks can be combined to create robots move in specific ways when actuated but also respond to external stimuli by deforming around them. For example, Wang et al. [171] and Deimel et al. [31] use PneuNets and FREEs to develop grasping robots.

A growing number of soft robot architectures aim to consider *behavioural sequences* rather than instantaneous responses to actuation. Instead of simply considering instantaneous behaviour, soft roboticists consider successive behaviour of a soft system under a sustained or repeated input. Peristaltic and pipe-crawling tasks for soft robots often consider cyclic actuation of a parallel or segmented structure to generate locomotion [45, 91, 109, 146]. The vine robot of [57] can be constrained in specific locations so that it bends around anticipated obstacles (e.g. climbing up and through a hole). These examples and others show some ways in which sequential environmental interaction can create new and meaningful behaviours.

Yet, these sequences are shape-constrained. Peristaltic motion is radially symmetric, as is the eversion motion of the vine robot. The work in the previous chapter discusses auxetic patterning on flat surfaces, curved surfaces, and tubes to develop greater variation in the shapes that that pneumatic soft robots can achieve. Yet, the initial shape of the soft robot or actuator is still constrained by the surface on which auxetic beam patterning is achievable. This chapter investigates a way of patterning auxetic beam networks on conic frusta, expanding the shape morphing capabilities of these soft actuators.

This chapter shows that soft actuators comprised of conic frusta with auxetic surfaces can be used to develop soft robots with sequential motion. A new design framework is proposed. This framework is based on patterning of auxetic beam networks that enables the creation of pinch points, resistive areas, and reservoirs for fluidic actuation. The work evaluates how beam network kinetics affect air flow, and use the developed principles to design a variety of demonstrative non-cyclindrical soft systems with encoded actuation sequences.

Section 6.2 discusses the compliant beam building block used here, and explains how antagonistic arrangements of the building block can result in auxetic motion. It further develops design rules for patterning the design building block onto conic frusta and cylindrical segments of any size, and describes an experiment on devices made from combinations of these surfaces. Section 6.3 gives results of the experiments, and Section 6.4 provides conclusions and avenues for future work.

Soft robots with embedded motion and timing can offer unprecedented dexterity and efficiency. In particular, complex motions can be performed without complicated controllers or numerous, cumbersome power lines. Dexterous motion can be mechanically programmed in to a soft robot so that it performs the same sequential motions in new environments while deflecting around obstacles. This chapter presents an early step toward achieving this functionality for an even greater variety of soft robot morphologies.

6.2 Materials and Methods

A design methodology is presented in which curved beams are patterned in antagonistic configurations to create auxetic motion (i.e. a net increase in surface area) when internal pressure is applied. An antagonistic configuration of Bézier-curved beams with auxetic behaviour is termed a Representative Auxetic Element (RAE). RAEs of varying parameters may be patterned on complex surfaces to produce net shape change. In this section, the proposed design methodology is described in detail, including developing the RAE through Bézier-curved compliant beams and patterning RAEs on flat surfaces, curved surfaces and conic frusta.

6.2.1 Curved, Compliant Beams Form a Design Building Block

The kinematics of one compliant beam form a design building block for various auxetic surfaces. The compliant beam element used in this chapter differs from the circular segment-based beam of Chapter 5. The curvature and size of this beam are characterized by a Bernstein polynomial with five control points $\vec{c}_i = [c_{x,i} c_{y,i}]^T$, $i \in \{0, 1, 2, 3, 4\}$. The equation for $\vec{x}$, the position of any point along the curve, parameterized by $t \in [0, 1]$ is then

$$\vec{x} = (1-t)^4 \vec{c}_0 + 4t(1-t)^3 \vec{c}_1 + 6t^2(1-t)^2 \vec{c}_2 + 4t^3(1-t)\vec{c}_3 + t^4 \vec{c}_4. \tag{6.1}$$

In the initial design constraints are applied so that, as shown in Figure 6.1:

$$\vec{c}_0 = \begin{bmatrix} 0 \\ 0 \end{bmatrix} \tag{6.2}$$

$$\vec{c}_1 = \begin{bmatrix} x_1 \\ 0 \end{bmatrix} \tag{6.3}$$

$$\vec{c}_2 = \begin{bmatrix} w/2 \\ h/2 \end{bmatrix} \tag{6.4}$$

$$\vec{c}_3 = \begin{bmatrix} w/2 \\ h \end{bmatrix} \tag{6.5}$$

$$\vec{c}_4 = \begin{bmatrix} w \\ h \end{bmatrix}. \tag{6.6}$$

Each beam is built from a curve of width w and height h and has length l. This curve further has a non-dimensional relationship h/w, referred herein as the "aspect ratio" of the curve. Under the constraints defined by Eqns. 6.1 thru 6.6, the design of a compliant beam with a rectangular cross-section of side lengths a and b can be fully characterized by its width w, aspect ratio h/w, thickness b and depth a. Manufacturing constraints (i.e. printer bed size and resolution) constrain the available length-scales and thicknesses for patterned beam designs.

Compliant beams can be compressed or stretched by moving control point $\vec{c}_4$. As $\vec{c}_4$ changes, the rest of the curve will deform in such a way as to balance internal forces. In particular, the horizontal displacement of $\vec{c}_4$ by a distance d . Any imposed $d > 0$ will result in a positive vertical displacement of $\vec{c}_4$ and a horiztonal tensile force F_{tens}. An imposed $d < 0$ will result in a negative vertical displacement of $\vec{c}_4$ and a horiztonal compressive force F_{comp}. Figure 6.1 shows kinematics of the basic beam element and RAE building blocks.

When placed in antagonistic configurations, these curved beams form Representative Auxetic Elements (RAEs) that can be patterned to create auxetic kinematics. Figure 6.1D and E show two ways the Bézier-curved compliant beams may be pat-

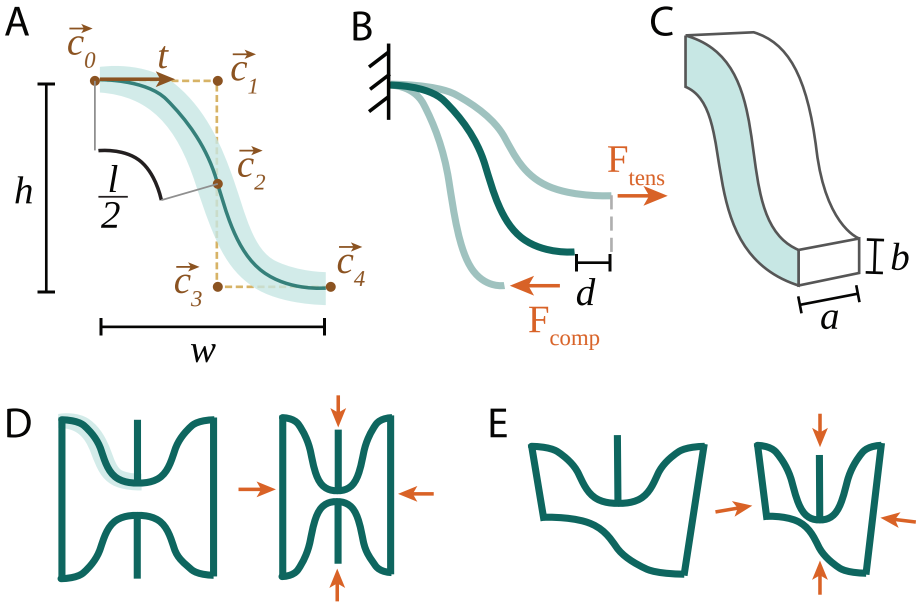

Figure 6.1: (A) Design building block: thin Bézier-curved beam with control points $\vec{c}_i$, $i \in \{0, 1, 2, 3, 4\}$, parameter t and aspect ratio h/w. (B) Same Bézier-curved beam as part a, shown with deformations under a tensile force F_{tens} and a compressive force F_{comp}. (C) Cross section of the beam with width a and height b. (D) Two rows of antagonistically placed curved beams form a Representative Auxetic Element (RAE). When placed in a symmetric pattern, this RAE compresses about its center under compressive load. (E) Another example of a RAE, with asymmetric deformation under a compressive load.

terned to form a RAE; the top schema show a stress-free configuration while the bottom depict the configuration under compressive forces. In both cases, lateral compression of each RAE results in longitudinal compression, and vice-versa. This is one example of the RAEs' auxetic behavior.

Because the beam is characterized by a 4th-degree curve, it is not possible to geometrically solve for a unique closest-fitting transformation for a given end displacement d. Therefore, Finite Element Analysis (FEA) is used to understand the relationship between horizontal displacement of $\vec{c}_4$ and horizontal resultant force F on the beam.

Finite Element Analysis was performed on a variety of curved beams spanning the

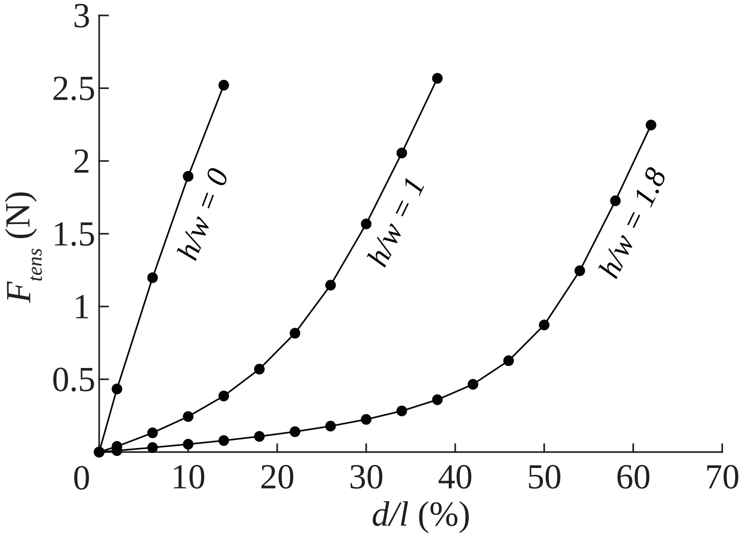

Figure 6.2: Resultant force F perpendicular to beam cross-section on a curved beam, building block extended by distance d, expressed as a percentage of the beam's total length l.

feasible space of aspect ratio h/w. Using a linear elastic model with tensile modulus, tensile strength and yield strength from the data sheet of the intended construction material [158], the resultant force F_{tens} due to imposed horizontal displacement d expressed as a percentage of each beam's total length l was evaluated. Each design evaluated had the same cross section dimensions $a = 1.75$ and $b = 0.8$. A tetrahedral mesh was used with an element size of 0.1mm and a tolerance of 0.005. Imposed horizontal end displacement d was imposed as a percent of the beam's total length l in increments of 2% until most of the beam material stress exceeded yield.

The results of this analysis, shown in Figure 6.2, give an overview of the loading-deformation behaviour of Bézier beams of varying aspect ratio. As the aspect ratio increases, the beams can undergo increasing amounts of end displacement before reaching a mostly yielded state. The beam with aspect ratio 0 is a straight beam, and its force increases most in proportion to d/l.

The results shown here can serve as a design baseline for development of beam systems with specified size and stiffness.

6.2.2 Patterning on Curved Surfaces and Conic Frusta

Here, rules are developed for patterning RAEs onto flat surfaces, curved surfaces, and conic frusta. From these patterning rules, a variety of 3D auxetic surfaces with varying compliance can be generated. Figure 6.3 shows a complex funnel-shaped surface decomposed into cylindrical segments and conic frusta. The following sections detail geometric rules for patterning RAEs on such surfaces.

Kinematics for patterning Representative Auxetic Elements (RAEs) onto flat surfaces, curved surfaces, and cylindrical segments are given in [144] for beams composed of circular segments. For patterning Bézier curved beams, similar relationships can be used. For patterning a flat surface of height L and width Y with one row of n RAEs whose beams have width w, aspect ratio q, and are initially separated by a vertical distance d,

$$Y = \quad nw \tag{6.7}$$

$$L = \quad \tfrac{2w}{q} + d. \tag{6.8}$$

A cylindrical surface of length L, radius R and opening angle γ can be projected to a flat surface of height L and width $Y = \gamma R$, allowing the previous methods to be used. Figure 6.3 B shows a cylindrical segment from the complex surface in Figure 6.3A with radius R, height L and opening angle $\gamma = 2\pi$. This can be projected to the flat sheet shown in Figure 6.3C, with height L and with $2\pi R$.

Since only a whole RAE element will produce auxetic behavior, n is constrained to be a natural number. A consequence of this constraint is that only an even number of Bézier-curved beams may be used to pattern a sheet.

To create the closed shapes demonstrated in this work, combinations of flat surfaces, surfaces with circular curves, and conic frusta are used. To pattern RAEs on a frustum, a similar strategy to the one for curved surfaces is followed: first, a geometrically flattened frustum is considered. It is filled with distorted RAEs such that they fit in to the dimensions of the flattened frustum surface.

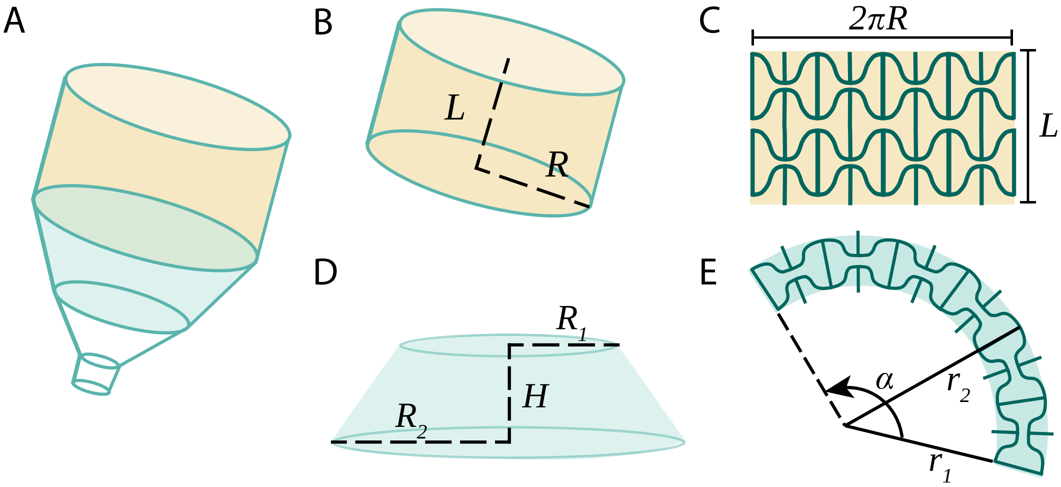

Figure 6.3: (A) Complex funnel-shaped device composed of cylindrical surfaces and conic frustum. (B) Cylindrical surface of length L and radius R. (C) Example of Patterned RAEs on the cylindrical surface which can be flattened to a rectangle of width $2\pi R$ and height L. (D) Conic frustum having radii R_1 and R_2 and height H. (E) Example of patterned RAEs on the conic frustum shown in D, which can be flattened to an arc-like sheet with radii r_1 and r_2 and opening angle α.

A circular cone segment of radii R_1 and R_2 and height H is shown in Figure 6.3D. The flattened frustum (Fig. 6.3E) can be described by two circular segments of arc angle α at distance $\sqrt{H^2+(R_2-R_1)^2}$ apart. The arc angle α is given by

$$\alpha = 2\pi \frac{R_2}{\sqrt{H^2+(R_2-R_1)^2}\left(1+\frac{R_1}{R_2-R_1}\right)}. \tag{6.9}$$

The distance r_1 of the inner circle from the origin is

$$r_1 = \sqrt{H^2+(R_2-R_1)^2}\frac{R_1}{R_2-R_1}. \tag{6.10}$$

The distance r_2 is

$$r_2 = r_1 + \sqrt{H^2+(R_2-R_1)^2}. \tag{6.11}$$

To pattern RAEs on flattened frusta, single rows of compliant beams are considered. Two compliant beams arranged in opposition are called an antagonistic beam pair. For auxetic behaviour to be maintained, these rows should meet the following compatibility conditions. As in curved sheets and cylindrical segments, only a natural number of RAEs (and therefore an even number of compliant beams) can be used to avoid discontinuities on the beam lattice. Further, adjacent rows of compliant beams with radii r_i are not allowed to overlap or create discontinuities. Finally, the RAE beams must be distorted to fit into the conic pattern. Control points $\vec{c}_0$ and $\vec{c}_4$ move so that two characteristic widths $w_1 = x_1 = \vec{c}_1|_1 - \vec{c}_0|_1$ and $w_2 = \vec{c}_4|_1 - \vec{c}_3|_1$ emerge. This constraint can be expressed in terms of the width w_i of a compliant beam in that row, where, for $2m$ RAEs per row, giving:

$$\alpha r_i = 2mw_i. \tag{6.12}$$

The height of each compliant beam h_i is then constrained by the fact that compliant beams on different rows should not intersect. For a frustum with $p+1$ rows, all patterned with $2m$ antagonistic beam pairs, with index $i \in [1, p]$ and compliant beam thickness b,

$$2(h_i + b) < r_i - r_{i-1}. \tag{6.13}$$

Aspect ratio of beam patterned on a conic frustum is measured w. r. t. the flat, undistorted beam.

It is possible to transition from a row having $2m$ antagonistic beam pairs (i.e., $4m$ individual beams per row)and flattened frustum radius r_2 to one having a smaller flattened frustum radius r_1 and m antagonistic beam pairs (i.e., $2m$ individual beams per row); the resulting RAE is horizontally asymmetric is shown in Figure 6.1D. Because of radial symmetry, a frustum patterned with an even number of asymmetric RAEs like those of Figure 6.1D should nonetheless experience symmetric deformation in the radial and hoop directions under internal pressurization.

Using the expressions for α and r_i in terms of frustum dimensions (Eqns. 6.9, 6.10 and 6.11) under the constraints in Eqn. 6.12 and 6.13 allows us a relation between dimensions of the frustum and admissible RAE patterns.

6.2.3 Experiments

Fluidic devices were developed from compound auxetic surfaces to test how relative compliance of fluidic reservoirs and pinch points affect sequence in soft robotics actuation.

Using the design rules outlined in the previous section, three devices having the funnel-like shape shown in Figure 6.4A were constructed. The structures consisted of a cylindrical surface with $L = 54mm$ and $R = 34.5mm$ patterned with 3 rows of 8 RAEs. The base of the cylinder attached to a conic frustum of $R_1 = 19.5mm$, $R_2 = 34.5mm$ and $H = 38mm$ patterned with 2 rows of 8 RAEs. A second frustum with $R_1 2.5mm =$, $R_2 = 19.5mm$ and $H =$ patterned with one row of 4 RAEs attached to the first frustum. A cylindrical pinch zone with $R = 2.5mm$, $L = 10mm$ and one row of 2 RAEs was attached to the second frustum. All RAEs had the cross section dimensions $a = 1.75mm$ and $b = 1mm$. Fluctuations in the total length of the device were $\pm 1mm$ due to fabrication variation. The devices were 3D printed on a Sinterit Lisa model using their proprietary material Flexa Grey.

The devices were separated into zones: a fill zone consisting of the larger cylindrical surface, a transition zone consisting of the first frustum, and a pinch zone consisting of the second frustum and the smaller cylinder. Devices were compared. Each was designed with varying triads of RAEs patterned on each of these sections, as shown in Figure 6.4. Five devices total were constructed and tested.

A plastic film produce bag (Amazon.com) was folded and placed within each device so that the bag's opening extended out of the device's fill zone, and the bottom of the bag extended 15cm from the pinch zone. The bag and the device were mounted vertically on a Bunsen stand. The bag opening was attached to a 3.175mm ID tube, that routed air from a lab air compressor. A pressure sensor (Honeywell, SSCDANN005PGAA5) was mounted off the air inlet tube near the bag opening. A

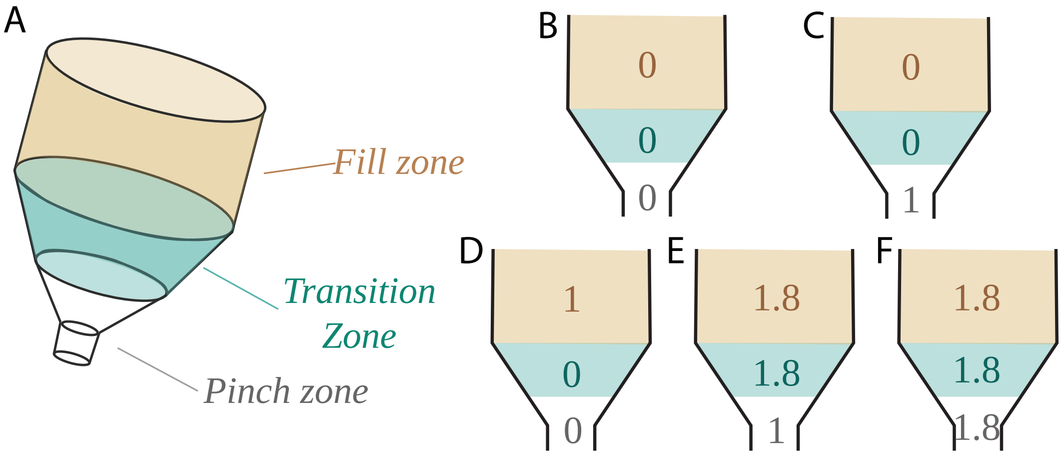

Figure 6.4: Compliance combinations on auxetic pinch devices. (A) Auxetic valve schematic showing cylindrical fill zone, conical pinch point with a small-diameter outlet and transition zone in between. (B)-(F) Schemata of samples tested with varying compliance levels in fill zone transition zone, and pinch zone. Numbers shown are the aspect ratio h/w of RAEs used. An aspect ratio of 0 corresponds to a horizontal, straight beam. The highest aspect ratio used was 1.8.

pressure gauge with digital display was also mounted near the bag opening. A hole was punched in the bottom of the produce bag below the pinch zone and a 1.58mm ID tube was secured. This tube was attached to a second pressure sensor. The test platform used to conduct experiments is shown in Figure 6.5.

The air compressor was set to 517±17 kPa and a manual regulator was opened slowly to allow flow into the device; this controlled the pressure at the air inlet. When the produce bag began to observably expand, the manual regulator was released and left at its current opening state. After the lower portion of the produce bag appeared to be fully expanded, the pressure in the air compressor was vented to eventually reach atmospheric pressure. At the conclusion of each test, the air inlet tube was released from the air compressor allowing the device to drain more fully. Throughout, the pressure sensors recorded air inlet and produce bag pressures at 8Hz. A 1080P webcam (Logitech) took 30fps video of each test. Each test was repeated three times, or until the auxetic device broke. Video stills of one test are shown in Figure 6.6.

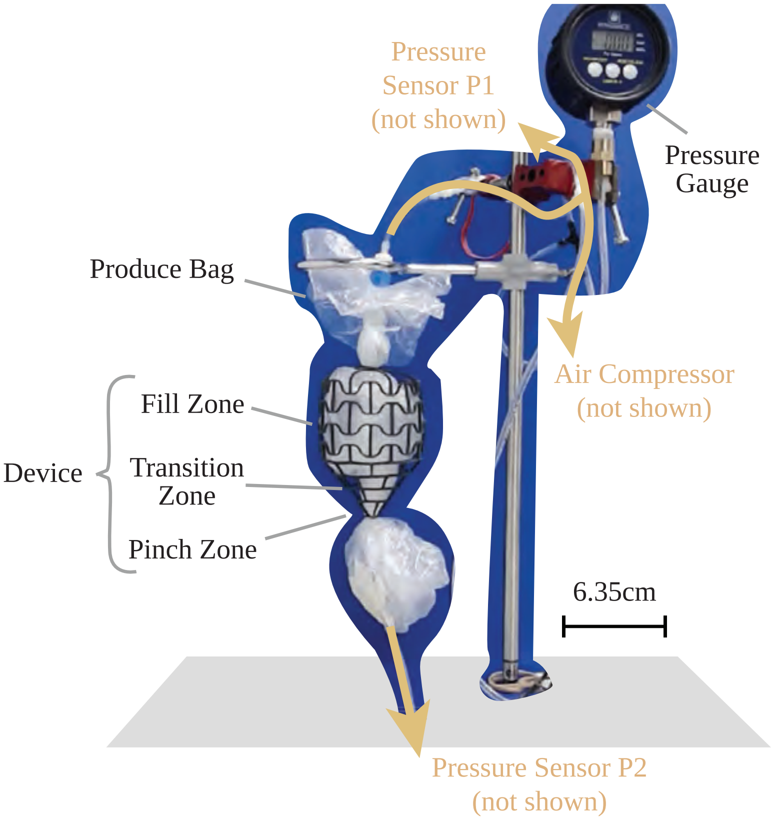

Figure 6.5: Platform used to test effect of auxetic devices on fluid flow. Device is shown in center with produce bag inside. Pressure gauge with digital readout is located at the top right. Fluid-carrying tubes are marked with gold lines. The air compressor and pressure sensors are not shown. The device shown in the photo is the same as Figure 6.4D.

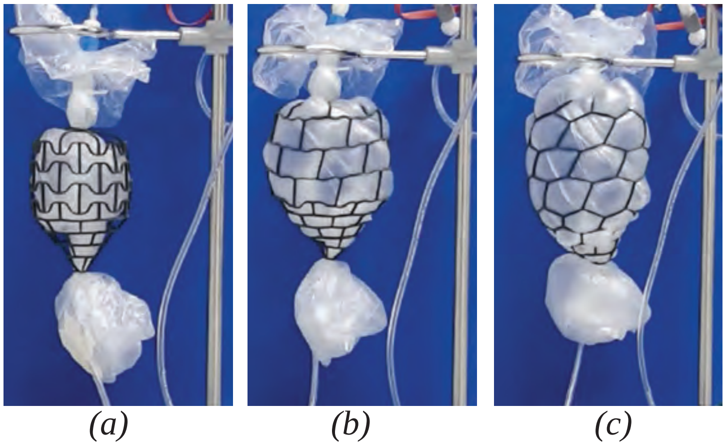
(a) (b) (c)

Figure 6.6: Photos of the device test for the device design shown in Figure 6.4D. *(a)* Device at atmospheric pressure. *(b)* Initial response to pressurization P_1. *(c)* The fill zone is fully expanded and the bottom bag is almost fully expanded.

6.3 Results

The above experiment was performed on five devices. Using similar principles, prototype devices showing sequential actuation were made.

6.3.1 Combining Fluidic Reservoirs and Pinch Points

Pressure at the air inlet and the lower portion of the produce bag are shown with respect to time in Figures 6.7 - 6.11. For all cases, P_1 refers to measurements from the air inlet pressure sensor while P_2 refers to measurements at the bottom of the bag after the pinch zone.

Figure 6.7 shows the response of P_2 to air inlet pressure input P_1 for a device with beams of aspect ratio 0 in the fill, transition, and pinch zones (Fig. 6.4B). Here, P_2 tracks P_1 more closely than it does in the tests shown below. In particular, the step-like inputs at 50s in the second test (Fig. 6.7b) and 20s in the third test (Fig. 6.7c) only result in small differences between P_1 and P_2, on the order of 0.5kPa. The volume constraint provided by the device is a likely reason for closer tracking; air coming into the device from the compressor fills a smaller volume before it becomes

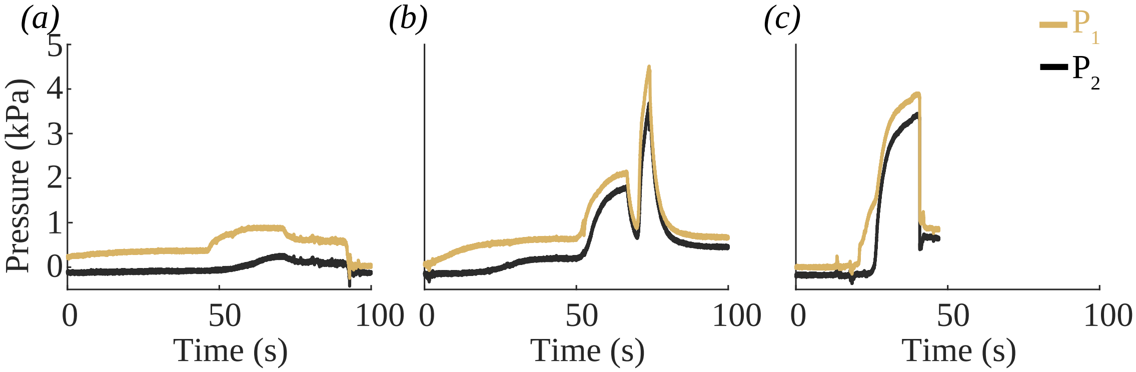

Figure 6.7: Pressure P_1 and P_2 for a produce bag and device with beams of aspect ratio 0 in all zones (Fig. 6.4B). *(a)* First test, *(b)* second test, *(c)* third test.

compressed by the produce bag walls.

Figure 6.8 shows the response of P_2 to air inlet pressure input P_1 for a device with beams of aspect ratio 0 in the fill and transition zones and 1 in the pinch zone (Fig. 6.4C). Here, P_2 follows P_1 slightly, but less closely than it did for the device having beams of aspect ratio 0 in all zones. The device broke by tearing at the pinch zone at 100s in the first trial.

Figure 6.9 shows the response of P_2 to air inlet pressure input P_1 for a device with beams of aspect ratio 1 in the fill zone and 0 in the transition and pinch zones (Fig. 6.4D). Here, P_1 follows P_2 slightly, but less closely than it did for the device having beams of aspect ratio 0 in all zones. After the first trial, the bag was incorrectly mounted to the device and therefore only one test is shown.

Figure 6.10 shows the response of P_2 to air inlet pressure input P_1 for a device with beams of aspect ratio 1.8 in the fill and transition zones, and 1 in the pinch zone (Fig. 6.4E). Here, a clear delay between P_2 and P_1 is evident in all trials. Step-like inputs of P_1 at time 19s in the first trial, time 3s in the second trial, and time 53s in the third trial are lagged by P_2 by approximately 28s in the first trial, 47s in the second trial, and 30s in the third trial. After it begins to rise, P_2 follows P_1, but, again, does not become equal to P_1 while P_1 is significantly higher than atmospheric pressure. The device broke by fracture of the pinch zone at 120s in the third trial.

Figure 6.11 shows the response of P_2 to air inlet pressure input P_1 for a device

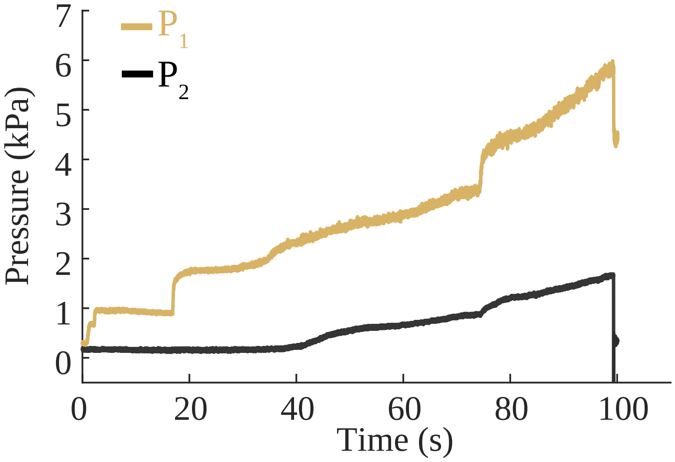

Figure 6.8: Pressure P_1 and P_2 for a produce bag and device with beams of aspect ratio 0 in the fill and transition zones and 1 in the pinch zone (Fig. 6.4C). The device broke by tearing at the pinch zone at 100s in the first trial.

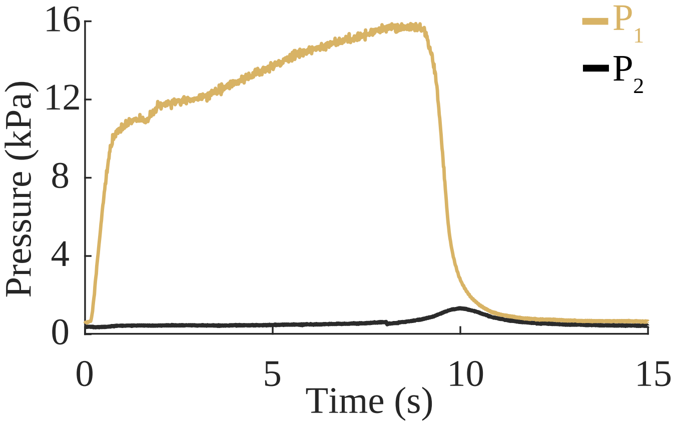

Figure 6.9: Pressure P_1 and P_2 for a produce bag and device with beams of aspect ratio 1 in the fill zone and 0 in the transition and pinch zones (Fig. 6.4D). After the first trial, the bag was incorrectly mounted to the device.

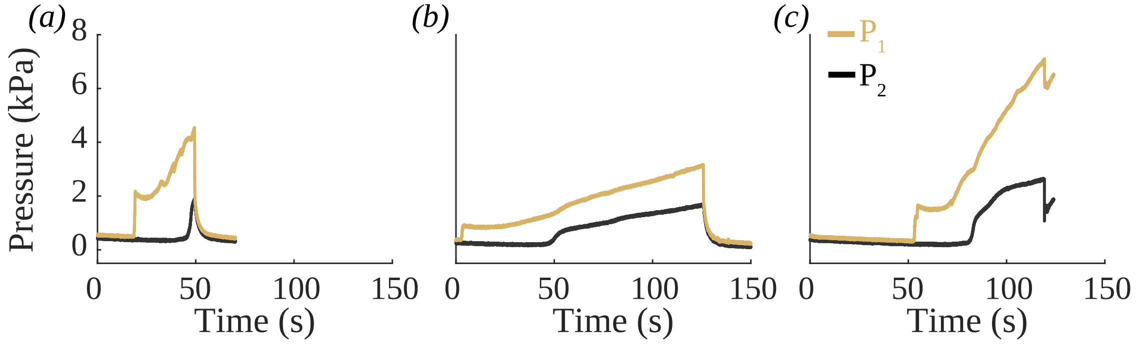

Figure 6.10: Pressure P_1 and P_2 for a produce bag and device with beams of aspect ratio 1.8 in the fill and transition zones, and 1 in the pinch zone (Fig. 6.4E). *(a)* First test, *(b)* second test, *(c)* third test. The device broke by fracture of the pinch zone at 120s in the third trial.

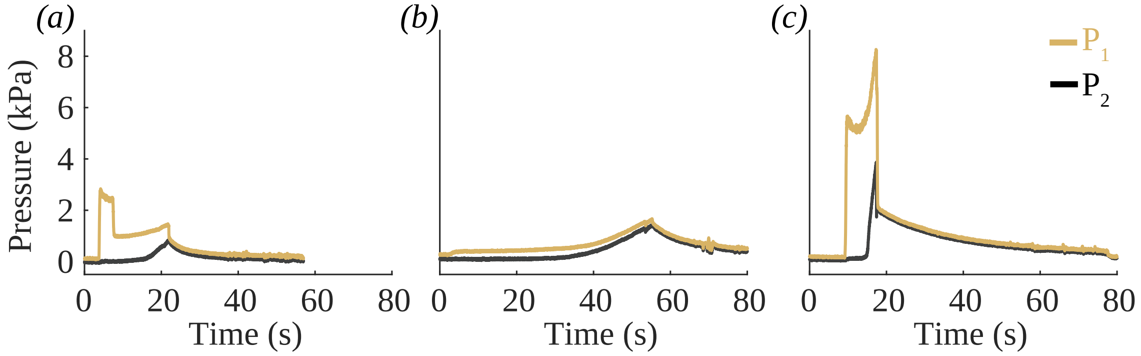

Figure 6.11: Pressure P_1 and P_2 for a produce bag and device with beams of aspect ratio 1.8 in all zones (Fig. 6.4F). *(a)* First test, *(b)* second test, *(c)* third test.

with beams of aspect ratio 1.8 in all zones (Fig. 6.4F). Here, a clear delay between P_2 and P_1 is evident in the first and third trials. Step-like inputs of P_1 at time 4s in the first trial and time 9s in the third trial are lagged by P_2 by approximately 13s in the first trial and 6s in the third trial. The second trial, with no step-like P_1 inputs, shows closer tracking of P_2 with P_1.

These experiments show that devices with auxetic fill zones and pinch areas can affect air pressurization over time in a soft fluidic chamber. In particular, the possibility of a delay between inlet pressure and the pressure reached inside a chamber is established. Further, head loss between P_1 and P_2 is observed in several trials.

6.3.2 Fluid-Sequenced Device Prototypes

Using the pressurization lag effect established in the previous experiments, prototype devices that actuate sequentially were created. Pressurization of these prototypes was done manually using a squeeze valve attached to an air compressor set at 103 ±17 kPa, via a 3.175mm inner diameter tube.

Figure 6.12 shows selected frames from a video of a device containing 3 fill zones with beams of aspect ratio 1.0, placed in series with transition zones with beams of aspect ratio 1.8, and pinch points with beams of aspect ratio 0 between them. These frames, selected in increments of 4s, show the sequential nature of the inflation of this prototype. The squeeze valve connecting the compressed air to the prototype is opened at $t = 0s$. At a time $t = 4s$, the rightmost fill zone has expanded. At $t = 8s$, the rightmost fill zone is fully expanded. At $t = 12s$, the center fill zone has begun to expand, and by $t = 16s$, all fill zones have expanded.

Figure 6.13 shows selected frames from a video of a device containing 3 fill zones with beams of aspect ratio 1.8, placed in series with transition zones with beams of aspect ratio 1.8, and pinch points with beams of aspect ratio 1.8 between them. These frames, selected in increments of 2s, show the sequential nature of the inflation of this prototype the differs from the inflation of the prototype with beams of aspect ratio 0 in the pinch zone. Inflation begins at $t = 0s$. When $t = 2s$, the rightmost fill zone has begun to expand, while at $t = 4s$, both the rightmost and center fill

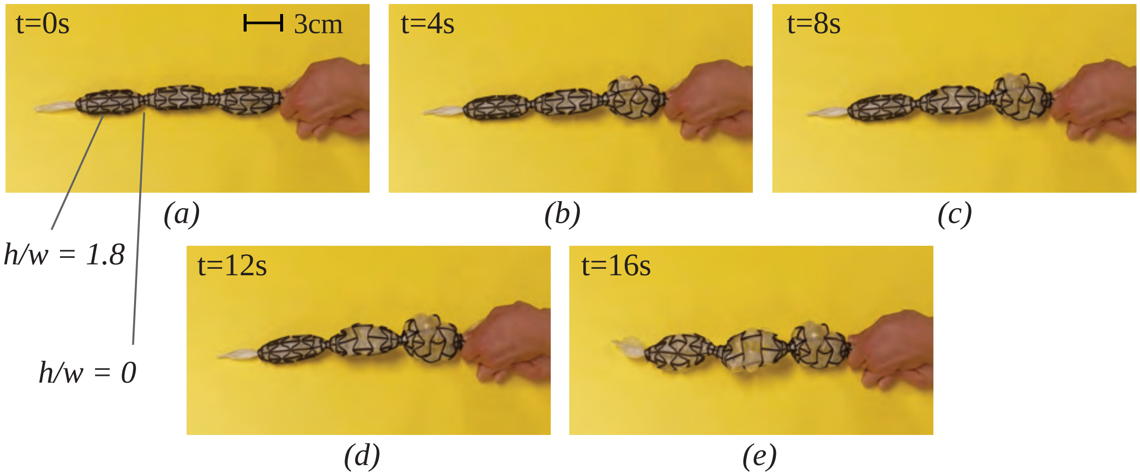

Figure 6.12: Video frames selected at intervals of 4 seconds for a prototype device, filled with one produce bag, containing beams of aspect ratio 0 at the pinch and transitions zones, and beams of aspect ratio 1.8 in fill zones.

zones have expanded. At $t = 6s$, all fill zones are approximately equally expanded. Between $t = 6s$ and $t = 8s$, all fill zones reach maximum expansion. In each series device prototype, positioning of the fill zones against the background causes them to push against the background and rotate when their volume increases.

Figure 6.14 shows selected frames from a video of a device containing 3 fill zones with beams of aspect ratio 1.8 in a parallel configuration. Each fill zone is placed in series with a pinch zone, and the beam aspect ratio used in each pinch zone varies between 0 and 1.8. A strain-limiting beam is left on each fill zone so that the structure bends as volume increases. Inflation begins at $t = 0s$. When $t = 2s$, the bottom structure begins to bend out of the plane of the page. At $t = 4s$, the bottom structure bends further out of the plane of the page while the middle structure begins to bend out of the plane of the page. By $t = 12s$, the bottom and middle structure have bent further out of the plane of the page while the top structure has bent upwards. Black circles with white outlines are overlaid on every frame to compare the current end point of each structure with its location at atmospheric pressure. The moving shadows of each structure also provide a way to compare motion. Figure 6.15 shows the same device's sequential motion as it knocks down three separate rows of dominos

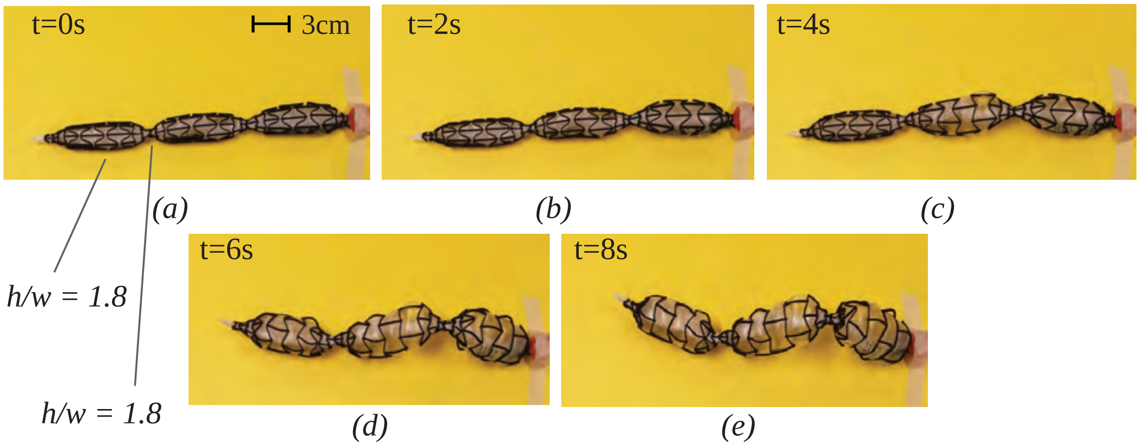

Figure 6.13: Video frames selected at intervals of 2 seconds for a prototype device, filled with one produce bag, containing beams of aspect ratio 1.8 in all zones.

under pressurization from a bike pump.

6.4 Conclusion

This chapter establishes basic design rules for patterning auxetic beam networks on curved surfaces and conic frusta as well as compatibility conditions for combining differently patterned surfaces. Bézier-curved beams were introduced as a design building block whose antagonistic placement results in an auxetic surface. Kinematics and loading behaviour of these design building blocks were studied.

By building devices consisting of connected auxetic surfaces with differing kinematic and kinetic properties, the potential of this design framework to create devices that act as expandable fluidic reservoirs with pinch points was demonstrated. The pilot study performed shows the existence of a delay effect as air from a pressurized source fills two expandable volumes separated by chambers of varying compliance.

However, these results open questions for further analysis and experimentation. First, the mechancial analysis presented here connects deformation to loading on the level of the design building block. Devices made from various beam networks and surfaces should be analyzed as well for development of appropriate soft robot

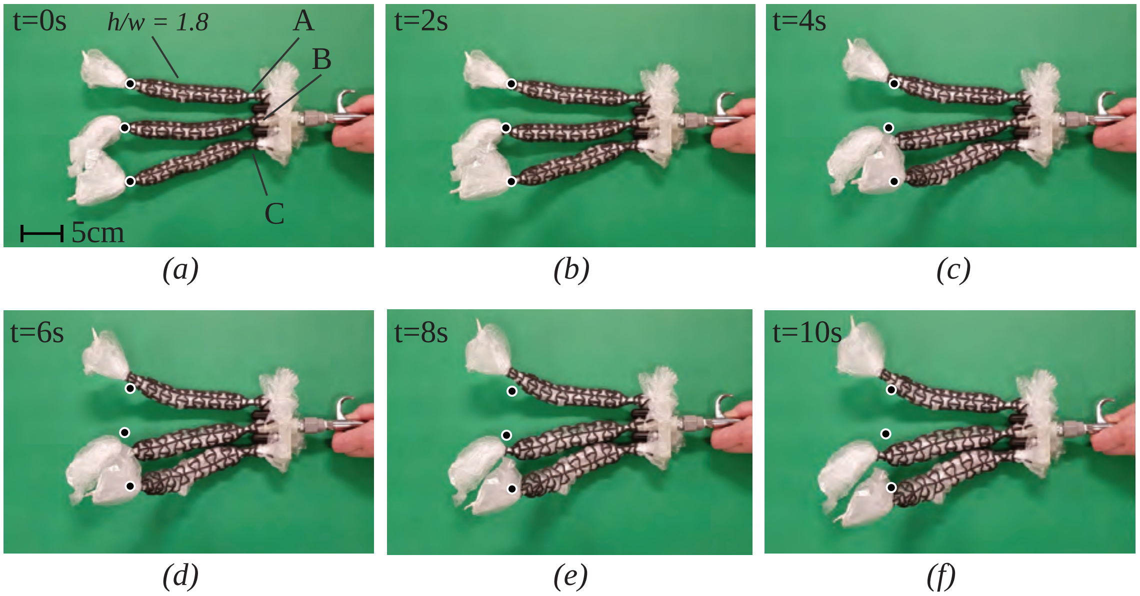

(a) (b) (c)

(d) (e) (f)

Figure 6.14: *(a)-(f)*: Video frames selected at intervals of 2 seconds for a prototype device containing varying pinch zone designs. All actuators in this compound device have beams of aspect ratio h/w 1.8 in the fill zones and one strain limiting beam in the center, but varying aspect ratio of beams in the pinch zones. For the pinch zone marked by A, $h/w = 0$. For the pinch zone marked by B, $h/w = 1$. For the pinch zone marked by C, $h/w = 1.8$. Black circles with white outlines mark the positions of the ends of each structure in the device before they are inflated. This device is filled with three produce bags; one per bending actuator. Ends of the produce bags extend past the ends of the auxetic structures.

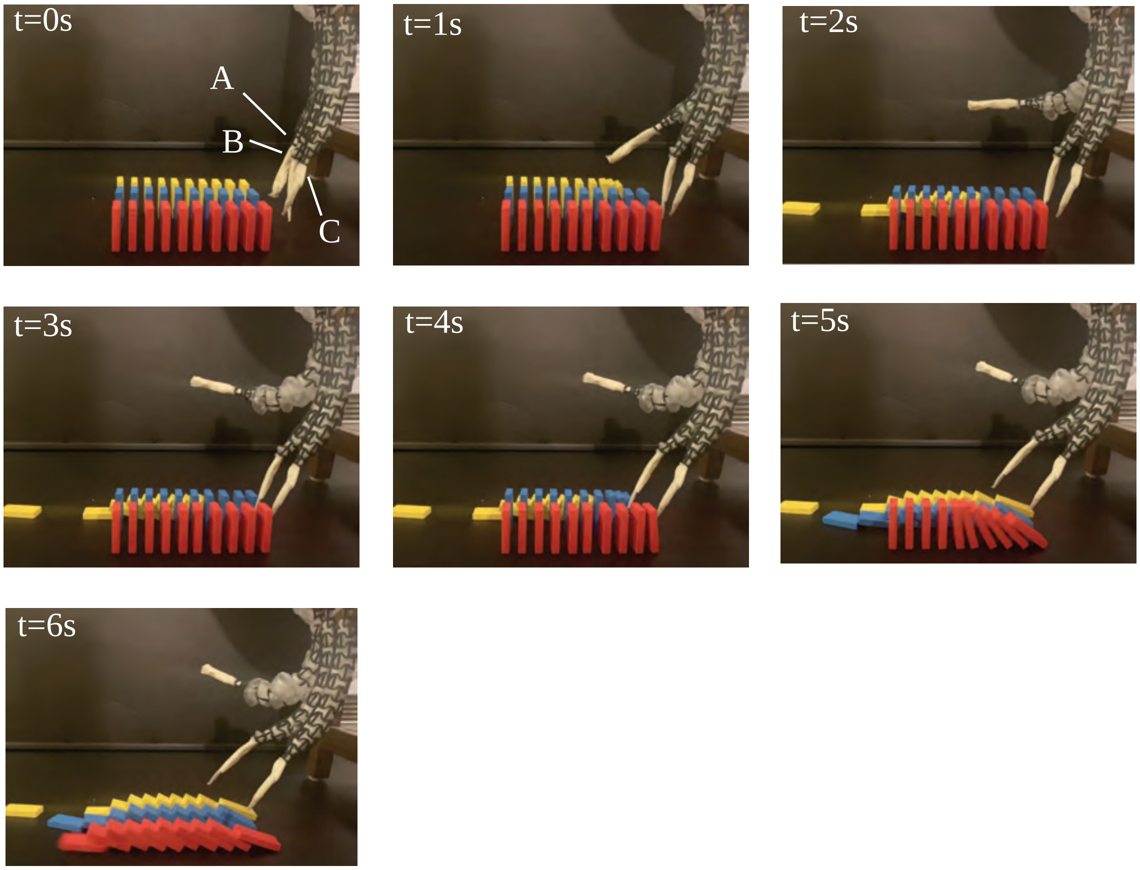

Figure 6.15: Video frames at intervals of 1s of bending actuator device performing sequential domino task. All actuators in this compound device have beams of aspect ratio h/w 1.8 in the fill zones and one strain limiting beam in the center, but varying aspect ratio of beams in the pinch zones. For the pinch zone marked by A, $h/w = 0$. For the pinch zone marked by B, $h/w = 1$. For the pinch zone marked by C, $h/w = 1.8$. Ends of the produce of the produce bag stick out of the auxetic structures and are covered with masking tape.

designs.

Second, while the pilot experimental study establishes the time lag effect of air flow within these devices and its potential usefulness in soft robotics, conclusions about how the compliance of the design building blocks affects the timing behaviour cannot yet be drawn. Intuition says that the relative volume change of each device's fill zone and the compliance at the opening of the pinch zone should influence the behaviour of the working fluid. Yet, quantitative differences between designs are difficult to identify because the inlet pressure P_1 is significantly different in every trial. Further, while a pressurization delay of P_2 and a head loss $P_1 - P_2$ are observed in several trials, it is difficult to judge which phenomenon is dominant. Using an electronic pressure regulator rather than a manual valve would greatly increase the repeatability of each experiment so that designs could be compared. Multiple tests of a given device should be performed at varying pressure inputs so that head loss and time delay may be compared and assessed.

Several prototype devices show promise for useful devices in soft robotics such as locomotion robots and manipulators. A more detailed, experiment-based study of fill and pinch zone design can clarify the connection between design building blocks and specific functionality.

6.5 Summary

There is a need to develop soft robots with the capability to perform complex sequential tasks without human or electronic intervention or signals. This chapter examines how auxetic design bluiding blocks may be used to design soft robots that combine fluidic resistance and volume capacity for sequential motion. The work presented here establishes basic design rules for patterning auxetic beam networks on curved surfaces and conic frusta as well as compatibility conditions for combining differently patterned surfaces. Bézier-curved beams were introduced as a design building block whose antagonistic placement results in an auxetic surface. Kinematics and loading behaviour of these design building blocks were studied through Finite Element Analysis (FEA).

CHAPTER 7

Design and Deployment of Soft Robots with Strain-Hardening Auxetic Kirigami

This chapter has been previously published and is used with permission from the Institute of Electrical and Electronics Engineers (IEEE). It may be referenced as:

Sedal, Audrey, Memar, Amirhossein, Liu, Tianshu, Mengüç, Yiğit, and Corson, Nick. Design of Deployable Soft Robots through Plastic Deformation of Kirigami Structures. *IEEE Robotics and Automation Letters* 5(2): 2272 - 2279.

7.1 Introduction

Deployable robots can transit from a compact form factor into an expanded shape better-suited for specific tasks or environments. This characteristic of deployability is useful for robots that need to be transported in a confined space (e.g. a space shuttle or underwater vehicle) before reaching their intended operating environment, or robots that need to pass through small spaces (e.g. a cave opening) before beginning an exploratory task.

A suitable deployable robot should be easy to fabricate, able to change function when it changes scale, and have a deployed shape that is well-suited to its intended usage. Therefore, designing for deployability requires careful consideration of the structural components involved. Rigid parts of the robot structure need to be integrated in a compact way, yet need to be arranged, connected and actuated so that a desired deployed shape is achievable. Some "tensegrity" designs mix rigid beams with tensile elastic components to achieve a desired deployment shape [41, 110, 180]. Other modules [181, 183] integrate rigid panel-like elements with flexible hinges; these are often termed "origami" robots. However, robots made with discrete, rigid components may have limited, and often complicated deployment schemes. Further, they often require fabrication of special components and high-effort assembly process.

One way to reduce the volumetric and kinematic limitations from rigid components is to replace them with soft pneumatic structures. Soft pneumatic structures are intrinsically deformable in their non-deployed state, meaning that they can be easily folded, pressed, or packed into compact configurations while retaining the ability to transform into their deployed shapes. The structures in [161] deploy through the inflation of truss-like pneumatic tubes, which become stiffer as air pressure increases. Easy fabrication and assembly is another key advantage of soft pneumatic structures in deployable robotics. The relatively simply constructed vine robot in [11] can deploy and operate in a variety of conditions, under a variety of environmental constraints. In [138], inflatable furniture and other static objects are fabricated by heat-sealing the flat cut sheets of inextensible thermoplastic polymer. In each of these examples, no advanced or especially precise fabrication is required, yet the devices achieve the specified deployed shapes. However, purely pneumatic soft structures have limitations in their deployed state. Such designs often require a minimum pressure to retain their deployed shape while functioning [161], resulting in a consistent power input requirement. Woven reinforcement materials, such as the meshes used in Meshworm [146] and CMMWorm [63], also offer tunable deformations constrained by the fibers in the mesh, but tuning the elastic recovery of such a structure without additional actuation is difficult due to fibers sliding against one another. Further, the motion of these robots in their deployed state is not necessarily easy to design or control: the deployable vine robot of [11] does not have a simple retraction scheme, and the tendon actuation of [161] limits the space of available motions.

Compared to other structures and materials that can achieve large-scale stretching and recovery, kirigami structures have two key advantages. They are easier to fabricate and offer the possibility for mechanical programming of their kinematics in

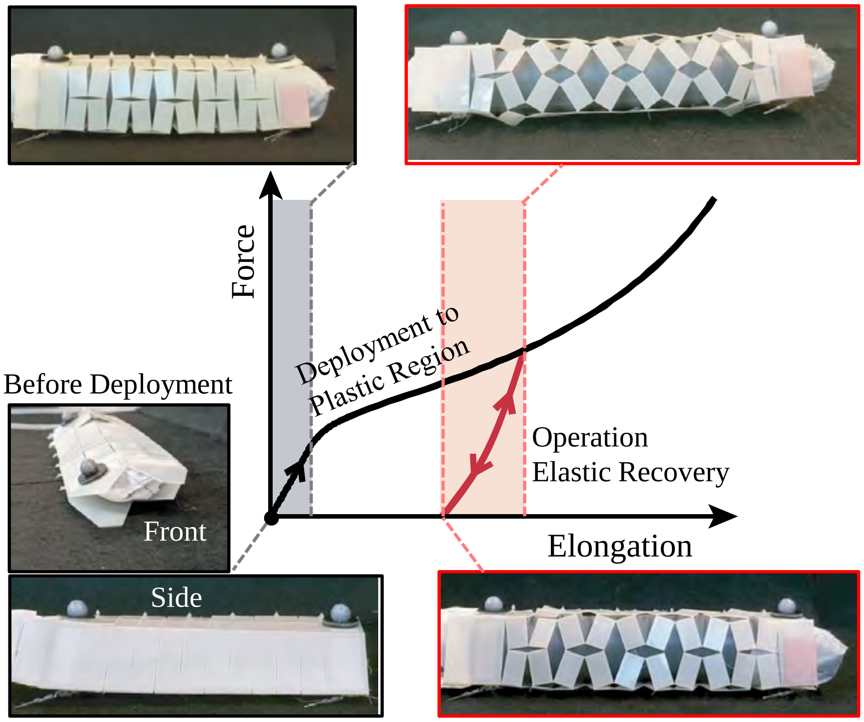

Figure 7.1: Force-Elongation plot of kirigami structure: Elasto-plastic deployment region is shown in black, with corresponding robot photos outlined in black. Operating range is shown in red, with corresponding robot photos outlined in red.

the simple fabrication process. Kirigami-patterned mechanisms are easy to fabricate due to the fact that they can be cut on planar sheets of material, have mechanically programmable stiffness properties and offer the potential to be integrated into deployable robots. By patterning networks of thin cuts on a flat sheet, it is possible to change the kinematics of the sheet material under loading and design a variety of behaviours. Kirigami-patterned structures are already an often-used basis for deployable static structure design, appearing in mechanisms and structures ranging from millimeter-scale [172], to architecture scale [77]. Further, kirigami patterns can be integrated with soft pneumatic actuation. Deformations of a kirigami structure can add function to a low-stiffness or low-impedance soft system.

In [35], various arrangements of buckled kirigami cuts are shown to produce linear and rotational actuation. Controlled buckling of a kirigami structure in [127] causes asymmetric friction that enables an extending actuator to crawl on rough surfaces. Because of their scalability, relatively easy fabrication, and design degrees of freedom, kirigami-based structures present a promising opportunity in the design of deployable robots.

Design of deployed states for kirigami structures has been well-investigated in the kinematic context [77, 162]. In contrast, loading properties of a kirigami structure require more characterization: while kirigami structures have been analyzed for their elastic stiffness [68], buckling response [126], and ultimate tensile strength [66], elasto-plastic deformation and loading have been neglected. Yet, plasticity occurs in a great variety of materials and has the potential to be leveraged in robotics; in particular, the phenomenon of strain hardening under plastic deformation can produce deployable robots with mechanical intelligence. A plastically deformed robot structure has unique benefits: it can be kept in its deployed state without requiring a consistent power input, while elastic recovery in the deployed structure can accommodate external loads. To utilize the benefit of plasticity, a material with large range for plastic deformation and hardening needs to be chosen.

Loading-deformation behaviour of a robotic structure can be mechanically programmed by imposing plastic deformation. Depending on the initial cut dimensions and degree of plastic deformation undergone, the shape and size of the elastic recovery curve will change (Fig. 7.1), as will the resulting stiffness profile of the structure. In the case of the strain-hardening material shown in Fig. 7.1, a cut structure can be loaded to a specific point, and then operate in its deployed state with a springback range wider than the initial elastic range of the robot.

This chapter proposes a design methodology for robotic kirigami structures that takes use-case deformation, loading and stiffness into consideration from the beginning of the design process. A a model for plasticity in the stretching of a kirigami structure is developed. Then, a design methodology showing ways to leverage mechanical plasticity in a deployable robotics context is described. Specifically, creation of kirigami structures that have an increased elastic region, and specified stiffness, in their deployed states is shown. The benefits of such a plastically-deformed structure are demonstrated through integration into a soft, deployable crawling robot. Methodology is shown for design the deployed shape of the kirigami structure such that its corresponding springback characteristics matches the stiffness of the actuator to which it is attached. By better understanding the plastic loading properties of kirigami structures in robotic applications, roboticists can create stronger designs with precise mechanical behaviour and known loading characteristics.

7.2 Plastic Kirigami Model and Validation

This section described a static analysis on the plastic deformation of a kirigami cut structure. The model presented below relies on three key assumptions: that there is no buckling of the structure, no out-of-plane motion of the structure, and that the joints in the structure act as Euler-Bernoulli beams with no length change along their neutral axes.

7.2.1 Plastic Kirigami Model Description

This work considers kirigami structures with orthogonal patterned cuts for our modeling and experimentation. However, a similar approach can be applied to other types of cuts. The orthogonal patterned cuts on a sheet with length l_0 and width w_0

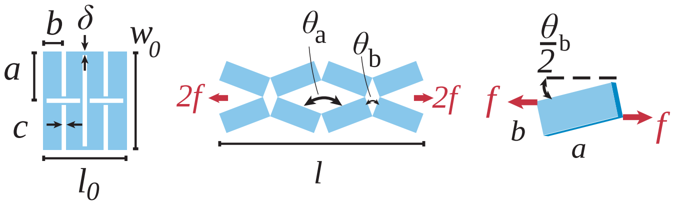

(a) (b) (c)

Figure 7.2: Kirigami structure in initial (left) and deformed (right) states. This structure has 2 rows of n cuts of length a, and m cuts of length b. The distance between orthogonal cuts is δ, and the width of the cuts is c. Its initial width is w_0 and its initial length is l_0. When an axial force f is applied, the structure has length l and opening angles θ_a and θ_b as shown.

are shown in Fig. 7.2. The first cut family has 2 rows of n cuts of length a, and the second cut family has m cuts of length $2b$. The distance between orthogonal cuts is δ. To understand loading on the structure, it is important to understand these kinematics alongside the elasticity and plasticity of the material. Consideration of the same sheet in a deformed configuration after a tensile force f is applied to it (Fig. 7.2) can follow. The opening angle between two cuts segments of length a is θ_a. The opening angle between two cut segments of length b is $\theta_b = \pi - \theta_a$.

The kinematic relation between l in terms of a, b, and θ_b, derived in [162], is given by

$$\frac{l}{l_0} = \frac{a}{b}\cos\frac{\theta_b}{2} + \sin\frac{\theta_b}{2}. \tag{7.1}$$

In the deformed configuration, each rectangle of material in the sheet will have horizontal forces f on each of its corners (Fig. 7.2c). The total moment τ applied through joints on each of these 4 corners is balanced by the moment due to misalignment of the axial force f:

$$\tau = f\left[a\sin\left(\frac{\theta_b}{2}\right) - b\cos\left(\frac{\theta_b}{2}\right)\right]. \tag{7.2}$$

The bending moment M on each cut junction relates to the total moment τ by $\tau = 4M$. Yet, this moment M also depends on the properties of the joint in

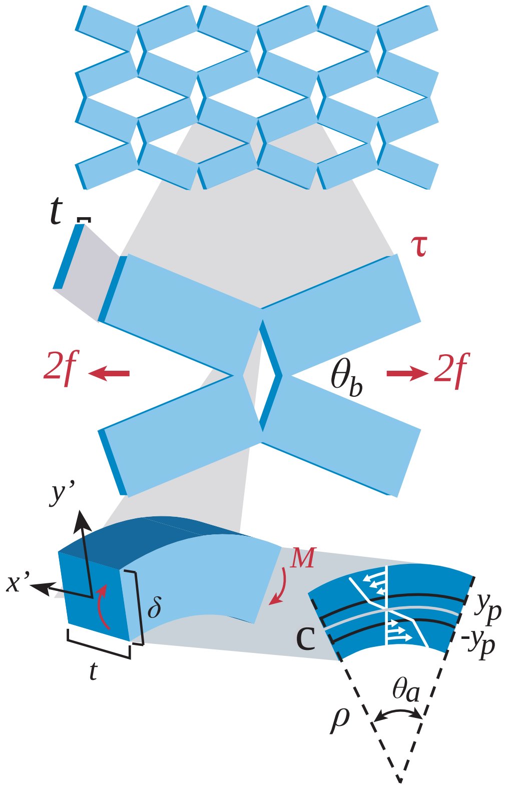

Figure 7.3: Kirigami cut junctions during deformation. Top: Two adjacent kirigami structures as defined in Fig. 7.2 with $2n$ cuts of length a, m cuts of length b, force f applied in the x direction, and opening angles of $\theta_{a,b}$. Center: Kirigami repeating element, from the larger cut structure with moment τ on each corner. Bottom left: A cut junction of height δ and thickness t, with local coordinates x' and y'. Bottom right: cut view of the same cut junction with stresses shown by white arrows. For $|y'| < y_p$, the stresses are elastic. For $|y'| > y_p$, the stresses are plastic.

its bent state. To develop this relationship, it is necessary to assume that the cut junctions act as elastic-plastic bending beams, where tensile stress is assumed to be small compared to bending stress. Each cut junction is considered as a beam with bending angle θ_a, radius of curvature ρ, height δ and thickness t, with coordinates x' and y' describing the location of a point on the cut beam's cross-section (Fig. 7.3). In [126], similar assumptions are made, but plasticity is neglected. For a structure in equilibrium, one can find that the moment is a function of both the kinematic properties and the beam stresses σ_{xx}. Then, the following relationship can be used to find M and the corresponding force on the structure f:

$$\begin{aligned} M &= \frac{f}{4}\left[a \sin\left(\frac{\theta_b}{2}\right) - b \cos\left(\frac{\theta_b}{2}\right)\right] \\ &= \int_{-\frac{t}{2}}^{\frac{t}{2}} \int_{-\frac{\delta}{2}}^{\frac{\delta}{2}} y' \sigma_{xx}(y', \rho) dy' dx'. \end{aligned} \tag{7.3}$$

A development of the relationship between the sheet's material properties and its stress $\sigma_{x'x'}$ by approximating the cut structure material as a bilinear isotropic hardening material [59] is shown below. The 1D constitutive equations for the stress σ, in terms of the Young's modulus E, elastic and plastic strains ε_{elast} and ε_{plast}, yield stress σ_{yield}, and hardening function (here, a constant) E_h are then

$$\sigma_{elast} = E\varepsilon_{elast} \tag{7.4}$$

for the elastic case. Stress σ_{plast} for a material in the plastic regime with linear isotropic hardening is written in terms of the plastic modulus E_h as

$$\sigma_{plast} = \sigma_{yield} + E_h(\varepsilon_{xx} - \varepsilon_{yield}). \tag{7.5}$$

Here, the plastic strain is the difference between the deformed strain and the yield strain: $\varepsilon_{plast} = \varepsilon - \varepsilon_{elast}$. Since the elastic regime of this material is linear, one can assume that

$$\sigma_{yield} = E\varepsilon_{yield}. \tag{7.6}$$

Assuming the central axis of the beam does not change length , the strain in the beam is given by

$$\varepsilon_{x'x'} = \frac{y'}{\rho}. \tag{7.7}$$

Initially, the moment M is fully elastic across the whole cross-sectional area A of the beam, giving

$$\begin{aligned} M(\rho) &= \iint\limits_A y'\sigma_e(x,\rho)dA \\ &= \frac{E}{\rho}\int_{-\frac{t}{2}}^{\frac{t}{2}}\int_{-\frac{\delta}{2}}^{\frac{\delta}{2}} y'^2 dy'dx' \\ &= \frac{E}{\rho}\frac{\delta^3 t}{12}. \end{aligned} \tag{7.8}$$

However, parts of the beam cross-section yield as the curvature $1/\rho$ increases. The variable y_p is the cross-section coordinate in y' where the beam transitions from elastic to plastic deformation (Fig. 7.3). Since the neutral axis of the beam does not change length, the top part ($y' > y_p$) of the beam is in tensile plasticity, while the bottom ($y' < -y_p$) is in compressive plasticity. The general expression for $M(\rho)$ in (7.3) is then split about $\pm y_p$:

$$\begin{aligned} M(\rho) &= M_{elast}(\rho) + M_{plast}(\rho) \\ &= t\frac{E}{\rho}\int_{-y_p}^{y_p} y'^2 dy' + 2t\int_{y_p}^{\frac{\delta}{2}} y'(\sigma_{yield} + E_h(\varepsilon_{xx} - \varepsilon_{yield}))dy'. \end{aligned} \tag{7.9}$$

It is possible to find the value of y_p by setting $\sigma_{yield} = \sigma_{xx}(y_p)$ and using (7.4) and (7.7):

$$\sigma_{yield} = E\frac{y_p}{\rho}. \tag{7.10}$$

Assuming that the beam bends as a circular segment, and that the cut kerf of the laser cutter c is 0.25mm, it is possible to find ρ (shown in Fig. 7.3) as a function of θ_b as

$$\rho(\theta_b) = \frac{c}{\pi - \theta_b}. \tag{7.11}$$

Finally, equating the expressions for $M(\rho)$ from (7.3) and (7.9), and isolating the force f gives

$$f(\theta_b) = \frac{4M(\rho(\theta_b))}{a\sin\left(\frac{\theta_b}{2}\right) - b\cos\left(\frac{\theta_b}{2}\right)}. \tag{7.12}$$

The force f in (7.12) tends toward infinity as its denominator tends to zero. This model's singularity at $a\sin(\frac{\theta_b}{2}) - b\cos(\frac{\theta_b}{2}) = 0$ is equivalent to the kinematic locking equations shown in prior analysis [162].

Using the relationship between the axial force f on the structure, the kinematic parameter θ_b, and the cut pattern parameters a, b, δ and t, designers can select parameters for kirigami structures that have specified loading-deformation relationships during plastic deformation.

7.2.2 Experimental Validation of Plasticity Model

To experimentally verify the plasticity model, a tensile experiment on 4 sheets of varying design parameters b and δ was performed. The kirigami pattern samples were cut from 0.178mm (0.007in) thickness sheets of BoPET (Mylar, DuPont-Teijin) using a CO2 laser cutter (Epilog Fusion M2). BoPET was chosen because of its known strain-hardening property [39] and compatibility with CO2 laser cutters. The values of design parameter chosen for each sample can be found in Table 7.1. Common parameters for each sample were thickness $t = 0.178mm$, cut length $a = 12.70$mm, $n = 10$ and $m = 12$.

Table 7.1: Set Design Parameters for Validation Samples

Sample no.	b (mm)	δ (mm)
1	7.367	0.305
2	3.556	0.305
3	1.078	0.305
4	7.367	0.406

The kirigami sheet samples were tested on a tensile machine (Instron, 2350 load cell) using the ASTM standard tensile test method for plastics. Force f and axial elongation $l - l_0$ were measured.

Following the tests, a parameter fit was performed on the recorded force-elongation data to estimate the Young's modulus E, yield stress σ_{yield}, and plastic modulus E_h. While these values are given on the Mylar data sheet, it is also known that heating processes (such as the laser cutting process) have an effect on these parameters. For this reason, fits are performed fr E, σ_{yield} and E_h to the experimental data. The initial length l_0 of each structure was approximated as $l_0 = 2mb$. Then, (7.1) and (7.12) relates the length changes $\Delta l = l - l_0$ to the measured axial force f. With this formulation for f, Wolfram Mathematica's implementation of Brent's principal axis algorithm was used to minimize the Root Mean Square Error (RMSE) between the result of the parameterized model expression and the measured extension-force pairs. For feasibility, the operating region of the deployed robot should not approach the kinematic singularity. So, for each design, whose elongation at the kinematic singularity is given by Δl_{lock}, only force-elongation pairs where $\Delta l \leq 0.85\Delta l_{lock}$ were evaluated. Initial guess values for the material parameters were set as $E = 10^9$Pa, $\sigma_{yield} = 10^7$Pa, and $E_h = 10^8$Pa, order-of magnitude guesses based on the Mylar datasheet plots. The fit values for material parameters E, σ_{yield}, and E_h are listed in Table 7.2. The RMSE of force f for the fit was 3.72×10^{-2}N. Plots comparing the measurements to the force-elongation model with fitted parameters are shown in Fig. 7.4.

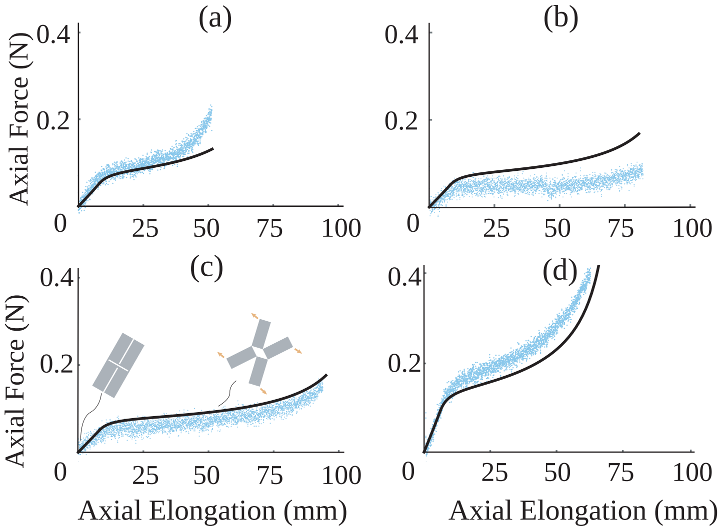

Figure 7.4: Force-elongation measurements (points) and proposed model (lines) for the tested kirigami structure samples. (a) Sample 1, (b) Sample 2, (c) Sample 3, (d) Sample 4.

7.3 Relationship between Elasto-Plastic Properties, Operating Dimensions, and Stiffness

Our design task is to choose the parameters a, b, n, m, t and δ for two benchmarks: (i) achieving an appropriate range of operating lengths Δl_{dep} due to elastic recovery of the structure after a deployment force f_{dep} is applied, and (ii) achieving a stiffness Z that matches or exceeds that of the actuator in its off-state. The force-elongation plot in Fig. 7.5 shows the deployment and operating regions of a sample kirigami structure obtained from both loading and unloading. This plot is used to describe the relationship between elasto-plastic properties, operating dimensions, and structure stiffness. This material and cut pattern are also used for the fabrication of the crawling robot of section 7.4.

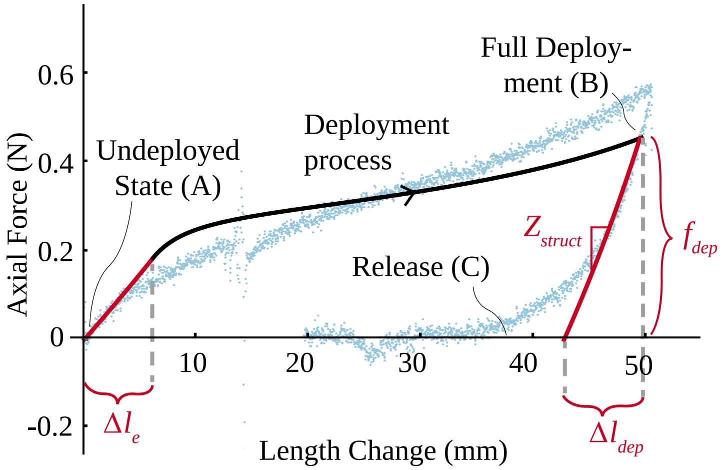

Figure 7.5: Measured (points) and modeled (lines) force-elongation relationship of a plastically deformed kirigami structure with $a = 12.7mm$, $b = 7.366$mm, $n = 10$, $m = 12$, $t = 0.356$mm and $\delta = 0.406$mm, and the material properties E, σ_{yield}, and E_h as given in Table 7.2.

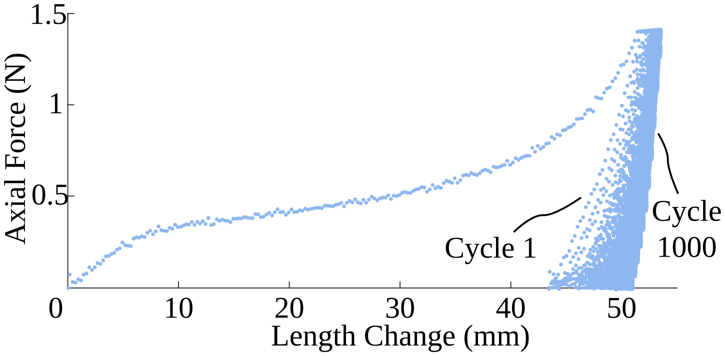

Figure 7.6: Force-controlled cycle experiment on a kirigami structure with $a = 12.7$mm, $b = 7.366$mm, $n = 10$, $m = 12$, and $\delta = 0.406$mm.

Table 7.2: Material Parameters fit from Tensile Experiment

Parameter	Values (Pa)
E	7.343×10^8
σ_{yield}	1.045×10^7
E_h	5.801×10^7

7.3.1 Deployed Length and Elastic Recovery

The desired length range in the structure's deployed state is determined by both the structure kinematics and the deployment force f_{dep}. It is assumed that $\delta << b$, and it is thus negligible when considering the gross deformation of the structure. In the initial compact configuration of the structure, $\theta_b = \pi$, and length $l_0 = 2mb$ (marked as point A on Fig. 7.5). Then, when a force f_{dep} is applied, the opening angle becomes $\theta_b = \theta_{dep}$, and the maximum deployed length $l = l_{dep}$: this configuration is marked by point B on Fig. 7.5. The deployment process is the transition between points A and B. Deployment length l_{dep} and force f_{dep} is determined in terms of θ_{dep} using (7.1) and (7.12) as

$$l_{dep} = 2m(a \cos \frac{\theta_{dep}}{2} + b \sin \frac{\theta_{dep}}{2}). \tag{7.13}$$

$$f_{dep} = \frac{4M(\rho(\theta_{dep}))}{a \sin(\frac{\theta_{dep}}{2}) - b \cos(\frac{\theta_{dep}}{2})}. \tag{7.14}$$

The operating region is between points B and C on Fig. 7.5. Given a deployment force f_{dep}, we are interested in the estimation of length change in springback Δl_{dep}. Taking the deployed point B from Fig. 7.5 as a reference configuration, the force $f_{op} \leq f_{dep}$ is considered as the operational force that changes the opening angle from θ_{dep} to some $\theta_b \in [\theta_{dep}, \pi]$. This force is determined by (7.12), with a perturbation ΔM on the joint bending moment:

$$f_{op}(\theta_{dep}, \theta_b) = 4\frac{M(\theta_{dep}) + \Delta M(\theta_{dep}, \theta_b)}{a \sin(\frac{\theta_b}{2}) - b \cos(\frac{\theta_b}{2})}, \tag{7.15}$$

Since springback of the beam is purely elastic, $\Delta M(\theta_{dep}, \theta_b)$ based on (7.8) is:

$$\Delta M(\theta_{dep}, \theta_b) = E\frac{\delta^3 t}{12}\left[\frac{1}{\rho(\theta_{dep})} - \frac{1}{\rho(\theta_b)}\right]. \tag{7.16}$$

The length change in springback, Δl_{dep} is then the distance between l_{dep} and point C on Fig. 7.5. At point C, the axial force on the structure is zero. Solving (7.15) for $f_{op} = 0$ and replacing M from (7.9) gives the criterion for θ_0 for which $f = 0$:

$$\Delta M(\theta_{dep}, \theta_0) = -\, M(\theta_{dep}). \tag{7.17}$$

Obtaining θ_0 from (7.17), the solution for the operating length range Δl_{dep} is then

$$\Delta l_{dep}(\theta_{dep}, \theta_0) = l_{dep} - 2m\left(a\cos\frac{\theta_0}{2} + b\sin\frac{\theta_0}{2}\right). \tag{7.18}$$

7.3.2 Stiffness

Stiffness of the structure during operation is given by the slope Z (Fig. 7.5) of the operating region of the deployed kirigami structure. For simplicity, this region is approximated as linear. The simplified expression for the structure's springback stiffness is then

$$Z_{simplified} = \frac{f_{dep}}{\Delta l_{dep}}. \tag{7.19}$$

Design methodologies incorporating nonlinearity of the springback stiffness are left to future work.

7.3.3 Cycle Life

Four force-controlled cyclic tensile tests were performed on kirigami samples with $a = 12.7$mm, $b = 7.366$mm, $n = 10$, $m = 12$, and $\delta = 0.406$mm. The maximum force for each test was 0.4N, 0.6N, 0.8N and 1.4N respectively; all within the structure's plastic zone. The maximum velocity was 150mm/min. In each case, the structure

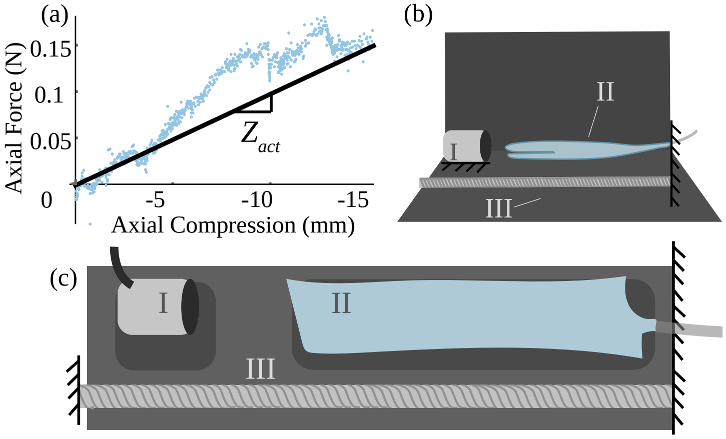

Figure 7.7: Compressive actuator characterization. (a) Compression-Force plot of deflated everting actuator including data (points) and linear stiffness fit (line). (b) Schematic of side view of actuator characterization experiment. (c) Schematic of top view of actuator characterization experiment. In both (b) and (c), I refers to the force sensor (ATI Nano 17), II refers to the soft everting actuator, and III refers to the lead screw.

survived over 1000 cycles. Fig. 7.6 shows the force-elongation curve of the structure in the 1.4N test. Some creep is noticeable: springback on the early cycles is larger than later cycles due to plastic hardening. The apparent springback impedance (slope) appears to increase as cycles continue. Yet, a limit cycle appears to be reached.

7.4 Implementation: Deployable Crawling Robot

In this section, a plastic kirigami structure is designed to match stiffness with a pneumatic actuator, creating a soft deployable crawling robot. Deploying from a relatively flat compact state, the robot is small enough to slide through tight spaces. After deployment, the crawling robot benefits from a longer step length, and body retraction through springback of the plastically deformed structure.

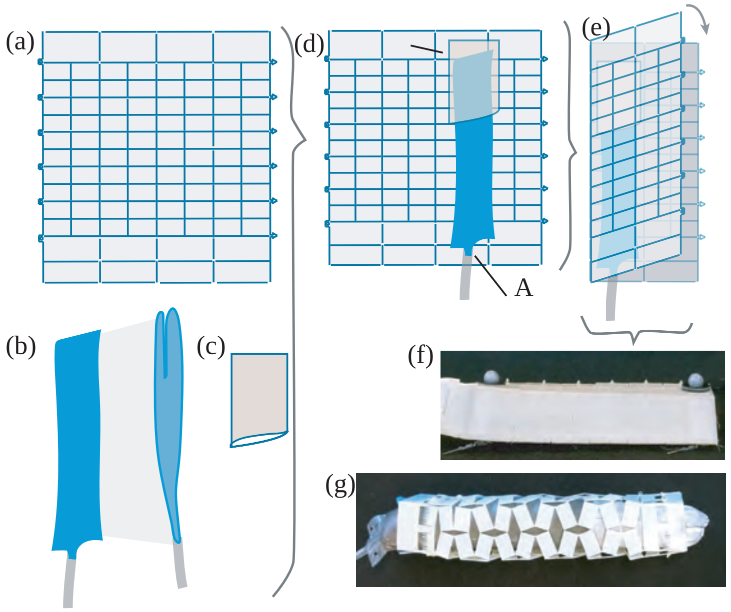

Figure 7.8: Schematic of crawling robot components and assembly. (a) Laser-cut flat kirigami pattern. (b) Everting soft actuator (Left: top view. Right: side view.) (c) Nylon cap. (d) Actuator and cap placement on kirigami pattern. At point A, actuator base is taped to kirigami structure. At point B, fabric cap is taped to kirigami structre. Actuator end is then inserted into fabric cap without tape or glue. (e) Folding of kirigami pattern over cap and actuator. (f) Crawling robot in compact state with motion tracking markers. (g) Crawling robot after deployment (markers not shown).

7.4.1 Actuator Characterization

A soft everting actuator [11] was chosen for integration because of its light weight, and inability to retract after pressure is applied. The actuator was made from heat-sealed polyurethane (Elastollan, BASF), and characterized its force in the operating pressure, as well as its off-state stiffness in recovery at atmospheric pressure. The soft everting actuator was placed in series with a force sensor (ATI Nano 17) and held in place with a paper linear guide. It was inflated to 5kPa, and then deflated back to atmospheric pressure. While at atmospheric pressure, a lead screw system was used to further compress the actuator by 15mm to measure its off-state stiffness. This stiffness test was performed 3 times; data from one of the trials is shown in Fig. 7.7. Again approximating the actuator stiffness as linear, a line was fit to data from each of the 3 trials. The average measured stiffness of the actuator was $Z_{act} = 9.43$ N/m and the maximum force achieved by the actuator was 1.78N. For effective integration with the kirigami structure, the off-state stiffness of the actuator should be less than or equal to the springback stiffness of the structure. In terms of (7.19):

$$Z_{act} \leq \frac{f_{dep}}{\Delta l_{dep}}. \tag{7.20}$$

7.4.2 Structure Design and Assembly

The crawler used a kirigami pattern with $a = 12.7$mm, $b = 7.366$mm, $n = 10$, $m = 12$, and $\delta = 0.406$mm. It was assembled from 4 adjacent patterns with these parameters cut on a BoPET sheet of thickness $t = 0.356$mm. It was then folded the cut sheet into an enclosure (Fig. 7.8). It was assumed that any unfolding during deployment did not result in bending forces on the kirigami sheet.

Two sheets of thermoplastic urethane (BASF Elastollan, 0.11mm sheet) were heat sealed at 145°C to fabricate the actuator. The everting end was heat sealed closed, while a plastic tubing (1.57mm inner diameter) was glued to the other end. The actuator's diameter was 19mm. A fabric cap (Nylon, 70 Denier) was sewn and attached to the front end of the kirigami enclosure to transmit actuator force to the kirigami structure. The everting actuator was coated with talc powder to reduce friction, and placed the folded actuator with its everting end inside the fabric cap. The back end of the actuator and a small segment of the tubing were attached to the back of the enclosure. Anisotropic friction was added to the bottom of the crawler by attaching angled pins to the kirigami structure. The crawler crawled over sheets of polyester felt.

7.4.3 Crawler Experiments

Two experiments were performed on the crawler. In each, it was initially deployed by raising the internal pressure to a specified value P_{dep}, using a pressure regulator

(Festo VEAB). Then, a cycle of amplitude P_{dep} was applied to the actuator at 0.18Hz for 120 seconds. The position of each end of the crawler was recorded at 100Hz using an OptiTrack$^{\text{TM}}$ system with 2 cameras (Prime 17W). Each marker was tracked from its initial location at the beginning of the experiment. A schematic of the experimental setup is given in Fig. 7.9. In the first experiment, P_{dep} was 4kPa. In the second experiment, P_{dep} was 20kPa. The first experiment is referred to as the "short step" experiment, while the second is the "long step" experiment.

Transmission loss of the system was evaluated. For a deployment scenario with no transmission loss, the deployed opening angle θ_{dep} of the crawler structure along all 4 sides and all 4 corners would give us $F_{act,nl} = 8f(\theta_{dep})$ with f given in (7.14). The corresponding extension is then given by (7.7). For a given internal pressure and ideal cylinder-piston model and assuming the TPU wall does not stretch, we expect that the force at the tip of the actuator F_{act} is given by $F_{act,nl} = \pi(D/2)^2P$, where $D = 19$mm. However, there were transmission losses in converting input pressure to force and displacement due to the friction of the everting actuator with itself and the fabric cap. To evaluate the losses, an effective diameter D_e was considered, giving $F_{act,loss} = \pi(D_e/2)^2P$. By performing a test where the actuator was inflated to 18 kPa, an effective diameter of $D_e = 11.6$mm was estimated. This effective diameter was later used to predict the crawler's deformations and step sizes.

Further, the performance of the plasticity model was evaluated in the integrated crawler. Using the design specifications a, b, n, m, t and δ noted above, the model predicted the operating ranges, i.e. step sizes, Δl_{d1} and Δl_{d2}. Then, the size of each step $\Delta l_{d1,n}$ and $\Delta l_{d2,n}$ was measured for both experiments, as well as the permanent length change $l_{d,perm}$ in the long-step experiment.

7.4.4 Results

The motion of the crawler was recorded and related to the plasticity model. In the short-step experiment, the crawler stayed in its elastic region, while in the long-step experiment it reached the plastic region during deployment. Figures 7.10a and b show the measured motion of the crawler body for the first 60 seconds in the short-

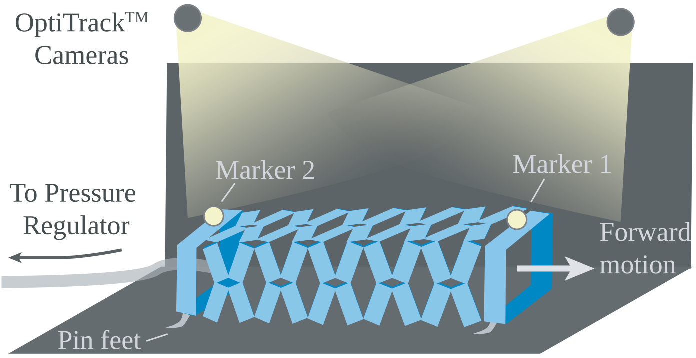

Figure 7.9: Schematic of tracking experiment on crawler. Bent pins on the crawler base enable asymmetric friction on a felt surface. Markers and cameras track the motion of the crawler across the felt.

and long-step experiments, respectively. Specifically,there is net positive (forward) motion of both markers while the motion of each marker in one pressure cycle are annotated. In the short-step experiment, actuator displaced a total of 2.46mm. In the long-step experiment, the actuator displaced a total of 63.3mm. Table 7.3 lists the modeled and average measured step sizes and permanent length changes for each experiment. Using these step sizes, and the corresponding modeled forces (maximum force of 0.12N in the short step experiment, and 0.25N in the long step experiment) the structure stiffness was calculated in the short-step experiment as 32.3 N/m per row of cuts (258.4 N/m overall for the 4-sided structure), and the structure stiffness in the long-step experiment as 33.4 N/m (267.2 N/m overall for the 4-sided cut structure). Slippage the pin on felt substrate is observable by the slight relaxation of the robot's displacement between steps.

7.5 Discussion

This work developed a model for plasticity in kirigami based on plastic deformation of Euler-Bernoulli beams, and validated it with a variety of samples with different design parameters. Fitting material properties gave results within the ex-

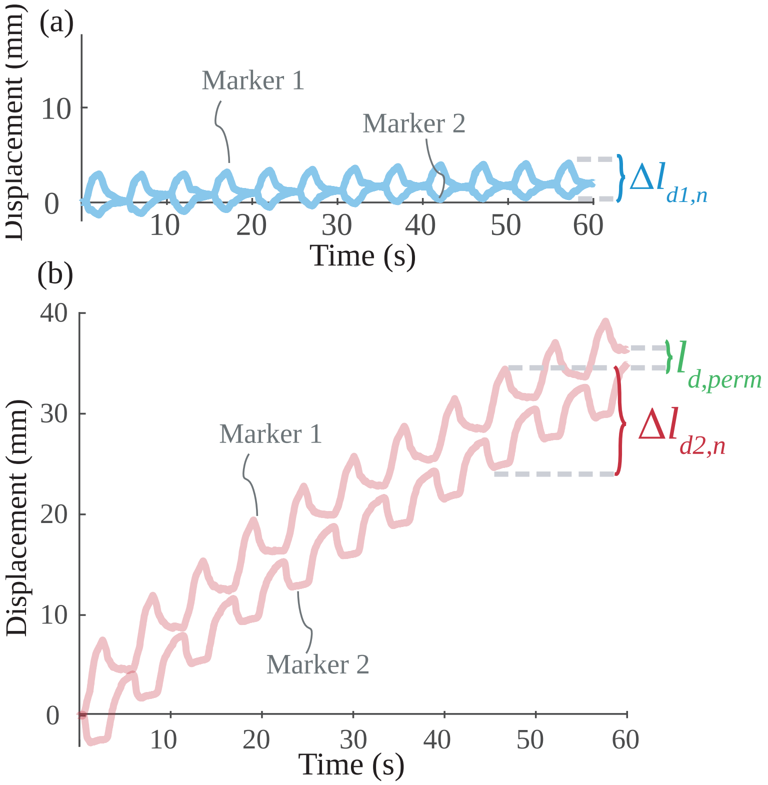

Figure 7.10: Two deployment and operation experiments at different levels of deformation. (a) Position along the crawling robot's forward direction (Fig. 7.9) of the markers over time for the first 60 seconds of the short-step experiment. (b) Position along the crawling robot's forward direction (Fig. 7.9) of the markers over time for the first 60 seconds of the long-step experiment. In blue, the portion of the force-elongation curve corresponding to the short-step experiment, with step length Δl_{d1} is shown. In red, the portion curve corresponding to the long-step experiment, with step length Δl_{d2} is shown.

Table 7.3: Predicted and measured step sizes

		Experiment	
		Short Step (mm)	Long Step (mm)
Δl_{dep}	Predicted	3.88	9.60
	Meas. Mean (Std.)	3.80 (0.02)	8.00 (0.60)
$\Delta l_{dep,perm}$	Predicted	0.00	1.77
	Meas. Mean (Std.)	0.00(0.00)	1.09 (0.34)

pected order of magnitude based on the data sheet of our chosen material. Agreement of these parameters is evidence that the plasticity model functions as intended: there do not appear to be additional hardening or softening phenomena in these structures that affect the parameter fits. The second, more important piece of evidence that the plasticity model functions as intended is agreement between model and experiment across all tested samples (RMSE $<$ 9.4%N), and ability of the model to extrapolate using the same material parameters to a sample of higher thickness (Fig. 7.5). Agreement enables use of the model in a soft, deployable crawling robot. A kirigami structure was designed whose stiffness during elastic recovery exceeded that of the soft everting actuator. When the actuator was cyclically pressurized between a set point and atmospheric pressure, the robot took steps whose sizes were determined by both the deployment level and the pressure input at that specific cycles.

Plastic deformation benefited the crawler: its step size was greater after deployment into the plastic region (the long-step experiment), compared to the short-step experiment where the crawler remained in its elastic region. Cycle life of the structure design used in the crawler exceeded 1000 cycles even at a larger maximum force (1.4N in the cycle test vs. 0.25N in the crawler prototype).

The key limitation of this approach is the irreversible nature of the deployment. After a kirigami structure has been plastically deformed, external forces are required to return it to its initial kinematic configuration. Then, it will no longer have the same loading behavior that it had before plastic deformation. Though kirigami structures have a long cycle life within the deployed range, creep and out-of-range forces could significantly shorten the fatigue life of such a structure. Yet, relatively low expense and ease of manufacturing of kirigami structures make them suitable for single-use deployments followed by bounded repeating loads and deformations. A second limitation of our approach is that it assumes an absence of out-of-plane loading on the kirigami structures. The plasticity theory developed here can, however, be expanded to 3D kinematics and loading. Such an analysis would form the basis for exploring deployable kirigami robots with more complex 3D geometries: flat structures could deploy into complex 3D shapes. Further, the crawling robot presented here is a proof-of-concept prototype. This work can be expanded into the design and control of more sophisticated kirigami robots using different cut patterns than the orthogonal ones given here. One example is the rotating triangle pattern used for deployable shells by [77].

7.6 Conclusion

Usually soft roboticists aim to avoid plastic deformation of parts in robot design. Yet, in materials that harden under strain, plastic deformation can be valuable tool in design and control. In this work, a design method is proposed for soft robotic structures that leverages this plasticity. In easy to fabricate, mechanically programmable kirigami structures, plastic strain hardening can enable deployability from an initially compact state to a larger functional volume, and can increase the range of elastic forces, and range of motion, and therefore work, feasible after deployment. Though this plastic model does not capture tensile behavior of a kirigami structure near its kinematic singularity, it provides strong agreement (within 0.037N) within the operating region, and provides the basis for the deformation-based design methodology shown in the following section.

The work presented here gives a theoretical and experimental basis for designing soft robots that leverage a fuller range of polymer properties by including plastic strain hardening. It is shown that plastic deformation of a kirigami structure can be used to create a deployable robot with no power draw in its deployed state.

It is further shown how plasticity can be leveraged to selectively match stiffness to a soft actuator, enabling robot that is able to crawl uniquely because of these stiffness matches: the soft actuator lengthening the body, and elastic recovery (a.k.a. springback) of the kirigami structure contracting it again. This plasticity basis for soft robot design can be used in a variety of soft robotics applications.

7.7 Summary

Kirigami-patterned mechanisms are an emergent class of structure with auxetic properties that are easy to fabricate and offer the potential to be integrated into deployable robots. A design methodology is proposed for robotic kirigami structures that takes into consideration the deformation, loading, and stiffness of the structure under typical use cases. It is shown how loading-deformation behavior of a kirigami structure can be mechanically programmed by imposing plastic deformation. A model is developed for plasticity in the stretching of a kirigami structure. The creation of kirigami structures that have an increased elastic region, and specified stiffness, in their deployed states is shown. Benefits of such a plastically-deformed structure are shown by integrating it into a soft deployable crawling robot: the kirigami structure matches the stiffness of the soft actuator such that the deployed, coupled behavior serves to mechanically program the gait step size.

CHAPTER 8

Conclusions and Future Work

8.1 Conclusions

The purpose of this dissertation is to introduce and evaluate continuum mechanical models in soft robotics. Robots made from soft and compliant materials have the potential to be useful in exploratory robots, home and assistive robotics, and medical applications. Yet, due to compliance across a soft robot's structure and impedance matching to their environments, soft robots are difficult to characterize within existing robotics frameworks.

The gap between promise and effective implementation of soft robots exists because we lack fundamental tools that can evaluate a soft robotic deformation, rather than rigid body displacement, and contend with blended actuation and structural function across a soft robot. In this dissertation, models of nonlinear elasticity, viscoelasticity, and auxetic behaviour of materials and structures are proposed with specific uses investigated in soft robotics ranging from design to embedded mechanical intelligence. This dissertation partially answered core questions about whether continuum mechanical models can represent soft robotic systems, what physical phenomena should be incorporated into the models, and how physical insight from continuum mechanics can be used to inspire novel robot architectures.

Continuum mechanical models can describe the behaviour of the Fiber-Reinforced Elastomeric Enclosure (FREE), a commonly used soft robotic actuator. The continuum mechanical model presented has certain core functions that previous models had not achieved: in particular, the model allowed for prediction of end force and torque on FREEs based on their fiber angle, kinematic configuration, and internal pressure. In comparison to a linear lumped-parameter model and neural network, the continuum mechanical model generalized best across the eight FREE samples of varying fiber orientation tested, despite having the lowest peak performance. The continuum mechanical model performed with similar normalized error for any combination of data used in parameter fitting. Yet, the lumped-parameter model and neural network achieved a lower normalized error than the continuum mechanical model when trained and tested on the same FREE sample. Because the continuum mechanical model generalizes across the design space, it is ideal for evaluating FREE designs that have not yet been constructed, as well as exploring how changes to material properties, fiber orientation, tube dimensions, kinematic configuration and actuation may affect FREE performance without time-intensive prototyping and data collection.

Adding viscoelasticity, an inherent property of polymers, to continuum mechanical models of FREEs enables new predictions. A new continuum mechanical model for viscoelasticity of both the fiber and elastomer in a FREE was presented (Chapter 4). The work showed the ability to explain new behaviors unaccounted for by the nonlinear elastic theory including a change in the axial force on a FREE from compressive to tensile over time. Both the level of relaxation of a FREE's fiber and elastomer, as well as the timing of the relaxation, can affect FREE behavior. Analysis showed that early, rapid fluctuations in the relative stiffness of the fiber and elastomer result in unusual behaviour of the FREE after a pressure input. It is possible that rapid initial fluctuations of this type cause FREEs to be difficult to control in settings where fast motion is required but feedback sample rate is limited. Experimentation and dynamic analysis of viscoelasticity of FREEs may help to answer emerging questions about how sensing, actuation, and material time-dependence influence the behaviour of FREE-based robots.

Continuum mechanical models can serve as bases for new soft robot architectures. Concepts for soft robots with augmented functionally based reinforcement designs consisting of antagonistically patterned compliant, curved beams were discussed (Chapters 5 and 6). Soft robot functionality due to plastic deformation of kirigami-based auxetic reinforcements was also explored (Chapter 7). The continuum mechanical analysis of the dissertation further showed how the opposing design principles of distributed and lumped compliance may be useful in different soft robotic contexts. The beam-based auxetic actuators (Chapters 5 and 6) utilize distributed compliance as the key operating principle, while the lumped compliance is key to the motion of the kirigami-based soft robot design (Chapter 7). Desirable robotic behaviour are achieved in both of these architectures, despite the differences between compliance strategy and dominant physical phenomena. Networks of beams with distributed compliance allow tunable shape morphing behaviour by modifying the length and orientation of the beams, and strain hardening of lumped-compliant kirigami junctions allows the stiffness of the robot body to be set according to salient conditions.

This work established that continuum mechanical models can be useful in representing the behavior of soft robots, can be a valuable tool in design of new soft robotics architectures, and a that a diverse set of physical phenomena may be important in soft robotics depending on a robot's particular morphology and use context. Models for FREEs, a particular type of soft robot actuator, were investigated (Chapters 2–4). A wide variety of ways that continuum mechanical modeling can inform the design of novel soft robotic concepts were shown as well (Chapters 5–7). The work provides a broad set of physical phenomena that may be useful in soft robotics.

8.2 Contributions

The contributions of this dissertation span theory, experiment, and design synthesis. The specific contributions are:

1. The solution to a nonlinear, elastic continuum mechanical problem reflecting static loading on a FREE. Predictive capability of the solution is shown through comparison to experimental data and design case studies illustrate ways to

match a FREE design to its intended operating conditions.

    (a) A comparison of models connecting FREE loading and deformation that are vastly different in mathematical structure. The comparison includes the nonlinear model that forms the previous contribution.
    (b) A data set spanning the FREE design space, loading space, and configuration space. These measurements enabled the model comparison to take place, as well as future benchmarking studies.

2. A new model for viscoelasticity of FREEs allowing effects of both fiber and matrix relaxation. The model predicts experimental phenomena in FREEs that were not well-explained by previous models. Further, it allows predictive capabilities for FREEs in regimes where their component fiber and elastomer may be made of novel polymers that are highly viscoelastic.

3. Design methodologies for soft robots with deformable surfaces based on auxetic behavior

    (a) A design methodology for patterning compliant beams to create an auxetic reinforcement for soft robots.
    (b) Prototype demonstrations soft, pressurized devices with auxetic reinforcement undergoing novel shape changes and demonstrations of the influence of the a soft device's initial shape on fluid flow within the device.
    (c) A design methodology leveraging the springback phenomenon of plastically deformed auxetic kirigami structures under strain hardening. A crawling robot prototype providing an example of this design methodology.

8.3 Future Work

This dissertation provided partial answers to the questions of: (1) whether continuum mechanical models can describe soft robotic behaviour, (2) which physical phenomena are most important to incorporate into models of soft robots, and (3) how understanding continuum mechanical phenomena may form bases for novel soft robotic architectures. Further investigation should seek to provide complete answers to these questions and highlight particular ways to close the gap between soft robots' promise and implementation. Throughout this work, both theoretical and practical challenges have been uncovered. The particular suggested avenues below may form the next phase of research to make soft robotics useful in the contexts where they have the most promise.

The question of which physical phenomena are most important in soft robotics remains open. While elasticity and visco-elasticity have been shown to play an important role in FREE behaviour, there exist many other physical phenomena that may be crucial for deployment of FREEs, as well as other soft actuators in the wide array of human-assistive and human-collaborative applications where they show promise. One phenomenon which may prove especially impactful is material aging: a study of the long-term behavior of FREEs and other soft robots has not yet been performed, and material aging behaviour may significantly alter a FREE's strength and repeatability. Key potential use cases for soft robots such as home use, exploration, and medical care rely on long-term deployment of soft devices in environments which may have harsh conditions or a lack of availability of maintenance tools. For deployment of soft robots to be useful in these contexts, it is important to understand how aging of polymers, bonding agents, and other components affects soft robots' ability to perform in their respective use cases. Clearer connections between material choice, fabrication, and device performance can help soft robot designers and control engineers develop robots that work reliably outside the lab. A study of long-term behaviour of soft actuators may incorporate a mathematical model of material aging into the continuum mechanical frameworks presented throughout this dissertation. Or, a material aging study may involve repetition of the experimental procedures of Chapters 3 and 5 on the same samples across time to track how fit parameters and behavioral trends evolve. The baseline methods for modeling and evaluating soft actuators provided in this dissertation may form valuable benchmarks for tracking degradation of actuator performance over time.

This dissertation has provided tools for evaluation of FREEs that enable model-based evaluation of loading and deformation in vast design and configuration spaces. These models have reduced the need for physical prototyping and trial and error in development of FREE-based soft robotic systems. Yet, the available design concepts, materials, and use cases for FREEs may still fall outside of the provided experimental validation. Soft robots operating in particular contexts will not necessarily have straightforwardly measurable input-output behaviour using the experimental platforms described here. Future design tools in soft robotics should include practices that take a soft robot's operating environment into account so that appropriate materials and configurations are explored rather than an overly vast design and configuration space.

Finally, the work in this dissertation focuses mostly on the actuator level in soft robotics. The systems observed, such as FREEs and auxetic-reinforced soft actuators, have a single input from the working fluid. Scaling problems abound as we try to place fluidic soft actuators in series and parallel configurations. Maintaining a source of pressurized working fluid becomes challenging as actuators are introduced, and routing the working fluid to the actuators requires increasingly large volumes. Further, draining actuators to atmosphere after pressurization becomes slower and more cumbersome as the drainage pipes get longer and narrower. The result is that seemingly elegant soft, fluidic devices need to have several hidden tethers, air compressors, and pumps to operate. New soft robot design methodologies should incorporate improved, scaled-down hardware for fluid pumping and draining, as well as chemical and combustion technologies that enable untethered pressurization of soft actuators [93]. One candidate for acting as scaled-down control hardware is the auxetic fill zone and pinch point-based design framework presented in through auxetic beam-based actuation (Chapter 6): the thin auxetic surfaces are mounted externally to the enclosure and may act as both structure and control hardware.

The work shown here is an exemplar of how soft robotics benefits from interdisciplinary study. Continuum mechanical theories, which lie outside of traditional robotics, bring new understanding to soft robotics. These insights, as well as insights from other fields that are traditionally outside of robotics, should be leveraged as we continue to develop soft robotic technologies.

BIBLIOGRAPHY

BIBLIOGRAPHY

[1] Yasmin Ansari, Mariangela Manti, Egidio Falotico, Yoan Mollard, Matteo Cianchetti, and Cecilia Laschi. Towards the development of a soft manipulator as an assistive robot for personal care of elderly people. *International Journal of Advanced Robotic Systems*, 14(2):1729881416687132, 2017.

[2] Haruhiko Asada. Lecture notes 2.12 - introduction to robotics, Fall 2013.

[3] Yuanyuan Bai, Yanhui Jiang, Baohong Chen, Choon Chiang Foo, Yongcun Zhou, Feng Xiang, Jinxiong Zhou, Hong Wang, and Zhigang Suo. Cyclic performance of viscoelastic dielectric elastomers with solid hydrogel electrodes. *Applied Physics Letters*, 104(6):062902, 2014.

[4] JR Barber and A Cardou. Intermediate mechanics of materials. *Applied Mechanics Reviews*, 54:B104, 2001.

[5] MILLIARD F Beatty and DO Stalnaker. The poisson function of finite elasticity. *Journal of applied mechanics*, 53(4):807–813, 1986.

[6] JS Bergström and MC Boyce. Deformation of elastomeric networks: relation between molecular level deformation and classical statistical mechanics models of rubber elasticity. *Macromolecules*, 34(3):614–626, 2001.

[7] Antonio Bicchi and Giovanni Tonietti. Fast and" soft-arm" tactics [robot arm design]. *IEEE Robotics & Automation Magazine*, 11(2):22–33, 2004.

[8] Joshua Bishop-Moser and Sridhar Kota. Design and modeling of generalized fiber-reinforced pneumatic soft actuators. *IEEE Transactions on Robotics*, 31 (3):536–545, 2015.

[9] Joshua Bishop-Moser, Girish Krishnan, Charles Kim, and Sridhar Kota. Design of soft robotic actuators using fluid-filled fiber-reinforced elastomeric enclosures in parallel combinations. In *2012 IEEE/RSJ International Conference on Intelligent Robots and Systems*, pages 4264–4269. IEEE, 2012.

[10] Joshua Bishop-Moser, Girish Krishnan, and Sridhar Kota. Force and moment generation of fiber-reinforced pneumatic soft actuators. In *2013 IEEE/RSJ International Conference on Intelligent Robots and Systems*, pages 4460–4465. IEEE, 2013.

[11] Laura H Blumenschein, Lucia T Gan, Jonathan A Fan, Allison M Okamura, and Elliot W Hawkes. A tip-extending soft robot enables reconfigurable and deployable antennas. *IEEE Robotics and Automation Letters*, 3(2):949–956, 2018.

[12] Callie Branyan and Yigit Menguc. Soft snake robots: Investigating the effects of gait parameters on locomotion in complex terrains. In *Intelligent Robots and Systems (IROS), 2018 IEEE/RSJ International Conference on*, 2018.

[13] Daniel Bruder, Audrey Sedal, Joshua Bishop-Moser, Sridhar Kota, and Ram Vasudevan. Model based control of fiber reinforced elastofluidic enclosures. In *Robotics and Automation (ICRA), 2017 IEEE International Conference on*, pages 5539–5544. IEEE, 2017.

[14] Daniel Bruder, C David Remy, and Ram Vasudevan. Nonlinear system identification of soft robot dynamics using koopman operator theory. *arXiv preprint arXiv:1810.06637*, 2018.

[15] Daniel Bruder, Audrey Sedal, Ram Vasudevan, and C David Remy. Force generation by parallel combinations of fiber-reinforced fluid-driven actuators. *arXiv preprint arXiv:1805.00124*, 2018.

[16] Daniel Bruder, Brent Gillespie, C David Remy, and Ram Vasudevan. Modeling and control of soft robots using the koopman operator and model predictive control. *arXiv preprint arXiv:1902.02827*, 2019.

[17] Matteo Bruggi, Valentina Zega, and Alberto Corigliano. Synthesis of auxetic structures using optimization of compliant mechanisms and a micropolar material model. *Structural and multidisciplinary optimization*, 55(1):1–12, 2017.

[18] Andrea Calanca, Riccardo Muradore, and Paolo Fiorini. A review of algorithms for compliant control of stiff and fixed-compliance robots. *IEEE/ASME Transactions on Mechatronics*, 21(2):613–624, 2016.

[19] Bryan Gin-ge Chen, Bin Liu, Arthur A Evans, Jayson Paulose, Itai Cohen, Vincenzo Vitelli, and CD Santangelo. Topological mechanics of origami and kirigami. *Physical review letters*, 116(13):135501, 2016.

[20] Sung-Seen Choi. Characterization of bound rubber of filled styrene-butadiene rubber compounds using pyrolysis-gas chromatography. *Journal of Analytical and Applied Pyrolysis*, 55(2):161–170, 2000.

[21] Ching-Ping Chou and Blake Hannaford. Static and dynamic characteristics of mckibben pneumatic artificial muscles. In *Proceedings of the 1994 IEEE international conference on robotics and automation*, pages 281–286. IEEE, 1994.

[22] Ching-Ping Chou and Blake Hannaford. Measurement and modeling of mckibben pneumatic artificial muscles. *IEEE Transactions on robotics and automation*, 12(1):90–102, 1996.

[23] Matteo Cianchetti, Tommaso Ranzani, Giada Gerboni, Iris De Falco, Cecilia Laschi, and Arianna Menciassi. Stiff-flop surgical manipulator: mechanical design and experimental characterization of the single module. In *2013 IEEE/RSJ International Conference on Intelligent Robots and Systems*, pages 3576–3581. IEEE, 2013.

[24] Matteo Cianchetti, Tommaso Ranzani, Giada Gerboni, Thrishantha Nanayakkara, Kaspar Althoefer, Prokar Dasgupta, and Arianna Menciassi. Soft robotics technologies to address shortcomings in today's minimally invasive surgery: the stiff-flop approach. *Soft robotics*, 1(2):122–131, 2014.

[25] Eulalie Coevoet, Thor Morales-Bieze, Frederick Largilliere, Zhongkai Zhang, Maxime Thieffry, Mario Sanz-Lopez, Bruno Carrez, Damien Marchal, Olivier Goury, Jeremie Dequidt, and Christian. Duriez. Software toolkit for modeling, simulation, and control of soft robots. *Advanced Robotics*, 31(22):1208–1224, 2017.

[26] Fionnuala Connolly, Conor J Walsh, and Katia Bertoldi. Automatic design of fiber-reinforced soft actuators for trajectory matching. *Proceedings of the National Academy of Sciences*, 114(1):51–56, 2017.

[27] Costantino Creton and Matteo Ciccotti. Fracture and adhesion of soft materials: a review. *Reports on Progress in Physics*, 79(4):046601, 2016.

[28] Richard Critchley, Ilaria Corni, Julian A Wharton, Frank C Walsh, Robert JK Wood, and Keith R Stokes. A review of the manufacture, mechanical properties and potential applications of auxetic foams. *physica status solidi (b)*, 250(10): 1963–1982, 2013.

[29] Tory M Cross, Kevin W Hoffer, David P Jones, Patrick B Kirschner, Elizabeth Langvin, and James C Meschter. Auxetic structures and footwear with soles having auxetic structures, August 2 2016. US Patent 9,402,439.

[30] Riccardo De Pascalis, William J Parnell, I David Abrahams, Tom Shearer, Donna M Daly, and David Grundy. The inflation of viscoelastic balloons and hollow viscera. *Proceedings of the Royal Society A*, 474(2218):20180102, 2018.

[31] Raphael Deimel and Oliver Brock. A novel type of compliant and underactuated robotic hand for dexterous grasping. *The International Journal of Robotics Research*, 35(1-3):161–185, 2016.

[32] Cosimo Della Santina, Robert K Katzschmann, Antonio Bicchi, and Daniela Rus. Dynamic control of soft robots interacting with the environment. 2018.

[33] Cosimo Della Santina, Dominic Lakatos, Antonio Bicchi, and Alin Albu-Schäffer. Using nonlinear normal modes for execution of efficient cyclic motions in soft robots. *arXiv preprint arXiv:1806.08389*, 2018.

[34] Hasan Demirkoparan and Thomas J Pence. Swelling of an internally pressurized nonlinearly elastic tube with fiber reinforcing. *International journal of solids and structures*, 44(11-12):4009–4029, 2007.

[35] Marcelo A Dias, Michael P McCarron, Daniel Rayneau-Kirkhope, Paul Z Hanakata, David K Campbell, Harold S Park, and Douglas P Holmes. Kirigami actuators. *Soft matter*, 13(48):9087–9092, 2017.

[36] Krishna Manaswi Digumarti, Andrew T Conn, and Jonathan Rossiter. Euglenoid-inspired giant shape change for highly deformable soft robots. *IEEE Robotics and Automation Letters*, 2(4):2302–2307, 2017.

[37] Khaled Elgeneidy, Niels Lohse, and Michael Jackson. Bending angle prediction and control of soft pneumatic actuators with embedded flex sensors–a data-driven approach. *Mechatronics*, 50:234–247, 2018.

[38] Daniel P Ferris, Joseph M Czerniecki, and Blake Hannaford. An ankle-foot orthosis powered by artificial pneumatic muscles. *Journal of applied biomechanics*, 21(2):189–197, 2005.

[39] DuPont-Teijin Films. *Mylar Polyester Film, Product Information.* 222367D datasheet, 2019.

[40] Yuan-cheng Fung and Pin Tong. *Classical and computational solid mechanics.* World Scientific, 2001.

[41] Hiroshi Furuya. Concept of deployable tensegrity structures in space application. *International Journal of Space Structures*, 7(2):143–151, 1992.

[42] Ignacio Galiana, Frank L Hammond, Robert D Howe, and Marko B Popovic. Wearable soft robotic device for post-stroke shoulder rehabilitation: Identifying misalignments. In *Intelligent Robots and Systems (IROS), 2012 IEEE/RSJ International Conference on*, pages 317–322. IEEE, 2012.

[43] Alan N Gent. *Engineering with rubber: how to design rubber components.* Carl Hanser Verlag GmbH Co KG, 2012.

[44] Mark Gilbertson, Darrin Beekman, Biswaranjan Mohanty, Saeed Hashemi, Sangyoon Lee, James D Van de Ven, and Timothy M Kowalewski. Force analysis and modelling of soft actuators for catheter robots. In *ASME 2016 Dynamic Systems and Control Conference, DSCC 2016*, page 78. American Society of Mechanical Engineers, 2016.

[45] Mark D Gilbertson, Gillian McDonald, Gabriel Korinek, James D Van de Ven, and Timothy M Kowalewski. Serially actuated locomotion for soft robots in tube-like environments. *IEEE Robotics and Automation Letters*, 2(2):1140–1147, 2017.

[46] Morgan T Gillespie, Charles M Best, Eric C Townsend, David Wingate, and Marc D Killpack. Learning nonlinear dynamic models of soft robots for model predictive control with neural networks. In *2018 IEEE International Conference on Soft Robotics (RoboSoft)*, pages 39–45. IEEE, 2018.

[47] Michele Giorelli, Federico Renda, Gabriele Ferri, and Cecilia Laschi. A feed-forward neural network learning the inverse kinetics of a soft cable-driven manipulator moving in three-dimensional space. In *Intelligent Robots and Systems (IROS), 2013 IEEE/RSJ International Conference on*, pages 5033–5039. IEEE, 2013.

[48] Michele Giorelli, Federico Renda, Marcello Calisti, Andrea Arienti, Gabriele Ferri, and Cecilia Laschi. Neural network and jacobian method for solving the inverse statics of a cable-driven soft arm with nonconstant curvature. *IEEE Transactions on Robotics*, 31(4):823–834, 2015.

[49] Francesco Giorgio-Serchi, Andrea Arienti, Francesco Corucci, Michele Giorelli, and Cecilia Laschi. Hybrid parameter identification of a multi-modal underwater soft robot. *Bioinspiration & biomimetics*, 12(2):025007, 2017.

[50] Nathaniel N Goldberg, Xiaonan Huang, Carmel Majidi, Alyssa Novelia, Oliver M O'Reilly, Derek A Paley, and William L Scott. On planar discrete elastic rod models for the locomotion of soft robots. *Soft robotics*, 6(5):595–610, 2019.

[51] Alain Goriely and Michael Tabor. Rotation, inversion and perversion in anisotropic elastic cylindrical tubes and membranes. *Proceedings of the Royal Society A: Mathematical, Physical and Engineering Sciences*, 469(2153): 20130011, 2013.

[52] Olivier Goury and Christian Duriez. Fast, generic, and reliable control and simulation of soft robots using model order reduction. *IEEE Transactions on Robotics*, (99):1–12, 2018.

[53] Joseph D Greer, Tania K Morimoto, Allison M Okamura, and Elliot W Hawkes. Series pneumatic artificial muscles (spams) and application to a soft continuum robot. In *2017 IEEE International Conference on Robotics and Automation (ICRA)*, pages 5503–5510. IEEE, 2017.

[54] Guo-Ying Gu, Ujjaval Gupta, Jian Zhu, Li-Min Zhu, and Xiangyang Zhu. Modeling of viscoelastic electromechanical behavior in a soft dielectric elastomer actuator. *IEEE Transactions on Robotics*, 33(5):1263–1271, 2017.

[55] ZY Guo, XQ Peng, and B Moran. Mechanical response of neo-hookean fiber reinforced incompressible nonlinearly elastic solids. *International journal of solids and structures*, 44(6):1949–1969, 2007.

[56] Hai-Chao Han, Jennifer KW Chesnutt, Justin R Garcia, Qin Liu, and Qi Wen. Artery buckling: new phenotypes, models, and applications. *Annals of biomedical engineering*, 41(7):1399–1410, 2013.

[57] Elliot W Hawkes, Laura H Blumenschein, Joseph D Greer, and Allison M Okamura. A soft robot that navigates its environment through growth. *Science Robotics*, 2(8):eaan3028, 2017.

[58] C Heinrich, M Aldridge, AS Wineman, J Kieffer, Anthony M Waas, and K Shahwan. The influence of the representative volume element (rve) size on

the homogenized response of cured fiber composites. *Modelling and simulation in materials science and engineering*, 20(7):075007, 2012.

[59] Rodney Hill. *The mathematical theory of plasticity*, volume 11. Oxford university press, 1998.

[60] Tatsuhiro Hiramitsu, Koichi Suzumori, Hiroyuki Nabae, and Gen Endo. Experimental evaluation of textile mechanisms made of artificial muscles. In *2019 2nd IEEE International Conference on Soft Robotics (RoboSoft)*, pages 1–6. IEEE, 2019.

[61] Gerhard A Holzapfel. Structural and numerical models for the (visco) elastic response of arterial walls with residual stresses. In *Biomechanics of Soft Tissue in Cardiovascular Systems*, pages 109–184. Springer, 2003.

[62] Gerhard A Holzapfel, Thomas C Gasser, and Ray W Ogden. A new constitutive framework for arterial wall mechanics and a comparative study of material models. *Journal of elasticity and the physical science of solids*, 61(1-3):1–48, 2000.

[63] Andrew D Horchler, Akhil Kandhari, Kathryn A Daltorio, Kenneth C Moses, Kayla B Andersen, Hillary Bunnelle, Joseph Kershaw, William H Tavel, Richard J Bachmann, Hillel J Chiel, et al. Worm-like robotic locomotion with a compliant modular mesh. In *Conference on Biomimetic and Biohybrid Systems*, pages 26–37. Springer, 2015.

[64] Cornelius O Horgan and Giuseppe Saccomandi. A new constitutive theory for fiber-reinforced incompressible nonlinearly elastic solids. *Journal of the Mechanics and Physics of Solids*, 53(9):1985–2015, 2005.

[65] A Hošovskỳ, J Pitel', K Židek, M Tóthová, J Sárosi, and L Cveticanin. Dynamic characterization and simulation of two-link soft robot arm with pneumatic muscles. *Mechanism and Machine Theory*, 103:98–116, 2016.

[66] Doh-Gyu Hwang and Michael D Bartlett. Tunable mechanical metamaterials through hybrid kirigami structures. *Scientific reports*, 8(1):3378, 2018.

[67] Filip Ilievski, Aaron D Mazzeo, Robert F Shepherd, Xin Chen, and George M Whitesides. Soft robotics for chemists. *Angewandte Chemie*, 123(8):1930–1935, 2011.

[68] Midori Isobe and Ko Okumura. Initial rigid response and softening transition of highly stretchable kirigami sheet materials. *Scientific reports*, 6:24758, 2016.

[69] Hao Jiang, Xinghua Liu, Xiaotong Chen, Zhanchi Wang, Yusong Jin, and Xiaoping Chen. Design and simulation analysis of a soft manipulator based on honeycomb pneumatic networks. In *2016 IEEE International Conference on Robotics and Biomimetics (ROBIO)*, pages 350–356. IEEE, 2016.

[70] Dejun Jing, James A Ashton-Miller, and John OL DeLancey. A subject-specific anisotropic visco-hyperelastic finite element model of female pelvic floor stress and strain during the second stage of labor. *Journal of biomechanics*, 45(3): 455–460, 2012.

[71] Robert K Katzschmann, Andrew D Marchese, and Daniela Rus. Autonomous object manipulation using a soft planar grasping manipulator. *Soft robotics*, 2 (4):155–164, 2015.

[72] DongWook Kim and Yong-Lae Park. Contact localization and force estimation of soft tactile sensors using artificial intelligence. In *2018 IEEE/RSJ International Conference on Intelligent Robots and Systems (IROS)*, pages 7480–7485. IEEE, 2018.

[73] Glenn K Klute and Blake Hannaford. Accounting for elastic energy storage in mckibben artificial muscle actuators. *Journal of dynamic systems, measurement, and control*, 122(2):386–388, 2000.

[74] Glenn K Klute, Joseph M Czerniecki, and Blake Hannaford. Mckibben artificial muscles: pneumatic actuators with biomechanical intelligence. In *1999 IEEE/ASME International Conference on Advanced Intelligent Mechatronics (Cat. No. 99TH8399)*, pages 221–226. IEEE, 1999.

[75] Jeffrey R Koller, Deanna H Gates, Daniel P Ferris, and C David Remy. 'body-in-the-loop'optimization of assistive robotic devices: A validation study. In *Robotics: Science and Systems*, 2016.

[76] Mina Konaković-Luković, Pavle Konaković, and Mark Pauly. Computational design of deployable auxetic shells. *AAG 2018, Advances in Architectural Geometry 2018*, pages 94–111, 2011.

[77] Mina Konaković-Luković, Julian Panetta, Keenan Crane, and Mark Pauly. Rapid deployment of curved surfaces via programmable auxetics. *ACM Transactions on Graphics (TOG)*, 37(4):106, 2018.

[78] Sridhar Kota. Shape-shifting things to come. *Scientific American*, 310(5): 58–65, 2014.

[79] Girish Krishnan, Joshua Bishop-Moser, Charles Kim, and Sridhar Kota. Kinematics of a generalized class of pneumatic artificial muscles. *Journal of Mechanisms and Robotics*, 7(4), 2015.

[80] Roderic Lakes. Foam structures with a negative poisson's ratio. *Science*, 235: 1038–1041, 1987.

[81] Roderic Lakes. Deformation mechanisms in negative poisson's ratio materials: structural aspects. *Journal of Materials Science*, 26(9):2287–2292, 1991.

[82] Roderic S Lakes. Negative-poisson's-ratio materials: auxetic solids. *Annual review of materials research*, 47, 2017.

[83] Christina Larson, B Peele, S Li, S Robinson, M Totaro, L Beccai, B Mazzolai, and R Shepherd. Highly stretchable electroluminescent skin for optical signaling and tactile sensing. *Science*, 351(6277):1071–1074, 2016.

[84] Cecilia Laschi, Matteo Cianchetti, Barbara Mazzolai, Laura Margheri, Maurizio Follador, and Paolo Dario. Soft robot arm inspired by the octopus. *Advanced Robotics*, 26(7):709–727, 2012.

[85] Arnaud Lazarus and Pedro M Reis. Soft actuation of structured cylinders through auxetic behavior. *Advanced Engineering Materials*, 17(6):815–820, 2015.

[86] Young Min Lee, Hyuk Jin Lee, Hyung Pil Moon, Hyouk Ryeol Choi, and Ja Choon Koo. Azimuthal shear deformation of a novel soft fiber-reinforced rotary pneumatic actuator. In *2019 International Conference on Robotics and Automation (ICRA)*, pages 7409–7414. IEEE, 2019.

[87] BM Lempriere. Poisson's ratio in orthotropic materials. *AIAA Journal*, 6(11): 2226–2227, 1968.

[88] Jeffrey Ian Lipton, Robert MacCurdy, Zachary Manchester, Lillian Chin, Daniel Cellucci, and Daniela Rus. Handedness in shearing auxetics creates rigid and compliant structures. *Science*, 360(6389):632–635, 2018.

[89] Chih-Hsing Liu, Chen-Hua Chiu, Ta-Lun Chen, Tzu-Yang Pai, Yang Chen, and Mao-Cheng Hsu. A soft robotic gripper module with 3d printed compliant fingers for grasping fruits. In *2018 IEEE/ASME International Conference on Advanced Intelligent Mechatronics (AIM)*, pages 736–741. IEEE, 2018.

[90] Qin Liu, Qi Wen, Mohammad Mottahedi, and Hai-Chao Han. Artery buckling analysis using a four-fiber wall model. *Journal of biomechanics*, 47(11):2790–2796, 2014.

[91] XinJiang Lu, Kai Wang, and TeTe Hu. Development of an annelid-like peristaltic crawling soft robot using dielectric elastomer actuators. *Bioinspiration & Biomimetics*, 2020.

[92] Carmel Majidi. Soft robotics: a perspective—current trends and prospects for the future. *Soft Robotics*, 1(1):5–11, 2014.

[93] Carmel Majidi. Soft-matter engineering for soft robotics. *Advanced Materials Technologies*, 4(2):1800477, 2019.

[94] Carmel Majidi, Robert F Shepherd, Rebecca K Kramer, George M Whitesides, and Robert J Wood. Influence of surface traction on soft robot undulation. *The International Journal of Robotics Research*, 32(13):1577–1584, 2013.

[95] Andrew D Marchese, Konrad Komorowski, Cagdas D Onal, and Daniela Rus. Design and control of a soft and continuously deformable 2d robotic manipulation system. In *2014 IEEE international conference on robotics and automation (ICRA)*, pages 2189–2196. IEEE, 2014.

[96] Andrew D Marchese, Cagdas D Onal, and Daniela Rus. Autonomous soft robotic fish capable of escape maneuvers using fluidic elastomer actuators. *Soft Robotics*, 1(1):75–87, 2014.

[97] Andrew G Mark, Stefano Palagi, Tian Qiu, and Peer Fischer. Auxetic metamaterial simplifies soft robot design. In *2016 IEEE International Conference on Robotics and Automation (ICRA)*, pages 4951–4956. Ieee, 2016.

[98] Ramses V Martinez, Jamie L Branch, Carina R Fish, Lihua Jin, Robert F Shepherd, Rui MD Nunes, Zhigang Suo, and George M Whitesides. Robotic tentacles with three-dimensional mobility based on flexible elastomers. *Advanced materials*, 25(2):205–212, 2013.

[99] William McMahan, V Chitrakaran, M Csencsits, D Dawson, Ian D Walker, Bryan A Jones, M Pritts, D Dienno, M Grissom, and Christopher D Rahn. Field trials and testing of the octarm continuum manipulator. In *Robotics and Automation, 2006. ICRA 2006. Proceedings 2006 IEEE International Conference on*, pages 2336–2341. IEEE, 2006.

[100] José Merodio, Giuseppe Saccomandi, and Ivonne Sgura. The rectilinear shear of fiber-reinforced incompressible non-linearly elastic solids. *International Journal of Non-Linear Mechanics*, 42(2):342–354, 2007.

[101] Seyed M Mirvakili, Douglas Sim, Ian W Hunter, and Robert Langer. Actuation of untethered pneumatic artificial muscles and soft robots using magnetically induced liquid-to-gas phase transitions. *Science Robotics*, 5(41), 2020.

[102] Melvin Mooney. A theory of large elastic deformation. *Journal of applied physics*, 11(9):582–592, 1940.

[103] Bobak Mosadegh, Panagiotis Polygerinos, Christoph Keplinger, Sophia Wennstedt, Robert F Shepherd, Unmukt Gupta, Jongmin Shim, Katia Bertoldi, Conor J Walsh, and George M Whitesides. Pneumatic networks for soft robotics that actuate rapidly. *Advanced functional materials*, 24(15): 2163–2170, 2014.

[104] Philip Moseley, Juan Manuel Florez, Harshal Arun Sonar, Gunjan Agarwal, William Curtin, and Jamie Paik. Modeling, design, and development of soft pneumatic actuators with finite element method. *Advanced Engineering Materials*, 18(6):978–988, 2016.

[105] Seri Mastura Mustaza, Yahya Elsayed, Constantina Lekakou, Chakravarthini Saaj, and Jan Fras. Dynamic modeling of fiber-reinforced soft manipulator: A visco-hyperelastic material-based continuum mechanics approach. *Soft robotics*, 2019.

[106] Srinivas Neppalli, B Jones, William McMahan, V Chitrakaran, I Walker, M Pritts, M Csencsits, C Rahn, and M Grissom. Octarm-a soft robotic manipulator. In *2007 IEEE/RSJ International Conference on Intelligent Robots and Systems*, pages 2569–2569. IEEE, 2007.

[107] Raymond W Ogden. *Non-linear elastic deformations.* Courier Corporation, 1997.

[108] Cagdas D Onal and Daniela Rus. Autonomous undulatory serpentine locomotion utilizing body dynamics of a fluidic soft robot. *Bioinspiration & biomimetics*, 8(2):026003, 2013.

[109] Daniel Ortiz, Nick Gravish, and Michael T Tolley. Soft robot actuation strategies for locomotion in granular substrates. *IEEE Robotics and Automation Letters*, 4(3):2630–2636, 2019.

[110] Julian Panetta, Mina Konaković-Luković, Florin Isvoranu, E Bouleau, and M Pauly. X-shells: a new class of deployable beam structures. *ACM Transactions on Graphics (TOG)*, 38(4):83, 2019.

[111] Yong-Lae Park, Bor-rong Chen, Néstor O Pérez-Arancibia, Diana Young, Leia Stirling, Robert J Wood, Eugene C Goldfield, and Radhika Nagpal. Design and control of a bio-inspired soft wearable robotic device for ankle–foot rehabilitation. *Bioinspiration & biomimetics*, 9(1):016007, 2014.

[112] William J Parnell and Riccardo De Pascalis. Soft metamaterials with dynamic viscoelastic functionality tuned by pre-deformation. *Philosophical Transactions of the Royal Society A*, 377(2144):20180072, 2019.

[113] E Peña, B Calvo, MA Martínez, and M Doblaré. An anisotropic visco-hyperelastic model for ligaments at finite strains. formulation and computational aspects. *International Journal of Solids and Structures*, 44(3-4):760–778, 2007.

[114] XQ Peng and Jian Cao. A continuum mechanics-based non-orthogonal constitutive model for woven composite fabrics. *Composites part A: Applied Science and manufacturing*, 36(6):859–874, 2005.

[115] Michael P Perrone and Leon N Cooper. When networks disagree: Ensemble methods for hybrid neural networks. Technical report, BROWN UNIV PROVIDENCE RI INST FOR BRAIN AND NEURAL SYSTEMS, 1992.

[116] Michael Philen. Fluidic flexible matrix composite semi-active vibration isolation mounts. *Journal of intelligent material systems and structures*, 23(3): 353–363, 2012.

[117] Ryan St Pierre and Sarah Bergbreiter. Toward autonomy in sub-gram terrestrial robots. *Annual Review of Control, Robotics, and Autonomous Systems*, 2019.

[118] AC Pipkin and RS Rivlin. Minimum-weight design for pressure vessels reinforced with inextensible fibers. 1963.

[119] AC Pipkin and TG Rogers. A non-linear integral representation for viscoelastic behaviour. *Journal of the Mechanics and Physics of Solids*, 16(1):59–72, 1968.

[120] Panagiotis Polygerinos, Stacey Lyne, Zheng Wang, Luis Fernando Nicolini, Bobak Mosadegh, George M Whitesides, and Conor J Walsh. Towards a soft pneumatic glove for hand rehabilitation. In *2013 IEEE/RSJ International Conference on Intelligent Robots and Systems*, pages 1512–1517. IEEE, 2013.

[121] Panagiotis Polygerinos, Zheng Wang, Kevin C Galloway, Robert J Wood, and Conor J Walsh. Soft robotic glove for combined assistance and at-home rehabilitation. *Robotics and Autonomous Systems*, 73:135–143, 2015.

[122] Panagiotis Polygerinos, Zheng Wang, Johannes TB Overvelde, Kevin C Galloway, Robert J Wood, Katia Bertoldi, and Conor J Walsh. Modeling of soft fiber-reinforced bending actuators. *IEEE Transactions on Robotics*, 31(3):778–789, 2015.

[123] D Prall and RS Lakes. Properties of a chiral honeycomb with a poisson's ratio of -1. *International Journal of Mechanical Sciences*, 39(3):305–314, 1997.

[124] Michael B Pritts and Christopher D Rahn. Design of an artificial muscle continuum robot. In *Robotics and Automation, 2004. Proceedings. ICRA'04. 2004 IEEE International Conference on*, volume 5, pages 4742–4746. IEEE, 2004.

[125] GY Qiu and TJ Pence. Loss of ellipticity in plane deformation of a simple directionally reinforced incompressible nonlinearly elastic solid. *Journal of Elasticity*, 49(1):31–63, 1997.

[126] Ahmad Rafsanjani and Katia Bertoldi. Buckling-induced kirigami. *Physical Review Letters*, 118(8):084301, 2017.

[127] Ahmad Rafsanjani, Yuerou Zhang, Bangyuan Liu, Shmuel M Rubinstein, and Katia Bertoldi. Kirigami skins make a simple soft actuator crawl. *Science Robotics*, 3(15):eaar7555, 2018.

[128] Tommaso Ranzani, Giada Gerboni, Matteo Cianchetti, and A Menciassi. A bioinspired soft manipulator for minimally invasive surgery. *Bioinspiration & biomimetics*, 10(3):035008, 2015.

[129] Thierry Rey, G Chagnon, J-B Le Cam, and Denis Favier. Influence of the temperature on the mechanical behaviour of filled and unfilled silicone rubbers. *Polymer Testing*, 32(3):492–501, 2013.

[130] RS Rivlin. Large elastic deformations of isotropic materials iv. further developments of the general theory. *Philosophical Transactions of the Royal Society of London. Series A, Mathematical and Physical Sciences*, 241(835):379–397, 1948.

[131] RSl Rivlin. Large elastic deformations of isotropic materials. i. fundamental concepts. *Philosophical Transactions of the Royal Society of London. Series A, Mathematical and Physical Sciences*, 240(822):459–490, 1948.

[132] Matthew A Robertson, Hamed Sadeghi, Juan Manuel Florez, and Jamie Paik. Soft pneumatic actuator fascicles for high force and reliability. *Soft robotics*, 4 (1):23–32, 2017.

[133] Tryfan G Rogers and Allen C Pipkin. Asymmetric relaxation and compliance matrices in linear viscoelasticity. *Zeitschrift für angewandte Mathematik und Physik ZAMP*, 14(4):334–343, 1963.

[134] Elliott J Rouse, Luke M Mooney, and Hugh M Herr. Clutchable series-elastic actuator: Implications for prosthetic knee design. *The International Journal of Robotics Research*, 33(13):1611–1625, 2014.

[135] Daniela Rus and Michael T Tolley. Design, fabrication and control of soft robots. *Nature*, 521(7553):467, 2015.

[136] SM Hadi Sadati, Seyedeh Elnaz Naghibi, Ali Shiva, Ian D Walker, Kaspar Althoefer, and Thrishantha Nanayakkara. Mechanics of continuum manipulators, a comparative study of five methods with experiments. In *Annual Conference Towards Autonomous Robotic Systems*, pages 686–702. Springer, 2017.

[137] Mohammad Sanami, Naveen Ravirala, Kim Alderson, and Andrew Alderson. Auxetic materials for sports applications. *Procedia Engineering*, 72:453–458, 2014.

[138] Harpreet Sareen, Udayan Umapathi, Patrick Shin, Yasuaki Kakehi, Jifei Ou, Hiroshi Ishii, and Pattie Maes. Printflatables: printing human-scale, functional and dynamic inflatable objects. In *Proceedings of the 2017 CHI Conference on Human Factors in Computing Systems*, pages 3669–3680. ACM, 2017.

[139] Daisuke Sasaki, Toshiro Noritsugu, and Masahiro Takaiwa. Development of active support splint driven by pneumatic soft actuator (assist). In *Proceedings of the 2005 IEEE international conference on robotics and automation*, pages 520–525. IEEE, 2005.

[140] Sreeshankar Satheeshbabu. Open loop position control of soft continuum arm using deep reinforcement learning. 2018.

[141] Sreeshankar Satheeshbabu and Girish Krishnan. Designing systems of fiber reinforced pneumatic actuators using a pseudo-rigid body model. In *Intelligent Robots and Systems (IROS), 2017 IEEE/RSJ International Conference on*, pages 1201–1206. IEEE, 2017.

[142] Lloyd H Scarborough, Christopher D Rahn, and Edward C Smith. Fluidic composite tunable vibration isolators. *Journal of Vibration and Acoustics*, 134 (1):011010, 2012.

[143] Audrey Sedal, Daniel Bruder, Joshua Bishop-Moser, Ram Vasudevan, and Sridhar Kota. A continuum model for fiber-reinforced soft robot actuators. *Journal of Mechanisms and Robotics*, 10(2):024501, 2018.

[144] Audrey Sedal, Michael Fisher, Joshua Bishop-Moser, Alan Wineman, and Sridhar Kota. Auxetic sleeves for soft actuators with kinematically varied surfaces. In *2018 IEEE/RSJ International Conference on Intelligent Robots and Systems (IROS)*, pages 464–471. IEEE, 2018.

[145] Audrey Sedal, Alan Wineman, R Brent Gillespie, and C David Remy. Comparison and experimental validation of predictive models for soft, fiber-reinforced actuators. *arXiv preprint arXiv:1902.00054*, 2019.

[146] Sangok Seok, Cagdas Denizel Onal, Kyu-Jin Cho, Robert J Wood, Daniela Rus, and Sangbae Kim. Meshworm: a peristaltic soft robot with antagonistic nickel titanium coil actuators. *IEEE/ASME Transactions on mechatronics*, 18 (5):1485–1497, 2012.

[147] Sangok Seok, Cagdas Denizel Onal, Kyu-Jin Cho, Robert J Wood, Daniela Rus, and Sangbae Kim. Meshworm: a peristaltic soft robot with antagonistic nickel titanium coil actuators. *IEEE/ASME Transactions on mechatronics*, 18 (5):1485–1497, 2013.

[148] Ying Shan, Michael P Philen, Charles E Bakis, Kon-Well Wang, and Christopher D Rahn. Nonlinear-elastic finite axisymmetric deformation of flexible matrix composite membranes under internal pressure and axial force. *Composites Science and Technology*, 66(15):3053–3063, 2006.

[149] Ying Shan, Michael Philen, Amir Lotfi, Suyi Li, Charles E Bakis, Christopher D Rahn, and Kon-Well Wang. Variable stiffness structures utilizing fluidic flexible matrix composites. *Journal of Intelligent Material Systems and Structures*, 20(4):443–456, 2009.

[150] Robert F Shepherd, Filip Ilievski, Wonjae Choi, Stephen A Morin, Adam A Stokes, Aaron D Mazzeo, Xin Chen, Michael Wang, and George M Whitesides. Multigait soft robot. *Proceedings of the national academy of sciences*, 108(51): 20400–20403, 2011.

[151] Robert F Shepherd, Adam A Stokes, Jacob Freake, Jabulani Barber, Phillip W Snyder, Aaron D Mazzeo, Ludovico Cademartiri, Stephen A Morin, and George M Whitesides. Using explosions to power a soft robot. *Angewandte Chemie*, 125(10):2964–2968, 2013.

[152] Jongmin Shim, Sicong Shan, Andrej Košmrlj, Sung H Kang, Elizabeth R Chen, James C Weaver, and Katia Bertoldi. Harnessing instabilities for design of soft reconfigurable auxetic/chiral materials. *Soft Matter*, 9(34):8198–8202, 2013.

[153] KB Shimoga and AA Goldenberg. Soft robotic fingertips: part ii: modeling and impedance regulation. *The International journal of robotics research*, 15 (4):335–350, 1996.

[154] Gaurav Singh and Girish Krishnan. A constrained maximization formulation to analyze deformation of fiber reinforced elastomeric actuators. *Smart Materials and Structures*, 26(6):065024, 2017.

[155] Gaurav Singh, Chenzhang Xiao, Elizabeth T Hsiao-Wecksler, and Girish Krishnan. Design and analysis of coiled fiber reinforced soft pneumatic actuator. *Bioinspiration & biomimetics*, 13(3):036010, 2018.

[156] GF Smith and RS Rivlin. The strain-energy function for anisotropic elastic materials. In *Collected Papers of RS Rivlin*, pages 541–559. Springer, 1997.

[157] AJM Spencer. Part iii. theory of invariants. *Continuum physics*, 1:239–353, 1971.

[158] Sinterit Sp.zo.o. Flexa grey. URL `https://www.sinterit.com/wp-content/uploads/2014/05/Flexa-Grey_Specification.pdf?x32275`.

[159] Niko Sünderhauf, Oliver Brock, Walter Scheirer, Raia Hadsell, Dieter Fox, Jürgen Leitner, Ben Upcroft, Pieter Abbeel, Wolfram Burgard, Michael Milford, and Peter. Corke. The limits and potentials of deep learning for robotics. *The International Journal of Robotics Research*, 37(4-5):405–420, 2018.

[160] Koichi Suzumori, Satoshi Endo, Takefumi Kanda, Naomi Kato, and Hiroyoshi Suzuki. A bending pneumatic rubber actuator realizing soft-bodied manta swimming robot. In *Proceedings 2007 IEEE International Conference on Robotics and Automation*, pages 4975–4980. IEEE, 2007.

[161] Saiganesh Swaminathan, Michael Rivera, Runchang Kang, Zheng Luo, Kadri Bugra Ozutemiz, and Scott E Hudson. Input, output and construction methods for custom fabrication of room-scale deployable pneumatic structures. *Proceedings of the ACM on Interactive, Mobile, Wearable and Ubiquitous Technologies*, 3(2):62, 2019.

[162] Yichao Tang and Jie Yin. Design of cut unit geometry in hierarchical kirigami-based auxetic metamaterials for high stretchability and compressibility. *Extreme Mechanics Letters*, 12:77–85, 2017.

[163] Thomas George Thuruthel, Egidio Falotico, Federico Renda, and Cecilia Laschi. Model-based reinforcement learning for closed-loop dynamic control of soft robotic manipulators. *IEEE Transactions on Robotics*, 2018.

[164] Bertrand Tondu and Pierre Lopez. Modeling and control of mckibben artificial muscle robot actuators. *IEEE control systems*, 20(2):15–38, 2000.

[165] Barry A Trimmer, Ann E Takesian, Brian M Sweet, Chris B Rogers, Daniel C Hake, and Daniel J Rogers. Caterpillar locomotion: a new model for soft-bodied climbing and burrowing robots. In *7th International Symposium on Technology and the Mine Problem*, volume 1, pages 1–10. Mine Warfare Association Monterey, CA, 2006.

[166] Deepak Trivedi, Christopher D Rahn, William M Kier, and Ian D Walker. Soft robotics: Biological inspiration, state of the art, and future research. *Applied bionics and biomechanics*, 5(3):99–117, 2008.

[167] JD Ulmer, WM Hess, and VE Chirico. The effects of carbon black on rubber hysteresis. *Rubber Chemistry and Technology*, 47(4):729–757, 1974.

[168] Naveen Kumar Uppalapati, Gaurav Singh, and Girish Krishnan. Parameter estimation and modeling of a pneumatic continuum manipulator with asymmetric building blocks. In *2018 IEEE International Conference on Soft Robotics (RoboSoft)*, pages 528–533. IEEE, 2018.

[169] Michaël Van Damme, Pieter Beyl, Bram Vanderborght, Ronald Van Ham, Innes Vanderniepen, Rino Versluys, Frank Daerden, and Dirk Lefeber. Modeling hysteresis in pleated pneumatic artificial muscles. In *2008 IEEE Conference on Robotics, Automation and Mechatronics*, pages 471–476. IEEE, 2008.

[170] Allan Joshua Veale, Sheng Quan Xie, and Iain Alexander Anderson. Accurate multivariable arbitrary piecewise model regression of mckibben and peano muscle static and damping force behavior. *Smart Materials and Structures*, 27 (10):105048, 2018.

[171] Jiangbei Wang, Yanqiong Fei, and Wu Pang. Design, modeling, and testing of a soft pneumatic glove with segmented pneunets bending actuators. *IEEE/ASME Transactions on Mechatronics*, 24(3):990–1001, 2019.

[172] Wei Wang, Chenzhe Li, Hugo Rodrigue, Fengpei Yuan, Min-Woo Han, Maenghyo Cho, and Sung-Hoon Ahn. Kirigami/origami-based soft deployable reflector for optical beam steering. *Advanced Functional Materials*, 27(7): 1604214, 2017.

[173] Zhen-Pei Wang, Leong Hien Poh, Justin Dirrenberger, Yilin Zhu, and Samuel Forest. Isogeometric shape optimization of smoothed petal auxetic structures via computational periodic homogenization. *Computer Methods in Applied Mechanics and Engineering*, 323:250–271, 2017.

[174] Zheng Wang, Panagiotis Polygerinos, Johannes TB Overvelde, Kevin C Galloway, Katia Bertoldi, and Conor J Walsh. Interaction forces of soft fiber reinforced bending actuators. *IEEE/ASME Transactions on Mechatronics*, 22 (2):717–727, 2017.

[175] Robert J Webster III and Bryan A Jones. Design and kinematic modeling of constant curvature continuum robots: A review. *The International Journal of Robotics Research*, 29(13):1661–1683, 2010.

[176] Michael Wehner, Brendan Quinlivan, Patrick M Aubin, Ernesto Martinez-Villalpando, Michael Baumann, Leia Stirling, Kenneth Holt, Robert Wood, and Conor Walsh. A lightweight soft exosuit for gait assistance. In *2013 IEEE*

International Conference on Robotics and Automation, pages 3362–3369. IEEE, 2013.

[177] A Wineman. Nonlinear viscoelastic solids—a review. *Mathematics and mechanics of solids*, 14(3):300–366, 2009.

[178] Alan S Wineman and Kumbakonam Ramamani Rajagopal. *Mechanical response of polymers: an introduction.* Cambridge university press, 2000.

[179] Wei Yang, Zhong-Ming Li, Wei Shi, Bang-Hu Xie, and Ming-Bo Yang. Review on auxetic materials. *Journal of materials science*, 39(10):3269–3279, 2004.

[180] Davide Zappetti, Stefano Mintchev, Jun Shintake, and Dario Floreano. Bio-inspired tensegrity soft modular robots. In *Conference on Biomimetic and Biohybrid Systems*, pages 497–508. Springer, 2017.

[181] Zhenishbek Zhakypov, Christoph H Belke, and Jamie Paik. Tribot: A deployable, self-righting and multi-locomotive origami robot. In *2017 IEEE/RSJ International Conference on Intelligent Robots and Systems (IROS)*, pages 5580–5586. IEEE, 2017.

[182] Jun Zhang, Jun Sheng, Ciarán T O'Neill, Conor J Walsh, Robert J Wood, Jee-Hwan Ryu, Jaydev P Desai, and Michael C Yip. Robotic artificial muscles: Current progress and future perspectives. *IEEE Transactions on Robotics*, 35 (3):761–781, 2019.

[183] Ketao Zhang and Kaspar Althoefer. Designing origami-adapted deployable modules for soft continuum arms. In *Annual Conference Towards Autonomous Robotic Systems*, pages 138–147. Springer, 2019.